Measurement of the Flux of ^{8}B Solar Neutrinos at the Sudbury Neutrino Observatory

James Chilton Loach
Lincoln College, University of Oxford

Thesis submitted in partial fulfilment of the requirements for the degree of Doctor of Philosophy at the University of Oxford

Trinity Term, 2008

Measurement of the Flux of ^{8}B Solar Neutrinos at the Sudbury Neutrino Observatory

James Chilton Loach
Lincoln College, University of Oxford

Thesis submitted in partial fulfilment of the requirements for the degree of Doctor of Philosophy at the University of Oxford
Trinity Term 2008

Abstract

The Sudbury Neutrino Observatory (SNO) was a heavy water Čerenkov detector that had the unique ability to measure both the total active flux of solar neutrino, using a neutral current (NC) interaction, and the flux of electron neutrinos, using a charged current (CC) interaction. The experiment has demonstrated that neutrinos change flavour and that the total neutrino flux is consistent with the prediction of solar models.

This thesis presents results from the third phase of the experiment in which an array of ^{3}He proportional counters, called Neutral Current Detectors (NCDs), were deployed in the heavy water to detect neutrons produced in NC interactions of neutrinos with deuterium.

Converting the number of neutrons detected by the NCDs into a number of NC interactions required a knowledge of the neutron detection efficiency. This was determined using two methods: with a neutron calibration source mixed into the heavy water and with a calibrated Monte Carlo simulation. Methods for determining the strength of the mixed source, using a Ge detector and the PMT array, are presented, as well as significant improvements to the modelling of neutron propagation in the detector. Both methods were shown to be in agreement and the neutron detection efficiency was found to be 0.211 ± 0.07.

The total flux of solar neutrinos and the flux of electron neutrinos were statistically extracted from the NCD phase data using a technique that allowed a subset of the systematic parameters to have their values constrained by the neutrino data. The measured flux was

$$\Phi_{\mathrm{NC}} = 5.443^{+0.329}_{-0.327}\,(\mathrm{stat.})\,^{+0.318}_{-0.301}\,(\mathrm{syst.})\ \times 10^6\,\nu\,\mathrm{cm}^{-2}\,\mathrm{s}^{-1}$$

which is good agreement with standard solar models. The ratio of CC to NC fluxes, which is the fraction of electron neutrinos in the active neutrino flux, was found to be

$$\frac{\Phi_{\mathrm{CC}}}{\Phi_{\mathrm{NC}}} = 0.318^{+0.030}_{-0.031}\,(\mathrm{total})$$

On the assumption that the reduced flux of electron neutrinos was due to neutrino oscillations and that CPT invariance holds, a global fit to the results of solar experiments and the reactor anti-neutrino experiment KamLAND yielded the neutrino mixing parameters

$$\Delta m^2 = 7.94^{+0.42}_{-0.26} \times 10^{-5}\ \mathrm{eV}^2 \qquad \theta = 33.8^{+1.4}_{-1.3}\ \mathrm{degrees}$$

For my parents.

Acknowledgements

There are many people to thank for making this work possible and my years as a graduate student the formative ones that they've turned out to be.

Above all I want to thank my supervisor Nick Jelley, who has been a source of optimism, guidance, and patience throughout.

I've shared the ups and downs of graduate life with the Oxford students Jeanne, Jess, Charlotte, Wan, Gaby and Helen. The journey would not have been the same without sightseeing in Squamish, swimming in Sudbury or the relentless good humour from the far corner of the office.

I've enjoyed working with others at Oxford, notably Simon, Dave, Steve and, not least, Nick West, who helped both me and SNOMAN survive my forays into the code. Beverly, Kim and Sue have been patient guides through the mysteries of university regulations.

Within SNO I've had the pleasure of working with, and learning from, a remarkable group of people. Of the many I could mention, I want to thank a few in particular: Gene, Jimmy, Melin, Bruce and Carsten, who were fellow-neutron analysts, and Nikolai, Scott, Jason Goon and Blair of the signal extraction group. Jason Detwiler, Keith, Jaret, John Roberts, Marc and others have answered my questions. Christine, Aksel, Hamish and Art have given their time, energy and thoughts whenever I have asked.

I owe a huge amount of gratitude - I cannot express how much - to the Berkeley group who have supported me over the last year. In particular to Alan, for your sound advice and support behind the scenes, and to Gersende for sharing your goodwill and tiny office. It has been a privilege to work with such a pleasant and intelligent group of people and to spend time in such a beautiful corner of the world.

My final thanks are for Elisa who encouraged me to start this work all those years ago, and for Carolyn and Marta, whose endless patience and support helped me reach the end.

Was the Sun designed to provide a convenient laboratory for studying neutrino masses via oscillation? It almost seems that way.

JOHN BAHCALL
Neutrino Astrophysics (1989)

Contents

List of Figures

List of Tables

Glossary

3-ring One of the rings of NCD strings, when the strings were divided into 3 rings about a source position

6-ring One of the rings of NCD strings, when the strings were divided into 6 rings about a source position

ADC Analogue to Digital Converter

AV Acrylic Vessel

β_{14} A measure of the isotropy PMT hits in an event

CC Charged Current (neutrino interaction)

CNO cycle Minor energy- and neutrino-generating chain of nuclear reactions within the Sun; more important in larger stars

DAMN cuts A series of high level cuts for removing instrumental events

DAQ Data AcQuisition system

EGS4 A Monte Carlo code used to simulate the transport of electrons and gammas

EN External neutrons

ES Elastic Scattering (neutrino interaction)

FTN An algorithm for reconstructing event positions and directions using the PMT array

Hotspot A localised region of elevated radioactivity on the NCD array

HPGe High Purity Ge detector

ITR In Time Ratio, which is a measure of the fraction of PMT hits in an event that are prompt

LRF Laser Range Finder

MC Monte Carlo

MCNP Monte Carlo N-Particle transport code, used in this thesis to model neutron transport

MNS Maki-Nakagawa-Sakata

MSW Mikheyev-Smirnov-Wolfenstein

MXF MaXimum likelihood Fitter

NCD Neutral Current Detector

NC Neutral Current (neutrino interaction)

OCA Optical CAlibration

PDF Probability Distribution Function

PD Photodisintegration

pp chain Dominant energy- and neutrino-generating chain of nuclear reactions within the Sun

PSUP Photomultiplier Support Structure

RSP An algorithm for estimating event energies using the PMT array

SNOMAN SNO Monte Carlo and ANalysis software package

SNO Sudbury Neutrino Observatory

SSM Standard Solar Model

TPA Total Peak Area method for determining the number of counts in peak in Ge detector energy spectra

TSA Time Series Analysis used to study neutron calibration ^{252}Cf source data.

Chapter 1

Neutrinos and the Sun

> *Anaxagoras... incurred not only unpopularity, but even legal prosecution, by the tenor of his philosophical opinions, especially those on astronomy. To Greeks who believed in Helios and Selênê as not merely living things but Deities, his declaration that the Sun was a luminous and fiery stone, and the Moon an earthy mass, appeared alike absurd and impious. Such was the judgement of Sokrates, Plato, and Xenophon,... and the general Athenian public... [that] Perikles was compelled to send him away from Athens.*
>
> GEORGE GROTE
> Plato (1865)

For as long as man has had the capacity to wonder he must have done so about the Sun, the source of light and warmth that has crossed the sky each day for all of human history. Its importance to life must have been realised from the beginning and, throughout recorded history, it has found a place at the centre of myths and rituals built to explain the rhythms and vagaries of the world. Modern science has, as always, dispelled the myths but it has not diminished the Sun's importance; while no longer a deity it remains the source of energy that makes life possible, that drives the atmospheric and biological processes of the Earth.

The journey from the first speculations to our modern understanding has been coupled with the rise of science and, most of all, with the development of modern physics. Even a basic understanding of the Sun requires knowledge of all the fundamental forces of nature, and could not be achieved until as recently as the 1930s, when the weak interaction was first described. Throughout this journey, and still today, the Sun has been

more than just an object for study but also, because of its uniqueness in our immediate environment, a tool and a laboratory for studying fundamental physics: it has provided physicists with its electromagnetic spectrum, its gravitational field and its neutrinos.

There has been a particularly special relationship between solar and neutrino physics. The Earth-Sun system is the laboratory in which neutrino flavour change was first observed. The fusion reactions in the solar core generate a pure flux of electron neutrinos that is sent through the high density of the solar interior and then across 1.5×10^8 km of empty space before reaching the Earth. The comparison of measured fluxes with the predictions of solar models gave the first indications that neutrinos can change flavour and allowed parameters governing their oscillation to be measured. It also drove the development of precision solar models and measurement of their input parameters, and the eventual, beautiful agreement between theory and experiment has confirmed our understanding of the Sun.

The first experiment to detect solar neutrinos was the Homestake chlorine experiment [25], which took data from 1970 to 1994. It detected electron neutrinos using the inverse β-decay process

$$^{37}\mathrm{Cl} + \nu_e \rightarrow {}^{37}\mathrm{Ar} + \mathrm{e}^- \tag{1.1}$$

The measured interaction rate, corresponding to the production of less than one ^{37}Ar atom per day, disagreed with the predictions of solar models and became known as the *solar neutrino problem*. After being confirmed by further experiments and more refined solar models it was seen as strong evidence for the existence of either new solar physics or new neutrino physics.

The subject of this thesis, the Sudbury Neutrino Observatory (SNO), was an experiment designed to distinguish between the two possibilities, something which it did very successfully. SNO identified neutrino flavour change as the mechanism by making measurements of the combined flux of all active solar neutrinos and, separately, the flux of the flavour produced by the Sun. The difference of the ratio from unity demonstrated that neutrinos change flavour and explained the deficit in the Homestake experiment.

The ability of SNO to measure the combined flux of all neutrino flavours was unique. By comparing this flux to the predictions of solar models, SNO could test these models, independent of any details of neutrino flavour change. The comparison is important because neutrinos provide a unique window on the Sun: in their rate and energy spectrum they carry information from reaches of the Sun opaque to electromagnetic radiation, where the reactions that produce the neutrinos and generate the Sun's energy take place. The detection of solar neutrinos is the only direct evidence that nuclear reactions power the

Sun and the agreement between the total flux measured by SNO and model predictions is the first direct evidence that these nuclear processes are understood.

SNO's demonstration that neutrinos change flavour and the measurement of their oscillation parameters has been, and continues to be, important in the effort to produce a coherent model of the universe. But equally important is SNO's confirmation that our model of energy generation in the Sun is correct and that, after innumerable years of wondering, we do now understand the Sun.

This chapter presents background to both solar and neutrino physics. It first discusses the problem of the source of the Sun's energy and the construction of solar models. The remainder gives an overview of neutrinos within the standard model of particle physics (and extensions thereof), summarises the properties of neutrinos, and gives a survey of experimental results.

1.1 How the Sun shines

1.1.1 The source of the Sun's energy

Speculations

The enormity of the Sun's energy output was first quantified in independent measurements by Claude Pouillet [26] and John Herschell [27] in 1837. Allowing for corrections due to atmospheric absorption they measured solar constants close to the modern value of $L_\odot = 6500\ \mathrm{W\,cm^{-2}}$. The source of this energy was unknown and their research drew attention to the problem at a time when it was becoming amenable to quantitative study: the following decades saw the emergence of the principle of energy conservation and the development of thermodynamics. A number of theories appeared:

Mayer considered the problem of the Sun's energy [28] and showed that the fossil record disfavoured the most obvious explanations: that the Sun was a giant coal-burning furnace (the Earth was clearly older than the few thousand years such burning could sustain) or that it was a body that had initially been much hotter and was cooling slowly over time. In the same 1848 publication he proposed the *meteoric hypothesis* in which the Sun's heat had its origin in the kinetic energy of impacting meteorites. The idea remained in obscurity until it was independently proposed by Waterston in 1853 [29] and gained the influential support of Kelvin. The promising theory eventually foundered because of its incompatibility with the observed frequency of meteorite strikes on the Earth and

because there was no evidence for an increase in solar mass over time.

Some years before, in 1845, Waterston had proposed another theory, which turned out to be more compatible with observations, though at the time his papers were rejected for publication. He suggested gravitational contraction as the heat production mechanism and calculated that a reduction in the solar radius of 3 miles could maintain the current luminosity for about 9000 years [30]. It reached a wide scientific audience only after the success of his meteoric theory, which it quickly superseded, and remained in favour for much of the 19$^{\text{th}}$ century. Like that theory it too came to the attention of Kelvin, but more significantly to Helmholtz, who extended Waterston's calculations, finding that the gravitational collapse of the gaseous nebula from which the Sun was thought to have formed could maintain the solar luminosity for over 20 million years.

The English naturalist Charles Darwin was troubled by timescales of this order and felt that longer periods were necessary for evolution to have generated the current diversity of life. He made his own estimates for the age of geological features on the Earth, most notably the Weald in the first two editions of On the Origin of the Species [31] in 1859. The Weald is a valley in Kent between the chalk escarpments of the North and South Downs that was formed by the erosion of a dome-shaped structure known as an anticline. From an estimate of the mean rate of erosion Darwin calculated an age of 100-300 million years and noted that 'the denudation [erosion] of the Weald has been a mere trifle, in comparison with that which had removed masses of our Palaeozoic strata'. He believed the Earth was much older than 300 million years. However, Darwin actually removed these calculations, and all specific geological timescales, from later editions because they were irreconcilable with the views of Kelvin and others, which worried him greatly. Kelvin, it might be added, was at least as troubled by Darwin's theory of evolution by natural selection.

By the end of the 19$^{\text{th}}$ century it was clear the timescales for gravitational contraction were incompatible with geology and biology. Radioactive dating ultimately showed the great age of fossil bearing rocks [32] and the fossils themselves gave no indication of the large expected changes in the Sun's energy output over time.

Nuclear reactions

Tassoul and Tassoul [33] attribute the earliest suggestion of sub-atomic processes as the source of the Sun's energy to the geologist Thomas Chamberlin. In an 1899 paper [34] he made the analogy with latent chemical energies and wondered if atoms might be 'the complex organisations and the seats of enormous energies' exceeding even the 'enormous

resources that reside in gravitation'. It was a prescient idea and the study of radioactivity, notably of the large heating power of radium, soon gave it a firm grounding.

Given the discoveries in radioactivity at the turn of the century, it is perhaps remarkable that it wasn't until the 1930's that the exact mechanism for solar energy generation took its modern form. Knowledge of nuclear physics was won very slowly. The difficulties were twofold: first the challenge of conducting controlled experiments at nuclear scales and energies, and second the time it took to develop the theoretical framework to understand the experimental results, with the new ideas of quantum mechanics and relativity.

Nuclear fission had been ruled out as the mechanism by 1915 when it became clear that the abundance of heavy elements in the Sun was too low to generate the required amount of energy. Another possibility was suggested in that year by Harkins [35] who calculated the huge energy released from the conversion of hydrogen into helium and recognised its possible role in the Sun. Some years later, in 1920, the mechanism was proposed independently by Perrin [36, 37] and most famously by Eddington [38].

The way that fusion worked was slowly unravelled over many years. The particular chains of nuclear reactions by which the conversion of hydrogen to helium occurs in the Sun, known as the *pp (proton-proton) chain* and the *CNO (carbon-nitrogen-oxygen) cycle*, were formulated in 1938-39 through the work of Bethe, Critchfield and Weizsäcker (see for example [39]).

The two chains of nuclear reactions account for almost all energy production in main sequence stars: the pp chain dominates in stars with masses less than or comparable to the mass of the Sun and the CNO cycle dominates in those much larger. The rates of the processes have strong and distinct temperature-dependencies - the pp rate increases as T^5 and the CNO rate as T^{15} - and so prediction of the relative and absolute rates requires robust modelling of the solar interior. Modern solar models indicate that the pp chain is responsible for 98.4% of the Sun's energy output [1].

The pp chain was first developed by Bethe and Critchfield; they estimated the rate of the process and showed that it was consistent with the Sun's energy output. The chain of reactions is shown, in its modern form, in Figure 1.1.

The overall reaction is

$$4\,\mathrm{p} \rightarrow {}^4\mathrm{He} + 2\,\mathrm{e}^+ + 2\,\nu_e \tag{1.2}$$

where the two positrons annihilate with electrons and 26.73 MeV is released. The domi-

nant neutrino producing reaction is

$$\mathrm{p} + \mathrm{p} \rightarrow {}^{2}\mathrm{H} + \mathrm{e}^{+} + \nu_e \tag{1.3}$$

which produces *pp neutrinos* with an end point energy of 0.42 MeV. Less numerous are the mono-energetic *pep neutrinos* produced in

$$\mathrm{p} + \mathrm{e}^{-} + \mathrm{p} \rightarrow {}^{2}\mathrm{H} + \nu_e \tag{1.4}$$

Both of these reactions have deuterium in the final state, which takes part in further reactions and leads the pp chain to one of four terminations. The most probable PPI chain produces no further neutrinos. The next most probable is the PPII chain, which produces mono-energetic 0.384 MeV or 0.862 MeV ^{7}*Be neutrinos* via

$${}^{7}\mathrm{Be} + \mathrm{e}^{-} \rightarrow {}^{7}\mathrm{Li} + \nu_e \tag{1.5}$$

followed by the PPIII chain, which gives ^{8}*B neutrinos*; these have an end point energy of 15 MeV and are produced following the β^{+}-decay of ^{8}B produced in

$${}^{7}\mathrm{Be} + \mathrm{p} \rightarrow {}^{8}\mathrm{B} + \gamma \tag{1.6}$$

The least probable termination results in *hep neutrinos* with energies of up to 18.77 MeV via

$${}^{3}\mathrm{He} + \mathrm{p} \rightarrow {}^{4}\mathrm{He} + \mathrm{e}^{+} + \nu_e \tag{1.7}$$

The CNO cycle was independently discovered by Bethe and Weizsäcker in 1938. They realised that if other chemical elements were present in a star at its formation - that it was not composed initially of only hydrogen and helium - then other energy-producing reactions were possible. They engaged in systematic investigations and came across the remarkable CNO cycle. As in the pp chain four protons are converted into an alpha particle with the release of 26.73 MeV, but the path taken is very different. The CNO cycle uses ^{12}C as a catalyst: the isotope converts, in turn, into ^{13}N, ^{13}C, ^{14}N, ^{15}O, ^{15}N, and then back to ^{12}C, making a closed loop. Two low energy neutrinos are produced in this cycle.

1.1.2 Modelling the Sun

The task of building a coherent model of the Sun, suitable for predicting neutrino fluxes, is much more involved than identifying the energy generation mechanism. The Sun must be described as a whole, including radiation transport, material transport, thermodynamic

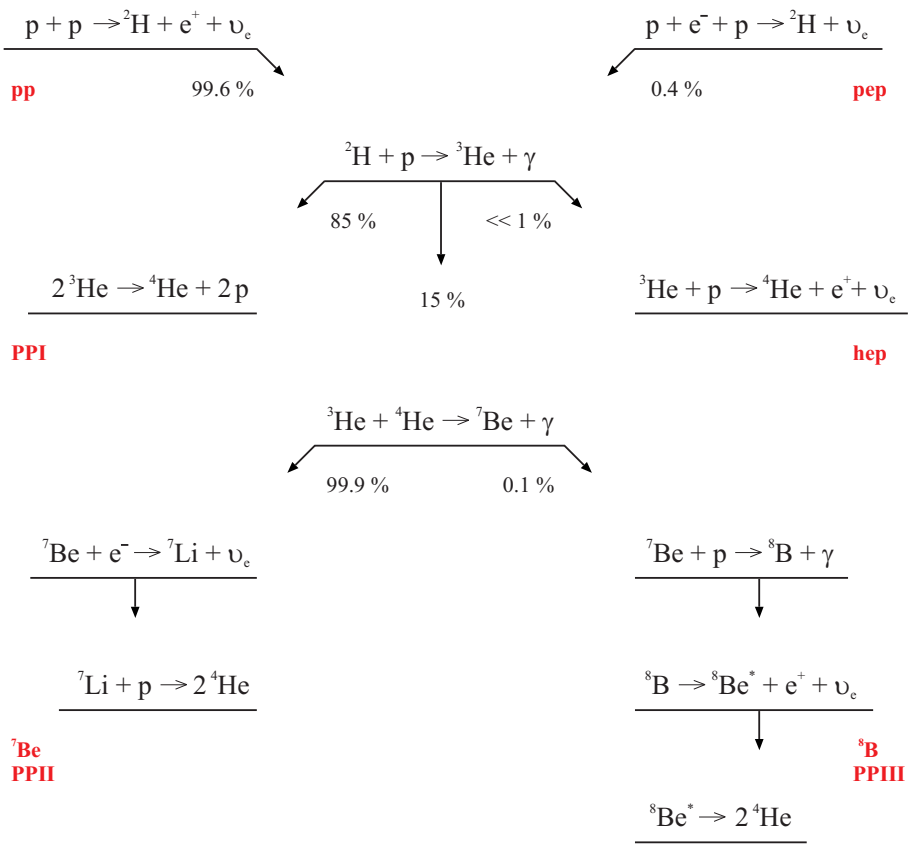

Figure 1.1: The pp chain.

Table 1.1: Important solar parameters (from [1]).

Parameter	Value
Photon luminosity ($L_\odot$)	3.86×10^{26} J s^{-1}
Neutrino luminosity	$0.023\, L_\odot$
Mass ($M_\odot$)	2.0×10^{30} kg
Radius ($R_\odot$)	696 000 km
Age	$\sim 4.55 \times 10^9$ y
Effective surface temperature	5.78×10^3 K
Central temperature	15.6×10^6 K
Initial helium abundance by mass (Y)	0.27
Initial heavy element abundance by mass (Z)	0.020

behaviour and variations in chemical composition, subject to boundary conditions in space and time.

The standard approach is to model the development of the Sun since its formation, subject to constraints on its initial composition and to the requirement that the model reproduce the current, observable properties of the Sun. The physical processes that govern stellar evolution are well understood in principle and the considerable sophistication of solar models is due to the numerical techniques they employ. The uncertainties in their predictions are mainly due to uncertainties on input parameters.

This section gives an overview of the main components of a solar model: the equations of stellar evolution, input parameters, boundary conditions, and calculational techniques. A more detailed discussion can be found in the book by Bahcall [1]. The most recent results from the widely-respected Bahcall model can be found in [2].

The equations of stellar evolution

The Sun is a main sequence star with a radius of 696 000 km and a mass of 2.0×10^{30} kg. Some of its important properties are given in Table 1.1.

Its gross structure can be divided into distinct regions as a function of radius: a dense, hot inner core, where nuclear fusion occurs; the radiation zone, in which radiative energy transfer dominates; the convection zone, in which convective energy transfer dominates; the opaque photosphere, in which the Sun's visible light is produced; and beyond this, a low density atmosphere.

Solar models begin with the basic equations of stellar evolution, which can be written

as follows, under the good assumption of spherical symmetry:

- *Hydrostatic equilibrium.*
$$\frac{\mathrm{d}P}{\mathrm{d}r} = -\frac{GM\rho}{r^2} \tag{1.8}$$
where G is the gravitational constant, P and ρ are the pressure and density, respectively, at a radius r, and M is the mass enclosed within r. This relationship expresses the fundamental balance between gravity and the pressures due to radiation and matter that resist collapse. The sun is treated as a quasistatic system.

- *Mass continuity.*
$$\frac{\mathrm{d}M}{\mathrm{d}r} = 4\pi r^2\rho \tag{1.9}$$
reflects the conservation of mass.

- *Luminosity gradient.*
$$\frac{\mathrm{d}L}{\mathrm{d}r} = 4\pi\rho\varepsilon \tag{1.10}$$
where L and ε are the luminosity and the energy generation rate, respectively, at a radius r. The luminosity is defined as the radiative energy per unit time through a sphere at radius r. This equation reflects conservation of energy; the flux of energy generated by nuclear reactions in the solar core follows the temperature gradient outwards in radius. Neglecting convection and small contributions from mechanical energy generation (for example, gravitational contraction) the observed luminosity is given by
$$L_\odot = \int_0^{R_\odot} \frac{\mathrm{d}L}{\mathrm{d}r}\mathrm{d}r \tag{1.11}$$
where $R_\odot$ is the solar radius.

- *Temperature gradient.*
$$\frac{\mathrm{d}T}{\mathrm{d}r} = -\frac{3\kappa L\rho}{16\pi\sigma c r^2 T^3} \tag{1.12}$$
where κ is the opacity, σ is the Stefan-Boltzmann constant and T is the temperature. This equation describes radiation transport, which is the dominant energy transport mechanism in all but the outer regions of the Sun.

These equations are accompanied by the equations of state, which express the pressure, opacity and energy generation rate as functions of density, temperature and chemical composition.

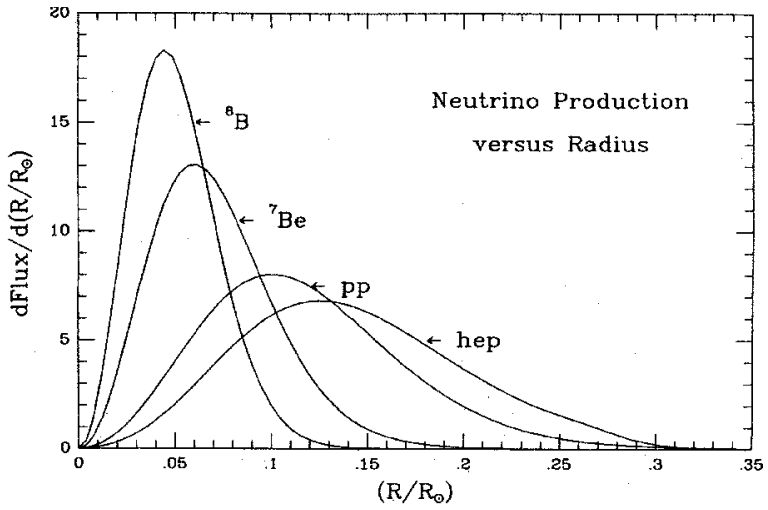

Figure 1.2: The radial production profile of pp chain neutrinos [1].

More refined models also include machinery for dealing with diffusion, in particular the gravitational settling of heavier elements such as ^{7}Li, and convection in the Sun's outer regions.

Input parameters, boundary conditions and calculational procedure

The main boundary condition that must be satisfied by Eq. 1.8 to 1.12 is the outer radial boundary condition, which is relatively unimportant for processes occurring in the solar core, such as neutrino production. This is rather fortuitous as the outer regions of the Sun are those most strongly affected by convection and turbulence, which are difficult to model. The typical approach is to assume convective equilibrium and the standard relationships between pressure and temperature that apply in this regime.

The initial chemical abundances are taken from two sources: spectroscopic measurements of the photosphere and of CI carbonaceous chondrite meteorites, which are known to be representative of the matter from which the solar system formed. Abundances from both sources are in excellent agreement [40]. In solar models the abundances are parametrised by three numbers: X, the mass fraction of hydrogen; Y, the mass fraction of helium; and Z, the mass fraction of elements heavier than helium. The ratio Z/X is one of the most important parameters. The parameter Y is difficult to measure and it is left as an adjustable parameter.

Radiative opacities determine the rate of energy transfer from the core to the outer regions of the Sun and calculating them is extremely complex. It requires a knowledge

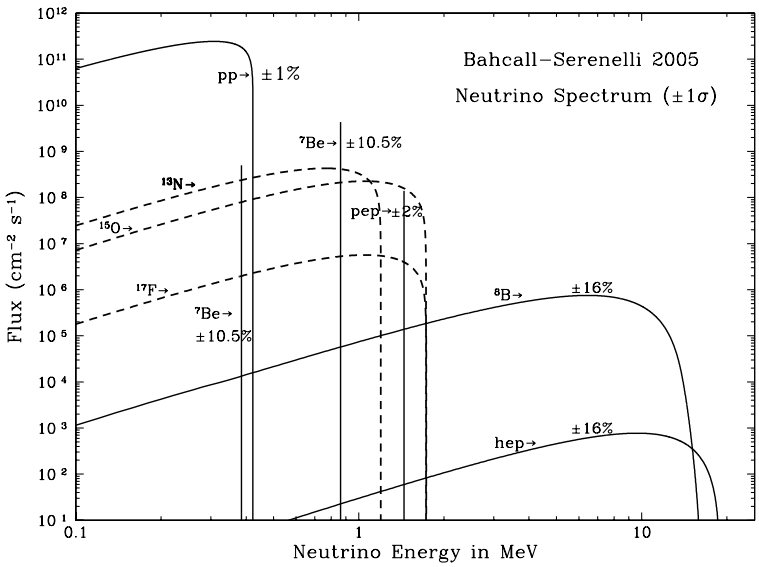

Figure 1.3: The predicted solar neutrino energy spectrum [2] showing pp (solid lines) and CNO neutrinos (dashed lines).

of the relative chemical abundances and a detailed simulation of the relevant statistical mechanics and atomic physics. Calculating solar opacities is a peaceful application of codes built originally for simulating nuclear weapons.

Nuclear reaction cross sections are the final important ingredient. Typical nuclear reactions within the Sun occur between charged particles at keV energies so the dominant mechanism is quantum mechanical tunnelling. The cross section for this process is conventionally parametrised by

$$\sigma(E) = \frac{S(E)}{E} \exp(-2\pi\eta) \tag{1.13}$$

where η is the Somerville parameter

$$\eta = \frac{zZe^2}{\hbar\nu}. \tag{1.14}$$

The term $\exp(-2\pi\eta)$, known as the Gamow penetration factor, is responsible for reducing many nuclear fusion cross sections to levels un-measurable in the laboratory at low solar energies (and consequently for ensuring the slow hydrogen burn rate and long life of the Sun). Experimental measurements are limited to the 100 keV scale but, because of the form of Eq. (1.14), can be scaled down in energy with reasonable precision; S(E) is expanded as a Taylor series and the coefficients fit to the experimental data. Recent measurements by the LUNA collaboration, using an underground accelerator to reduce

backgrounds, have made the best low energy measurements of a number of reactions, in particular ^{3}He(^{3}He,2p)^{4}He [41] and d(p,γ)^{3}He [42].

Solar models begin with a main sequence star of homogeneous composition and evolve it forward in time, typically in steps of 1×10^9 years, until the current age of the Sun is reached. There are usually two free parameters - the He mass fraction Y and an initial entropy-like variable - that are iterated until an accurate description of the current Sun is reached, meaning values of $M_\odot$, $L_\odot$ and $R_\odot$ differing from their present values by typically less than 1 part in 10^5.

The primary outputs of solar models are the current solar temperature profile, density profile, and chemical composition. These outputs can be used to predict the rate of the nuclear reactions in the core, in particular the relative rates of the different branches of the pp chain, from which predictions for the observed neutrino fluxes and energy spectra can be made. Figure 1.2 shows a radial neutrino production profile and Figure 1.3 shows a flux and energy spectrum prediction.

Helioseismology

The basic test of a solar model is its ability to converge to a state matching the current Sun in all of its observable parameters, but particularly mass, radius, luminosity and neutrino flux. It is important to note, though, that aside from comparison of these quantities, there is a further, very effective way of testing solar models called *helioseismology*, which is the study of the propagation of pressure waves within the Sun.

Pressure waves are produced by the turbulence in the convection zone and particular frequencies are amplified by constructive interference as they propagate between the boundaries of the convection zone with the radiation zone and the photosphere - the Sun acts as a resonant cavity. The frequencies of the modes are sensitive to the internal composition of the Sun, which makes compositions of measured and predicted oscillation frequencies very instructive. Figure 1.4 shows the radial dependence of the speed of sound, which can be inferred from the oscillation frequencies, and the excellent agreement with theory - the predicted and measured speeds agree to better than 0.1% between 0.05 and 0.95 $R_\odot$.

Helioseismology provides tests of many important parameters and, as such, is an invaluable tool for solar modellers. Its integration over the physics of the solar interior allows strong constraints to be placed on the rates of the dominant nuclear reactions but the relative rates of others can be changed with little effect on the oscillation frequencies.

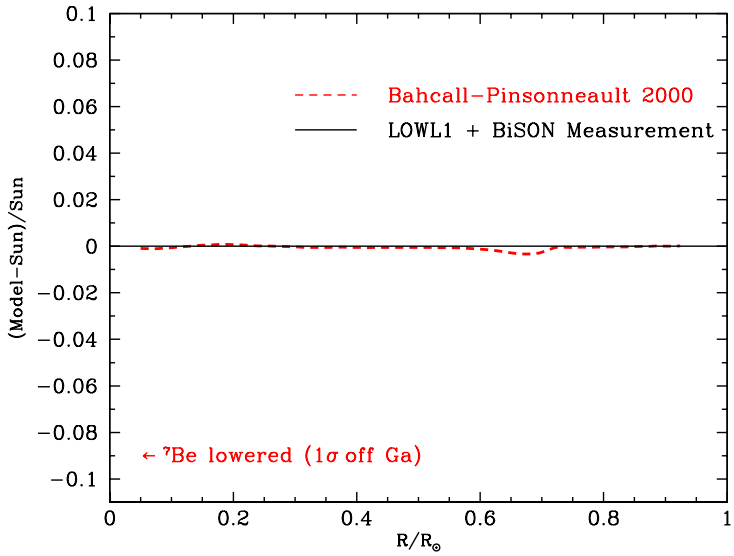

Figure 1.4: Agreement between sound speeds calculated using standard solar models (dashed line) and those measured helioseismologically [3].

1.2 The physics of massive neutrinos

1.2.1 Neutrinos and the standard model

The standard model of particle physics is a unified mathematical description of the electromagnetic, weak and strong interactions of the known elementary particles. The elementary particles are spin-1/2 fermions, which interact via the exchange of force carrying bosons. They are arranged in three generations, each consisting of two oppositely charged quarks, a charged lepton and neutrino.

Before the discovery of neutrino mass, a massless neutrino was present in each generation as the left-handed, uncharged partner of the left-handed charged lepton. Each left-handed doublet was accompanied by a right-handed charged lepton singlet. Experiment dictates that weak interactions couple only to ν_{L} and $\bar{\nu_{\mathrm{R}}}$ and this is reflected in the structure of the model.

To allow for neutrino mass, modifications are required to the minimal standard model as a non-zero neutrino mass is inconsistent with the particle's status as a Dirac particle existing in one helicity state - masses generated by the Higgs field involve both helicity states. There are two ways in which the model can be extended: by adding a right-handed Dirac neutrino state or by treating the neutrino as a Majorana particle,

meaning that it is its own anti-particle.

If the neutrino is a Dirac particle, as all charged fermions must be to conserve electric charge, then extra right-handed neutrino and left-handed anti-neutrino states must be added to each generation. The results of experiments, expressed in the basic symmetry of the standard model, dictate that these extra states must be sterile: to preserve the basic $\mathrm{SU_C}(3) \times \mathrm{SU_L}(2)$ structure, right-handed neutrinos would have to be singlets with respect to weak interaction and therefore be unable to interact weakly.

If the neutrino is a Majorana particle then it is its own anti-particle; the states ν_{L} and $\bar{\nu_{\mathrm{R}}}$ would be left-handed and right-handed states of the same particle. Majorana particles fit elegantly into generalisations of the standard model, where they take part in a see-saw mechanism, which can be used to explain the small neutrino mass scale.

1.2.2 Mixing

Whether neutrinos are Dirac or Majorana particles, it has been established that the weak eigenstates, in which neutrinos are produced, differ from the mass eigenstates, which govern their propagation. This difference generates the phenomena of neutrino oscillations: a neutrino produced in a given flavour eigenstate has a finite probability of being detected as a different flavour at a different time or point in space.

The neutrino flavour eigenstates ν_α ($\alpha = e, \mu, \tau$) can be written in terms of the mass eigenstates ν_i(i = 1, 2, 3)

$$|\nu_\alpha\rangle = \sum_i U_{\alpha i} \, |\nu_i\rangle \tag{1.15}$$

where $U_{\alpha i}$ is the Pontecorvo-Maki-Nakagawa-Sakata (PMNS) matrix. The nine parameters in this unitary matrix can be expressed in terms of 3 mixing angles and 1 CP-violating phase.

It is instructive, and often useful, to consider the mixing between two neutrino generations, say between electron and muon neutrinos. In this case the matrix U depends only on a single parameter and can be written

$$U = \begin{pmatrix} \cos\theta_{12} & \sin\theta_{12} \\ -\sin\theta_{12} & \cos\theta_{12} \end{pmatrix} \tag{1.16}$$

such that

$$|\nu_e\rangle = \cos\theta_{12} \, |\nu_1\rangle + \sin\theta_{12} \, |\nu_2\rangle \tag{1.17}$$

$$|\nu_\mu\rangle = -\sin\theta_{12} \, |\nu_1\rangle + \cos\theta_{12} \, |\nu_2\rangle \tag{1.18}$$

The mass eigenstates are stationary states and therefore have a time dependence given by

$$|\nu_1(t)\rangle = e^{-iE_1 t}\,|\nu_1(0)\rangle \tag{1.19}$$

$$|\nu_2(t)\rangle = e^{-iE_2 t}\,|\nu_2(0)\rangle \tag{1.20}$$

Now suppose there is a source of electron type neutrinos at $(x,t) = (0,0)$ of fixed energy E. The probability for finding the neutrino to still be electron type at a time t after its production is given by

$$P(\nu_e \to \nu_e) = |A(\nu_e \to \nu_e)|^2 = |\langle \nu_e | \nu_e(t)\rangle|^2 \tag{1.21}$$

where

$$|\nu_e(t)\rangle = \cos\theta_{12} e^{-iE_1 t}\,|\nu_1(0)\rangle + \sin\theta_{12} e^{-iE_2 t}\,|\nu_2(0)\rangle \tag{1.22}$$

At all practical energies neutrinos are highly relativistic so $p \gg m_i$ and $E \sim p$, and E_i can be written

$$E_i = \sqrt{p_i^2 + m_i^2} \simeq p_i + \frac{m_i^2}{2p_i} \simeq E + \frac{m_i^2}{2E} \tag{1.23}$$

so Eq. (1.22) becomes

$$|\nu_e(t)\rangle = e^{-iE_1 t}\left(\cos\theta_{12}\,|\nu_1(0)\rangle + \sin\theta_{12} e^{i\frac{\Delta m_{12}^2 t}{2E}}\,|\nu_2(0)\rangle\right) \tag{1.24}$$

where $\Delta m_{12}^2 = m_1^2 - m_2^2$. After some algebra, the probability P can then be written

$$P(\nu_e \to \nu_e) = 1 - \sin^2 2\theta_{12} \sin^2\left(\frac{\Delta m_{12}^2 L}{4E}\right) \tag{1.25}$$

where t has been replaced by L, which is the distance from the source to the measuring point. $P(\nu_e \to \nu_e)$ is referred to as the *survival probability*.

Examining Eq. (1.25) it can be seen that the survival probability oscillates with a characteristic length

$$L = \frac{4\pi E}{\Delta m_{12}^2}$$

which is the distance travelled by the neutrino before it returns to its initial state i.e. until the point where the probability of measuring it to be an electron neutrino is 1. The mixing angle θ_{12} determines the oscillation amplitude and the mass squared difference sets the oscillation length.

If the neutrino source has dimensions comparable to or larger than L, or produces neutrinos with a range of energies, then the average survival probability is given by

$$\overline{P(\nu_e \to \nu_e)} = 1 - \frac{1}{2}\sin^2\theta_{12}$$

The maximum suppression is therefore 1/2.

1.2.3 Matter enhancement

The considerations above apply to oscillations in vacuum, but if the neutrinos travel through a dense medium then the situation becomes more complex as propagation is affected by interactions with the medium. These interactions are not the same for all neutrinos flavours: electron neutrinos can scatter from electrons via the CC and NC interactions but muon and tau neutrinos can scatter only via the NC interaction. This difference in potential affects the flavour composition of a neutrino beam and is known at the *MSW* effect after Wolfenstein [43] who discovered it and Mikhaev and Smirnov who applied it to solar neutrinos [44].

Consider the case of two flavour mixing, but this time in the presence of a uniform medium. Electron neutrinos experience an additional potential V_w in their Hamiltonian, compared to muon and tau neutrinos, which alters their forward scattering amplitude. The weak potential V_w is given by

$$V_w = G_F\sqrt{2}N_e \tag{1.26}$$

where N_e is the electron density. This is equivalent to an extra effective mass so that m^2 becomes

$$m^2 = (E + V_w)^2 - p^2 \simeq m^2 + 2EV_w \tag{1.27}$$

Thus, the mass squared of the electron neutrino increases by

$$2\sqrt{2}G_F N_e E \tag{1.28}$$

The algebra from the previous section can be repeated with V_w included. The Schrödinger equation for the propagation of the flavour states is

$$i\frac{\mathrm{d}}{\mathrm{dt}}\begin{pmatrix}\nu_e\\ \nu_\mu\end{pmatrix} = M\begin{pmatrix}\nu_e\\ \nu_\mu\end{pmatrix} \tag{1.29}$$

where M is the mass matrix. For propagation in vacuum, M can be written

$$M_V = \frac{\Delta m^2}{4p}\begin{pmatrix}-\cos 2\theta & \sin 2\theta\\ \sin 2\theta & \cos 2\theta\end{pmatrix} \tag{1.30}$$

where terms giving the same phase factor to both flavours are neglected. For propagation in matter, M is given by

$$M_M = \frac{\Delta m^2}{4p}\begin{pmatrix}-\cos 2\theta + A & \sin 2\theta\\ \sin 2\theta & \cos 2\theta - A\end{pmatrix} \tag{1.31}$$

where $A = 2\sqrt{2}G_F N_e p/\Delta m^2$. If a matter mixing angle θ_m is defined such that

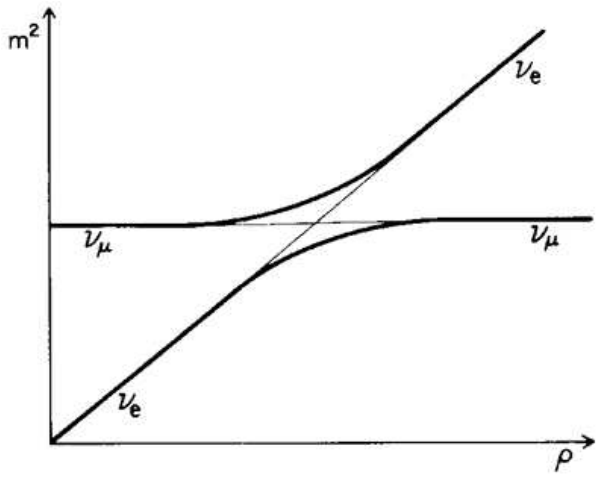

Figure 1.5: The MSW effect, for a small vacuum mixing angle [4]. The masses of the ν_e and ν_μ flavour eigenstates as a function of solar radius (light lines). The top dark line shows the development of a ν_e as it leaves the production point in the solar core and converts into a ν_μ.

$$\frac{\Delta m^2}{4p}\begin{pmatrix} -\cos 2\theta + A & \sin 2\theta \\ \sin 2\theta & \cos 2\theta - A \end{pmatrix} = \frac{\Delta m_m^2}{4p}\begin{pmatrix} -\cos 2\theta_m & \sin 2\theta_m \\ \sin 2\theta_m & \cos 2\theta_m \end{pmatrix} \tag{1.32}$$

then matter and vacuum mixing angles are related by

$$\tan 2\theta_m = \frac{\sin 2\theta}{\cos 2\theta - A} = \frac{\tan 2\theta}{1 - (L_\nu/L_m)\sec 2\theta} \tag{1.33}$$

where the vacuum oscillation is $L_\nu = 4\pi p/\Delta m^2$, as before, and the electron interaction length is $L_m = 4\pi/(2\sqrt{2}G_F N_e)$, so that $A = L_\nu/L_m$. Regardless of the value of θ, as long as $\Delta m^2 > 0$ (i.e. $m_2 > m_1$) a resonance can occur at an electron density equal to

$$N_e = \Delta m^2 \frac{\cos 2\theta_{12}}{2\sqrt{2}G_F p} \tag{1.34}$$

at which point the mixing becomes maximal.

Figure 1.5 shows the effect of this mechanism in the Sun where the electron density varies as a function of radius. This schematic figure applies to the situation where the vacuum mixing angle is small. The figure shows ν_e and ν_μ masses as a function of radius: the ν_μ mass is independent of electron density and is represented by a straight line, while the ν_e mass is proportional to electron density. At the resonance, where $\theta_m = \pi/4$, the ν_e has a mass that in vacuum would be largely identified with the ν_μ flavour eigenstate. It can be shown (see [1]) that, as long as the electron density changes slowly and adiabatically, transitions between the mass states ν_1 and ν_2 are suppressed and when the neutrino exits

the Sun in remains mostly ν_2; in the diagram the ν_e produced in the solar core follows the solid line and leaves the Sun as a ν_μ.

In the Sun the resonance condition is not met for low energy neutrinos and their behaviour is governed by vacuum oscillations. However, for higher energy neutrinos it can be met and results in greater suppression of the electron neutrino flux than possible with vacuum oscillations alone [4]. It can be shown [45] that the average survival probability in the presence of a matter oscillation resonance becomes

$$\overline{P_{MSW}(\nu_e \to \nu_e)} = \frac{1}{2} + \left(\frac{1}{2} - P_{jump}\right) \cos 2\theta_m \cos 2\theta_{12} \tag{1.35}$$

where θ_m is determined using the density at the ν_e production point and P_{jump} is the probability of jumping from one adiabatic mass state to the other, which is small because of the slowly changing electron density in the Sun. In contrast to the equivalent expression for vacuum oscillations (Eq. (1.2.2)) the minimum value of this expression can approach 0, rather than 1/2, making it a more powerful suppression mechanism.

The smoking gun signature for matter oscillations, as opposed to vacuum oscillations, is the characteristic energy dependence; the relatively larger suppression of neutrinos with enough energy to pass through resonance compared to those of lower energy. This can be observed by comparing the suppressions observed in experiments with different energy thresholds or by looking for distortions to the energy spectra of neutrinos produced with a continuous energy distribution. The former has been observed over the range of solar neutrino experiments but no measurement has yet been made of matter-induced spectral distortions.

A further signature for matter oscillations is the so-called *day-night effect* in which the solar neutrino flux measured during daytime differs from that measured during the nighttime, when the neutrinos have to pass through the additional mass of the Earth. During the night, the neutrino beam can be regenerated by the inverse of the process occurring in the Sun. This process, whereby a ν_μ can be converted into a ν_e is illustrated in Figure 1.5. It is predicted to be a small effect and has not yet been observed.

1.3 Evidence for neutrino mass and oscillations

1.3.1 Oscillation parameters

In three flavour neutrino mixing, the matrix U, which connects the flavour and mass eigenstates, can be factorised as

$$U = \begin{pmatrix} 1 & 0 & 0 \\ 0 & c_{23} & s_{23} \\ 0 & -s_{23} & c_{23} \end{pmatrix} \cdot \begin{pmatrix} c_{13} & 0 & s_{13}\, e^{-i\delta} \\ 0 & 1 & 0 \\ -s_{13}\, e^{i\delta} & 0 & c_{13} \end{pmatrix} \cdot \begin{pmatrix} c_{12} & s_{12} & 0 \\ -s_{12} & c_{12} & 0 \\ 0 & 0 & 1 \end{pmatrix} \tag{1.36}$$

where $s_{\alpha i} = \sin\theta_{\alpha i}$, $c_{\alpha i} = \cos\theta_{\alpha i}$, $\theta_{\alpha i}$ is the mixing angle and δ is the CP-violating phase. This form is convenient because, experimentally, θ_{13} is found to be small and $\Delta m^2_{23} \gg \Delta m^2_{12}$, meaning that mixing in the θ_{12} 'solar sector' and the θ_{23} 'atmospheric sector' can be approximated by two flavour oscillations, as described in the previous sections.

A full characterisation of the neutrino oscillation phenomena requires measurements of the four parameters in the matrix and the mass squared differences Δm^2_{12} and Δm^2_{23}. Meaningful measurements have been made of, or limits placed on, all the parameters except δ. Recent values are

Parameter	Value.	Main experiment(s)	Ref.
$\tan^2\theta_{12}$	$0.47^{+0.06}_{-0.05}$	SNO, KamLAND	[5]
$\sin^2\theta_{23}$	> 0.95	MINOS	[6]
$\sin^2\theta_{13}$	< 0.19	CHOOZ	[46]
Δm^2_{12}	$7.59^{+0.21}_{-0.21} \times 10^{-5}$ eV^2	SNO, KamLAND	[5]
Δm^2_{23}	$(2.43 \pm 0.13) \times 10^{-3}$ eV^2	MINOS	[6]

where uncertainties correspond to 68% confidence level except for CHOOZ which corresponds to 90% confidence level. The limit on $\sin^2\theta_{13}$ was quoted using $\Delta m^2_{23} = 1.9 \times 10^{-3}$ eV^2 and would be slightly lower for the value of Δm^2_{23} in the table. The solar sector mixing parameters do not include the data analysed in this thesis.

The following section describes the measurements of these parameters and of attempts to fix the mass hierarchy (the ordering in mass of the states ν_1, ν_2, ν_3) and scale (the absolute as opposed to the relative mass scale).

1.3.2 The solar sector

Measurements of θ_{12} and Δm^2_{12} are dominated by the SNO and KamLAND experiments.

The SNO experiment (described in detail in the next section) measured the total flux of solar neutrinos above ~ 5 MeV and its electron neutrino component. The physics signatures were the ratio of the ν_e flux to the total neutrino flux ($\nu_e + \nu_\mu + \nu_\tau$) and the ratio of ν_e fluxes during day and night. The results of the experiment are consistent with the primary oscillation mechanism being matter oscillations within the Sun.

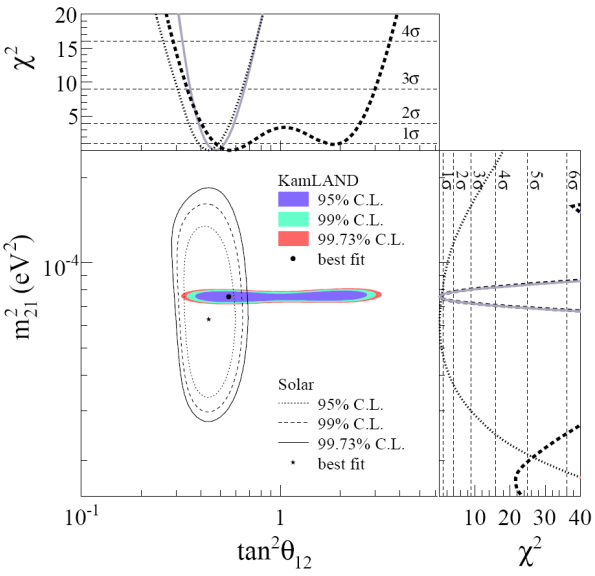

Figure 1.6: Contours showing allowed values of the solar sector mixing parameters [5]. This plot does not include the results from this thesis.

The observation of a ν_e to $(\nu_e + \nu_\mu + \nu_\tau)$ ratio of less than unity demonstrates that neutrinos change flavour. Its particular value places a strong constraint on θ_{12} and non-observation of a day-night effect, which would have been evidence for matter-regeneration of the ν_e flux within the Earth, places a weak constraint on Δm^2_{12}. The interpretation of the ν_e flux suppression in terms of the MSW effect means that $m_2 > m_1$.

The KamLAND experiment detects electron anti-neutrinos from nuclear reactors in Japan and South Korea. The typical baseline (reactor-experiment separation) is 180 km and $\bar{\nu_e}$ neutrinos are detected using the inverse beta decay process

$$\bar{\nu_e} + \mathrm{p} \rightarrow \mathrm{e}^+ + \mathrm{n} \tag{1.37}$$

whose signature is light from annihilation of the e^+ and a delayed 2.2 MeV γ from capture of the neutron by a proton. The active volume is 1000 tonnes of ultra-pure liquid scintillator contained in a transparent nylon balloon and instrumented with 1879 photomultiplier tubes. The combination of KamLAND's average baseline and a $\bar{\nu_e}$ energy spectrum extending to $\sim$ 7 MeV makes the experiment sensitive to vacuum oscillations in the same region of $\theta_{12} - \Delta m^2_{12}$ parameter space that SNO is sensitive to via matter oscillations.

KamLAND [47, 48, 5] observes a deficit in the anti-neutrino flux and a distortion in the detected neutrino energy spectrum characteristic of vacuum oscillations. There are

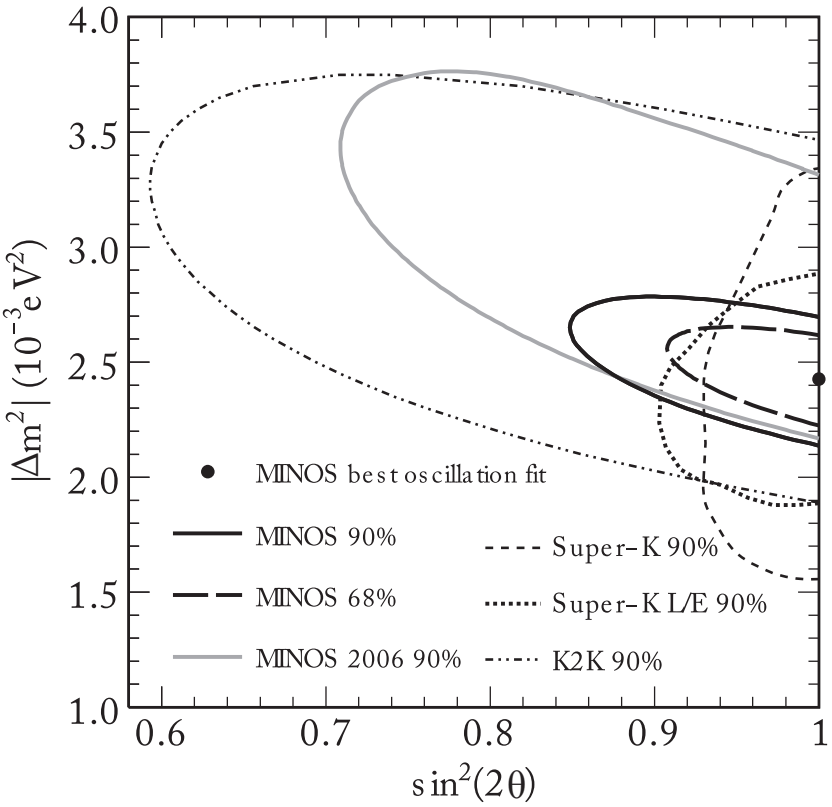

Figure 1.7: Contours showing allowed values for the atmospheric mixing parameters [6].

no matter oscillations because of the short baseline, low energies and low density of the Earth. KamLAND's results place a strong limit on Δm^2_{12} and a weaker one on θ_{12}.

If CPT invariance is assumed, so that the neutrino and anti-neutrino oscillation parameters are identical, then the results of the solar experiments and of KamLAND can be combined. Figure 1.6 shows the KamLAND and solar results (dominated by SNO) superimposed and in excellent agreement.

1.3.3 The atmospheric sector

The first direct evidence for neutrino mass was found in the analysis of atmospheric neutrino data taken by the Super-Kamiokande water Čerenkov detector [49].

Atmospheric neutrinos are produced by interactions of cosmic rays with nuclei in the Earth's atmosphere. Copious numbers of pions are produced in these reactions, which decay to muons and anti-muons with their accompanying neutrinos; additional muon

and electron neutrinos are produced when the muons decay. GeV-range neutrinos are produced uniformly at the same rate all around the Earth and so the measured upward- and downward-going fluxes at any point should be equal. Super-Kamiokande found that this was true for electron neutrinos but not for muon neutrinos, providing evidence that neutrinos have mass. This was interpreted as being due to their oscillation into tau neutrinos while passing through the Earth. Analysis of the data allowed Δm^2_{23} and θ_{23} to be measured.

In much the same was as KamLAND is able to probe the solar parameter space using a terrestrially generated neutrino source, so muon-neutrino-producing accelerator neutrino experiments are able to probe the atmospheric neutrino parameter space. K2K [50] and MINOS [6] are the most important experiments of this type. Each consists of an accelerator producing muon neutrinos, a near detector close to the source to characterise the beam and a far detector, positioned 250 km away for K2K and 735 km away for MINOS, to characterise the beam after oscillation. Both experiments have observed a deficit and seen the expected distortion to the energy spectrum. MINOS is a more recent and higher precision experiment.

Atmospheric and accelerator data can of course be combined to yield the best estimates for θ_{23} and Δm^2_{23}. The results of a recent global analysis are shown in Figure 1.7.

1.3.4 θ_{13} and CP violation

A parameter of particular importance in the mixing matrix is θ_{13}, which must be non-zero to allow CP violation to be measured. A measurement of CP violation in neutrinos would be of immense cosmological interest.

No measurement has yet been made of θ_{13} but there are two active approaches: a search for $\bar{\nu_e}$ disappearance in short baseline reactor neutrino experiments and ν_e or $\bar{\nu_e}$ appearance in a long baseline accelerator neutrino experiment. A measurement of a sufficiently large θ_{13} would motivate the construction of a neutrino factory, which is a high-intensity neutrino source using muon-storage rings, that could make a measurement of the CP-violating phase δ.

1.3.5 Remaining questions

The neutrino mass spectrum has only been partly resolved by existing experiments: measurements in the solar sector yield Δm^2_{12} and establish that $m_2 > m_1$ and those in the

atmospheric sector determine Δm^2_{23}. That leaves two pieces of information missing: the ordering of the ν_2 and ν_3 mass states - to establish the mass hierarchy - and the absolute mass of one of the neutrinos.

The mass hierarchy can be established from the study of the matter interactions of accelerator neutrinos. The absolute mass scale may be determined by the study of the β energy spectrum end point in tritium β decay, by measuring the effective Majorana mass in double beta decay, or from cosmological models. The strongest constraint is currently provided by the latter - [51] calculate a limit on the sum of the neutrino mass states of 0.17 eV at 95% confidence level.

Chapter 2

Measuring the flux of solar neutrinos

The first principle is that you must not fool yourself - and you are the easiest person to fool.

RICHARD FEYNMAN (1974)

2.1 The three phases of SNO

The SNO experiment used a heavy water target to detect ^{8}B solar neutrinos. The use of heavy water gave SNO the unique ability to measure both the total flux of solar neutrinos and its electron neutrino component. The experiment was proposed by Herb Chen [52] in 1984.

Neutrinos interact with heavy water in three ways, which are illustrated in Figure 2.1. They are

$$\nu_e + \mathrm{d} \rightarrow \mathrm{p} + \mathrm{p} + \mathrm{e}^- - 1.44 \text{ MeV} \tag{2.1}$$

$$\nu_x + \mathrm{e}^- \rightarrow \nu_x + \mathrm{e}^- \tag{2.2}$$

$$\nu_x + \mathrm{d} \rightarrow \mathrm{p} + \mathrm{n} + \nu_x - 2.22 \text{ MeV} \tag{2.3}$$

where the symbol ν_x refers to any neutrino flavour.

The charged-current (CC) interaction (Eq. 2.1) is sensitive only to electron-type neutrinos and its signature was the Čerenkov light produced by the final state electron. The threshold is 1.44 MeV and there is a weak correlation between the directions of the

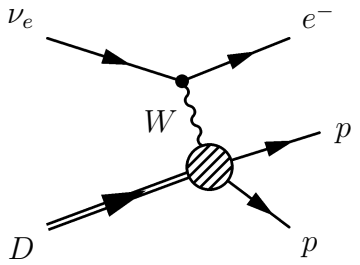

(a) Charged-current

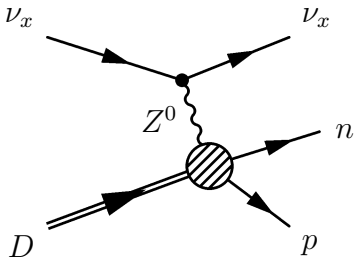

(b) Neutral-current

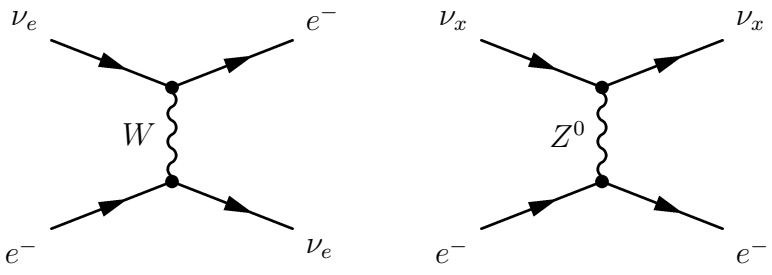

(c) (d)

Elastic scattering

Figure 2.1: Diagrams of the neutrino interactions in SNO. Adapted from [7].

electron and neutrino; the distribution of angles is given by

$$f(\cos\theta_\odot) \simeq 1 - \frac{1}{3}\cos\theta_\odot \tag{2.4}$$

where $\theta_\odot$ is the angle between the directions. There is a correlation between the electron and neutrino energies.

The elastic-scattering (ES) interaction (Eq. 2.2) is sensitive to all neutrino flavours, though preferentially to ν_e, by a factor of ~ 6 at solar neutrino energies compared to its sensitivity to ν_μ or ν_τ. This is because electron neutrinos can scatter via both W and Z^0 exchange whereas muon and tau neutrinos are restricted to the latter. The signature was again a final state Čerenkov electron and events were distinguished from CC events by the strong correlation between the neutrino and electron directions, which generates a sharp peak in the distribution of electron directions, pointing away from the Sun. At SNO energies the ES cross section is approximately 10 times smaller than CC, making this a minor interaction.

The neutral-current (NC) interaction (Eq. 2.3) is equally sensitive to all neutrino flavours. It has a threshold of 2.2 MeV and its signature was the production of the final state neutron. There was no correlation between the properties of the detected neutron and the neutrino - all energy and direction information was lost because neutrons scattered many times and thermalised before capture. The neutrons were counted via a different mechanism in each phase of the experiment: in the first phase using the gamma produced following capture back on a deuteron; in the second phase using the gamma cascade produced following capture on ^{35}Cl, introduced into the detector in the form of common salt; and in the third phase by capture on ^{3}He in an array of proportional counters anchored in the heavy water. The three phases are described in the following sections, after a brief description of the detector.

The detector is shown in Figure 2.2. It was designed and instrumented primarily to detect Čerenkov light from CC, ES and NC interactions in the heavy water - CC and ES from the final state electrons and NC from Compton-scattered electrons produced in (n,γ) reactions.

The target was 1000 tonnes of heavy water contained in a transparent acrylic vessel (AV) of diameter 12 m and thickness 5.5 cm, suspended by ropes from a deck structure at the top of the cavity. The AV had a cylindrical neck, or chimney, of diameter 1.5 m allowing access to the heavy water for deployment of calibration sources. Outside the AV was a region of ultra pure light water shielding and beyond that an array of 9456 20 cm photomultiplier tubes (PMTs), which were fixed to a 17.8 m diameter geodesic steel structure. Between the structure and cavity walls was a further region of light water

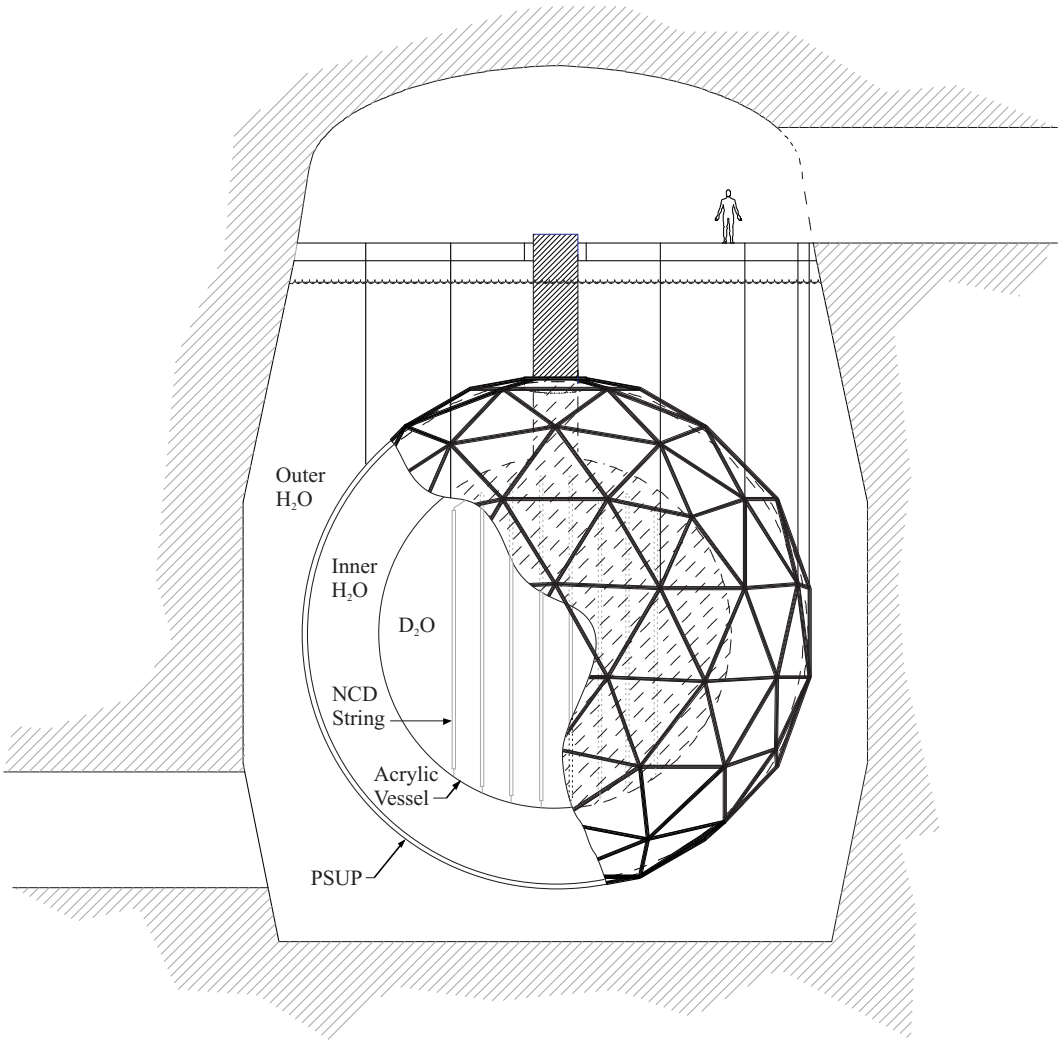

Figure 2.2: The SNO detector. Adapted from [8].

acting as both a shield from radioactivity in the rock and as a muon veto. The AV had transparent acrylic anchor blocks arranged on a grid in the lower half of the detector to anchor the proportional counters in the final phase of the experiment.

The detector was located at a depth of 2092 m (5890 ± 200 m water equivalent [53]) in the Creighton Nickel Mine in Sudbury, Canada. At this depth the cosmic ray muon flux is highly attenuated and only ~ 70 muons interacted in the heavy water per day.

Water purification systems maintained low levels of U, Th (and their daughters) in the light and heavy water and strict material selection procedures ensured very low levels in the fixed materials.

2.1.1 The D_2O phase

In the first phase of the experiment [54, 55], which ran from November 2, 1999 to May 31, 2001, neutrons were detected using the reaction

$$\mathrm{n} + \mathrm{d} \rightarrow \mathrm{t} + \gamma + 6.25 \text{ MeV} \tag{2.5}$$

in which a neutron captured on a deuteron producing a single 6.25 MeV gamma in the final state. The gamma typically Compton scattered an electron and the resultant Čerenkov light was detected.

This phase provided a precise measurement of the CC flux. The NC measurement was more limited, for two reasons: the first was the difficulty in distinguishing the CC electron from the Compton-scattered NC electron - in a fit, making no assumption on the neutrino energy spectrum, the only distinguishing observables were radius and direction from the Sun, in which CC and NC events did not differ strongly; the second was the low d(n,γ) cross section of 0.5 mb, which gave a neutron detection efficiency of only 14.4%, and correspondingly low statistics. It was possible to make a measurement of the NC flux using only radius and direction from the Sun as observables, but to made a good measurement the neutrino energy spectrum had to be assumed and energy used as an additional distinguishing variable.

2.1.2 The Salt phase

In the second phase of the experiment [9], which ran between July 26, 2001 and August 28, 2003, 2 tonnes of NaCl were added to the heavy water to improve the neutron response

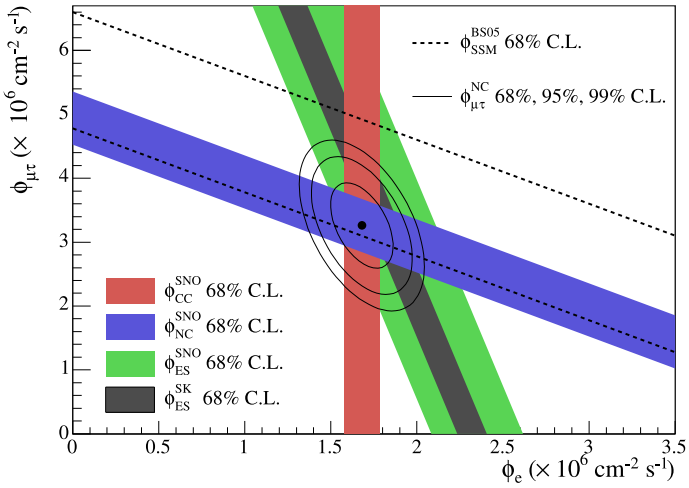

Figure 2.3: Results from the salt phase [9]. The plot shows the flux of muon + tau neutrinos versus the flux of electron neutrinos.

of the detector. Neutrons were detected using the reaction

$$n + {}^{35}Cl \rightarrow {}^{36}Cl + \gamma s + 8.6 \text{ MeV} \tag{2.6}$$

in which the neutron captured on ^{35}Cl emitting a cascade of gammas with a total energy of 8.6 MeV.

The addition of salt increased the neutron detection efficiency (to 41%) because of the large ^{35}Cl(n,γ) cross section of 44 b. It also allowed CC and NC events to be more easily distinguished: the gamma cascade produces multiple Compton-scattered electrons and therefore Čerenkov light that is more isotropic than that produced by a single CC electron. A good measurement of the NC flux could be made with no assumption on the neutrino energy spectrum. The results are shown in Figure 2.3.

2.1.3 The NCD phase

In the third phase of the experiment the salt was removed and an array of ^{3}He proportional counters, known as NCDs (neutral-current detectors), were deployed in the heavy water. Neutrons were detected using the reaction

$$n + {}^{3}He \rightarrow p + t + 764 \text{ keV} \tag{2.7}$$

There were three main reasons for changing the neutron detection mechanism so radically from the first two phases:

- *The CC-NC correlation was broken.*

  In the salt and D_2O phases there was a significant correlation between the CC and NC fluxes, which arose because of the large overlap of the distributions in each of the observables. In the NCD phase the correlation was much reduced because the CC and NC events were recorded in effectively independent detectors - CC events in the PMT array and NC events mainly in the NC array. These are the salt and NCD phase correlation matrices:

Salt phase			
	CC	ES	NC
CC	1.00		
ES	-0.16	1.00	
NC	**-0.52**	-0.06	1.00

NCD phase			
	CC	ES	NC
CC	1.00		
ES	0.24	1.00	
NC	**-0.19**	0.02	1.00

- *The systematics on the NC flux were different.*

  The systematic uncertainties associated with the NC measurement were substantially different to previous phases. SNO was a systematics-limited experiment and the exchange of one set of systematics on the NC flux for another was an extremely powerful check that the estimates for both sets of systematic uncertainties were robust.

- *Neutron contamination of the CC spectrum was diminished.*

  NC neutron events were the largest background to the CC signal in the first two phases but in the NCD phase they were greatly reduced in number: the ratio of NC to CC PMT events in the NCD phase was ~ 0.14 compared to ~ 0.92 in the salt phase. The benefit of this reduction in 'background' was somewhat offset by the interference of the NCD array with the detection of Čerenkov light but, even accounting for this, it was possible to make a measurement of the CC *flux* with comparable precision to previous phases. Note that the energy threshold was higher than in previous phases so the measurement necessarily provided less information on the CC (and therefore ^{8}B neutrino) energy *spectrum*.

The challenges of the NCD phase were accounting for the shadowing and reflection of Čerenkov light by the counters, handling the radioactivity introduced into the detector in the materials of the array, and identifying neutron events in the counters above the background of instrumental and radioactive backgrounds.

2.2 Detecting neutrons

2.2.1 The NCD array

The NCD array was an array of ^{3}He proportional counters which detected neutrons via the reaction

$$n + {}^3He \rightarrow p + t + 764 \text{ keV}$$

and recorded the ionisation produced by the final state proton and triton. Such counters are widely used for neutron detection, but the design of an array suitable for use inside the target of a low background Čerenkov detector presented unique challenges. The array had to have the following properties:

- high neutron capture efficiency,
- geometry causing minimal interference with Čerenkov light from CC reactions,
- low radioactive contamination to minimise the background to the NC signal from ionisation due to alphas produced inside the counters and neutrons produced by photodisintegration of deuterons external to the counters,
- provide sufficient information on the characteristics of the ionisation to allow neutron events to be distinguished from instrumental events and those due to radioactivity,
- mechanical stability over long periods of time in the large pressures at the bottom of the heavy water and in an environment subject to seismic disturbances.

The need for a high capture efficiency and small interference with Čerenkov light fixed the basic geometry of the array, which consisted of long, thin counters sparsely distributed throughout the heavy water. The high ^{3}He neutron capture cross section of 5316 b meant that the counters, with a diameter of 5 cm, remained effectively black to neutrons.

The need for low backgrounds required that the amount of material added to the detector be minimised, that the material added have as small an amount of radioactive contamination as possible, and what contamination there was be accurately measured. The nickel counter walls, in particular, were made extremely thin; specialist low-background processes were used to produce the bodies; and the long periods of underground storage prior to deployment used to allow cosmogenic activity to decay away.

The ability to separate events due to neutrons from backgrounds required a combination of gas properties and counter radius such that ionisation from typical events was

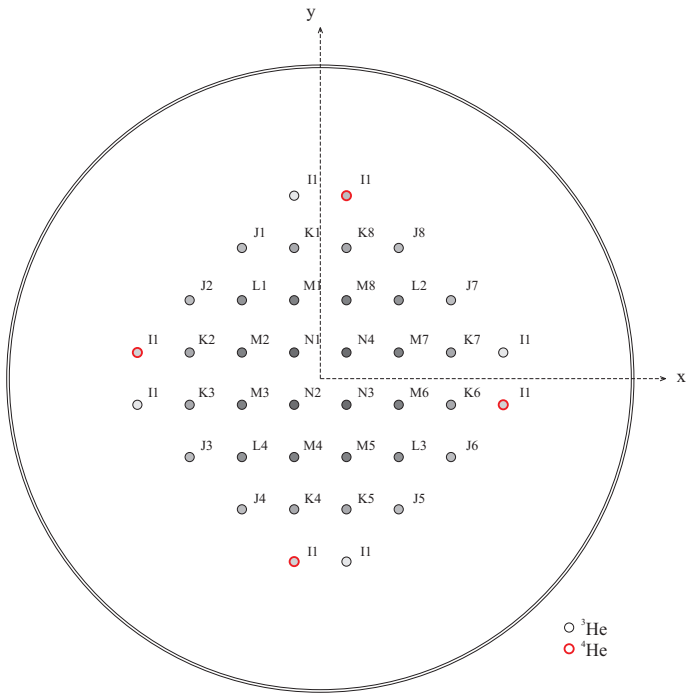

Figure 2.4: The NCD array looking down into the detector in the negative z direction.

contained within the counters - that the probability of particles colliding with the walls be minimised. Pulses were digitised to allow comparison of the energy deposition profiles between different pulses. Some counters were filled with ^{4}He rather than ^{3}He to allow the study of backgrounds; the radiation transport properties of the two gases are identical but ^{4}He could not capture neutrons.

Each NCD was a string of 3 or 4 counters laser-welded together in series. Strings were buoyant and were anchored to fixtures built into the acrylic vessel. Signals were read out from strings via cables leaving the tops of the strings and exiting the detector through the AV neck. The cables were attached to the anode wires using flexible resistive couplers.

The geometrical arrangement of the NCDs is shown in Figure 2.4. Cartesian and spherical coordinates systems were defined with respect to an origin at the centre of the PSUP, which approximately coincided with the centre of the AV. In the Cartesian system the z-axis is vertical and parallel with the NCDs. The only spherical coordinate used in this thesis is $r = (x^2 + y^2 + z^2)^{1/2}$.

The NCDs were positioned on a 1 m grid; in the xy-plane they were clustered towards the centre of the detector, though vertically they extended to within 10s of cm

of the AV. The clustering in the xy-plane was to reduce the length of the cables (and therefore the amount of associated U and Th in the detector) and to optimise the neutron detection efficiency.

The array geometry was originally optimised for a measurement of 1/3 of the standard solar model rate, which called for a 96 string arrangement. However, given the strong indication from the first two phases that the NC flux was consistent with expectations the array could be reduced to 40 strings comprising 156 individual counters and 398 m of active length.

A diagram of an NCD string is shown in Figure 2.5. The average wall thickness was ~ 400 μm and the copper anode wire had a diameter of 50 μm. The counter gas was a mixture of 85% ^{3}He or ^{4}He by pressure with 15% CF_4 at a pressure of 2.50 ± 0.01 atm. The ^{3}He density was 1.07×10^{-4} g cm^{-3}.

The nickel used in the counters was produced in a chemical vapour deposition (CVD) process. The process began with a source of nickel which was heated in a carbon monoxide atmosphere. Under pressure at $\sim$ 50 C nickel combines with carbon monoxide to form gaseous $Ni(CO)_4$, a process which reverses at $\sim$ 175 C. Using this cycle nickel could be extracted from the source and deposited onto cylindrical mandrels with diameters equal to the inner diameters of the counters. The nickel was purified because, while U and Th also form carbonyls, they do not do so reversibly at these temperatures.

Finished counter bodies were stored underground to allow cosmogenic activity to decay away and were etched and electropolished to remove any contamination from the handling and storage processes, in particular the alpha-emitting radon daughter ^{210}Po, which was discovered on the surfaces in relatively high concentration.

Electrical field lines close to the counter ends were necessarily distorted by the counter geometry, so fused silica insulators were fitted around the anode wires at these points to prevent deposited ionisation from being collected. This caused a small reduction in the active volume of the array - and hence in the neutron detection efficiency - but prevented distorted pulses, which would have been difficult to model, from entering the data steam.

Strings were installed using a remotely operated vehicle (ROV), which was a custom built submersible used to guide the NCD anchors into their fixtures.

After deployment, two discrete sources of radioactive contamination were discovered on strings K2 and K5. Using a variety of methods the composition of these *hotspots* could be determined and accounted for in the analysis; the way in which this was done is

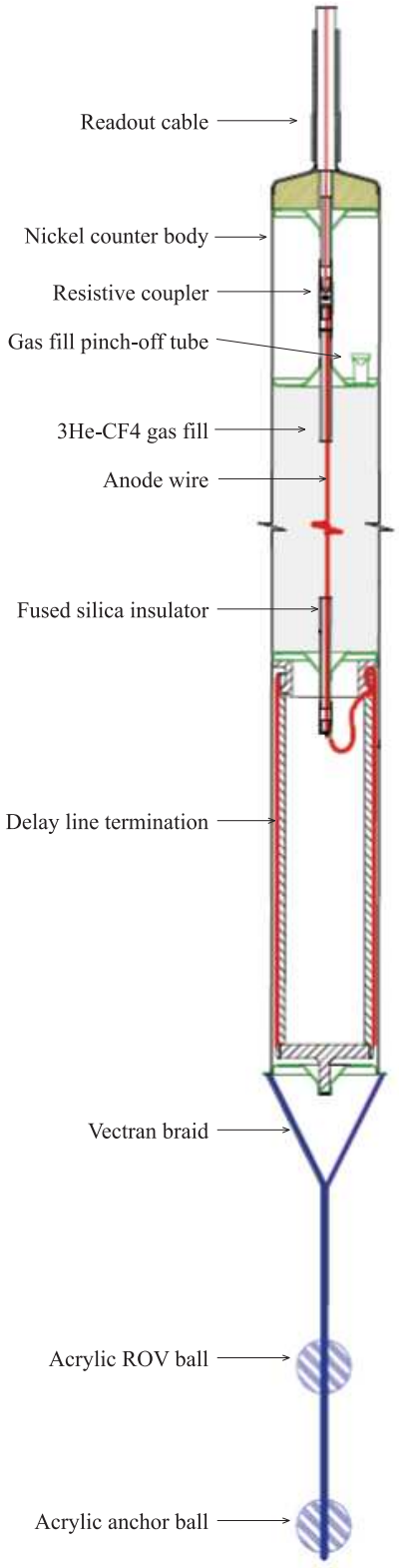

Figure 2.5: An NCD string. Adapted from [8].

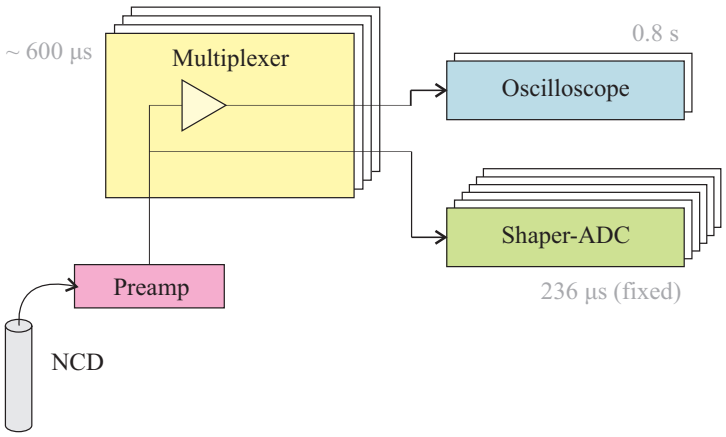

Figure 2.6: Schematic diagram showing the main components of the NCD electronics. The numbers in grey indicate the dead time associated with each component.

discussed in detail in Section 8.2.4. Other mechanical defects observed in the array were a leak of ^{3}He into the counter-interspace region on string K5; permanent or periodic electrical disconnect due to faulty resistive couplers on strings K2 and M8; and gain instabilities on string K7.

2.2.2 Data acquisition

The NCD data acquisition system (DAQ) was designed to detect neutrons from two different sources with very different characteristic event rates: ^{8}B solar neutrinos and neutrinos from a possible galactic supernova.

A galactic supernova of the magnitude expected every 100 years would have produced a large burst of neutrons with a kHz event rate, and the number of events and relative timing would be of immense physical interest. For low rate solar neutrino data the main issue was the ability to distinguish neutron events from backgrounds and instrumentals and, to this end, the detector was required to digitise individual pulses to allow discrimination based on the energy deposition profiles.

To achieve the goals of high rate data collection and pulse digitisation in a cost effective manner, a system was designed that had two paths with independent triggers: a fast pulse integration path with a threshold set on event charge and a slower digitisation path with a threshold set on pulse amplitude. A simplified diagram of the system is shown in Figure 2.6.

The pulse integration path is referred to as the *shaper-ADC* system. Signals were

integrated by a series of operational amplifiers and compared to a threshold set string-by-string. There was one shaper-ADC for every 6 or 7 strings and the dead time was fixed at 236 μs. To verify the dead time each channel was fitted with a scalar counter to count the number of times the signal crossed the threshold but was not read out.

The digitisation path is referred to as the *scope* system. The path began in the multiplexer - one box for up to 12 strings - where signals were log-amplified to help deal with the large dynamic range. If the pulse passed a given threshold, again set string-by-string, the multiplexer attempted to digitise the event using one of a pair of oscilloscopes. If a scope was available it digitised the pulse at a rate of 1 GHz for 15 μs. The dead time associated with each multiplexer was typically 600 μs and with each scope, 0.8 s.

Events selected for data analysis had to trigger both the shaper-ADC and scope systems.

2.2.3 Events in the counters

The physics events in the counters were neutron captures and events due to alphas, electrons and gammas from radioactive backgrounds. Alphas were by far the most important background to the neutron signal.

A neutron capturing in a counter produced a back-to-back proton-triton pair with total energy 764 keV, which was the maximum amount of energy that could be deposited as ionisation (the triton and proton carried 191 and 563 keV respectively). The minimum amount of energy typically deposited in the gas was 191 keV, occurring when the proton struck the counter wall immediately after being produced. Some of the topologies are illustrated in Figure 2.9. Both the proton and neutron have Bragg peaks and neutron events, with suitable geometries, generated characteristic double-peaked pulses.

Alpha events had a single Bragg peak and the pulses were therefore single-peaked. They ranged in energy up to $\sim$ 9 MeV and had a spectrum that was featureless in the neutron region (191-764 keV). Over the whole energy range, the spectrum for U and Th chain *bulk alphas* produced within the nickel walls was featureless, but the Po surface alphas produced a large peak at 5.3 MeV.

Electrons and gammas produced long, low energy pulses that made them easy to distinguish from neutrons and alphas.

Individually, background neutrons were indistinguishable from signal neutrons because they typically scattered many times and thermalised before capture. The main pro-

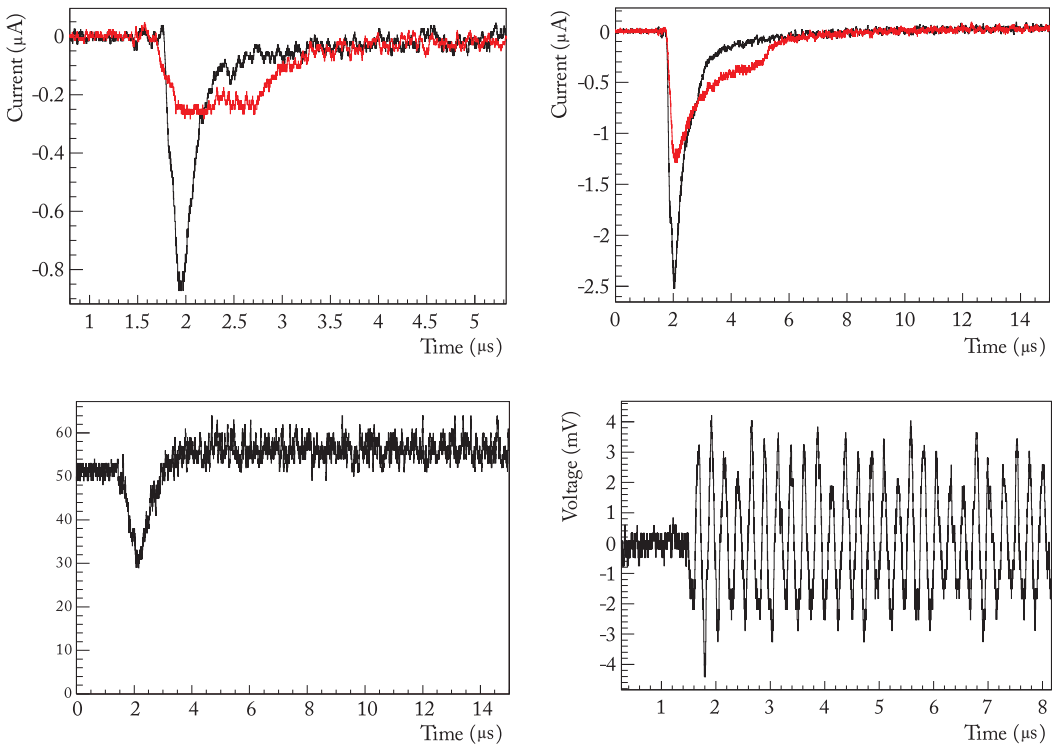

Figure 2.7: Example pulses: neutron (top left), alpha (top right), J3 instrumental (bottom left), and oscillatory noise event (bottom right). In the neutron and alpha panels the red lines are pulses where the ionisation was deposited along a path oriented close to the counter radius, perpendicular to the wire, and the black lines represent pulses where it was deposited close to parallel with the wire.

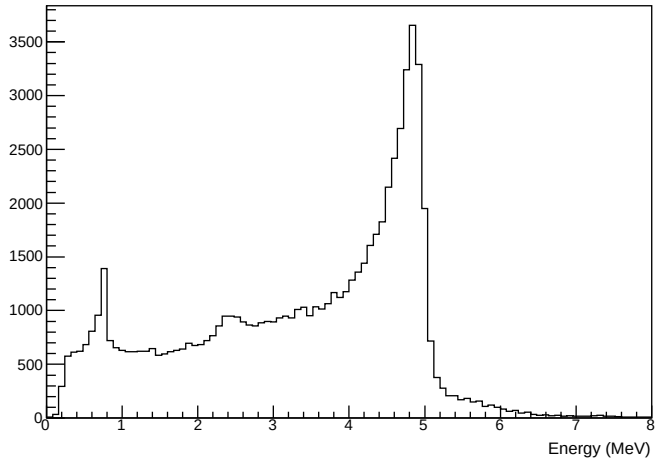

Figure 2.8: Shaper-ADC energy spectrum for the neutrino data set.

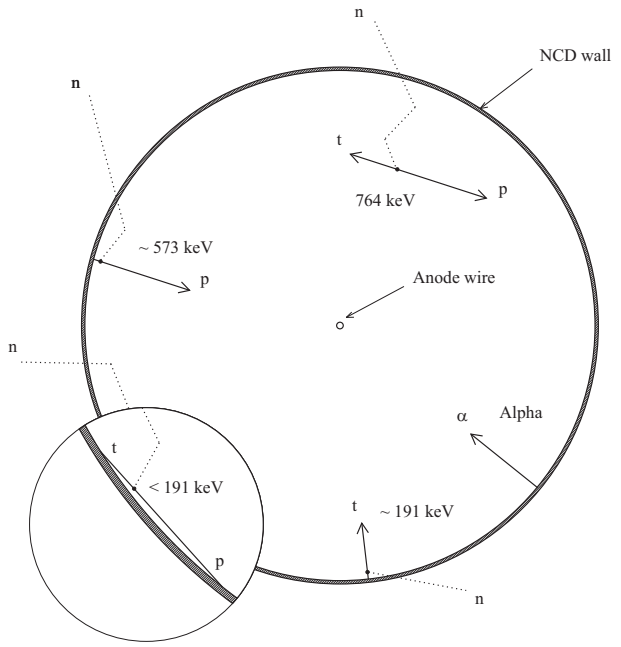

Figure 2.9: Different types of neutron event showing the amounts of energy deposited in the gas.

duction mechanism was the photodisintegration (PD) of deuterons by low energy gammas from U and Th in the materials of the detector:

$$\gamma + {}^2\mathrm{H} \rightarrow {}^1\mathrm{H} + \mathrm{n} - 2.2\ \mathrm{MeV} \tag{2.8}$$

The number of background neutrons was determined by assays, which directly measured levels of U and Th, and by an analysis of low energy events detected by the PMT array [56].

Non-physics instrumental events were primarily due to electrical discharges and could be easily distinguished from physics events based on pulse shape. Two sets of instrumental cuts were developed for this task, one in the time domain and one in the frequency domain. Events selected for data analysis had to pass both sets of instrumental cuts. Two classes of low energy event on strings J3 and N4 proved difficult to distinguish from neutrons; the way in which they were handled in the final analysis is described in Section 8.2.4.

Example signal, background and instrumental pulse shapes are shown in Figure 2.7. A shaper-ADC energy spectrum from neutrino data-taking is shown in Figure 2.8.

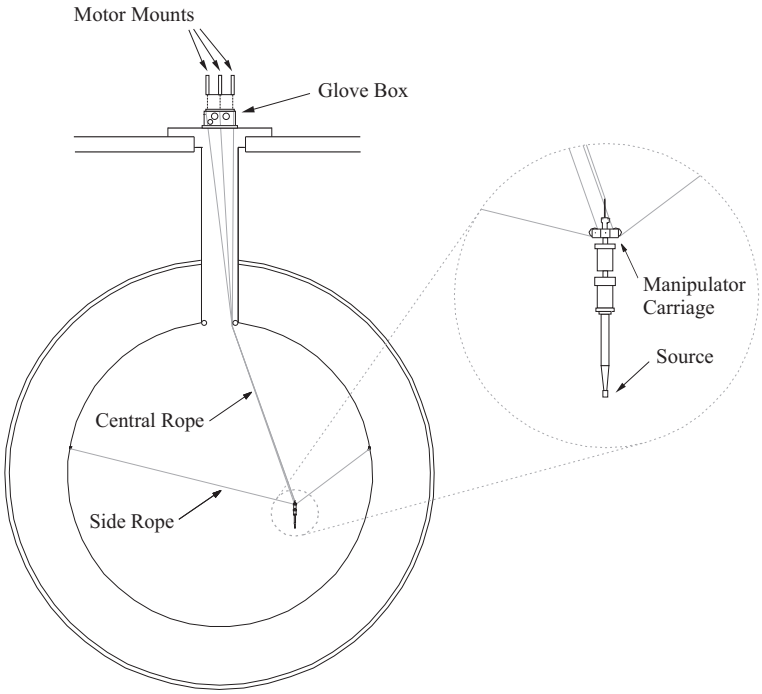

Figure 2.10: The calibration source manipulator system. Adapted from [8].

2.3 Detecting Čerenkov light

2.3.1 The PMT array

The PMT array consisted of 9456 20 cm photomultiplier tubes custom made for SNO with low radioactivity glass and components. 9438 of the tubes faced inwards to detect neutrino events; 91 faced outwards to instrument the light water region, making it an effective muon veto; 4 were installed in the detector neck to veto events caused by static discharges in the gas above the heavy water; and 23 were mounted on a removable sled to allow studies of material ageing.

The tubes facing inwards were fitted into reflective concentrators, which increased the effective photocathode coverage by $\sim 60\%$. Magnetic compensation coils built into the cavity walls cancelled the vertical component of the Earth's magnetic field, increasing the collection efficiency by an average of 10%.

Event positions and directions were estimated using a time-of-flight fitter and energies using a position-dependent conversion applied to the number of hit PMTs.

2.4 Calibration

2.4.1 Electronics calibrations

Regular electronics calibrations were required for both the NCD and PMT arrays.

For the NCD array there were two classes of calibration: one measured the response of the electronics and one searched for anomalous behaviour symptomatic of electrical disconnects at the resistive couplers connecting the anode wires to the cables.

The electronics response calibration was used to determine the linearity of the system, to quantify the shaper-ADC and digitisation thresholds and to measure the parameters governing the logarithmic amplification and digitisation of pulses. Electrical pulses of various shapes were injected into the preamplifier and compared with the recorded pulses to extract the parameters of interest.

The electrical disconnect calibrations were performed to search for failure of the resistive couplers. During the NCD phase one string suffered a permanent failure and another experienced intermittent failure. The disconnects were discovered by the observation of anomalously long periods where no events were observed in the detectors. To guard against this behaviour in other strings, on shorter and therefore less noticeable timescales, a calibration task was implemented that injected a distinctive square pulse into a preamplifier every minute, and looked for reflected pulses with shapes indicative of disconnects. None were found on any other strings.

PMT electronics calibrations were used to measure various parameters such as the discriminator thresholds and timing.

2.4.2 Physics calibrations

Calibration sources were used to determine the response of the NCD and PMT arrays to physics events. Two different classes of source were used: *point sources* positioned at discrete locations around the detector using a manipulator system (see Figure 2.10) and *distributed sources*, which were radioisotopes injected into the heavy water to produce uniform sources. The vast majority of calibration data were taken with point sources.

The manipulator could position the source in almost any position in two perpendicular vertical planes in the detector; the movement of the source was constrained to these planes by the geometry of the NCD array. The source could be positioned with an accuracy of 1-2 cm on the central axis of the detector and with less accuracy, though

Table 2.1: Calibration sources used during the NCD phase.

Class	Source	Description	Calibration	PMT	NCD
Point	Laserball	Isotropic light; discrete wavelengths (337-619 nm)	Optics and position reconstruction	yes	
	^{16}N	6.13 MeV γ; triggered	Energy estimation	yes	
	^{8}Li	β-decay electrons; end point $\sim$ 14 MeV	Energy estimation	yes	
	Th	Low energy gammas	Low energy backgrounds	yes	
	AmBe	n and 4.4 MeV γ	Neutron detection eff.	yes	yes
	^{252}Cf	Fission neutrons	Neutron detection eff.	yes	yes
Dist.	^{222}Rn	Low energy gammas; neutrons via ^{2}H(γ,n)^{3}H	Low energy backgrounds	yes	
	^{24}Na	Low energy gammas; neutrons via ^{2}H(γ,n)^{3}H	Neutron detection eff.; low energy backgrounds	yes	yes

always better than 5 cm, at other positions.

A list of the calibration sources is given in Table 2.1. The individual calibrations are described below:

- *Optics* (laserball).

  These calibrations were used to measure the timing response of each PMT, measure the optical properties of the detector components, fit the positions of the NCD strings (see Section 4.3.2), and assess systematic uncertainties and define functions to account for NCD shadowing for use in the position reconstruction fitters [57, 58]. The laserball was a pulsed laser source combined with a diffuser ball to produce near-isotropic light.

  Event positions were estimated using the information provided by the optics calibrations and the FTN event reconstruction algorithm [59]. FTN used the relative timing of PMT hits and a model of the detector response to infer event positions.

- *Energy* (^{16}N, ^{8}Li).

  The goal of the energy calibration was to estimate the parameters in a model converting the number of hit PMTs into an event energy and assign systematic uncertainties.

Event energies were estimated using the information provided by the energy calibrations, optical calibrations and the RSP energy estimator [60]. RSP used the number of prompt PMT hits and a model of the detector response to infer event energies. The energy deposited in the detector is referred to as effective kinetic energy. The output of the RSP estimator is numerically equal to the sum of the effective kinetic energy and the electron mass.

- *Low energy backgrounds* (Th, ^{24}Na, ^{222}Rn)

  Source runs were used in the *in situ* low energy background analysis to create probability distribution functions for light from U- and Th-chain activity in the detector materials that could be used to fit the amount of activity due to each and thereby infer the number of neutrons produced by the activity, via deuteron photodisintegration.

- *Neutron detection efficiency* (AmBe, ^{252}Cf, ^{24}Na)

  This was the measurement of the probability that a NC neutron produced in the detector would be detected by the PMT or NCD array. It is one of the main subjects of this thesis and will be discussed in detail in subsequent chapters.

2.5 Thesis outline

This thesis describes two analyses: the measurement of the flux of ^{8}B neutrinos, most importantly via the NC interaction, which is sensitive to all active neutrino flavours; and the measurement of one of the important component numbers in that analysis - the probability that a neutron produced in an NC interaction was detected.

These analyses were performed as part of a collaboration of many people doing closely related work. The physics chapters of this thesis concentrate on areas in which the author took a leading role and efforts have been made to cite the contributions of others where appropriate.

The five chapters following this one describe the neutron detection efficiency analysis. Chapter 3 acts as an overview, explaining how the various components fitted together; Chapter 4 describes work that the author undertook to ensure accurate modelling of neutron propagation in the NCD phase Monte Carlo; Chapters 5 and 6 describe methods for measuring the strengths of the neutron calibration sources; and Chapter 7 describes a method for determining the neutron detection efficiency using point sources, as an

alternative to the principle method, which used a neutron source distributed uniformly in the heavy water.

Chapter 8 describes the statistical extraction of the solar neutrino fluxes from the NCD phase data. Much of this chapter explains how the component analyses - calibration measurements, background measurements, instrumental cuts etc. - were brought together into a statistical extraction code. The work of the author was to develop the code and techniques for combining the analyses that made best use of the available information and allowed accurate estimation of the uncertainties on the physics parameters.

Chapter 3

The neutron detection efficiency

Measure what is measurable, and make measurable what is not so.

GALILEO GALILEI
(c. 1630)

This chapter outlines the measurement of the neutron detection efficiency - the probability that a neutron produced in the heavy water was detected. It describes the philosophy behind the analysis and provides a background to the following chapters, which focus on particular aspects to which the author was the main contributor. It also summarises the results.

3.1 Neutrons in SNO

Most neutrons produced in SNO came from one of three sources:

- *NC neutrino interactions.*

  NC interactions produced neutrons uniformly throughout the heavy water with typical energies of $\lesssim 0.5$ MeV. They thermalised rapidly and survived a mean life of 21 ms before capture. The detector regions where they captured are listed in Table 3.1.

  The NCD array captured 26.4% of all NC neutrons but the detection efficiency was somewhat less because six strings were removed from the analysis due to mechanical

Table 3.1: Percentages of neutrons produced by NC neutrino interactions capturing in various regions and on various nuclei, taken from a Monte Carlo simulation. Missing entries are zero or negligible. The inactive NCD regions are regions where the ionisation was not collected.

Capture isotope	Capture region								
	D_2O	H_2O	AV	NCD				Other	Total
				Active	Inactive	Ni	Cables		
H	10.95	6.09	28.54				0.08	2.25	47.91
D	17.90								17.90
^{16}O	3.37								3.38
^{17}O	0.03								0.03
^{3}He				25.27	1.14			0.00	26.41
Ni						2.24			2.24
Other			0.19					0.02	0.20
Total	32.25	6.09	28.73	25.27	1.14	2.24	0.08	2.27	

defects or contamination and ionisation was not collected from some regions of the gas (see Chapters 2 and 4 for details). The detection efficiency was 21.0%.

In the heavy water the equivalent numbers were 34.3% captured and 4.9% detected by the PMTs. Here the difference was because some captures did not produce gammas and many gammas were removed by analysis cuts, particularly those in radius and energy.

- *Deuteron photodisintegration by radioactive backgrounds.*

  U and Th chain gammas with an energy greater than 2.2 MeV (see Figures A.1 and A.2) could photodisintegrate deuterons and liberate neutrons in the heavy water via the reaction

  $$\gamma + {}^{2}\mathrm{H} \rightarrow {}^{1}\mathrm{H} + \mathrm{n} - 2.2\ \mathrm{MeV} \tag{3.1}$$

  U and Th were present in the largest quantities in the D_2O, H_2O, the NCD Ni bodies and the two NCD hot spots. The amounts of U and Th, the numbers of neutrons produced and the neutron detection efficiencies varied between the sources. The NCD neutron detection efficiencies depended most strongly on the mean production radius - neutrons produced by activity within the array were the most likely to be captured and those produced by activity in the light water were least likely. The total number of PD background neutrons detected by the NCDs was $\sim 1/8^{\mathrm{th}}$ of the NC signal.

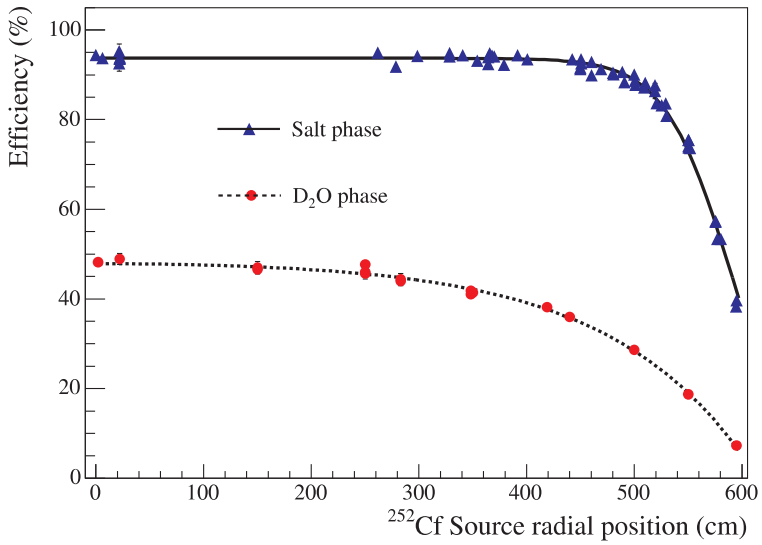

Figure 3.1: D_2O and salt phase neutron detection efficiencies as a function of radius. The points are measurements taken with a ^{252}Cf source [9]. The fits are to analytical models of the dependence of the efficiency on radius.

- *(α,n) reactions in the acrylic vessel.*

  These reactions occurred in the acrylic vessel and produced neutrons at high radii. They are referred to as *AV (α,n) neutrons*. The detection efficiency for these neutrons is not considered further in this thesis, but a full description can be found in [61]. The number detected in the NCDs was $\sim 1/50^{\text{th}}$ of the NC signal.

3.2 Goals and methods

The goal of this analysis was to measure the PMT and NCD neutron detection efficiencies for signal NC neutrons and background photodisintegration neutrons. Of these, the efficiency for NC neutrons in the NCD array was by far the most important - NC neutrons were the main physics signal and were detected in the largest number. Unless specified otherwise this is the efficiency being considered.

In the ideal neutron calibration a neutron source of known strength would be introduced into the detector and would generate neutrons with the same energy and spatial distributions as NC neutrons. The source strength and number of neutrons detected

would then lead trivially to the detection efficiency. In the real world calibrations are not perfect:

- *Source strength.*

  The uncertainty on the source strength is a basic limit on the precision of an absolute efficiency measurement.

- *Backgrounds.*

  Non-neutron events must be removed from the data stream or otherwise accounted for.

- *Energy.*

  Neutrons of different energies can take part in different nuclear reactions or in the same reactions but with different probabilities - they propagate differently. The difference in energy between calibration source and signal neutrons means that, in general, an efficiency measured with the former will have to be corrected before it can be applied to the latter.

- *Spatial distribution.*

  Differences in the spatial distribution of calibration source and signal neutrons can result in substantial systematic uncertainties. If the aim is to mimic the distribution of the signal neutrons then there is an uncertainty associated with the ability to quantify the difference. If the aim is to sample the efficiency using point sources then there is an uncertainty associated with the thoroughness of the sampling and the knowledge of the source positions.

- *Time variations.*

  Calibrations take place at distinct points in time but produce results that must be applied to continuous periods of signal data taking. The stability of the efficiency must be folded into the final uncertainty.

In the D_2O and salt phases the neutron detection efficiencies were measured using point sources. The efficiency was sampled at various points and the results fit to an analytical function, which could be derived because of the simplicity and symmetry of the detector. Radial profiles from the D_2O and salt phases are shown in Figure 3.1. A similar approach was not possible in the NCD phase because the spherical symmetry of the detector was broken by the NCD array, and so two new techniques were used.

The first approach, known as the *^{24}Na method*, was to mimic the NC signal using a novel distributed source - the radioisotope ^{24}Na injected into the heavy water to produce a uniform source of low energy neutrons by photodisintegrating deuterons. This calibration was performed twice during the NCD phase and measurements with point sources were used to assess the stability of the efficiency over time. A similar calibration was attempted using the isotope ^{222}Rn instead of ^{24}Na.

The second approach was to calculate the number theoretically, using a Monte Carlo simulation, and use point source data to tune and test the simulation. The tuning was done in a relative way that was independent of source strength and used calibration data taken on a monthly basis throughout the NCD phase. Systematic uncertainties were assigned to the Monte Carlo input parameters. This is known as the *point source method*.

The two methods were complementary - they were almost completely independent and produced results in excellent agreement. They are described in turn in the following sections.

3.3 The ^{24}Na method

3.3.1 Overview

The aim of the ^{24}Na method was to produce and use a neutron calibration source that mimicked the neutrons produced by NC interactions. The radioisotope ^{24}Na was injected into the heavy water to produce a uniform source of low energy neutrons by photodisintegrating deuterons.

The decay scheme of ^{24}Na is shown in Figure 3.2. The isotope β-decays to ^{24}Mg with a half-life of 14.96 hours and produces 1.37 and 2.75 MeV gammas from the decay of 4.12 MeV excited state of ^{24}Mg. The 2.75 MeV gamma is above the deuteron photodisintegration threshold of 2.2 MeV and in SNO $\sim$ 1 gamma in 380 produced a neutron through this process. The combined light from the beta decay electron and the gammas could be detected by the PMT array and be used to measure the uniformity of the source.

The choice of radioisotope was governed by a number of considerations. The half-life had to be long enough to allow relatively easy transport from the production facility to the detector but be short enough to limit the amount of time that the background in the detector was too high for normal data taking. The final state product or products had to be stable, or rapidly decaying, and not compromise data taking or the water purification systems. In addition the isotope had to be available in a form free from contamination

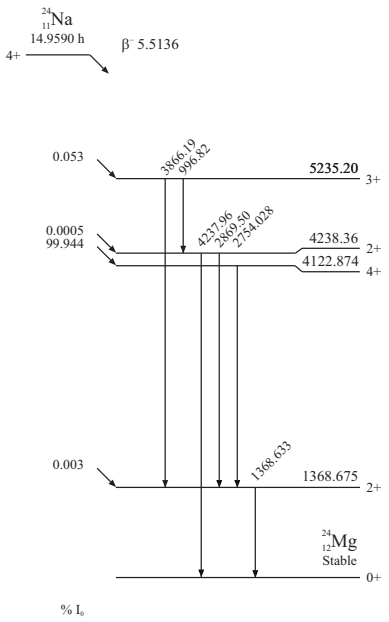

Figure 3.2: The decay scheme of ^{24}Na. The dominant decay channel (BR $\sim$ 1.0) is the one containing the 1.369 and 2.754 MeV gammas.

by other radioisotopes.

^{24}Na was ideal because of its 15 hour half life and its availability to SNO in a verifiably pure form - it could be manufactured by neutron-activation of concentrated ultra pure D_2O brine remaining from the salt phase of the experiment. SNO also had experience dealing with ^{24}Na and its byproduct ^{24}Mg in that phase, where it was produced by neutron calibration sources and by Th sources (these produced neutrons by deuteron photodisintegration).

3.3.2 Measurements

The ^{24}Na calibration was performed twice during the NCD phase, in the middle of data taking (October 2005) and at the end (October 2006). In each measurement the D_2O brine was activated in a research reactor at the Royal Military College of Canada in Kingston, Ontario and then transferred to Sudbury. Before injection into the detector samples of brine were taken for use in determining the source strength.

In the 2005 measurement the brine was injected at a number of points along the detector z-axis using a custom-built device fitted to the source manipulator system. In the 2006 measurement the brine was injected into the water systems and entered the heavy

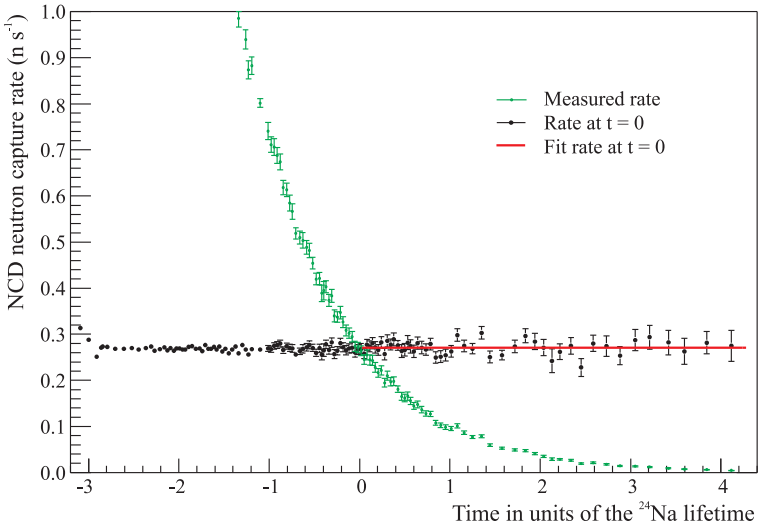

Figure 3.3: The NCD neutron capture rate as a function of time in the 2005 measurement [10]. The green points show the neutron detection rate in each run and the black points show it corrected to the time at the start of counting.

water from the bottom of the acrylic vessel. In both cases the heavy water was circulated to ensure thorough mixing of the brine; this took 3 days for the first measurement and 2 days for the second. Figure 3.3 shows the neutron detection rate in the NCDs as a function of time in the first measurement.

3.3.3 Efficiency

The NC neutron detection efficiency was given by

$$\varepsilon_{NC} = f_{uniform} \cdot f_{edge} \cdot \frac{R}{A_n} \tag{3.2}$$

where R is the measured neutron detection rate, scaled to an arbitrary reference time, A_n is the neutron production rate, scaled to the same time, $f_{uniform}$ is a correction factor accounting for non-uniformities in the spacial distribution of the ^{24}Na and f_{edge} is a correction factor accounting for differences, mainly near the edge of the D_2O, in the distribution of neutrons produced by NC interactions and those produced by perfectly mixed ^{24}Na.

Table 3.2: Measurements of the ^{24}Na source strength A_n (in $\mathrm{n\,s^{-1}}$). The strengths for each measurement were scaled to a common reference time, mass and spatial distribution.

Data set	Source strength A_n ($\mathrm{n\,s^{-1}}$)								
	in situ (PMT)			*in situ* (NCD)			Ge		
	Value	Unc.	%	Value	Unc.	%	Value	Unc.	%
Dry run	84.8	$^{+2.7}_{-4.0}$	$^{+3.2}_{-4.7}$	80.0	1.4	1.8	88.1	2.1	2.4
2005	1.284	$^{+0.068}_{-0.065}$	$^{+5.3}_{-5.1}$	1.240	0.020	1.6	1.236	0.029	2.3
2006	0.810	$^{+0.046}_{-0.042}$	$^{+5.7}_{-5.2}$	0.838	0.013	1.5	0.857	0.020	2.3

Source strength (A_n)

The source strength was measured using samples of brine taken before it was injected into the heavy water. Two samples were taken from each source:

- *Ge detector sample.*

  One sample was counted using a Ge detector, which measured the gamma production rate. This was converted into a neutron production rate using the deuteron photodisintegration cross section. This analysis will be discussed in detail in Chapter 5.

- *in situ sample.*

  One sample was put in a small capsule and positioned at the centre of the SNO detector. The neutron detection rate was compared to that of a well-calibrated ^{252}Cf source placed in the same position, allowing the strength of the brine sample to be inferred. This measurement was done using the PMT and NCD arrays to detect neutrons concurrently, which gave two statistically independent measurements. This is known at the *in situ* method. The PMT-based analysis is discussed in Chapter 6 and the NCD-based measurement in [62].

The standard neutron candle in the D_2O and salt phases of the experiment was a well-calibrated ^{252}Cf source and the same source was used again as the efficiency standard in the *in situ* ^{24}Na source strength measurements. A nice feature of the Ge detector measurement was that it did not depend on the ^{252}Cf source and therefore guarded against any mistakes in its calibration.

The *in situ* measurements had potential for greater precision because they did not require a knowledge of the photodisintegration cross section, on which there is a $\sim 2\%$ experimental uncertainty. This photodisintegration cross section was required to convert the measured gamma production rate into a neutron production rate and was the dominant uncertainty in the Ge detector measurement. In the *in situ* methods the dominant uncertainties were statistics, detector stability (NCDs) and position reconstruction (PMTs).

The results from the three methods are summarised in Table 3.2. In this table 'dry run' refers to a practice measurement in which the brine was activated and had its strength measured but was not injected into the detector; the data were useful for comparing the different methods. The results for the different methods in the 2005 and 2006 measurements were in good agreement but there was a statistically significant discrepancy in the dry run, for which no firm explanation has been found (it is possible that it was due to an inconsistency in the reference times). In general the NCD and Ge measurements were the most precise and of similar precision.

For each data set, the three source strength measurements were combined, under the reasonable assumption that they were uncorrelated. The only significant correlation was between the NCD and PMT *in situ* measurements but the latter carried little weight in the combination. The final results were:

Data set	Source strength A_n (n s^{-1})			
	Value	Unc.	%	$\chi^2/d.o.f.$
Dry run	82.8	2.6	3.1	5.4
2005	1.241	0.016	1.3	0.22
2006	0.842	0.011	1.3	0.59

The error on the dry run number was inflated by $\sqrt{\chi^2/d.o.f.}$ to account for the lack of consistency between the results (see Appendix B).

Event rate (R)

The analysis used to extract neutron event rates is fully described in [63]. It was concerned with calculating

$$R = \frac{M}{T} \tag{3.3}$$

where R is the event rate, M is the number of neutron events in the NCDs and T is the livetime.

To calculate M the number of events recorded in the counters was corrected for sources of inefficiency - for example, due to data cleaning - and alpha background contamination. To calculate T the raw live time was corrected for dead times associated with hardware and offline cuts.

The analysis was repeated with different definitions of what constituted a neutron candidate event:

- Event triggers shaper-ADC only.
- Event triggers shaper-ADC and scopes (correlated event).
- Event triggers scopes only

and for different ranges of energy, as measured by the shaper-ADC system:

- 0.421-0.875 MeV (narrow range)
- 0.179-0.875 MeV (wide range)

After correcting for acceptance and dead times, all six event-energy range combinations were expected to yield the same result. Making comparisons between them was an important way to test models of the detector behaviour and was a powerful check on the results. The preferred combination was correlated events with a narrow energy range because it was the one least sensitive to noise and with the largest signal to background ratio.

Uncertainties on the event rates were assigned by examining the consistency of measurements over time and by propagating uncertainties on input parameters such as dead time constants. The measured rates were:

Data set	Detection rate R (n s^{-1})				
	Value	Stat.	Sys.	Tot.	%
2005	0.2708	0.0020	0.0027	0.0034	1.3
2006	0.1811	0.0016	0.0018	0.0024	1.3

Correction factors (f_{edge} and $f_{uniform}$)

The correction factor f_{edge} accounted for the difference between the neutron distribution produced by uniformly mixed ^{24}Na and by NC interactions. The author found that there

was an intrinsic non-uniformity to the ^{24}Na neutron distribution, which arose from the neutron production mechanism: 2.75 MeV gammas had a mean free path of 26 cm in heavy water and so a significant proportion of those produced close to the acrylic vessel escaped the heavy water before interacting. There was therefore a lower probability of ^{24}Na neutrons being produced at high radii - and therefore a larger probability of them being captured - than NC neutrons. From Monte Carlo simulations the correction factor was $f_{edge} = 0.970 \pm 0.008$.

The correction factor $f_{uniform}$ accounted for non-uniformities in the distribution of ^{24}Na in the heavy water. The uniformity of the source was assessed using the combined light from the β-decay electron and the 1.37 MeV and 2.75 MeV gammas, which yielded an energy spectrum peaking at ~ 3.6 MeV. The spatial distribution of the reconstructed events was the same as that of the neutrons produced by photodisintegration. A full description of this analysis can be found in [64].

The detector was divided up into $N \sim 1000$ elements of equal volume. For both data and uniform ^{24}Na Monte Carlo the probability of detecting a gamma in region i was calculated using

$$f_i = \frac{n_i}{\sum_{i=1}^{N} n_i} \tag{3.4}$$

where n_i is the number of events reconstructing in region i. The ratio of the probabilities for data and Monte Carlo ($R_i = f_i^{data}/f_i^{MC}$) was a measure of the non-uniformity associated with element i. In the limit of high statistics, a uniform source and an accurate simulation of the detector $\{R_i\} \to 1$.

For uniformly produced neutrons the neutron detection efficiency is given by

$$\varepsilon_{uniform}^{MC} = \frac{\sum_{i=1}^{N} n_i^{NCD}}{\sum_{i=1}^{N} m_i} \tag{3.5}$$

where m_i is the number of neutrons produced in element i and n_i^{NCD} is the number of these detected by the NCD array. Similarly, for neutrons produced non-uniformly, with a distribution parametrised by R_i, the detection efficiency is

$$\varepsilon_{non-uniform}^{MC} = \frac{\sum_{i=1}^{N} R_i\, n_i^{NCD}}{\sum_{i=1}^{N} R_i\, m_i} \tag{3.6}$$

so that $f_{uniform}$ is given by

$$f_{uniform} = \frac{\varepsilon_{uniform}^{MC}}{\varepsilon_{non-uniform}^{MC}} \tag{3.7}$$

For the 2005 measurement, the value was found to be $f_{uniform} = 0.9812 \pm 0.0021(\text{stat.})^{+0.0333}_{-0.0212}(\text{syst.})$. The systematic uncertainty was mainly due to imperfections in the Monte Carlo and uncertainties on position and energy reconstruction.

A major challenge in this analysis was understanding the response of the detector at ~ 3.6 MeV. The method described above required an accurate Monte Carlo simulation of the detector's optical response so that differences in the spatial distribution of the gammas could be interpreted as non-uniformities in the ^{24}Na distribution rather than mis-modelling of the detector. The challenge arose because of the low energy of the gammas. In general, the energy response of SNO varied as a function of position - the detector geometry meant that more light could be collected per MeV of energy deposited in some places than in others - but this variation was particularly large and troublesome at low energies, which are close to the detector hardware thresholds. SNO's hardware and analysis tools were not designed to study events below 3 MeV and the energy calibration, in particular, was tuned to higher energies.

The correction factor $f_{uniform}$ thus had two interpretations. If one hypothesised that the ^{24}Na was uniformly mixed then measuring $f_{uniform}$ consistent with 1 was a verification of uniformity and its uncertainty was a measure of the ability to measure it. Alternatively, if one thought there were reasons why the source might not be uniform then one could take the central value of $f_{uniform}$ at face value and consider it as a correction, with an uncertainty again representative of the ability to measure the uniformity. There were in fact good physical reasons to suppose that the ^{24}Na was uniform and so the former approach was taken.

The first argument for uniformity was that, during mixing, the flow entering and exiting the acrylic vessel would have been turbulent on a significant scale. The water flow of 200 L min^{-1} through a surface of 1 m^2 in the vicinity of the entry and exit points would been equivalent to 0.003 m s^{-1}. Using the kinematic velocity of water this corresponds to a Reynolds number of 3000, which is in the turbulent range. Turbulent flow on this scale would have generated persistent eddies, which would have considerably aided mixing, even if the flow through the bulk of the array was streamlined.

However, the main piece of evidence that the ^{24}Na was properly mixed came from a comparison of the 2005 and 2006 measurements. In each of these the source was injected very differently and the subsequent mixing set up distinct currents of ^{24}Na in the heavy water. The final light distributions in these measurements were identical but a little different from what would be expected for a uniform source. This can be seen in Figure 3.4, which shows a comparison of the radial light distributions between data and Monte Carlo

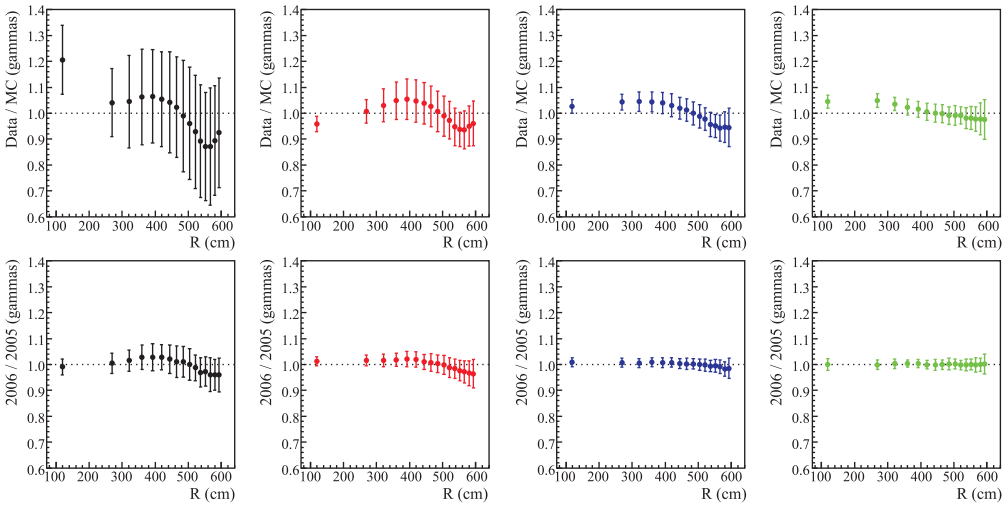

Figure 3.4: Mixing of the ^{24}Na: the ratio of the data and Monte Carlo radial light distributions (top plots) and the ratio of the 2006 and 2005 light distributions (lower plots). Time increases from left to right and the rightmost plots correspond to the steady state.

as a function of time in the upper plots and a comparison of 2005 and 2006 data in the lower plots; the difference between data and Monte Carlo persists over time but the 2005 and 2006 data show convergence to the same distribution. Comparisons of other variables such as x, y and azimuthal angle can be found in [64].

It is improbable that the ^{24}Na could converge to same spatial distribution in 2005 and 2006, and that distribution not be a uniform one. The difference between data and Monte Carlo, though consistent with statistics, was therefore taken to be due to mismodelling in the Monte Carlo.

In calculating the efficiency it was decided to take $f_{uniform} = 1$, and treat the error as measure of the ability of the analysis to demonstrate uniformity. The components of the error were 2.73% from symmetrising the statistical component of the uncertainty on $f_{uniform}$ above, 0.21% from the statistical error on that number and 0.75% from statistical ability of the ^{24}Na data to constrain the radial profile of the activity. The final correction factor was $f_{uniform} = 1.00000 \pm 0.02837$.

3.3.4 Results

The efficiencies derived in the 2005 and 2006 measurements, and calculated using Eq. (3.2), are given in Table 3.3. The two measurements were combined in the standard way using

Table 3.3: Summary of the results of the ^{24}Na method broken down in components correlated and uncorrelated between the measurements.

Data set	Detection efficiency ε_{NC}			
	Value	Cor.	Uncor.	Tot.
2005	0.2117	0.0069	0.0024	0.0073
2006	0.2087	0.0068	0.0026	0.0073
Combined	0.2102	0.0069	0.0018	0.0071

only the parts of the uncertainties uncorrelated between the measurements. The source strengths and the correction factors f_{edge} and $f_{uniform}$ were assumed to be 100% correlated. All but a component of 0.5% in the neutron capture rates, relating to the efficiency of the instrumental cuts, was assumed to be 100% uncorrelated. The final neutron detection efficiency was 0.210 ± 0.007[1].

3.4 The point source method

3.4.1 Overview

The point source method was a largely theoretical estimate of the neutron detection efficiency made using a Monte Carlo simulation. A model of the detector geometry and neutron propagation within it was constructed and used to predict the efficiency. Uncertainties were assigned on all of the input parameters. Point source calibration data taken using ^{252}Cf and AmBe sources (see Section 4.4) were used in three ways: to tune a parameter in the Monte Carlo - the concentration of hydrogen in the D_2O - on which there was a significant experimental uncertainty; to check that the Monte Carlo correctly predicted the efficiency as a function of position within and outside the NCD array; and to assign an uncertainty to the variation in detector response as a function of time. The final detection efficiency was independent of the calibration source strength and thus independent of the ^{24}Na method. The method is described in detail in Chapter 7.

[1]Note that this efficiency differs slightly from the value of 0.211 ± 0.007 used in the remainder of this thesis; the latter was taken from the final report of the neutron topic review committee [65], while the former was calculated by the author. The cause of the difference between the two is not known.

3.4.2 Results

The neutron detection efficiency was found to be 0.2101 ± 0.0032, which is in excellent agreement with the results of the ^{24}Na method. The point source method had the smaller uncertainty, by approximately 50%. Even so, the ^{24}Na result was used in the final analysis. This was because it was a direct measurement using a calibration source - an approach consistent with previous SNO publications - and because it did not require the assumption that nothing that had been neglected in the Monte Carlo.

Chapter 4

Modelling neutron propagation

Everything is vague to a degree you do not realise till you have tried to make it precise...

BERTRAND RUSSELL
The Philosophy of Logical Atomism (1949)

The Monte Carlo simulation of the SNO detector was an important tool in the neutron detection efficiency analysis. This chapter describes the development and testing of the model that was undertaken to prepare for the salt and NCD phases of the experiment. The following aspects of the simulation are considered:

- *Nuclear reactions.*

  Cross-sections for processes occurring in the detector and, where necessary, the simulation of final state gammas.

- *Media.*

  Densities and compositions of materials in the detector.

- *Geometry.*

  The models of the acrylic vessel, NCD array and neutron calibration sources.

- *Particle generation.*

  The energy and multiplicity of neutrons produced by neutron calibration sources and the gammas that accompany them.

Developments were guided by measurements of detector parameters made by the collaboration or published studies of relevant physical processes. Where possible the effects of the changes were evaluated by making comparisons with experimental data.

The chapter begins with an introduction to the SNO Monte Carlo followed by sections on nuclear reactions, detector media, detector geometry and neutron calibration sources.

4.1 The SNOMAN Monte Carlo

The SNO Monte Carlo and ANalysis software package SNOMAN [66] was used to process data and to simulate interactions in the detector. It was a FORTRAN-based package of processors, or software units, sharing a common ZEBRA data structure.

SNOMAN processors applied electronic and optical calibrations, instrumental cuts, position fitters and energy estimators to raw data, to produce calibrated data sets for physics analyses. The processors and data structure were designed to allow real and simulated data to be treated identically.

The Monte Carlo processor generated simulated data, accounting for the state of the detector (such as the PMT and NCD electronics thresholds) in the run being simulated. It contained models of particle production mechanisms, the physical parameters of the detector, particle transport and the data acquisition system.

Each particle production mechanism had a generator routine. SNOMAN could produce solar, atmospheric and supernova neutrinos; beta, beta-gamma and alpha decays; neutrons and fissions, amongst many others. Particles could be generated with user defined energies and spatial distributions.

SNOMAN modelled the transport of various particles across a huge energy range, though this thesis is concerned only with a subset: neutrons, electrons and gammas produced in normal neutrino and calibration data taking. Gammas ranged in energy from $\sim$ eV Čerenkov photons to $\sim$ MeV gammas produced following neutron captures. Neutrons ranged from thermal to $\sim$ MeV energies.

The propagation of these particles, with the exception of Čerenkov photons (which were handled by custom SNO code [67]), were handled by two industry-standard packages integrated into SNOMAN. Neutrons were propagated by MCNP [68] and electrons and gammas by EGS4 [69]. The physics governing the propagation of these particles is well-understood and by making use of standard software SNO benefited from years of testing

by many users in different contexts.

MCNP was incorporated in SNOMAN without any substantial changes [70] and only one modification was made to EGS4 - the inclusion of the photodisintegration reaction. The two codes were embedded in a common structure so, for example, when a neutron was captured in MCNP, custom SNO code decided whether any final state gammas should be simulated and, if so, looked up the properties of the cascade; the gammas were then handed to EGS4 which propagated them through the detector. If one of these gammas photodisintegrated a deuteron then the final state neutron was handed back to MCNP.

The final component of the particle propagation code was the SNOMAN geometry, which was a collection of routines describing the shapes, dimensions, arrangement and media of all the objects making up the detector. MCNP and EGS4 calculated cross sections with reference to the geometry code.

The challenge of modelling particle transport in SNO was primarily not a problem in simulating the basic physics, which is well understood. It was in correctly describing the geometry of the detector, the distributions of the particles produced by the sources and also, through calibration, the optical and electronic characteristics of the detector.

4.2 Nuclear reactions and media

4.2.1 Nuclear reactions

The cross sections of important nuclear reactions in the Monte Carlo were checked, following on from a previous study by Lyon [70]. This work was motivated by the significant changes in detector configuration that occurred between the salt and NCD phases (chiefly the insertion of the NCD array into the heavy water) and by the realisation that some materials were much more important than previously suspected. In particular, the author demonstrated the unexpectedly large probability of neutrons re-capturing on the materials of the neutron calibration sources.

Thermal neutron cross sections in the Monte Carlo were compared to experimental values. Cross sections were extracted by running simulations of mono-energetic neutrons at the centre of a large test volume of the material of interest. The probability of first interaction p_i of the neutron being a reaction of type i was related to the number density of the isotope n_i and the partial interaction cross section σ_i by

$$p_i = \frac{n_i \sigma_i}{\sum_j n_j \sigma_j} \tag{4.1}$$

where the sum in the denominator is over all isotopes and was evaluated using cross sections from the ENDF/B-VI library [71]. This equation was used to calculate partial cross sections σ_i for important reactions in the counter gas (^{3}He), CVD nickel (isotopes of nickel) and stainless steel (isotopes of iron, manganese and chromium). There was good agreement between simulations and experiment. A cross section of particular importance - that on ^{3}He was found to be 5315.8 ± 0.6 b in the Monte Carlo compared to the experimental value of 5316 b.

The author resolved an issue with the ^{2}H(n,2n)^{1}H reaction that had caused confusion in previous neutron detection efficiency analyses. The reaction has a threshold of 3.4 MeV and a cross section that increases monotonically to 0.1 b at 7 MeV. It was important to model correctly because it occurred for neutrons produced by AmBe and ^{252}Cf sources, which produced neutrons of relatively high energy, but not for NC neutrons, which produced neutrons of a lower energy. Efficiencies measured with the sources had to be reduced, to account for the extra neutron production, if they were to apply to NC neutrons.

For some time it was assumed that ^{2}H(n,2n)^{1}H was not modelled in SNOMAN. The reaction was accounted for by applying a correction of 1%, derived analytically by [72], to efficiencies measured with the ^{252}Cf source. However, the author found that the reaction was present but was hidden because of its obscure implementation in the ENDF libraries. Monte Carlo simulations indicated that the correction of 1% was too large by $\sim 30\%$ because the analytical calculation had neglected the moderating effect of the interactions of neutrons with oxygen in the heavy water.

Further investigation showed that correcting for ^{2}H(n,2n)^{1}H was actually unnecessary as its effect was compensated for by the neutron-absorbing ^{16}O(n,α)^{13}C reaction, which has a cross section with a similar magnitude and energy dependence. The cross sections are compared in Figure 4.1. Taking into account that there were twice as many ^{2}H nuclei as ^{16}O nuclei in the heavy water it is clear that the probability of the reactions occurring is very similar in the relevant energy range, below 10 MeV. Given the substantial experimental uncertainty on the ^{2}H(n,2n)^{1}H interaction in particular [73], the net correction accounting for the two reactions became consistent with zero. A survey of other interactions in SNO found none of comparable probability showing this energy dependence.

Explicit corrections of this nature were necessary only in the salt phase neutron efficiency analysis because that analysis was designed to be *data-based*. This means that the efficiency was derived from analysis of point source data and then corrected *a posteriori*

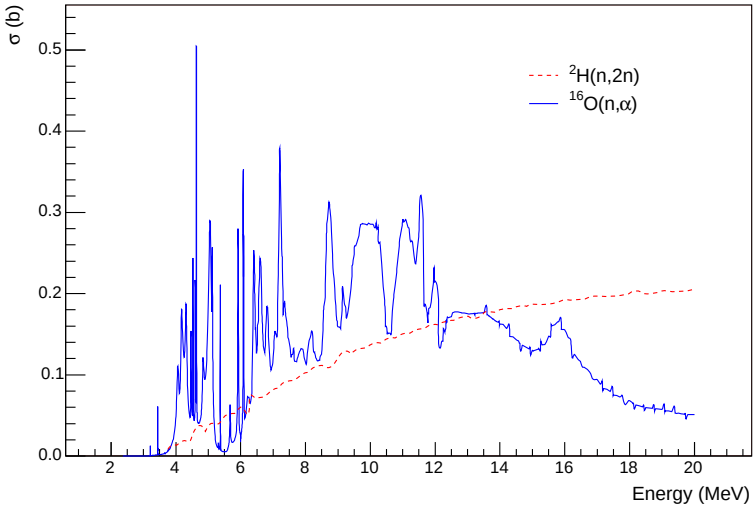

Figure 4.1: The ^{2}H(n,2n)^{1}H and ^{16}O(n,α)^{13}C cross sections as a function of energy.

for differences between point source and NC neutrons, using Monte Carlo where appropriate. In contrast, the corresponding analysis in the NCD phase was *Monte Carlo-based*, meaning that the NC efficiency was taken directly from Monte Carlo, which had been verified using point source data.

The (n,γ) gamma cascades in the Monte Carlo were checked for omissions and only two minor ones were found - the cascades produced following the reactions ^{16}O(n,γ)^{17}O and ^{17}O(n,γ)^{18}O. These were added using information from [74, 75]. The neutron capture cross sections of ^{16}O and ^{17}O are small but the reactions produced gammas extending in energy up to 3.9 MeV and were added for completeness.

4.2.2 Media

This section discusses two impurities that were present in the heavy water during the NCD phase. The low neutron capture cross section of deuterium (0.5 mb) meant that neutron propagation in the heavy water was sensitive to low concentrations of impurities such as ^{1}H (333 mb), ^{17}O (0.538 mb), ^{18}O (0.160 mb), ^{35}Cl (43.6 b), ^{37}Cl (433 mb) and ^{3}He (5333 b). Two of these were of particular interest:

- ^{1}H

  The isotope ^{1}H was present in the heavy water, mainly as HDO, because of the

incompleteness of the original deuterium enrichment. During the NCD phase Ford and Robertson [76] made a new measurement of the hydrogen number fraction of $f_H = (9.8 \pm 0.5) \times 10^{-4}$ using Fourier Transform Infrared (FTIR) spectroscopy. The hydrogen fraction was also fit using the SNO data in the analysis described in Chapter 7.

- ^{35}Cl

  The isotope ^{35}Cl was present in the heavy water during the NCD phase in the form of small quantities of NaCl remaining from the salt phase of the experiment. The amount was expected to decrease over the course of data taking as it was gradually removed by the reverse osmosis system.

  The concentration of NaCl was measured in two ways. The first used the conductivity of samples of D_2O and the following expression, which related the D_2O conductivity σ (μS cm^{-1}) to the mass of dissolved NaCl m (g)

$$m = 484.5 \times \sigma \tag{4.2}$$

  This linear relationship was obtained from measurements at SNO [77]. Masses derived in these measurements had estimated uncertainties of ±50%. The results were:

Date	Conductivity	NaCl Mass (g)	
	(μS cm^{-1})	Value	Unc.
9$^{\text{th}}$ Oct 2003	1.260	610	305
13$^{\text{th}}$ Jun 2004	0.511	248	124
1$^{\text{st}}$ May 2006	0.281	136	68

  The second method used commercial ICP-AES (Inductively Coupled Plasma-Atomic Emission Spectrometry) analyses, which were available as pre-screens for the ICP-MS (Inductively Coupled Plasma-Mass Spectrometry) process. ICP-AES analyses gave the concentration of sodium in units of parts per million, which were converted into masses of NaCl by assuming that the number densities of Na and Cl were identical. No uncertainties were available. These are the results:

Date	Na (ppm)	NaCl Mass (g)	
		Value	Unc.
1$^{\text{st}}$ Dec 2005	0.8	2340	n/a
15$^{\text{th}}$ Mar 2006	0.6	1755	n/a

They are compared to the conductivity measurements in Figure 4.2 and can be seen to be in disagreement by a factor of ~ 10. The reason for the discrepancy is not known and so both sets were treated as valid and a systematic uncertainty assigned to cover the difference between them.

The effect of the NaCl on the NC neutron detection efficiency was assessed using (rather statistically limited) Monte Carlo simulations, which were run for all of the NaCl concentrations. The general level of salt indicated by the conductivity measurements produced a drop in efficiency of $0.3 \pm 0.2\%$ while the level from the ICP-AES measurements produced a drop of $0.4 \pm 0.2\%$. In both cases the *change* in capture efficiency between the smallest and largest masses was statistically insignificant.

An NaCl impurity was not permanently implemented in SNOMAN but correction factors were calculated for NC, AmBe and ^{252}Cf neutron detection efficiencies predicted by the Monte Carlo. The correction was taken to be the mean effect of the two sets of concentrations with an uncertainty spanning the difference. The correction for NCD NC neutron efficiencies was 0.9964 ± 0.0025 and for AmBe/^{252}Cf efficiencies was 0.9971 ± 0.0029. In this thesis these small corrections were neglected in all analyses aside from the theoretical prediction of the NC neutron detection efficiency discussed in Chapter 7.

4.3 Detector geometry

4.3.1 Overview

This section describes upgrades made to the detector geometry model covering the NCD array, the acrylic vessel and the neutron calibration sources. A discussion of the unique mechanics of the SNOMAN geometry code can be found in Appendix C.

4.3.2 The NCD array

A detailed model of the NCD array geometry was constructed for the NCD phase of the experiment. This section describes the main features; technical details can be found in [78, 79, 80]. The model was based on the preliminary work of Brice and Duba. Heise collated much of the necessary information, particularly that recorded during the installation of the array.

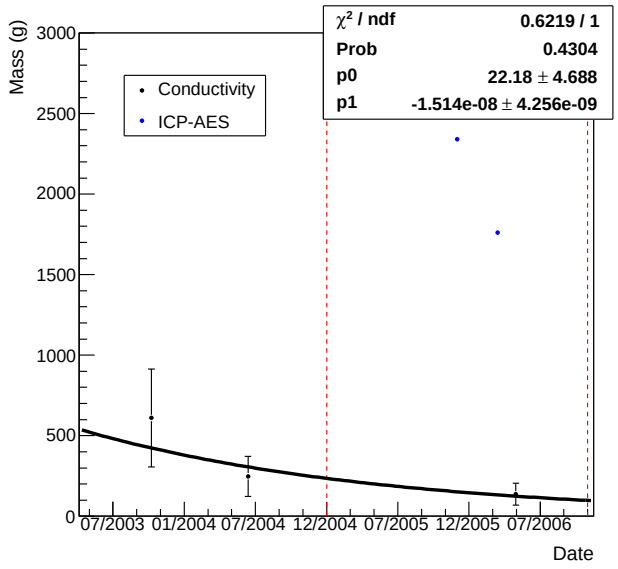

Figure 4.2: Measurements of the mass of NaCl in the heavy water. Neutrino data were taken in the period between the dashed lines. The conductivity measurements were fit to a decaying exponential.

The physical characteristics of an NCD string are shown in Figure 2.5. Most of the geometry was intrinsically quite simple - thin walled nickel tubes split into individual counters by end cap regions, with anchor assemblies at the bottoms and cables at the tops. The aim was to accurately model the positions and outer dimensions of the strings and to ensure that the masses of materials inside them were correct, even if some small geometric details were omitted.

The basic geometries of strings and cables in the Monte Carlo are shown in Figures 4.3 and 4.4. Each string was a cylinder of nickel containing 3 or 4 volumes of counter gas (either ^{3}He-CF_4 or ^{4}He-CF_4) known as *live volumes*. Between the live volumes were regions of inert Ar-CO_2 known as *dead volumes*. At the ends of each ^{3}He live volume were regions of gas where ionisation was not effectively collected, known as *live end regions*; these were implemented as separate geometry elements. Notable small omissions from the geometry were the anode wires and the extensions of the quartz feedthroughs into the counter gas.

Each cable was constructed from three primitive volumes: an arc from the top of the string to the acrylic vessel, a second arc running along the acrylic vessel to the neck and a cylinder leaving the neck vertically. This geometry was approximate as the exact positions of the cables between the string and neck were not known - they were relatively

flexible and not pulled taught.

These parts of the geometry model are worthy of comment or of particular relevance to the work in the rest of this thesis:

- *String positions and orientations.*

  NCD strings were anchored to fixtures built into the acrylic vessel, whose positions had been surveyed and were well-known. However, the tops of the strings were not fixed and they remained close to vertical because they were buoyant. The buoyancy was not large enough to ensure that the strings were absolutely vertical and so the positions of the tops had to be measured *in situ*. This was done using two independent methods. The first were fits to the optical calibration (OCA) data [57], which gave string positions and orientations, and the second were measurements made with a laser range finder (LRF) [81] to directly survey the positions of the string tops.

  The uncertainties on the OCA positions were estimated to be 50% smaller than those made using LRF. The mean string tilt (the mean difference in xy-coordinates of the tops and bottoms of the strings) was -3.01 ± 0.35 cm in the OCA measurements and -4.22 ± 0.70 cm in the LRF measurements.

  Simulations could be run with each individual geometry or with the weighted average of the two.

- *Counter walls.*

  The nominal thickness of the nickel counter walls was 360 μm. However, measurements were available of counter weights and lengths [82, 83] that allowed the wall thicknesses to be calculated, and implemented in the Monte Carlo, on a counter-by-counter basis. These measurements indicated that there were substantial deviations from the nominal thickness.

  The measurements available were of the weights and lengths of the nickel tubes, used to construct the counters, taken after their manufacture. The inner radius of all tubes was exactly 2.54 cm as this was the radius of the aluminium mandrels on which the Ni was deposited. The outer radii were calculated using the measured masses and a nickel density of 8.902 $\mathrm{g\,cm^{-3}}$ [84]. Account was then made of the mass removed during electropolishing, which was 56.8 g (20 μm) from the outside of each 2 m tube and 5 g (2 μm) from the inside, and etching, which removed an additional 3 g (1 μm) from both surfaces. The uncertainties on the masses removed were $\sim 20\%$.

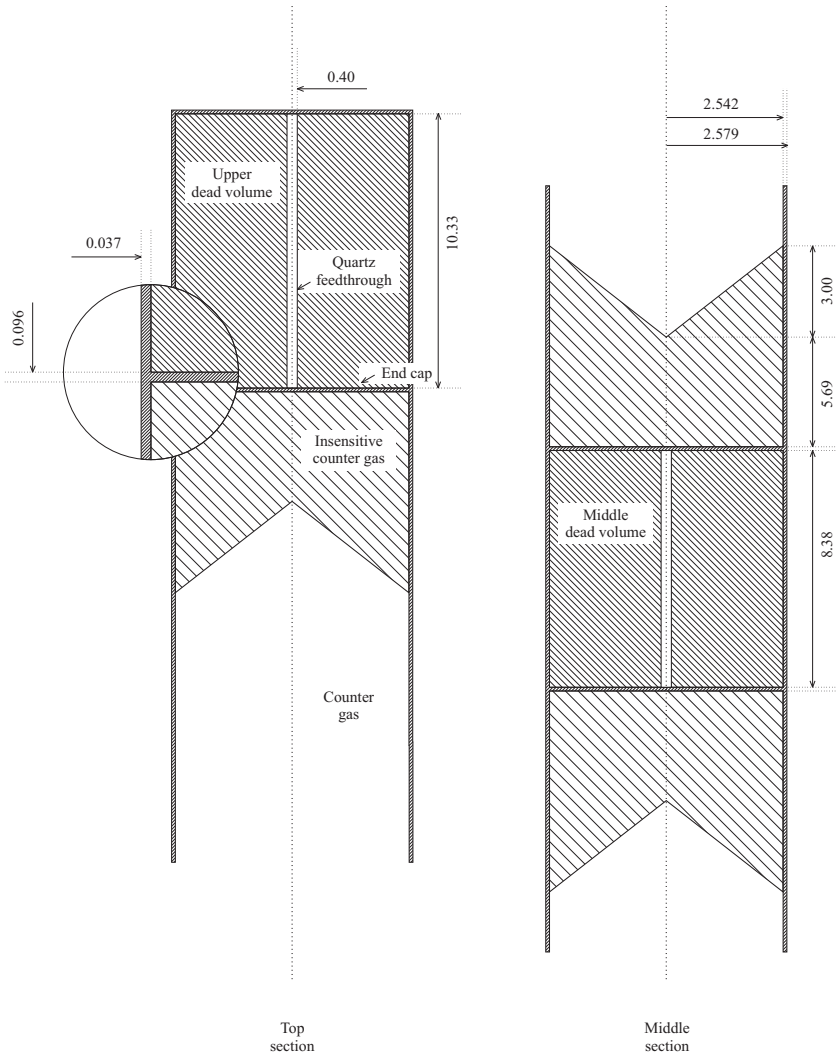

Figure 4.3: The Monte Carlo geometry of an NCD string showing the top of a string (left) and the section in between two counters (right).

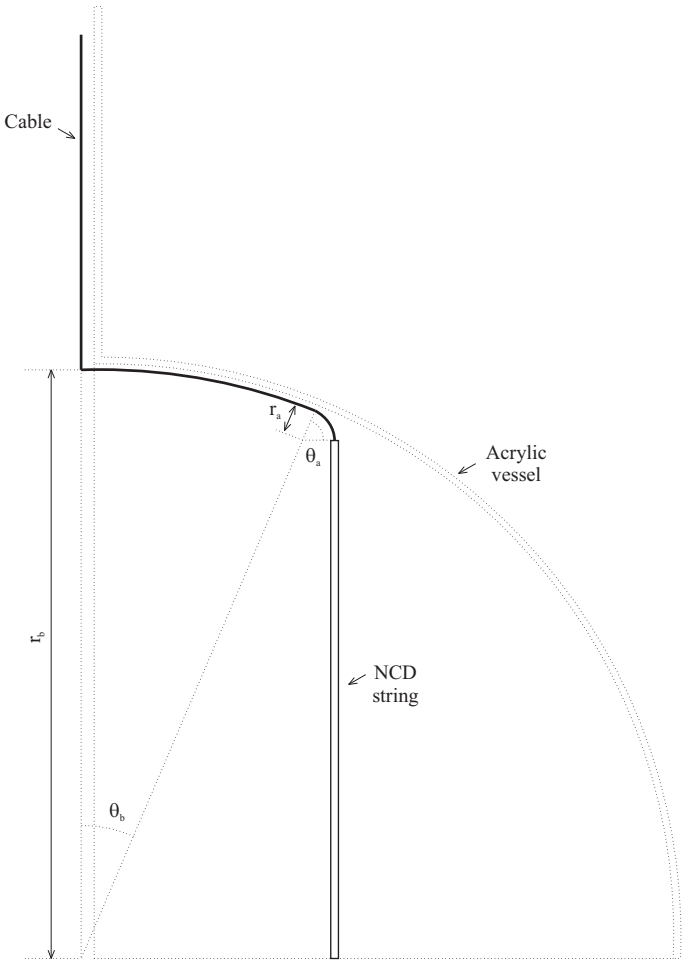

Figure 4.4: The Monte Carlo geometry of an NCD cable.

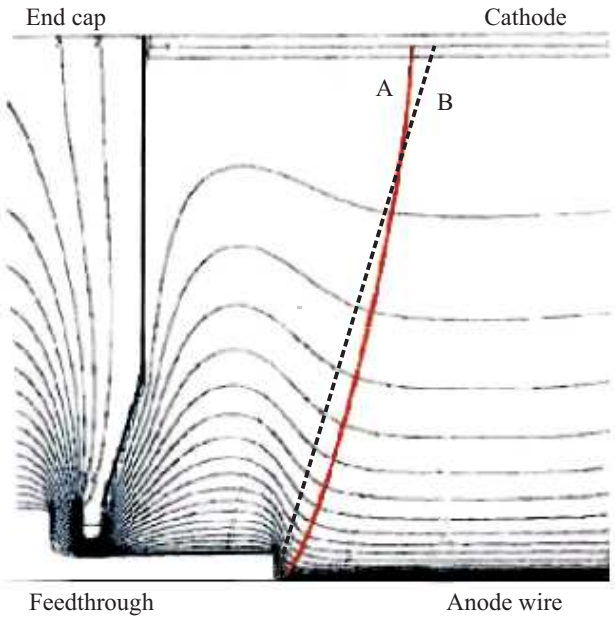

Figure 4.5: Simulated field lines at the end of a counter [11]. The region to the left of line B corresponds to one half of the lightly hatched regions in Figure 4.3.

The final inner radius for all counters was 2.542 cm and the average outer radius was 2.579 cm, making the average wall thickness 371 μm. The minimum wall thickness was 352 μm; the maximum wall thickness was 423 μm and the standard deviation was 9 μm. When a counter was made of two tubes welded together the outer radius was the length-weighted average of the component tubes. When no information was available for a particular tube, as was the case for 31 of the 156 counters, the outer radius was taken to be the average of the tubes for which information was available. A complete list of counter wall thicknesses can be found in [80].

The inner radius of the dead regions was decreased to account for the mass of nickel missing from the model due to the geometry simplifications in these regions. This amounted to a total of 10 kg over the array. The thickness was increased from 0.037 cm to 0.062 cm.

- *Live end regions.*

  At each end of the gas volume in each counter there was an insulating silica feedthrough tube that allowed the anode wire to pass from the counter gas into the end cap. These feedthroughs extended into the counters to produce regions of gas from which deposited charge was not collected. This feature was designed to reduce the effects of electrical field distortions at the ends of the counters on pulse shapes.

Figure 4.5 shows the simulated electric field lines close to the end of a counter. In the simulation all charge deposited to the right of the line A would have been collected by the anode. The charge deposited following a neutron capture was spread over a finite distance so, depending on the geometry of the track, the charge could either be completely collected, partially collected or not collected at all.

The end regions were simulated in the Monte Carlo by defining volumes close to the counter ends as separate geometry elements, so that captures within them could be identified. The extent to which charge was collected in a particular event was determined by the separate pulse simulation code. The surface A was approximated by a conical surface, labelled B, with a slope of $m = \Delta z/\Delta r = 1.2$ so that approximately the same *volume* was contained to left of surfaces A and B.

These regions captured a significant fraction of the neutrons produced in the detector and actually more than would be naïvely estimated from the volume of gas they contained, relative to the total (3.8%); for example, they captured 4.7% of NC neutrons. This was mainly because the ^{3}He neutron capture cross section was so high that most neutrons were captured nearer to the counter walls than to the anode, and close to the counter walls proportionally more of the counter lengths were end regions. A smaller effect was that a large proportion of NC neutrons were generated outside the array, at large radii, and those produced at high and low z were more likely to capture in end regions than those produced at small radii, within the array.

The modelling of the end regions was particularly important for the analysis of point AmBe and ^{252}Cf neutron source data. In some source locations the fraction of neutrons captured could be much larger or much smaller than for NC neutrons. For example, compared to 0.047 for NC neutrons, the fraction was only 0.02 for neutrons produced at $(x, y, z) = (0, 0, 400)$ cm but it rose to 0.07 for neutrons produced at $(x, y, z) = (0, 250, 0)$ cm, close to an end region.

4.3.3 The acrylic vessel

There were two changes to the geometry of the acrylic vessel in the NCD phase. The first was that, for the first time, it was correctly positioned with respect to the PMT array, which defined the detector coordinate system. Calibration source measurements and surveys [85] indicated that the centre to the acrylic vessel was -5.32 cm lower than the centre of the PSUP.

The second was extra material added around the base of the neck where it joined

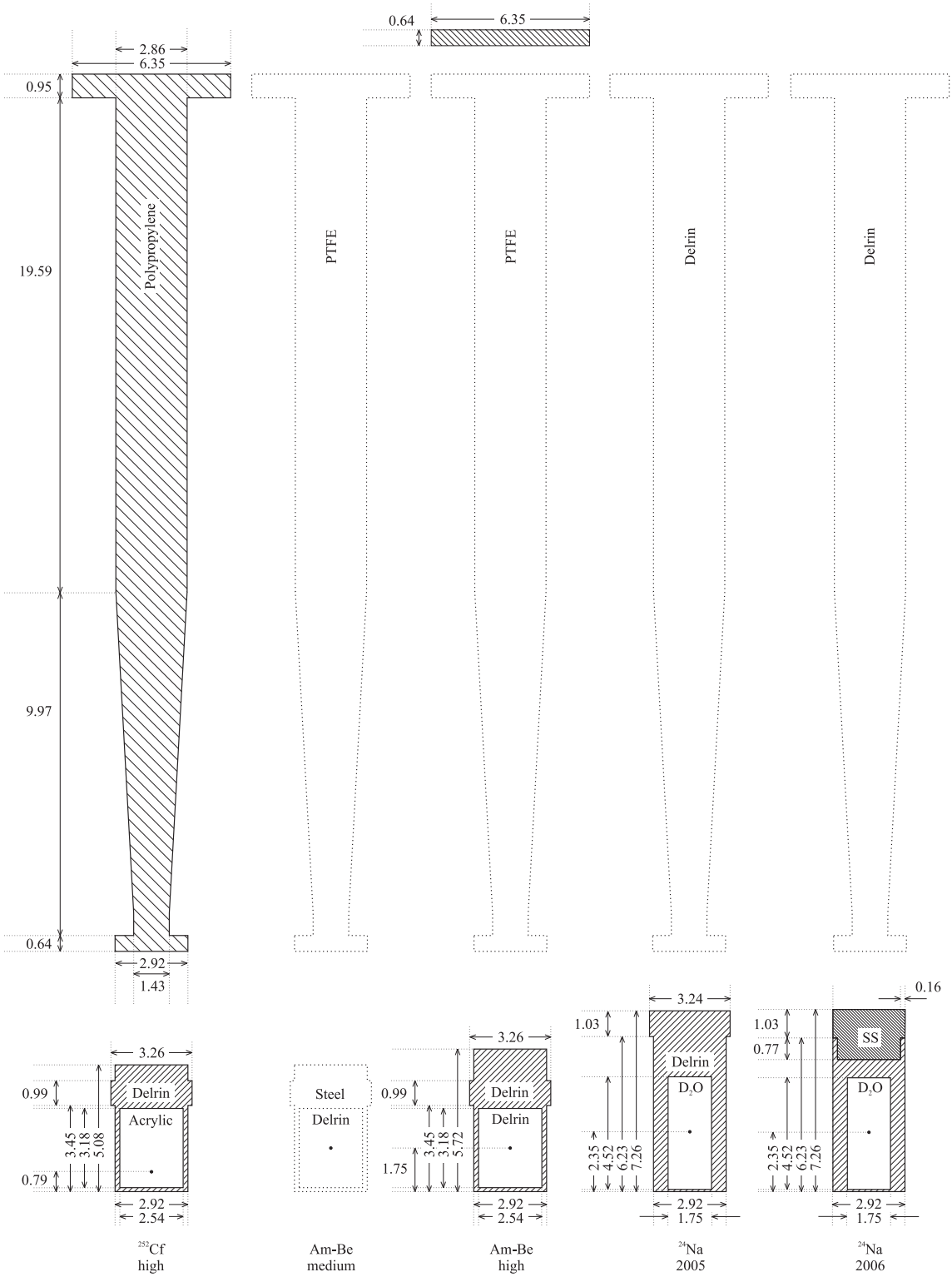

Figure 4.6: NCD phase neutron calibration sources.

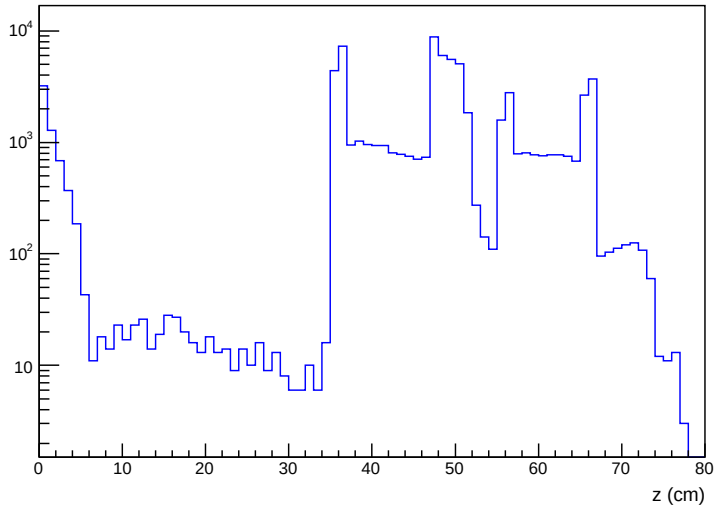

Figure 4.7: z-profile of source neutron captures on the materials of a source. The source activity was located at $z = 0$.

with the spherical part of the vessel. This mass of acrylic, used to strengthen the joint, had previously been omitted.

One omission in the geometry that remains is that of the acrylic anchor blocks to which the NCD anchors were attached. Their effect on light propagation was studied by Seibert [86] and found to be non-negligible; their effect on neutron propagation has not been studied but is expected to be small as they are on the acrylic vessel.

4.3.4 Neutron calibration sources

The geometry of each neutron calibration source was composed of three parts: the source housing, the stem and the weight/carriage apparatus, referred to as the *manipulator*, to which stems were attached. The first two are shown in Figure 4.6 and the latter in Figure 2.10. A range of different construction materials were used with different abilities to absorb neutrons, from weakly absorbing Teflon[1], used to make some of the cans, to strongly absorbing steel, which was mainly present in the manipulator.

The author was the first to appreciate the extent of neutron re-absorption on the materials of the sources, which could be more than 6% of all neutrons produced by a

[1]For a plastic, Teflon (C_nF_{2n}) is a particularly weak absorber of neutrons because it contains no hydrogen.

source. Figure 4.7 shows the z-distribution of captures in a source run Monte Carlo simulation where the source was located at $z = 0$. The bulk of the captures for this source were on the housing (below $z = 5$ cm) and manipulator (above $z = 34$ cm); there were relatively few captures on the Teflon stem.

The discovery of these captures helped resolve two long-standing issues in the understanding of neutron propagation in the salt phase of SNO. The first was that the neutron mean life predicted by the diffusion equation was smaller than that measured experimentally. After sink terms were included in the equation to approximate the effect of absorption on the source the lifetimes agreed [87]. The second was a disagreement between different estimates for the contamination of the source neutron spectrum by prompt ^{252}Cf source gammas (see below); the result of one method was biased because it confused gammas from neutrons capturing on the source with the prompt gammas.

The source geometries were modelled in particular detail and a database was built to ensure that simulations for each of the calibration runs were generated with the correct geometry. The efficacy of this database was limited by the quality of records kept by the experiment which meant that there was sometimes uncertainty over which stem was used in particular runs; however, the most important neutron-absorbing part of the geometry - the manipulator - was common to all.

4.4 Calibration sources

4.4.1 Overview

This section describes the physics of the point ^{252}Cf and AmBe neutron calibration sources and how the source interactions are modelled in the Monte Carlo.

4.4.2 The ^{252}Cf source

The ^{252}Cf source produced neutrons by spontaneous fission, typically in small bursts, each accompanied by the emission of prompt gammas and delayed neutrons from the decay of the fission fragments. It was important to model the properties of the neutrons and gammas in the Monte Carlo for various analyses, but particularly for testing the time series analysis (see Appendix D) and determining the contamination of the signal window in the *in situ* measurement of the ^{24}Na source strength (see Section 6.2).

The activity in the ^{252}Cf source was overwhelmingly due to the isotope ^{252}Cf but

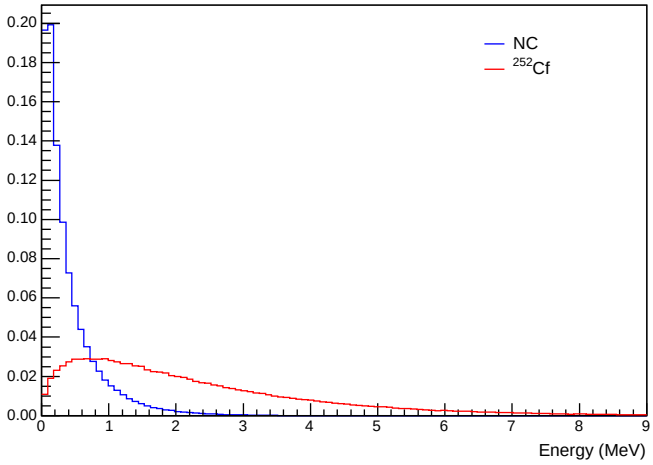

Figure 4.8: Energy spectra of ^{252}Cf and NC neutrons.

there was a small contribution due to ^{250}Cf, which produced $1.92 \pm 0.02\%$ of the neutrons on the source reference date of 12$^{\text{th}}$ June 2001 [88]. The fission of ^{250}Cf generates an average of 3.511 ± 0.037 neutrons per fission [89]. Its contribution to the activity was taken into account in source strength measurements but the isotope was not modelled in the Monte Carlo. The properties of ^{252}Cf were modelled in some detail:

- *Neutrons.*

  The neutron multiplicity distribution of ^{252}Cf was described by a Gaussian of mean 3.7676 ± 0.0047 and width 1.57 [89]. The energy spectrum of the prompt neutrons was modelled by a Maxwellian distribution with temperature 1.42 MeV (1.64×10^{10} K) [90]

  $$f_E dE = f_P \left(\frac{dp}{dE} \right) dE = 2 \sqrt{\frac{E}{\pi (kT)^3}} \exp \left(-\frac{E}{kT} \right) dE \tag{4.3}$$

  This energy spectrum is shown in Figure 4.8 where it can be compared to that of NC neutrons.

  The delayed neutrons, which were not modelled in SNOMAN, amounted to 0.0078 neutrons per fission [91]. $17 \pm 5\%$ of these had half-lives of less than 0.5 s [92].

- *Gammas.*

  The simulation of the gammas was somewhat more involved because there is a correlation between the total energy of the neutrons and the total energy of the

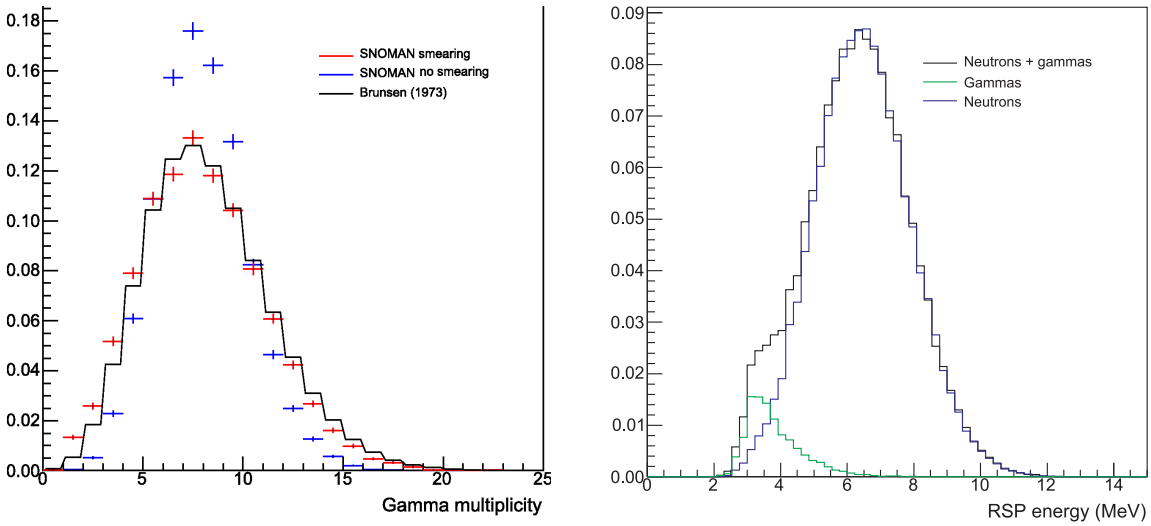

Figure 4.9: ^{252}Cf gamma multiplicity distributions in the Monte Carlo compared with experiment (left) and the energy spectrum from a ^{252}Cf salt run simulation (right).

gammas. Nifenecker et al. [93] found the following linear relationship between the average number of neutrons $\overline{n}$ and the average total energy of the gammas $\overline{E_{\gamma,tot}}$

$$\overline{E_{\gamma,tot}} = 0.75\,\overline{n} + 4.0 \text{ MeV} \tag{4.4}$$

The energy spectrum of individual gammas was described by

$$P(E_\gamma) = c\sqrt{E_\gamma}\exp\left(-\frac{E_\gamma}{E_0}\right) \tag{4.5}$$

which was taken from [94]. $E_0 = 0.62$ MeV and c is a normalisation constant.

In the Monte Carlo the relationship Eq. (4.4) had to be smeared so that for given n there was some realistic distribution of $E_{\gamma,tot}(n)$; recall that Eq. (4.4) related an *average* total gamma energy $\overline{E_{\gamma,tot}}$ to an *average* number of neutrons $\overline{n}$. Unfortunately no information was available on the distribution of $E_{\gamma,tot}(n)$, for fixed n, so the distributions had to be estimated using the gamma multiplicity distribution, which was known from the work of Brunson [95, 96]. He found the following multiplicity distribution, normalised to a gamma detection threshold of 140 keV

$$\Pi(G) = c_1\frac{c_2^G e^{-c_2}}{G!} + (1-c_1)\frac{c_3^G e^{-c_3}}{G!} \tag{4.6}$$

where G is the number of detected gammas per fission and the parameters are $c_1 = 0.675$, $c_2 = 6.78$ and $c_3 = 9.92$.

The value of $E_{\gamma,tot}$ from Eq. (4.4) was smeared in such a way that Brunson's multiplicity distribution could be reproduced, with an artificially imposed gamma detection threshold of 140 keV. The smeared energy $E'_{\gamma,tot}$ was given by

$$E'_{\gamma,tot}(n) = g(0, 2.15) + (0.75\,n + 4.0)\ \text{MeV} \tag{4.7}$$

where $g(0, 2.15)$ is a random number sampled from a Gaussian of mean 0 and width 2.15 MeV. The width of the Gaussian was chosen to reasonably approximate the multiplicity distribution. $E'_{\gamma,tot}(n)$ was not allowed to drop below zero. The simulated gamma multiplicity distributions are shown, with and without smearing, in the left hand plot of Figure 4.9. The level of agreement was more than adequate.

Tests of the simulation could be made by extracting various parameters from Monte Carlo runs and comparing them to experimental averages compiled by Valentine [96]. This table shows the comparison for 3 representative parameters

Quantity	SNOMAN		Experiment	
	Value	Unc.	Value	Unc.
Mean total gamma energy	6.85	0.01	6.95	0.3
Mean gamma energy	0.93	0.00	0.87	0.02
Mean gamma multiplicity	8.19	0.00	7.89	0.4

The effect of the gammas on the energy spectrum measured in a ^{252}Cf run is shown in Figure 4.9. This distribution cannot be compared directly to SNO data because of the large number of background events below 4 MeV.

The neutron production rate of the ^{252}Cf source was measured using various methods that will be discussed in Section 6.1. The resulting source strength was 16.55 ± 0.11 on 12$^{\text{th}}$ June 2001. The source strength at an arbitrary time $A(t)$ was calculated using

$$A(t) = A_0\, e^{-t/\tau_{252}} + f_{250}\, A_0 \left\{ e^{-t/\tau_{250}} - e^{-t/\tau_{252}} \right\} \tag{4.8}$$

where $A_0 = 16.55 \pm 0.11$ n s^{-1} is the activity on 12$^{\text{th}}$ June 2001, the ^{250}Cf half life is 13.08 y, the ^{252}Cf half life is 2.645 y and $f_{250} = 0.0192 \pm 0.0002$ is the relative number of neutrons produced by ^{250}Cf as opposed to ^{252}Cf. The error on this is given by

$$\delta A(t) = \delta A_0\, e^{-t/\tau_{252}} + A_0\, f_{250} \sqrt{\left(\frac{\delta A_0}{A_0}\right)^2 + \left(\frac{\delta f_{250}}{f_{250}}\right)^2} \left\{ e^{-t/\tau_{250}} - e^{-t/\tau_{252}} \right\} \tag{4.9}$$

where the uncertainties on τ_{250} and τ_{252} are neglected because they are small in comparison to the uncertainties on f_{250} and A_0.

4.4.3 The AmBe sources

The AmBe sources produced neutrons via (α,n) reactions. Approximately 60% of the neutrons were accompanied by a 4.4 MeV gamma.

AmBe sources consist of the long-lived alpha-unstable isotope ^{241}Am, which generates the alphas, and ^{9}Be, which readily undergoes (α,n) reactions. The two most important of the latter are

$$^{9}\mathrm{Be}(\alpha,\mathrm{n})^{12}\mathrm{C}, \quad \mathrm{Q} = 5.701 \text{ MeV}; \tag{4.10}$$

$$^{9}\mathrm{Be}(\alpha,\mathrm{n})^{12}\mathrm{C}^{*} \rightarrow {}^{12}\mathrm{C} + \gamma + 4.44 \text{ MeV}, \quad \mathrm{Q} = 1.261 \text{ MeV}. \tag{4.11}$$

where the second is responsible for the 4.4 MeV gamma. The cross sections of the two reactions have different dependencies on alpha energy and so their relative rates are somewhat dependent on the arrangement of the ^{241}Am and ^{9}Be within the source. There are two common arrangements: in *foil sources* the ^{9}Be is present as a foil next to the ^{241}Am and in *powder sources* the ^{9}Be and ^{241}Am are mixed together in a fine powder. One source of each type was used in SNO during the NCD phase (the source with the higher activity was the powder source).

This table from Croft [97] shows calculated and measured branching fractions for the 4.4 MeV gamma-producing reaction for various different AmBe sources

Ref.	Year	Method	B.R.	
			Value	Unc.
[98]	1968	Calc.	0.59	0.06
[99]	1970	Exp.	0.75	0.11
[100]	1986	Exp.	0.558	0.031
[97]	1988	Exp.	0.591	0.015
[97]	1988	Calc.	0.566	0.057

There is considerable variation, reflecting the variation in internal arrangements of the sources. Croft reported that the probability was relatively well defined only for powder sources (he measured 0.591 ± 0.015). In the Monte Carlo this number was used for both sources as sufficient information was not available to make an independent estimate for the foil source. This simplification had no consequences for any of the measurements discussed in this thesis.

The neutron energy spectra of AmBe sources are also somewhat dependent on the individual source characteristics. The left hand plot of Figure 4.10 shows one of two

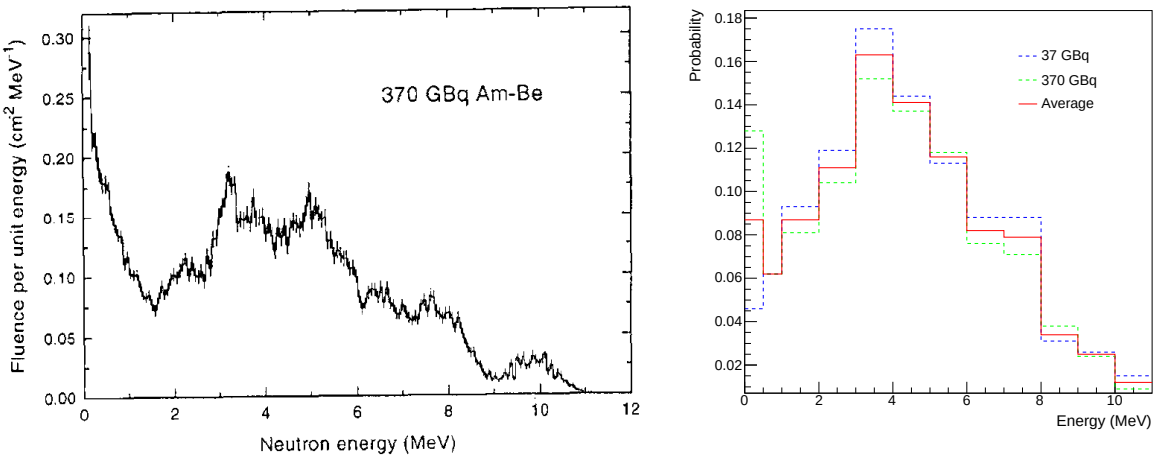

Figure 4.10: An experimental AmBe energy spectrum from [12] (left) and the Monte Carlo energy spectrum (right) which is the average of two measured spectra.

experimental spectra from Marsh [12]. The average of this spectrum and another, which did not exhibit the low energy rise, was implemented in the Monte Carlo in the form a binned PDF. The Monte Carlo spectrum is shown in the right hand plot of Figure 4.10.

As mentioned above, the energy spectrum was relatively unimportant for modelling neutron propagation in the D_2O but it did matter in the H_2O. Neutron calibration sources were deployed in the H_2O close to the surface of the acrylic vessel to calibrate the detection efficiency for neutrons produced within the acrylic of the vessel by (α,n) reactions. The neutron capture cross section on H is highly sensitive to neutron energy, at low energies, which made the neutron capture efficiency of the array for sources close to the acrylic vessel also very sensitive to the neutron energy. Figure 4.11 shows the H cross section as a function of energy and the array capture efficiency as a function of energy for a light water AmBe run; in the latter the x-axis gives the mean energy of a Gaussian of width 1.5 MeV from which the neutron energies were sampled.

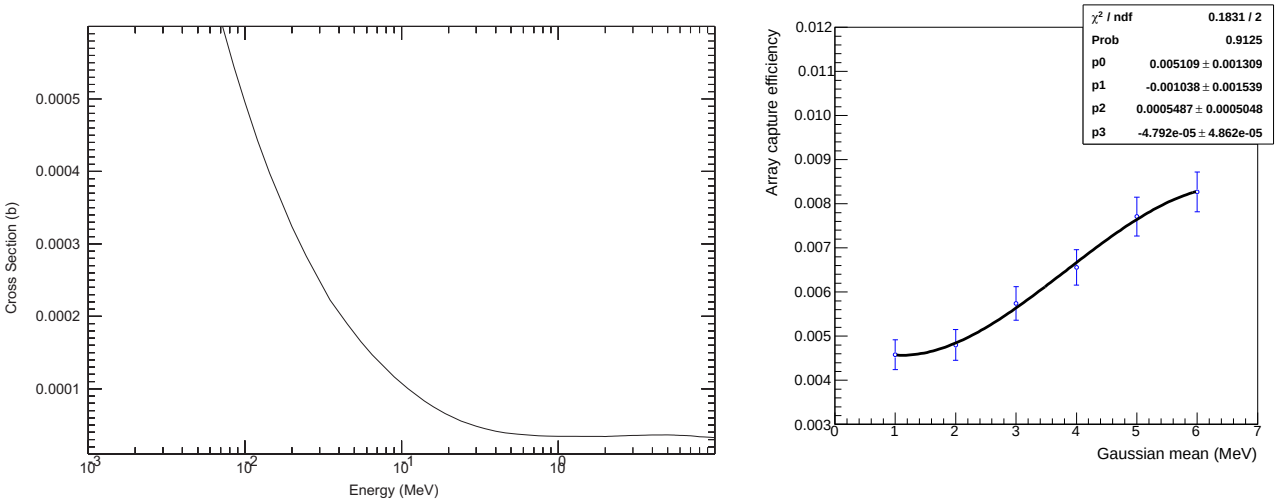

Figure 4.11: The energy-dependence of the neutron capture cross section on hydrogen (left) and the NCD array neutron capture efficiency as a function of neutron energy for a source placed just *outside* the acrylic vessel (right).

Chapter 5

Source strength measurements using a Ge detector

I am never content until I have constructed a mechanical model of the subject I am studying. If I succeed in making one, I understand; otherwise I do not.

WILLIAM THOMSON
Lecture notes on *Molecular Dynamics and the Wave Theory of Light*

This chapter presents measurements of the distributed ^{24}Na and ^{222}Rn neutron calibration source strengths using a Ge detector. It describes the process of converting the energy deposition spectra into source strengths. The main analysis tasks were as follows:

- *Efficiency calibration.*

  The efficiency of a Ge detector is the energy-dependent probability that a gamma deposits all of its energy in the sensitive region of the detector. The efficiency can be determined by taking measurements with calibration sources of known intensity. However, the efficiency is a strong function of gamma energy and source geometry, both of which differed between the calibration sources and the ^{24}Na and ^{222}Rn samples. The differences were accounted for by using a Monte Carlo simulation, tuned and verified with reference to calibration data, to predict the efficiencies.

- *Dead time measurement.*

  Dead time fractions as high as 16% and 63% were observed in the ^{24}Na and ^{222}Rn data respectively. These fractions had to be precisely quantified and corrected for.

- *Full-energy peak integration.*

  The numbers of counts in the peaks in the energy deposition spectra had to be determined consistently across all the calibration and sample data. The method for integrating peaks had to handle a variety of background shapes and produce numbers with statistical and systematic uncertainties.

- *Detector stability measurement.*

  Measurements were taken over a period of almost two years and the detector stability over than time had to be assessed.

- *Implementation of the deuteron photodisintegration cross section.*

  Ge detectors count gammas, but the NCD array was sensitive to neutrons produced by the gammas via photodisintegration. The cross section for this process has an appreciable uncertainty (2%) and was an irreducible systematic in the ^{24}Na source strength measurement. Its value and uncertainty had to be assessed and, ideally, other systematics controlled such that it was dominant.

All of these are discussed in the following sections. The analyses of the ^{24}Na and ^{222}Rn measurements were broadly similar so, for the sake of clarity, the analysis is discussed in detail only for the ^{24}Na measurements. The final section describes how the ^{222}Rn analysis differed and presents the ^{222}Rn results.

5.1 Ge detectors in general, and the SNO Ge detector in particular

5.1.1 Ge detectors

The semiconductor germanium can be used to build radiation detectors with excellent energy resolution. Ge forms solid crystals in which the valence-4 Ge atoms bond covalently with their neighbours. All valence electrons participate in covalent bonds so the valence band is full and the conduction band is empty; the two bands are separated by an energy gap of 0.66 eV. Energy supplied to the crystal, either thermally or through interaction with radiation, can excite electrons into the conduction band, leaving positively charged holes in the valence band, allowing the material to conduct.

Semiconductors are usually *doped* to improve their electrical properties. In a *p-type* material valence-5 atoms are introduced; four electrons form covalent bonds leaving

one electron per atom loosely bound and able to move easily through the lattice. These electrons form *donor states* just below the conduction band. In *n-type* materials, valence-3 atoms are added producing an excess of loosely-bound holes; these form *acceptor states* just above the conduction band.

If p-type and n-type materials are brought into contact in a *junction* the excess electrons in the n-type material diffuse into the p-type material and combine with the excess holes. This leaves a region around the junction, called the *depletion region*, across which the remaining charged donor and acceptor states produce an electric field.

The deposition of energy in the depletion region by radiation can create electron-hole pairs. In the electric field the electrons and holes flow in opposite directions, and, if totally collected, the total of number electrons can form an electronic pulse with an amplitude proportional to the energy of the radiation. A reverse bias voltage applied to the crystal can be used to increase the size of the depletion region, and therefore the sensitive region of the crystal, improving the charge collection efficiency.

A typical Ge detector consists of a p-type high purity Ge (HPGe) crystal partially surrounded by a thin layer of Li, which is a dopant that is *drifted* into the surface of the crystal to create an n-type layer. These layers are typically 0.1-1.5 mm thick and are regions from which no deposited charge is collected. They are known as *dead layers*. Gammas of moderate energies (hundreds of keV) pass easily into the sensitive region of the crystal - the range of a 100 keV gamma is $\sim$ 4 mm - whilst the detector is shielded from externally produced electrons and alphas, both by the dead layer and the materials surrounding the crystal - the range of a 1 MeV electron is $\sim$ 1 mm and that of a 5 MeV alpha is considerably less.

Ge detectors are favoured in the study of nuclear decays, despite the availability of cheaper and more efficient alternatives, because of their excellent energy resolution. For example, the typical energy resolution of a Ge detector (conventionally measured using the 662 keV line of ^{137}Cs) is $\sim$ 1 keV, while for a NaI scintillation detector it is $\sim$ 40 keV [13]. The origins of the high resolution are the small amount energy required to produce an electron hole pair (3 eV), consequent large number of events per interaction (220000 for the 662 keV gamma), and the high efficiency with which the electrons are collected.

In general the statistical contribution to resolution is actually smaller than would naïvely be calculated using Poisson statistics. As demonstrated by Fano [101], the energy deposited in the detector is constrained to a fixed total energy, that of the incoming gamma, and the amount deposited in each interaction is not continuous or independent. The correlation can act to reduce the statistical uncertainty. Fano showed that the $\sqrt{N}$

uncertainty of Poisson statistics is modified to

$$\frac{\delta N}{N} = \frac{\sqrt{FN}}{N} \tag{5.1}$$

where F is the *Fano factor*. A typical value for a Ge detector would be 0.13 [102]. In proportional gas counters it can be even lower but in a scintillation detector it is typically ~ 1.

The important processes by which gammas interact with a Ge crystal are shown schematically in Figure 5.1. At 1 MeV the dominant interaction is Compton scattering, followed in intensity by the photoelectric (PE) effect and pair production (PP). At lower energy the PE cross section becomes more important and the process dominates below 0.5 MeV. PP dominates above 10 MeV.

A typical Ge detector data acquisition system consists of a preamplifier, which converts the charge pulse from the detector into a voltage pulse; a linear amplifier, to amplify the millivolt preamp pulse into a pulse of a few volts; and a multichannel analyser (MCA), which converts the pulse amplitude into a digital value, which can be read out and stored.

5.1.2 Energy deposition spectra

A ^{24}Na energy deposition spectrum is shown in Figure 5.2 to illustrate the general features of such spectra.

^{24}Na decays with the simultaneous emission[1] of 1.369 and 2.754 MeV gammas. The spectrum therefore has three *full-energy peaks* corresponding to collection of all energy deposited by the 1.369 and 2.754 MeV gammas, and of both at once. The simultaneous absorption of two gammas from the same cascade is known as *true coincidence summing* (in contrast to *random coincidence summing* when the gammas are from different cascades). Associated with each of these peaks are *first* and *second escape peaks* with energies 511 and 1022 keV less than the full-energy peaks. Counts appear in the first escape peak when a PP positron, produced during absorption, annihilates and one of the 511 keV gammas escapes. A count appears in the second when both gammas escape. Below each full-energy peak is a *Compton edge* which corresponds to the maximum amount of energy that can be transferred to an electron in a Compton scattering event. The count lies at the edge, or below, in the *Compton continuum*, if the scattering gamma escapes the

[1] In all cascades analysed in this study the time between the emission of successive gammas is vastly smaller than the time-resolution of the detector.

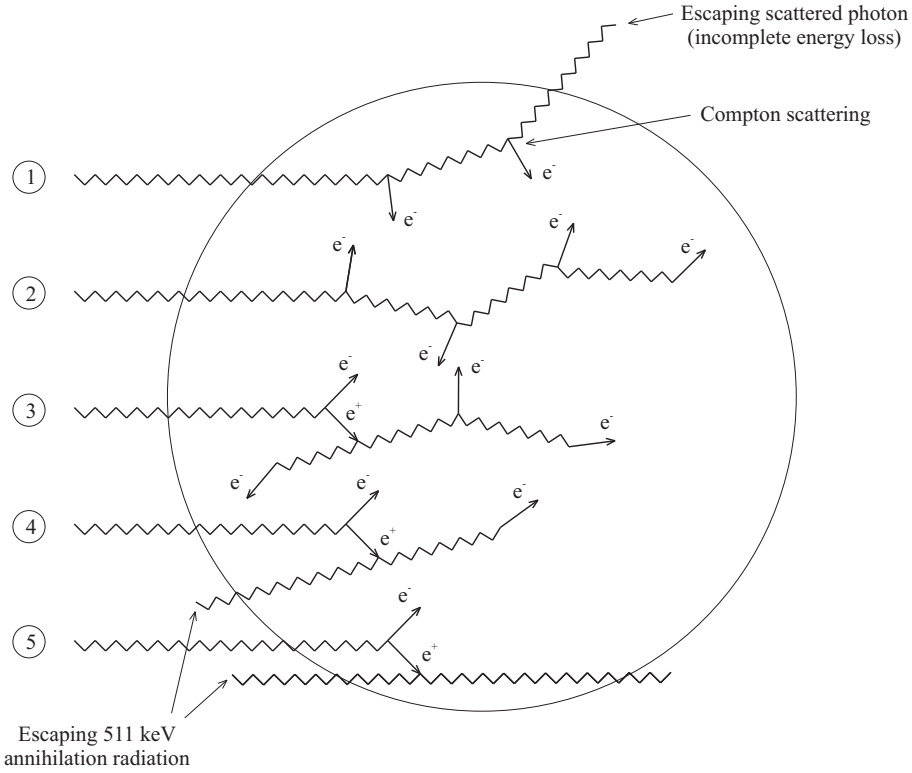

Figure 5.1: Processes by which a gamma can interact in a Ge detector. Event 1 contributes to the Compton continuum; events 2 and 3 lie in the full-energy peak; in event 4 a pair-produced gamma escapes and all other energy is absorbed, leaving a count in the first escape peak; in event 5 two pair-produced gammas escape, leaving a count in the second escape peak. Adapted from [13]

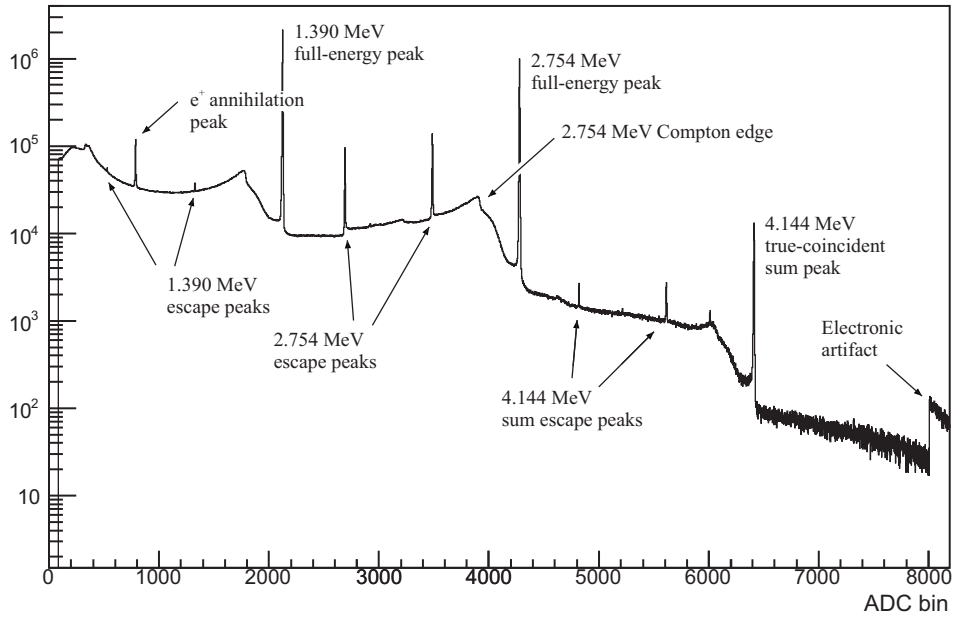

Figure 5.2: A ^{24}Na energy deposition spectrum produced by the SNO Ge detector.

crystal without interacting further. The peak at 511 keV is believed to originate from PP outside the Ge crystal; PP followed by annihilation of the positron produces back-to-back 511 keV gammas only one of which, because of the source-detector geometry, is likely to be detected.

5.1.3 The SNO Ge detector

The SNO Ge detector (Princeton Gamma-Tech, Princeton, NJ; model no. IGC 5021; serial no. 2518) contained a coaxial high purity p-type crystal mounted in a low background cryostat (model no. NPR/12-ULB-PB). The cryostat was positioned in a cavity formed by 2 inches of copper shielding inside 8 inches of lead shielding. The cavity was flushed with N_2 before the start of measurements to eliminate any radon and a N_2 atmosphere was maintained during data taking.

The detector electronics were configured in a standard way, described above, but with the addition of a pile-up rejection feature in the amplifier, which, at high count rates, decreased the time taken for the baseline to return to zero amplitude. The shaping time constant of the amplifier was 6 μs and the MCA had 8192 channels. Data acquisition was handled by the Maestro-32 package, version 6 (Ortec, Oak Ridge, TN). The computer clock was set to run permanently on EDT (eastern daylight time, which is Sudbury winter

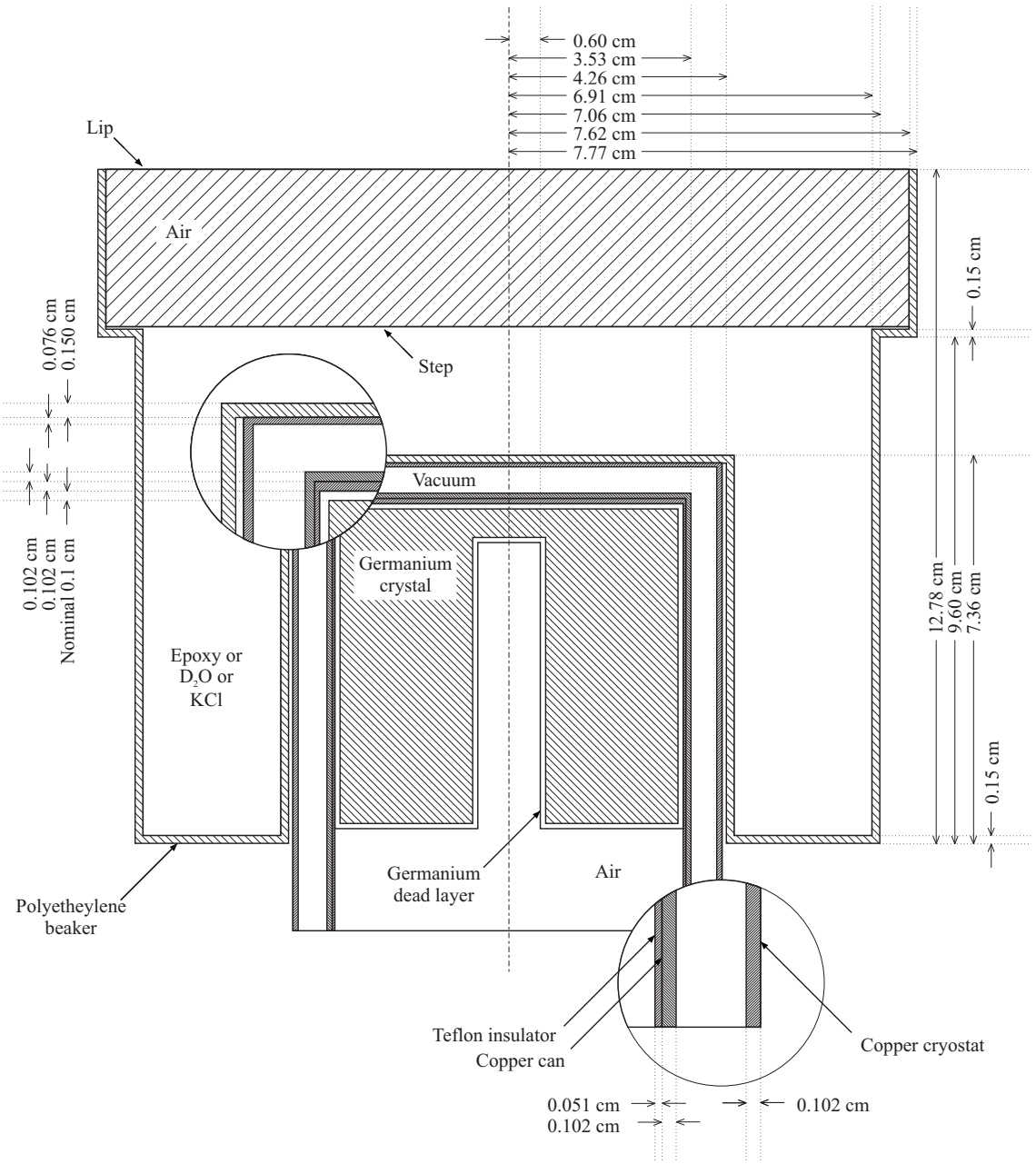

Figure 5.3: The Ge detector and Marinelli beaker geometry, as modelled in the Monte Carlo simulation. The actual Marinelli beakers had gently sloping sides.

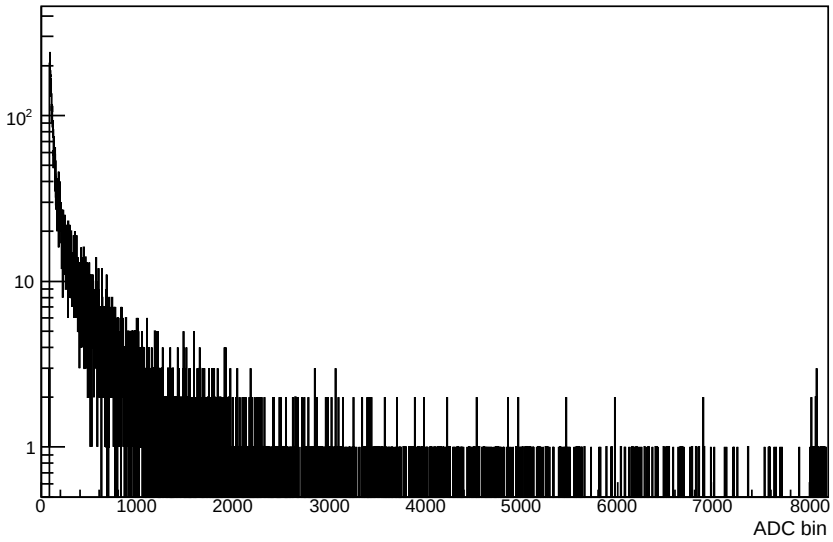

Figure 5.4: Background energy spectrum collected with an empty Marinelli beaker for 4 days. The highest ADC bin corresponds to 2.826 MeV.

time).

The detector had been underground, at the SNO facility, since 1997. For most of the time between then and these measurements it had been inactive, with the crystal at the ambient temperature [103]. The detector was cooled down and reconditioned in 2004/05 and since then had been in continuous use. Following reconditioning, studies demonstrated the energy linearity of the detector and measured its energy resolution to be 1.95 keV using the 1332.5 keV line of ^{60}Co [103]. This study is the first rigorous efficiency calibration.

Figure 5.4 shows a background energy spectrum collected with an empty Marinelli beaker (see below) for 4 days. Over the part of this spectrum which would contain the ^{24}Na peaks (approximately ADC bins 3000-8000) the background rate was negligible.

5.1.4 Calibration sources

This section describes the composition and geometry of the calibration sources used in this study. The analysis of data acquired using them is left to later sections.

All sources had a Marinelli beaker geometry (see Figure 5.3), designed to maximise

the number of counts for a given sample activity[2]. All Marinelli beakers were manufactured to the same specification and had nominal volumes of 1 litre. Some small differences in geometry between beakers were observed - quoted volumes and fill levels could not always be completely reconciled - and in such cases the fill level was taken as the measure of sample size when configuring the Monte Carlo.

The primary efficiency standard was a mixed radioisotope source, referred to as the *mixed source*. The source (QSA Global, Germany; source no. NB 518) consisted of a mixture of 8 radioisotopes homogeneously [104] suspended in an epoxy matrix, which produced gammas with energies in the range 81-1836 keV. The matrix had a density 1.5 $\mathrm{g\,cm^{-3}}$ (see Appendix G for details of its composition). The highest energy line was from ^{88}Y at 2.734 MeV. The highest energy line not produced in a cascade, and therefore subject to summing effects, was the 1115.5 MeV gamma from ^{88}Zn.

The one sigma uncertainty on each isotope's activity was quoted at 1.5% [20]. Communication with the source manufacturer revealed that these uncertainties were not independent. The activity of each nuclide was calculated from the mass of a reference solution added to the epoxy, whose activity was measured by the manufacturer and by PTB (Physikalisch-Technische Bundesanstalt). Some part of the uncertainty was therefore correlated - relating to the amount of reference solution added to the epoxy - and some part uncorrelated - relating to the relative amounts of each isotope in the solution. The manufacturer could provide little quantitative guidance on how to divide up the 1.5% uncertainty other than that it was likely to be mostly uncorrelated. The division was important as the less correlated the source strengths, the more information the calibration provided about the efficiency of the detector. The sources strengths were conservatively treated as being, on average, 50% correlated and 50% uncorrelated.

A high statistics mixed source run was used for the primary efficiency calibration. Additional lower statistics runs were used to monitor detector stability.

The other sources used in this analysis were custom-made using ^{40}K as the radioisotope, supplied in the form of crystalline KCl. ^{40}K is a naturally occurring isotope of potassium with a half-life of 1.3×10^9 years [14]. It decays by electron capture producing a 1460 keV gamma (see Figure 5.5) with probability 0.107 ± 0.002.

There were three KCl sources: the *solid KCl source* consisted of crystalline KCl packed into a Marinelli beaker [103]; the *first liquid KCl source* was a small amount of

[2]Historically the use of this geometry was motivated by the small size of Ge crystals and low detector efficiency. The disadvantage, particularly compared with a point source geometry, is the problem of accounting for absorption of radiation within the source. However, they remain a useful way of maximising count rates for low rate sources and minimising acquisition times for high rate sources.

Table 5.1: Mixed source radioisotopes [20, 14]. The reference time for the activities is Feb 1st 2005 06:00:00 EDT.

Isotope	Half-life (days)		Gamma	Ref. activity	Prob. gamma	
	Value	Unc.	(keV)	(kBq)	Value	Unc.
Ba-133	3841	7	80.997	1960	0.36680	0.00280
Co-57	271.74	0.06	122.061	1780	0.85600	0.00170
Co-57	271.74	0.06	136.474	1780	0.10680	0.00080
Ce-139	137.64	0.02	165.860	1680	0.79900	0.00040
Ba-133	3841	7	276.400	1960	0.07164	0.00020
Ba-133	3841	7	302.851	1960	0.18330	0.00060
Ba-133	3841	7	356.013	1960	0.62050	0.00190
Ba-133	3841	7	383.848	1960	0.08940	0.00030
Sr-85	64.84	0.02	514.005	7140	0.98400	0.00400
Cs-137	10968	18	661.657	3910	0.85100	0.00200
Mn-54	312.12	0.06	834.848	3720	0.99976	0.00000
Y-88	106.62	0.01	898.042	8030	0.94400	0.00300
Zn-65	243.66	0.09	1115.539	9140	0.50600	0.00220
Y-88	106.62	0.01	1835.969	8030	0.99240	0.00310
Y-88	106.62	0.01	2734.105	8030	0.00610	0.00020

KCl, from a different supplier, dissolved in D_2O [21]; the *second liquid KCl source* was a similar amount of KCl, from the same batch as the solid source, dissolved in D_2O. A summary of the different KCl sources is given in Table 5.2.

Using the KCl sources in the efficiency calibration was desirable for two reasons. First, the 1460 keV gamma was closer in energy to the ^{24}Na gammas than any usable line from the mixed source, and second, the source densities were closer to the ^{24}Na brine (and actually identical in the case of the liquid sources). However, it was discovered during this study (see Section 5.4) that KCl is an unsuitable material for use as a source standard, because of the apparent unreliability of manufacturer-measured purities. But the sources remained suitable for checking detector stability and the ability of the Monte Carlo to predict the *relative* efficiencies of sources of different densities.

5.2 A Monte Carlo simulation in SNOMAN

A Monte Carlo simulation of the Ge detector allowed efficiencies appropriate for ^{24}Na gammas to be derived from measurements made using calibration sources with different

Table 5.2: Summary of KCl sources. *Lip* and *step* are defined in Figure 5.3. The purities are those specified by the manufacturers. Fill levels and masses were taken from [21, 22]

Name	Material	Density ($g\,cm^{-3}$)	Fill	Purity (%)
Solid	Crystalline KCl (1725.8 g inc. beaker)	1.24	1 mm below step	99.2
Liquid 1	1170.4 g D_2O + 29.975(0.027) g KCl	1.105	30.5 mm below lip	99.95(0.05)
Liquid 2	1025.8 g D_2O + 102.8 g KCl	1.105	Step	99.2

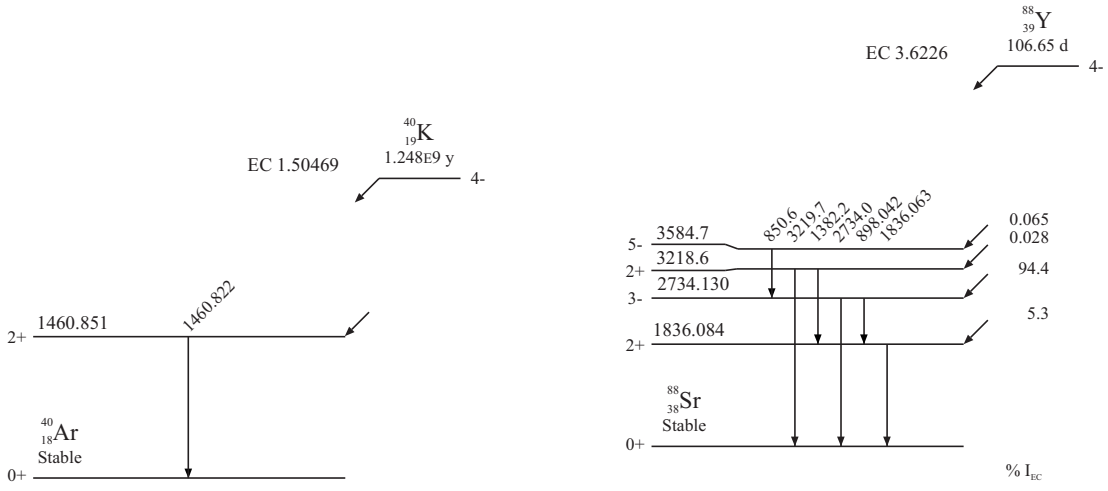

Figure 5.5: Decay schemes for ^{40}K (left) and ^{88}Y (right). Adapted from [14].

densities and producing gammas of different energies. It was the ideal way to extrapolate in density and in energy - the physics of photon and electron transport are well understood and there was sufficient computing power to keep statistical uncertainties small.

There is a substantial literature describing efforts to construct Monte Carlo simulations of Ge detectors (see [105] for a review), much of it describing the difficulty in getting agreement between data and simulation. The main problems arise from the lack of knowledge of the internal detector geometry and, to a lesser extent, the construction materials and charge-collection characteristics of the crystal (charge collection is not uniform throughout the detector volume due to imperfections in the crystal and non-uniformity of the electric field). This information is often not readily available, even from the manufacturer - Ge detectors are not mass-produced and have their own individual characteristics and histories of use and misuse. Helmer [105] states that *errors in manufacturers' detector position could be a few mm and that the detector axis is often not parallel to the housing axis'*.

There are two approaches to this general lack of information: the first is to measure the internal geometry (the most efficient method uses x-rays) and the second is to fit uncertain geometry parameters by comparison of calibration data and simulations. The second approach was taken in this study and the parameter chosen was the *dead layer*, a region of Ge surrounding the active part of the crystal, from which charge is not effectively collected. The manufacturer could not provide a precise value (only a nominal thickness of 1 mm) and it is a quantity with which the efficiency is strongly correlated. The aim was to constrain the dead layer thickness using the mixed source data and use the tuned Monte Carlo to predict efficiencies for ^{24}Na gammas.

The Monte Carlo was constructed within the SNO Monte Carlo framework (known as SNOMAN and described in detail in Section 4.1), which provided a geometry interfaced with the electron and photon transport package EGS4. SNOMAN has been tested extensively by the SNO collaboration and EGS4 is an industry-standard package. Adapting SNOMAN for the Ge detector simulation involved constructing the detector and calibration source geometry, adding the epoxy and KCl media, selecting appropriate EGS4 parameters and adding decay schemes and angular correlations for ^{24}Na and ^{88}Y. Each of these adaptions is discussed in turn.

As much information as possible was obtained on the internal detector construction and it was faithfully reproduced in SNOMAN: detector measurements were obtained from communications with the manufacturer and from drawings made during repairs; the gently sloping sides of the Marinelli beakers were approximated by vertical lines as frustums of

cones containing cavities were difficult to simulate in SNOMAN; the electronics behind and within the crystal were neglected, as was the copper and lead shielding; and the dead layer was assumed to have equal thickness over all surfaces of the crystal. The dead layer on the surface facing into the well may have been smaller than the one on the outer surface, but equal thickness was a good approximation as most gamma interactions were with the outer layer. Likewise there were few interactions of gammas with the electronics and shielding. Media were created for each of the sources and the density of the solid KCl medium was scaled to account for imperfect packing of the crystals in the Marinelli beaker.

EGS4 contains two parameters `ECUT` and `PCUT` which give the energies below which the transport of electrons and photons, respectively, are no longer simulated; these were set to 520 keV and 15 keV (close to the smallest possible) to maximise the quality of the simulated energy deposition spectra (see Figure 5.6).

The decay schemes of ^{24}Na and ^{88}Y, two isotopes whose gammas were produced in cascades, are shown in Figures 3.2 and 5.5. Only the 1.369 and 2.754 MeV ^{24}Na gammas and the 0.898, 1.836 and 2.734 MeV ^{88}Y gammas were included in the simulation as the branching ratios to other gammas were negligible. The ^{88}Y branching fractions are:

Cuml.	Energy (MeV)	
B.R.	Gamma 1	Gamma 2
0.00711	2.734	0.000
0.94496	1.836	0.898
1.00000	1.836	0.000

In addition to the energies and probabilities, the angular correlations between the gammas had to be included as they affect the likelihood of coincident summing. Angular correlations between two gammas can be parametrised in various ways, two common ones being in powers of $\cos^2\theta$ and in Legendre Polynomials, $P_n(\cos\theta)$:

$$W(\theta) = \sum_i^l a_i \cos^{2i}\theta$$

$$W(\theta) = \sum_i^l a_i P_{2i}(\cos\theta)$$

where $W(\theta)$ is the probability of θ being the angle between the gammas.

The ^{24}Na decay is a $4^+ - 2^+ - 0^+$ sequence producing two gammas which are almost

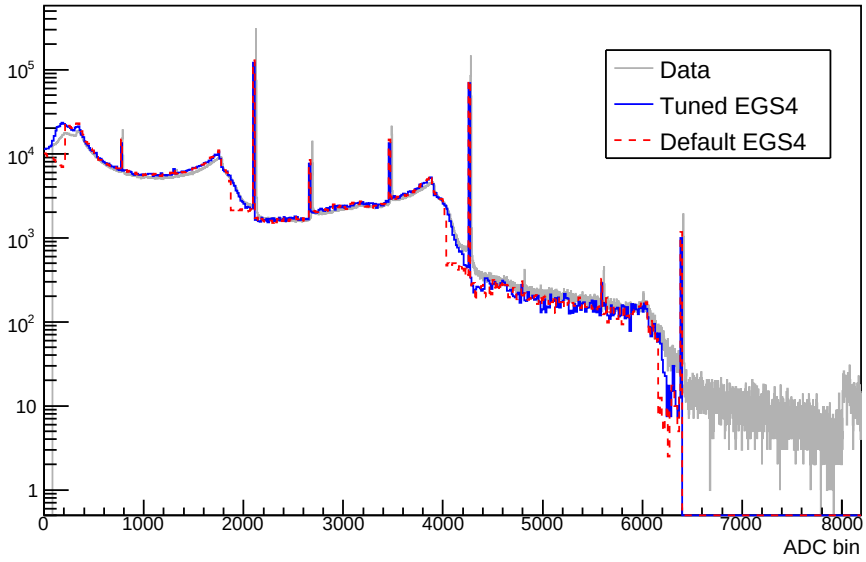

Figure 5.6: Simulated and experimental ^{24}Na energy deposition spectra.

entirely E2. The coefficients can be calculated analytically [106] and the expression is

$$W_{Na}(\theta) = 1 + \frac{1}{8}\cos^2\theta + \frac{1}{24}\cos^4\theta \tag{5.2}$$

For the ^{88}Y coefficients measured values [107] were used

$$W_Y(\theta) = 1 - 0.1283\,P_2(\cos\theta) - 0.0243\,P_4(\cos\theta) \tag{5.3}$$

5.2.1 Verification

There were a number of ways that the Monte Carlo could be verified. The three main ones were: testing the ability of the tuned Monte Carlo to reproduce the efficiencies measured with each of the mixed source isotopes, the relative efficiencies of the liquid and solid KCl sources and the ^{24}Na energy deposition spectra. The first two are discussed in Section 5.4.

Measured and simulated ^{24}Na energy deposition spectra are shown overlaid in Figure 5.6. All features of the spectrum are reproduced in the Monte Carlo. The differences are the magnitude of the rise in Compton back-scattering at low energies - because the material surrounding the Ge detector was not simulated; the width of the peaks - because

the energy resolution of the Monte Carlo was perfect; and a small discrepancy at high energies, above the 2.75 MeV peak.

A powerful quantitative test could be made by comparing relative peak areas in the ^{24}Na spectrum, which are sensitive to the modelling of detector geometry and angular correlations. The results are shown in Figure 5.7 and there was good agreement for the lower energy peaks, in particular. The agreement was less pleasing for the higher energy peaks, which makes sense given the differences seen in Figure 5.6. The higher energy peaks were not used for source strength measurements. A similar exercise was performed using the ^{88}Y lines in the mixed source data: ^{88}Y has lines at 0.898 and 1.836 MeV as well as true and random coincidence lines at 2.734 MeV (see Figure 5.5).

5.3 Full-energy peak integration

5.3.1 Determining peak areas

The shape of a typical full-energy peak can be described by the sum of three components:

- *Smoothly varying background.*

  Contributions from the Compton continua of other lines in the spectrum, usually described by a first or second order polynomial.

- *Gaussian.*

  Corresponds to complete charge collection; the width comes from the statistical variation in the number of electrons produced by a gamma of a given energy.

- *Skew Gaussian and/or step function.*

  The are often more counts just below peaks than just above. This can occur if the peak lies on the Compton edge of another; because Compton electrons sometimes don't deposit all of their energy before escaping the active region; and because of incomplete charge collection due to crystal imperfections.

There are various ways to determine peak areas. Two common ones are fitting the peak to a combination of the functions above (or equivalent) and estimating the background by interpolating under the peak from regions either side of it. Peak fitting is the most flexible and can cope with non-linear backgrounds and overlapping peaks.

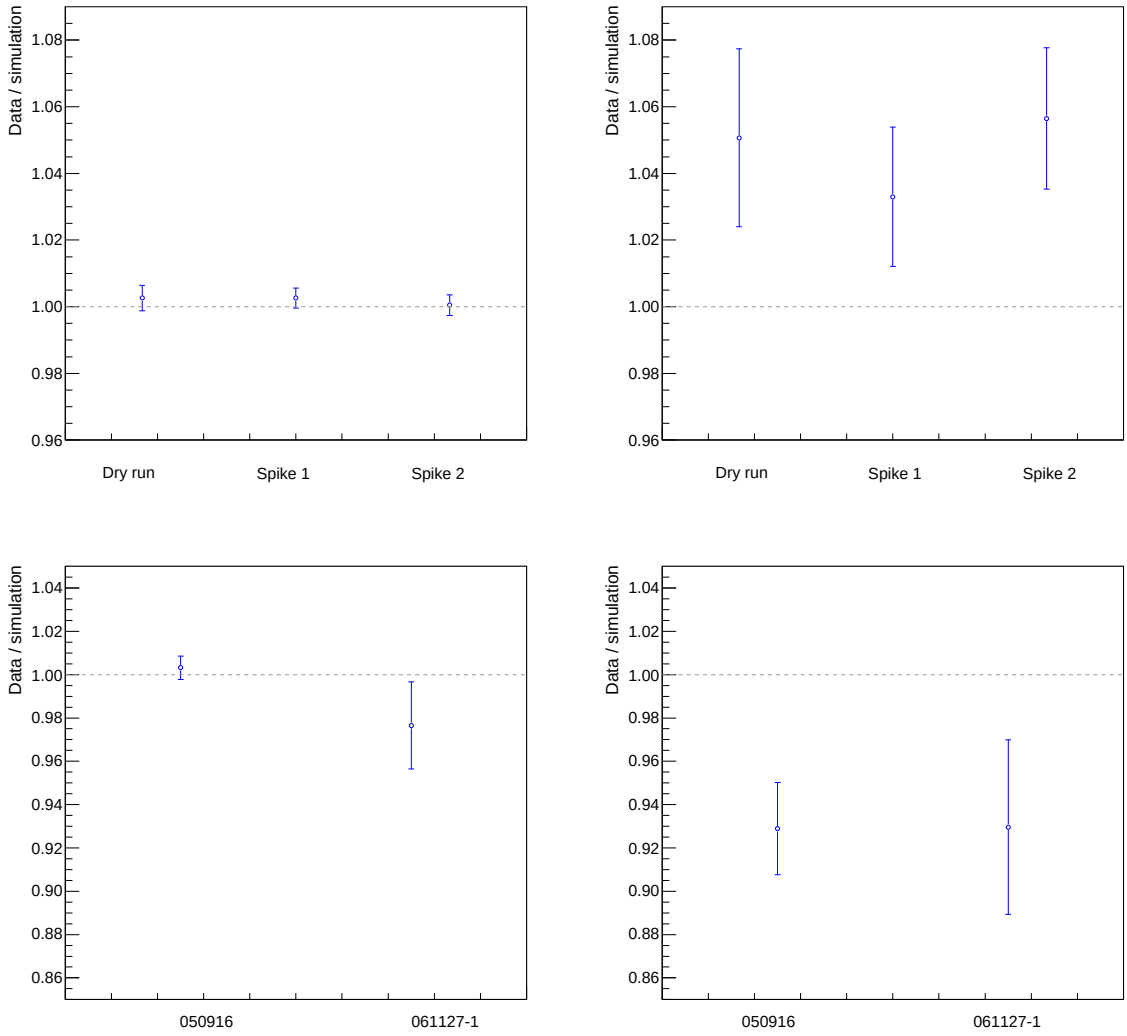

Figure 5.7: Comparisons between relative peak heights in data and Monte Carlo. ^{24}Na 2.754 / 1.369 (top left), ^{24}Na sum peak / 1.369 (top right), ^{88}Y 1.836 / 0.898 (bottom left), ^{88}Y sum / 0.898 (bottom right). In the ^{24}Na plots the comparison was made for all three measurements and for ^{88}Y it was made for the two highest statistics mixed source runs.

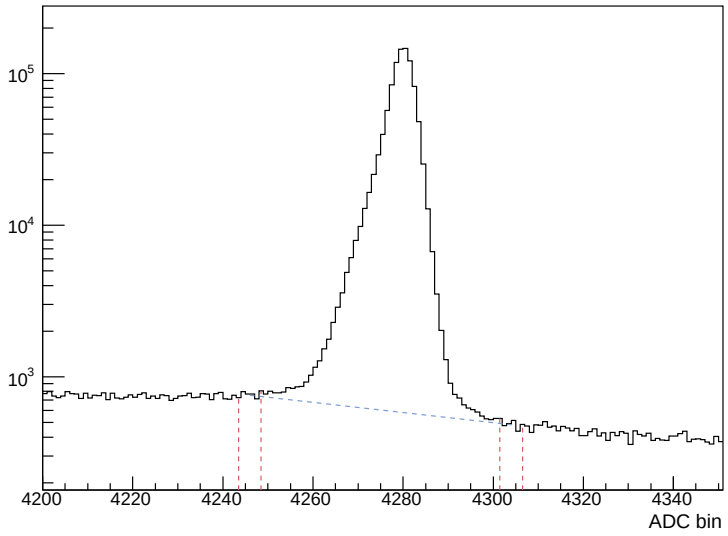

Figure 5.8: An example ^{24}Na peak showing the peak and background regions in the TPA interpolation method.

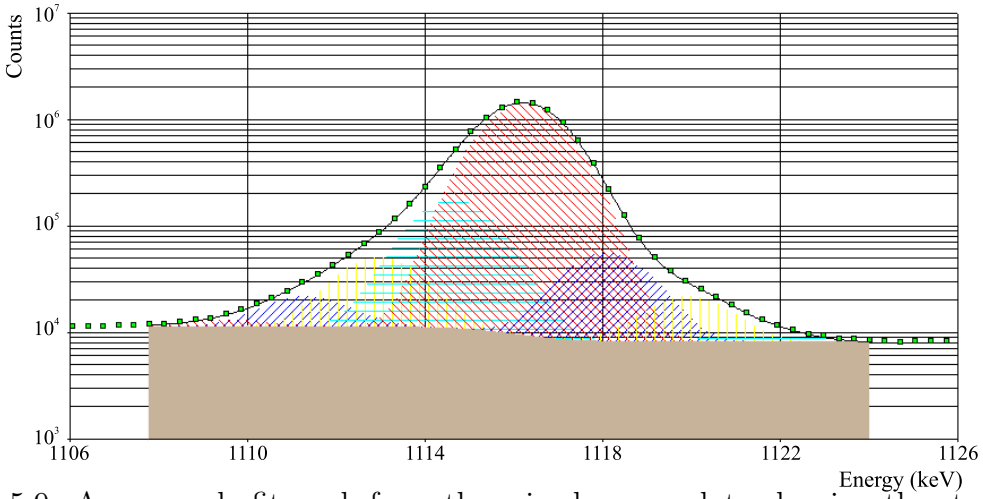

Figure 5.9: An example fit peak from the mixed source data showing the step function background continuum and eight Gaussians that describe the peak. The data points are green and the fit is black. Figure provided by Nirel [15].

Interpolation is rapid and easily applied to large amounts of data but can fail if peaks lie on non-linear backgrounds or if they are not well separated from adjacent peaks.

A combination of both methods was applied to the data in this study. The ^{24}Na measurements were taken in many small runs, each consisting of large peaks on smooth backgrounds, and were analysed using an interpolation method. Likewise the mixed source data that were used in the analysis of detector stability. However, peaks in the primary mixed source data were fit [23] to maximise the number that could be used.

This strategy made efficient use of calibration data and allowed consistent and rapid analysis of the many experimental and stability spectra. It rested on the assumption that, on average and where applicable, both methods gave the same results. The extent to which this was the case, and the calculation of a conversion factor between the two methods, is discussed below.

The particular interpolation method used in this study, referred to as the *total peak area (TPA)* method, is described in Appendix F. An example peak on which the TPA method was used is shown in Figure 5.8. It can be compared to a peak fit, shown in Figure 5.9.

5.3.2 Comparison between the methods

The level of agreement between fitting and the TPA method was investigated by applying both methods to the primary mixed source data. The results are shown in Table 5.3. They produce very similar peak counts, except where a peak overlapped with others, or where the background was highly non-linear.

On average the TPA method gave peak areas 0.3% larger than fitting. So a scale factor of 0.9967 - the weighted average of the scale factors - was applied to all data analysed with the TPA method. The standard deviation of the scale factors, 0.0058, was converted into a general systematic uncertainty of 0.59% applied to all peak areas.

5.4 Tuning the dead layer and the KCl anomaly

5.4.1 Analysis of calibration data

For the mixed source the full-energy peak efficiency ε_i for gamma i was given by

$$\varepsilon_i = \frac{N_i}{S_i} \cdot \frac{T_R}{T_L} \tag{5.4}$$

Table 5.3: Comparison between fit (from [23]) and interpolation (TPA) peak areas in the mixed source data. In the notes column NL means the peak lay on a particularly non-linear background and OP means that it overlapped significantly with an adjacent peak.

Isotope	Energy	TPA method				Fit	Comparison			
	(keV)	Counts	Uncertainty (%)			counts	Diff.	Scale	Unc.	Note
			Stat.	Sys.	Tot		(%)			
Ba-133	81.0	1617139	0.54	1.23	1.34	1700516	-5.03	1.0516	0.0141	NL
Co-57	122.1	8731522	0.12	1.01	1.02	8579800	1.75	0.9826	0.0100	
Co-57	136.5	1186982	0.73	2.34	2.45	1184641	0.20	0.9980	0.0245	
Ce-139	165.9	5465726	0.18	0.77	0.80	5177712	5.41	0.9473	0.0075	OP
Ba-133	276.4	1471039	0.52	0.50	0.72	1481355	-0.70	1.0070	0.0072	
Ba-133	302.9	3689553	0.21	0.19	0.29	3676517	0.35	0.9965	0.0028	
Ba-133	356.0	11412643	0.07	0.12	0.14	11354682	0.51	0.9949	0.0014	
Ba-133	383.8	1591569	0.41	0.36	0.55	1581508	0.63	0.9937	0.0054	
Sr-85	514.0	5949002	0.11	0.07	0.13	4789533	21.59	0.8051	0.0010	OP
Cs-137	661.7	21943586	0.03	0.08	0.08	21856992	0.40	0.9961	0.0008	
Mn-54	834.8	13045649	0.04	0.03	0.05	13004853	0.31	0.9969	0.0005	
Y-88	898.0	8837086	0.06	0.31	0.32	8752261	0.96	0.9904	0.0032	
Zn-65	1115.5	11663590	0.04	0.06	0.07	11628741	0.30	0.9970	0.0007	
Y-88	1836.0	5713957	0.05	0.03	0.06	5698784	0.27	0.9973	0.0006	
Y-88	2734.1	119356	0.32	0.12	0.34	118106	1.05	0.9895	0.0034	

Table 5.4: Measured detection efficiencies for each of the mixed source radioisotopes [23].

Isotope	Gamma	Efficiency	
		Value	Unc.
Ba-133	81.0	0.00599	0.00010
Co-57	122.1	0.02458	0.00037
Co-57	136.5	0.02720	0.00046
Ce-139	165.9	0.02979	0.00045
Ba-133	276.4	0.02671	0.00041
Ba-133	302.9	0.02591	0.00040
Ba-133	356.0	0.02364	0.00036
Ba-133	383.8	0.02285	0.00035
Sr-85	514.0	0.01929	0.00030
Cs-137	661.7	0.01619	0.00025
Mn-54	834.8	0.01415	0.00021
Y-88	898.0	0.01249	0.00019
Zn-65	1115.5	0.01174	0.00018
Y-88	1836.0	0.00773	0.00012
Y-88	2734.1	0.02608	0.00094

where

$$S_i = \frac{R_{0i} P_{\gamma i}}{\lambda_i} \left(e^{-\lambda_i (t_0 - t_R)} - e^{-\lambda_i (t_1 - t_R)} \right) \tag{5.5}$$

is the number of gammas i produced by the source in T_R, T_R is the real time, T_L is the live time, N_i is the number of counts in the full-energy peak, λ_i is the decay constant of the parent isotope, R_{0i} is the activity of the parent isotope at the reference time, t_R is the reference time, $P_{\gamma i}$ is the probability of gamma emission per parent decay, t_0 is the time at the start of measurement and t_1 is the time at the end of measurement.

The results from the primary calibration are shown in Figure 5.10 and Table 5.4. The efficiency curve fitted well to

$$\log_{10}\varepsilon = p_0 + p_1 E + \frac{p_2}{E} + \frac{p_3}{E^2} + \frac{p_4}{E^3} + \frac{p_5}{E^4} \tag{5.6}$$

which is a common efficiency curve parametrisation (see, for example, [108]).

For the KCl sources the full-energy peak efficiency was given by

$$\varepsilon = \frac{N}{S} \cdot \frac{T_R}{T_L} \tag{5.7}$$

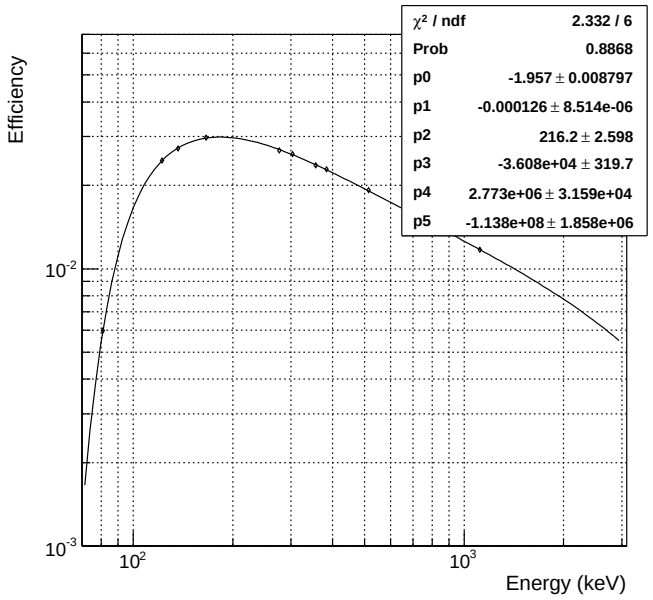

Figure 5.10: Efficiency as a function of energy measured using the mixed calibration source. The small $\chi^2/d.o.f.$ is because the efficiencies were assumed to be uncorrelated in this fit.

where

$$S = m_{sample}\,\eta\,\lambda\,f_{40}\,P_\gamma \cdot \frac{N_A}{m_K + m_{Cl}} \cdot (t_1 - t_0) \tag{5.8}$$

is the number of gammas i produced by the source in T_R, N is the number of counts in full-energy peak, m_{sample} is the sample mass, η is the sample purity (by mass), λ is the ^{40}K decay constant, R_0 is the ^{40}K activity (decays per second), P_γ is the probability of gamma emission per decay, $m_{\rm K}$ is the molecular mass of K and $m_{\rm Cl}$ is the molecular mass of Cl. The values of the some of these parameters are:

Parameter	Value
λ	$(5.554 \pm 0.013) \times 10^{-10}$ y^{-1}
P_γ	0.1066 ± 0.0018
$m_{\rm K}$	39.098 g mole^{-1}
$m_{\rm Cl}$	35.453 g mole^{-1}

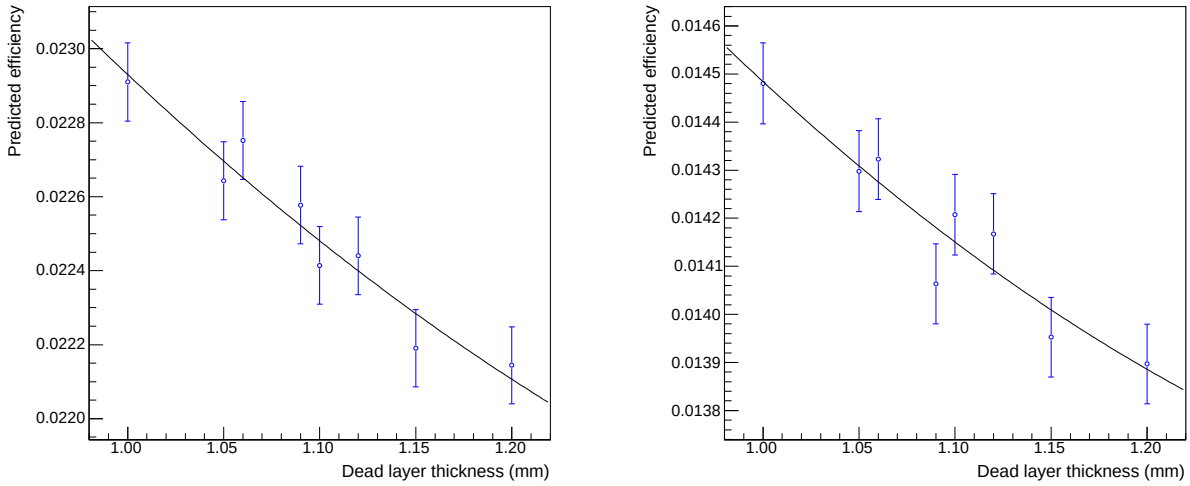

Figure 5.11: Two example Monte Carlo models for dead layer fitting: 383.8 keV ^{133}Ba peak (left) and 834.8 keV ^{54}Mn peak (right).

5.4.2 Tuning the dead layer

The primary mixed source calibration data were used to calibrate the Monte Carlo by using it to fit the dead layer. When calibrated the Monte Carlo could be used to predict the efficiencies for ^{24}Na gammas.

The dead layer was fit by minimising the expression

$$\chi^2 = \sum_i \left(\frac{\eta_i - \varepsilon_i(\delta)}{\sigma_i} \right)^2 \tag{5.9}$$

where the sum is over the source gammas i. $\varepsilon_i(\delta)$ are Monte Carlo predictions for the efficiency as a function of dead layer thickness δ, and $\eta_i \pm \sigma_i$ are the measured efficiencies. For the fit to return the correct uncertainty on δ the uncertainties σ_i had to be uncorrelated.

The models $\varepsilon_i(\delta)$ were obtained by running simulations for a series of dead layers (1.0-1.2 mm for mixed source data and 1.2-1.7 mm for KCl data) and fitting second order polynomials to the results. Two examples are shown in Figure 5.11.

As discussed in Section 5.1.4, the activities of the mixed source gammas were not independent and so the σ_i were correlated. The correlations were accounted for by dividing the uncertainty into it's uncorrelated and correlated parts, s_i and Δ_i respectively, related

by

$$\sigma_i^2 = s_i^2 + \Delta_i^2 \tag{5.10}$$

The minimisation was first performed with $\sigma_i = s_i$ to give the uncorrelated uncertainty on δ; it was then repeated with the $\varepsilon_i(\delta)$ shifted up and down by Δ_i. The average difference between the results was the correlated uncertainty on δ.

The mixed source fit residuals are shown in Figure 5.12. If the fit was performed over the energy range 276.4-1115.5 keV, the best fit dead layer was 1.094 ± 0.062 mm with a reduced χ^2 of 1.54. If the fit was performed over the full-energy range 81.0-1115.5 keV, the quality deteriorated significantly - the dead layer fitted to 1.029 ± 0.042 cm with a reduced χ^2 of 4.91. The deterioration was assumed to be due to imperfections in the detector geometry model, which lower energy gammas, with their small mean free paths, are more sensitive to. Higher energy gammas are more sensitive to the average geometry rather than the detailed modelling. The energy range 276.4-1115.5 keV was selected for this analysis because these gammas were closest in energy to the ^{24}Na gammas, which were the gammas the detector was being calibrated for.

These fits were repeated for the KCl sources and the results are shown in Figure 5.13. The initial results (shown above the dashed line) were inconsistent - the same dead layer could not reproduce the efficiencies measured using all the sources. To find the origin of this discrepancy various investigations were undertaken into the calibration sources, detector simulation and detector stability: mixed source data taken over an extended period of time was analysed to demonstrate the stability of the detector; to distinguish between a problem with the Monte Carlo or with the source strengths, calculations were made to determine whether the relative source self-absorptions predicted by the Monte Carlo agreed with expectations; and a second liquid KCl source was prepared, using the KCl from the same batch as the solid source, to check whether the Monte Carlo could predict the relative source self absorptions of two sources of different densities when the specific source strength was the same (independent of its absolute value). The results of these investigations are discussed in the following sections.

5.4.3 The stability of the detector

The stability of the detector was examined using both KCl and mixed source data: three KCl runs, taken between September 2004 and July 2006, and fourteen mixed source runs, taken between September 2005 and November 2006.

The results from the KCl source are shown in Figure 5.14. The ^{40}K half-life is so

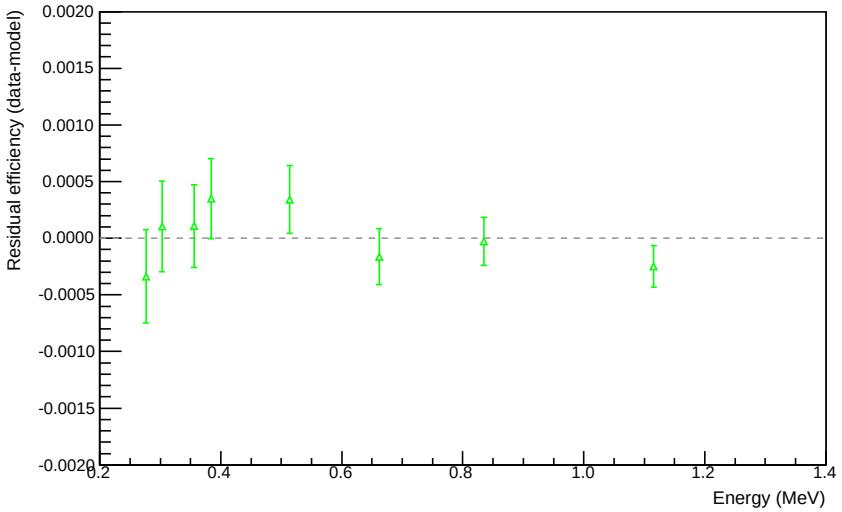

Figure 5.12: Measured minus simulated efficiency as a function of energy using the best fit dead layer.

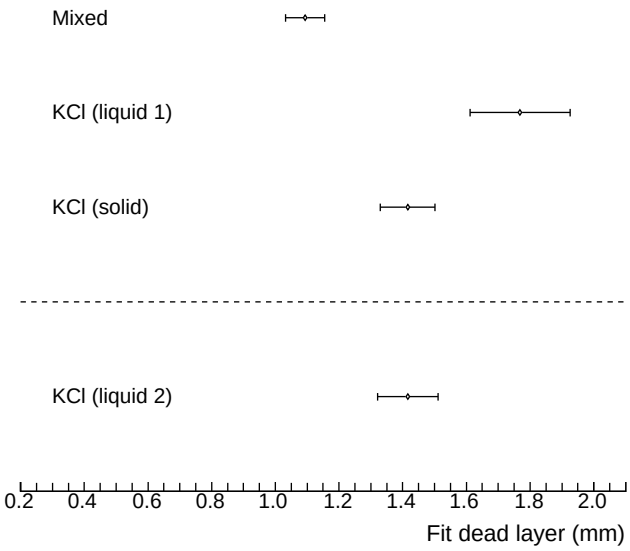

Figure 5.13: The best fit dead layer for each calibration source. Above the dashed line the discrepancy between the three sources is seen clearly. The agreement between the solid and second liquid KCl source (below the line) shows the ability of the Monte Carlo to extrapolate between two sources of very different density.

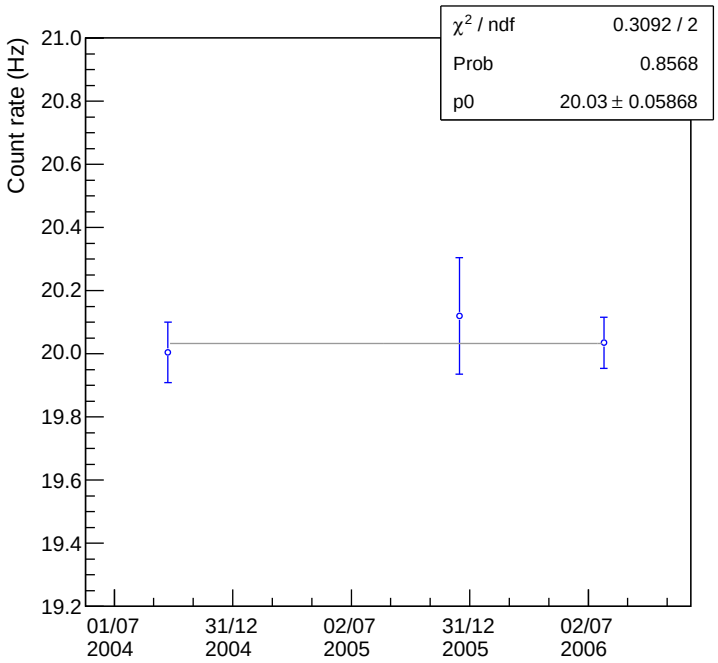

Figure 5.14: Stability of measurements made with the solid KCl source. Uncertainties are statistical only.

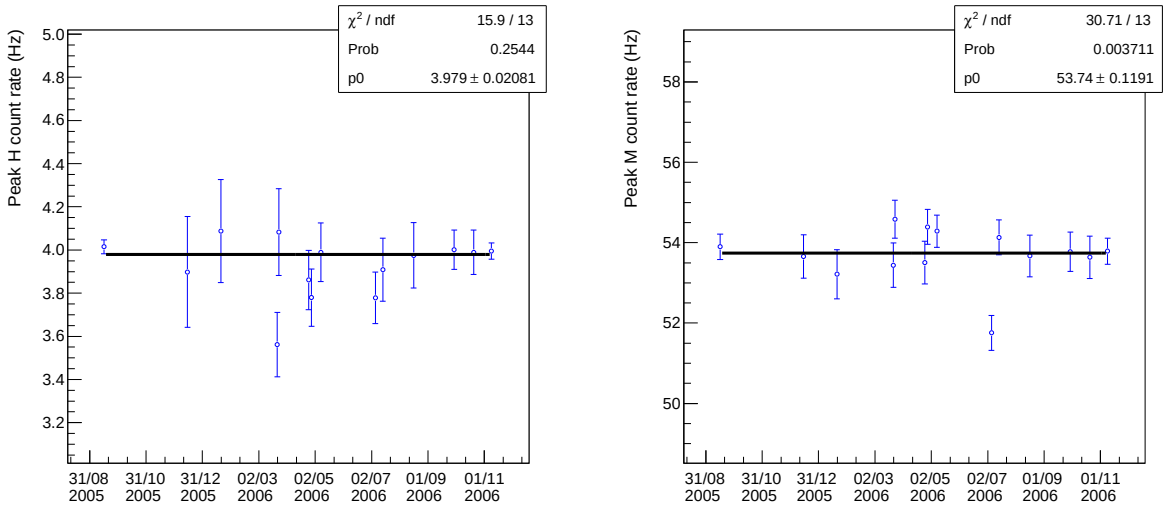

Figure 5.15: Stability of measurements made with the mixed source: 383 keV ^{133}Ba peak (left) and 1116 ^{65}Zn peak (right). Uncertainties are statistical only.

long that no correction had to be made for depletion of the ^{40}K in the KCl source from one run to the next.

Representative results from two gammas in the mixed source are shown in Figure 5.15. Half-lives in the mixed source ranged from 107 to 10968 days and so rates were corrected to an arbitrary reference time.

The KCl and mixed source time series, with uncorrelated errors only, fitted well to straight lines. In the fit to ^{65}Zn in the mixed source the large reduced χ^2 resulted from a single low point (possibly due to an incorrectly estimated background) and data taken in the run for other gammas showed no such effect. In general there was no evidence for significant variations in detector performance over time.

5.4.4 Self absorption in the calibration sources

A study was carried out to check that source self-absorptions predicted by the Monte Carlo were consistent with expectations, based on source densities, materials and geometry. The aim was to see whether the differences in fit dead layers could be explained by deficiencies in the Monte Carlo. Simulations were run with 1.5 MeV gammas, an energy for which D_2O mass attenuation coefficients were available.

Mass attenuation coefficients were calculated for all source materials using a method described in Appendix E. The mass attenuation coefficient of a material is a measure of it's ability to attenuate a beam of gammas; it depends on gamma energy, but is defined in a way that makes it independent of the material density. Mass attenuation coefficients for the calibration source materials are shown in Table 5.5 along with values of $f_a = N/N_0$, which is the fraction of gammas that have not interacted, as a function of material thickness. The thicknesses were meant to be representative of the path lengths traversed by gammas in the source material. Ratios of these quantities between the sources are given in Table 5.6.

It is reasonable to assume that the relative efficiencies of two sources were proportional to their relative f_a values. From Table 5.6, f_a for the solid KCl source was expected to be $\sim$1% lower than a liquid KCl source, compared to a Monte Carlo prediction of 1% lower. f_a for the solid KCl source was predicted to be $2.7 - 4.2\%$ lower than the mixed source compared to a Monte Carlo prediction of 5.5%.

These approximate calculations indicated differences between data and Monte Carlo at the 1-2% level at most, an order of magnitude smaller than would be needed to account for the variation in fit dead layers.

Table 5.5: Summary of net mass attenuation coefficients and $f_a = N/N_0$ values for the different sources.

Source	Mass attenuation coefficient at 1.5 MeV ($cm^2\,g^{-1}$)	Density ($g\,cm^{-3}$)	$f_a = N/N_0$		
			1.5 cm	2.0 cm	2.5 cm
KCl + D_2O	0.0516	1.105	0.9180	0.8921	0.8670
		1.1037	0.9181	0.8923	0.8672
D_2O	0.0517	1.105	0.9179	0.8920	0.8699
Solid KCl	0.0504	1.240	0.9106	0.8826	0.8554
Mixed	0.0536	1.500	0.8863	0.8514	0.8197

Table 5.6: Ratios of f_a values between the different sources for different effective thicknesses. The ratios are the 'column' source divided by the 'row' source.

Thickness (cm)	Source	KCl + D_2O	Solid KCl	Mixed
1.5	KCl + D_2O	1.000	0.992	0.965
	Solid KCl		1.000	0.973
	Mixed			1.000
2.0	KCl + D_2O	1.000	0.989	0.954
	Solid KCl		1.000	0.965
	Mixed			1.000
2.5	KCl + D_2O	1.000	0.987	0.945
	Solid KCl		1.000	0.958
	Mixed			1.000

5.4.5 Source strengths

The point below the dashed line in Figure 5.13 is for a second liquid KCl source, made using KCl from the same batch as the solid source. The fit dead layer was in good agreement with that fit using the solid source, which demonstrated the ability of the Monte Carlo to extrapolate correctly between sources made of different materials, irrespective of the source strength. This measurement indicated that the inconsistency of the first liquid with the second liquid and solid KCl sources was likely to be due to errors in the source strengths. Possible causes of source strength errors in the KCl sources were investigated.

One explanation would have been a variation in the isotopic composition from source to source, but the $^{39}K/^{40}K$ ratio, in particular, is fixed by very fundamental processes (its constancy is an assumption underlying the $^{40}Ar/^{39}Ar$ dating technique). Depletion of ^{40}K during KCl purification was considered improbable.

A more likely explanation was manufacturer error in the source purity measurements. Norman et al. [109] discovered such inaccuracies in experiments searching for differences in ^{40}K decays rates in different chemical environments[3]. Using neutron activation analysis they could determine the actual amount of potassium in their sources and found, for example, that their '99.998% pure' KCl and $KNbO_3$ sources were only $95.3 \pm 0.4\%$ and $81.8 \pm 0.3\%$ pure respectively. It appears [110] that the manufacturers only count 'metallic impurities'.

Using the mixed source dead layer, Monte Carlos were run to determine the KCl source detection efficiencies and these used to estimate the source purities:

Source	MC efficiency		Purity (%)	
	Value	Unc.	Value	Unc.
Liquid 1	0.01077	0.00008	86.4	1.8
Liquid 2	0.01077	0.00008	91.7	1.9
Solid	0.01067	0.00008	92.7	1.9

The purities fit for the two sources made with KCl from the same source (solid and second liquid) were in reasonable agreement (however, note that the errors on the purities resulted mainly from the uncertainty in the gamma emission probability on the decay of ^{40}K and were therefore largely correlated). Given the doubts over the source strengths, the KCl sources could not be used in the efficiency calibration or to cast doubt on the efficiency calibration using the mixed source. The agreement between the two KCl

[3]No differences were found.

Table 5.7: Predicted ^{24}Na efficiencies.

Peak	Efficiency			
	Value	Syst.	Stat.	Total
1.369	0.009946	0.000094	0.000018	0.0000958
2.754	0.005700	0.000058	0.000014	0.0000994
Sum	0.000083	0.000002	0.000002	0.0000941

sources demonstrated the ability of the Monte Carlo to extrapolate between sources of very different density and composition.

5.4.6 The efficiency for detecting ^{24}Na gammas

The best fit dead layer was 1.0939 ± 0.0618 mm and Monte Carlos run using this, the ^{24}Na source geometry, and the ^{24}Na gamma angular correlations, were used to predict the efficiency for ^{24}Na gammas. The results are given in Table 5.7.

5.5 Dead time

5.5.1 Understanding and modelling detector dead time

Dead times in Ge detectors can be considerable when counting high rate sources, such as the ^{24}Na brine. Dead time in the KCl data was less than 1% for all sources; in the mixed source data it was 2.6-4.7%; and in the ^{24}Na data it was in the range 0-16%. Dead time in the ^{24}Na and mixed source data will now be considered in turn.

If the dead time associated with an event is a constant τ, two fundamental dead time models can be distinguished. The dead time can be *non-extendable*, in which case any event occurring during τ is lost, or it can be *extendable*, in which case the event is still lost but it extends the time during which the system is unable to record events by an additional τ after it occurs.

If the dead time is non-extendable, it can be shown (see, for example, [111]), that the recorded event rate m is related to the true event rate n by

$$m = \frac{n}{1 + n\tau} \tag{5.11}$$

and if the dead time is extendable they are related by

$$m = ne^{-n\tau} \tag{5.12}$$

If the system dead time has multiple contributions from different components the relationship between m and n can be much more complicated.

The SNO Ge detector DAQ reported a live fraction for each run but the method by which this was calculated was unknown and the fraction had no associated uncertainty. In addition, analysis of ^{24}Na data corrected for the reported live time gave count rates that did not fall with the time constant expected from ^{24}Na .

Efforts were therefore made to determine the dead time from the data itself. This was possible because of the way the data were recorded - it was collected in a series of runs with lengths small compared to the half-life of the decaying isotope. The change in count rate from run to run changed the size of the dead time and allowed its magnitude to be determined, given a model for its behaviour. Cleveland [112] demonstrated that the detector dead time could be described by an extendable dead time model. This was done by comparing fit qualities between the extendable and the non-extendable dead times model applied to samples of ^{24}Na data.

5.5.2 Dead time in the ^{24}Na data

All ^{24}Na data were recorded in a series of small runs, with lengths short compared to the half-life. In each run the integral of the instantaneous count rate $m(t)$ was recorded between times t_b and t_e

$$N = \int_{t_b}^{t_e} m(t)dt \tag{5.13}$$

Using Eq. (5.12) and evaluating the integral, this becomes

$$N = \frac{1}{\lambda\tau}\left(e^{-n_0\tau e^{-\lambda t_e}} - e^{-n_0\tau e^{-\lambda t_b}}\right) \tag{5.14}$$

Background was neglected because it was both constant and vastly smaller than the event rate. The count rate at $t = 0$, n_0, and the dead time constant, τ, could be fit by minimising

$$\chi^2 = \sum_{i=1}^{18}\left(\frac{N_i - M_i}{\delta M_i}\right)^2 \tag{5.15}$$

where M_i is the number of counts recorded in run i.

Table 5.8: Dead time-corrected gamma detection rates n_0 at the start of the first Ge detector run taken with each source. All times are local to Sudbury.

Data	Start of counting	Peak	Dead time fit				
set	date / time		n_0 (s^{-1})	Unc.	τ (μs)	Unc.	χ^2/d.o.f.
Dry run	12/09/2005 15:14:29	1.369	7.60	0.02	872.3	679.3	0.86
		2.754	4.37	0.02	2218.0	1489.7	0.78
2005	30/09/2005 12:13:37	1.369	361.76	0.20	575.0	2.7	0.80
		2.754	207.95	0.14	1003.8	5.5	1.77
2006	27/10/2006 14:48:17	1.369	206.64	0.18	560.9	9.5	0.98
		2.754	118.7	0.12	1007.1	15.8	1.29

The results of fits to the dry run and both ^{24}Na measurements are given in Table 5.8. An example fit with residuals is shown in Figure 5.16. The fit qualities were good and there were no trends in the residuals. The dead time constant was not well constrained by the dry run data because the count rate, and therefore the magnitude of the dead time, was lower than in the other two data sets.

There was one peculiarity in the fits for which no firm explanation could be found - the extendable dead time constant τ varied as a function of energy. Its value for the 2.754 MeV ^{24}Na peak was approximately double that for the 1.369 MeV peak, meaning that higher energy events were less likely to be recorded. This behaviour perhaps originated from the longer ADC digitisation time typically associated with higher energy events.

5.5.3 Dead time in the mixed source data

The simple extendable dead time model could not be successfully applied to the mixed source data because the dead time was driven by many gammas produced with different energies at different rates. Attempts to generalise the model were also unsuccessful. So for the mixed source data the only option was using the dead time reported by the DAQ.

A comparison between the fit and DAQ dead times in the ^{24}Na data could be used to assess the accuracy of the DAQ dead time. The left hand plot of Figure 5.17 shows the ratio of the fit dead time fraction to that reported by the DAQ for the 1.369 and 2.754 MeV peaks in the 2005 measurement. There was a 6-8% disagreement that reached its maximum value in the limit of zero dead time.

The right hand plot shows the effect of the disagreement on the recorded number of

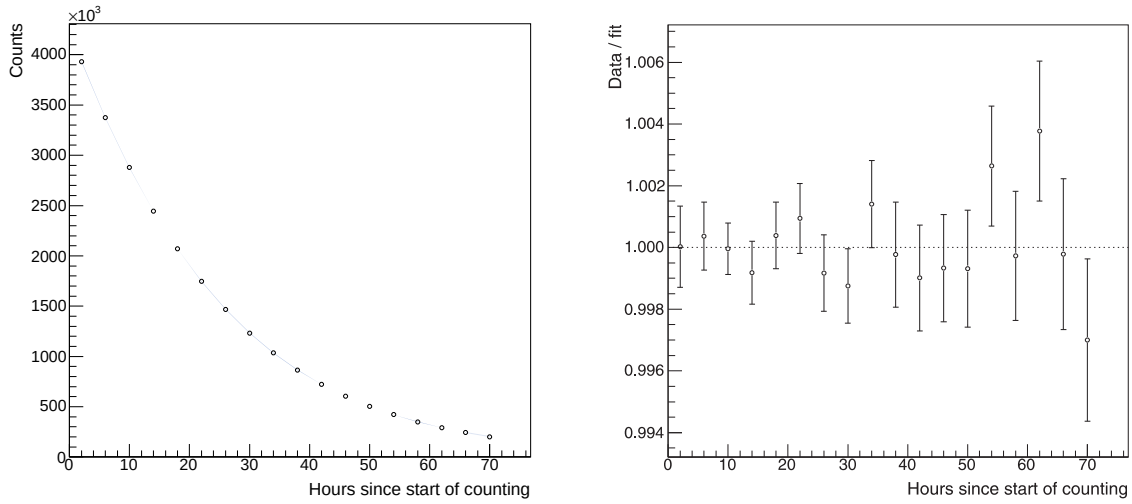

Figure 5.16: Dead time fit and residuals for the 1.369 MeV peak in the 2005 ^{24}Na measurement.

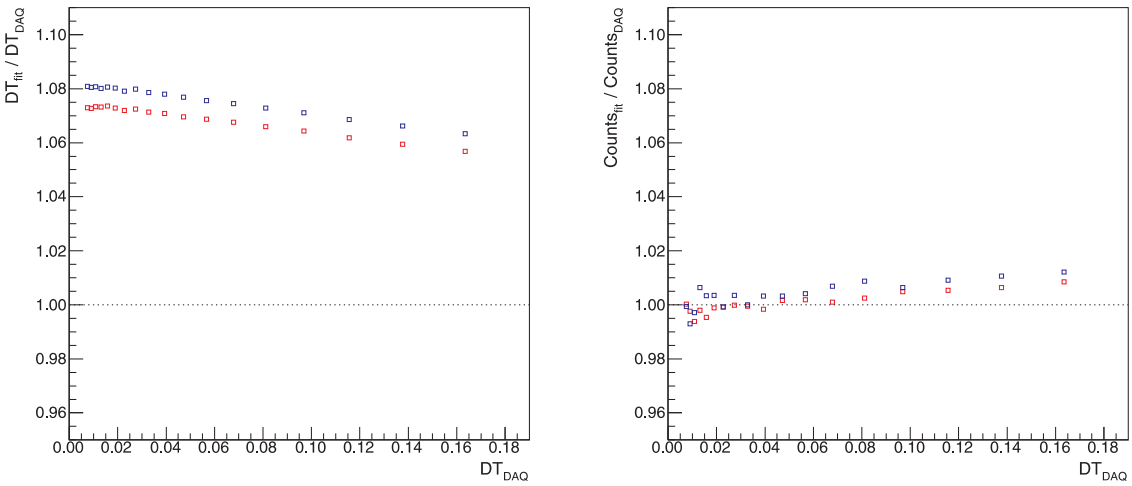

Figure 5.17: The left hand plot shows the ratio of fit to DAQ dead time fractions in the 2005 ^{24}Na measurement (1.369 MeV peak in red and 2.754 MeV peak in blue). The right hand plot shows the effect of the discrepancy on the recorded number of counts.

counts - i.e. the values plotted in the left hand plot weighted by the absolute magnitude of the dead time. In the region 2.6-4.7%, which encompasses the dead time fractions encountered in the mixed source data, the effect is negligible. Note also that the dead time is smaller for the lower energy ^{24}Na peak and that all mixed source gammas used for tuning the dead layer had even lower energies.

The conclusion was that using the DAQ dead time for the mixed source data and the fit dead time for the ^{24}Na data would lead to accurate and consistent dead times.

5.6 The ^{24}Na source strength

5.6.1 Probability of photodisintegration

The analysis has so far been concerned with calculating gamma production rates but these had to be converted into neutron production rates using the photodisintegration cross section. The conversions were done via the SNOMAN Monte Carlo so that the interaction of gammas in materials other than D_2O, such as the NCDs and AV could be accounted for. It was of course important that the photodisintegration cross section was properly modelled in SNOMAN. This section reviews the model and evaluates a representative probability of photodisintegration for ^{24}Na gammas.

The code which handles deuteron photodisintegration in SNOMAN is discussed at length in [70]. At energies below 25 MeV the cross section was described by an analytical model, calculated using *effective range theory* (ERT), multiplied by a phenomenological function whose three parameters were fit using published experimental data. At energies above 35 MeV a phenomenological fit due to [113] took over. In between the two, the cross section was smoothly interpolated.

Below 20 MeV the only nuclear moments contributing significantly to the interaction are E1 and M1. Over most of this energy range the M1 contribution is small relative to E1, but close to threshold it becomes relatively large. An expression for σ_{E1} can be derived which depends only on the initial photon energy, n-p triplet effective range and physical constants. A similar expression can be derived for σ_{M1}, depending additionally on the n-p singlet effective range. In the derivation of the latter a significant simplification is made - contributions due to meson exchange are neglected. No such processes occur in the E1 interaction.

The effect of neglecting meson exchange is significant. Noyes [114] estimates that including it increases σ_{M1} by $9.5 \pm 1.2\%$. In SNOMAN this is assumed to be energy-

Table 5.9: Sample and reference (injected) masses. The reference mass for the dry run was arbitrary (and only used to make comparisons between the methods) because no injection took place.

Data set	Sample mass (g)		Ref. mass (g)	
	Value	Unc.	Value	Unc.
Dry run	30.57	0.02	1406.2	n/a
2005	30.62	0.02	968.7	0.1
2006	32.76	0.02	549.8	0.4

independent and the ERT σ_{M1} is scaled up by 9.5%. The 1.2% taken as a systematic uncertainty.

The experimental data were fit to the phenomenological model

$$\sigma_C = \sigma_{PD} \sum_{n=0}^{m} a_n x^n \tag{5.16}$$

where σ_C and σ_{PD} are the corrected and theoretical cross sections, and $x = E_\gamma - E_0$, where E_0 is the threshold energy. The polynomial order m was fixed at 3 to give a good fit (probability 0.25) and small difference between the theoretical and fit cross sections at threshold (0.3%).

The statistical uncertainties on σ_{E1} and σ_{M1} due to input parameter uncertainties were 0.2% and 0.1% respectively. To first order, the uncertainty on σ_{E1} is independent of energy. The uncertainty on σ_{M1} was evaluated at ~ 4 MeV for convenience and has a weak energy dependence. To estimate the uncertainty on the phenomenological fit, Lyon used a Monte Carlo method. For 2.2-2.7 MeV gammas he estimated an uncertainty of 0.7%.

Determining an *overall* uncertainty was not straightforward. The data below 5 MeV is sparse and in his phenomenological fit, Lyon had only 4 points available, one at ~ 5 MeV with a 7% uncertainty, and 3 at ~ 2.75 MeV, with a combined uncertainty of 2%. He also implicitly assumed that the theoretical cross section was correct at threshold - he did not formally constrain the function at its lower bound, but rather used the level of agreement as a criteria for selecting the order m, along with the goodness of fit.

The effect of different shapes for the M1 contribution was also not investigated. But Sims [19], using the work of Chen [115], considered *effective field theory* (EFT) as an alternative to ERT for calculating σ_{E1} and σ_{M1}. She found that close to threshold EFT

Table 5.10: ^{24}Na gamma (R_γ) and neutron (A_m) production rates at the reference time (local to Sudbury). The gamma production rate is that of the sample measured by the Ge detector. The neutron production rate is that of the ^{24}Na source injected into SNO.

Data	Start of counting	Reference	Peak	R_γ (s^{-1})		A_m (n s^{-1})	
set	date / time	date / time		Value	Unc.	Value	Unc.
Dry run	12/09/2005 15:14:29	12/09/2005 16:16:00	1.369	725.99	9.28	88.07	2.06
			2.754	728.90	7.75	88.43	1.97
2005	30/09/2005 12:13:37	07/10/2005 12:37:00	1.369	14.82	0.18	1.236	0.029
			2.754	14.86	0.15	1.240	0.027
2006	27/10/2006 14:48:17	02/11/2006 21:20:00	1.369	20.27	0.23	0.857	0.020
			2.754	20.32	0.37	0.859	0.019

Table 5.11: Systematic uncertainties on the source strengths measured using the Ge detector. They were identical, within the quoted number of significant figures, in the 2005 and 2006 measurements

Item	Unc. (%)
^{24}Na decay constant	0.06
Photodisintegration probability	1.95
Ratio of sample and injected masses	0.07
Full-energy peak areas	0.59
Dead time fit (n_0)	0.05
Full-energy peak efficiency	1.09
Total	2.32

predicted a σ_{M1} 4-7% lower than ERT, and that the difference was energy-dependent. This difference is lower than the uniform 9.5% used by Lyon. On average, the SNOMAN cross section was found to differ from the EFT cross section by 2.2% (though this was half the uncertainty quoted in the EFT calculations - EFT and SNOMAN did agree within error over the energy range under study).

Overall it was felt that the model in SNOMAN was robust but that it was difficult to use the uncertainties associated with it to constrain the uncertainty on the photodisintegration cross section at 2.75 MeV because σ_C between 2.2-2.7 MeV depended on the choice of theoretical and phenomenological models. Instead, a conservative uncertainty was derived solely from experimental measurements at 2.75 MeV. Three measurements of the deuteron photodisintegration cross-section at 2.75 MeV [116, 117, 118], presumably those originally used by Lyon, were combined to yield a uncertainty of 1.9%.

From Monte Carlo simulations in SNOMAN the probability of photodisintegration for 2.7 MeV gammas, produced uniformly in SNO, was found to be 0.002601 ± 0.000052, where the uncertainty includes the 1.9% quoted above and a statistical uncertainty of 0.44%.

5.6.2 Source strengths

The gamma detection rates at the start of counting, the detection efficiency and the photodisintegration cross section together lead directly to the source strengths.

The gamma production rate at the reference time R_R was given by

$$R_\gamma = \frac{n_0}{\varepsilon} e^{-\lambda(t_R - t_0)} \tag{5.17}$$

where t_R is the reference time, t_0 is the start of counting, ε is the detection efficiency, and λ is the decay constant of ^{24}Na , 1.11208 ± 0.00009 days^{-1}. The neutron production rate A_m for the activated brine injected into SNO was then given by

$$A_m = R_\gamma \cdot P_{PD} \frac{m_{dist}}{m_{sample}} \tag{5.18}$$

where m_{sample} is the sample mass, m_{dist} is the mass injected into the detector, and P_{PD} is the probability of photodisintegration. The sample masses are given in Table 5.9, the results are given in Table 5.10 and a breakdown of the systematic uncertainties in **??**.

The source strengths derived using the lower energy 1.369 MeV peaks were used in the neutron detection efficiency analysis because they were closer in energy to calibration

data used to fix the dead layer. Little was to be gained from combining the results from the two peaks given their strong correlation. The recommended source strengths are:

Data set	Reference	A_m (n s^{-1})		
	date / time	Value	Unc.	%
2005	07/10/2005 12:37:00	1.236	0.029	2.3
2006	02/11/2006 21:20:00	0.857	0.020	2.3

5.7 The ^{222}Rn source strengths

5.7.1 Introduction

This section describes measurements of the strengths of the two distributed ^{222}Rn sources, which were deployed in the light and heavy water, and used to produce neutrons via photodisintegration and to construct background PDFs (see Chapter 3). The measurements and analysis were similar to those described above but there were important differences, resulting from the gaseous nature of ^{222}Rn and the strengths of the samples:

- *All of the ^{222}Rn prepared for injection was counted rather than just a sample.*

  This was to minimise the number of times the gas was transferred. The container that was designed to hold the gas during counting could receive the gas directly from the ^{222}Rn generator and could be connected to the detector water systems at injection. The vessel had fittings that allowed it to be flushed with N_2 to ensure that the efficiency of transferring the gas to the SNO detector was 100%.

- *^{222}Rn easily diffuses through many materials.*

  A standard plastic Marinelli beaker was unsuitable for holding a sample during counting and so a special metal container or *can*, with Marinelli-like geometry, was constructed (shown in Figure 5.18).

- *^{222}Rn is a gas.*

  There was no gaseous source available for calibrating the Monte Carlo and use had to be made of the existing ^{24}Na calibration. The different source self-absorptions and geometries had to be accounted for using Monte Carlo.

- *^{222}Rn produces no gammas directly.*

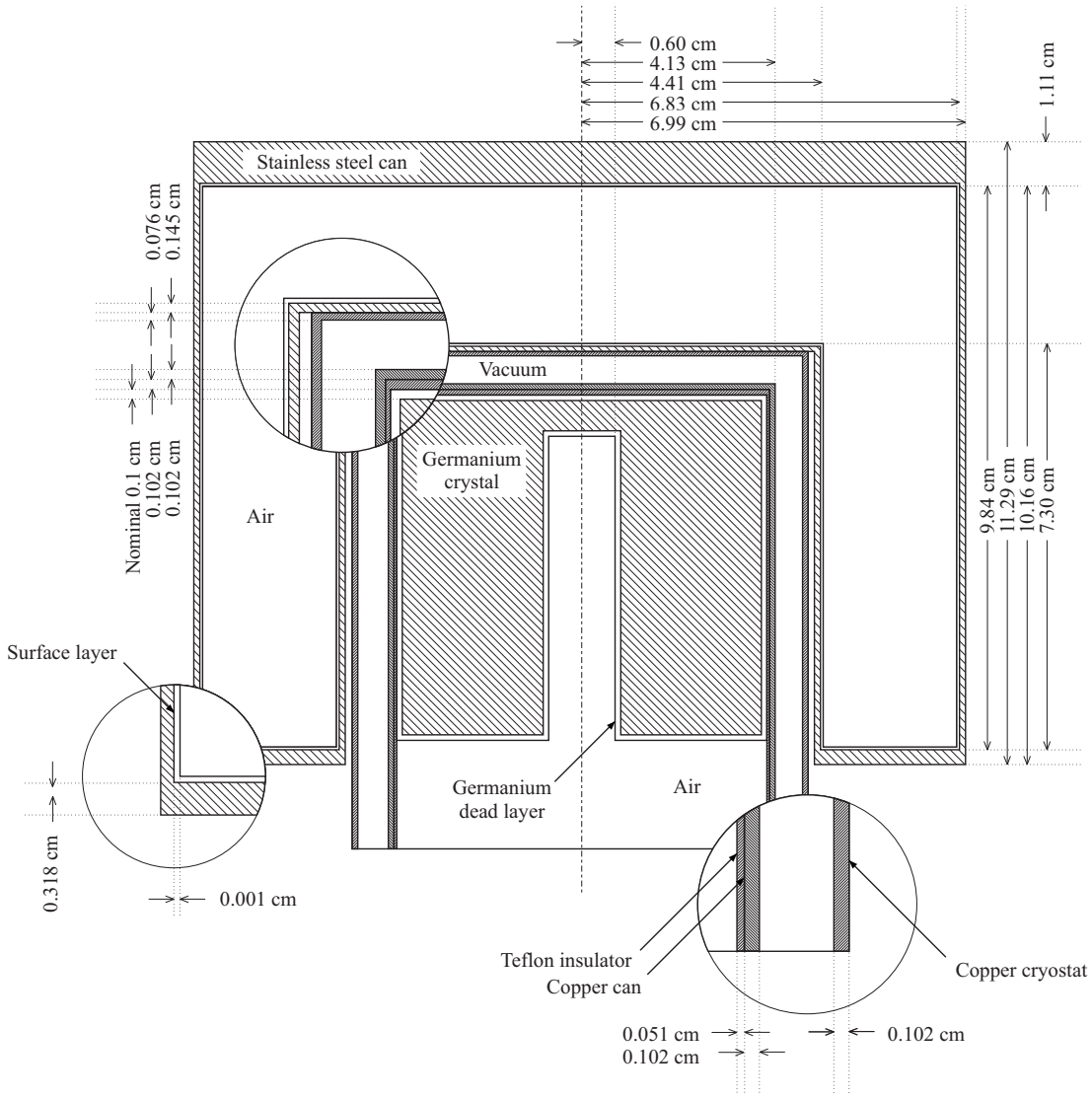

Figure 5.18: The radon can and Ge detector geometry as implemented in the Monte Carlo simulation.

^{222}Rn alpha decays and the gammas are produced by its daughters, in particular ^{214}Bi, which is the only one that gives gammas with enough energy to photodisintegrate deuterons. The decay scheme of ^{214}Bi is complex and the energy spectra collected during ^{222}Rn measurements were subject to extensive random and coincident summing. A Monte Carlo was used to disentangle the different spectral contributions.

- *The heavy water source was very weak and the light water source very strong.*

  The heavy water spike could be counted for only three hours (because of experimental constraints), which exacerbated the consequences of its low source strength. The light water source on the other hand, which was counted for five days, had an activity in the 10s of kBq and consequently generated large detector dead times - up to 63% - providing a stringent test of the dead time model.

The Monte Carlo was relied on more extensively in this analysis but was less well-calibrated because of the dissimilarity between the calibration source and sample. The measurement was less precise than ^{24}Na but much more precise than any of the alternatives [119, 120].

The following sections discuss the efficiency of the Ge detector in the new configuration; the method for evaluating peak areas and dead time; and the source strength calculations.

5.7.2 The efficiency for detecting ^{214}Bi gammas

Four lines were selected for analysis because of their strength and because they spanned a large fraction of the energy spectrum - they were ^{214}Bi gammas at 609, 1120, 1765 and 2204 keV.

The full-energy peak efficiencies for each of these were calculated using Monte Carlo. Simulations were run for ^{214}Bi only (the other main gamma-producing isotope ^{214}Pb only produces gammas below 0.5 MeV) using the dead layer thickness fixed in the ^{24}Na analysis. ^{214}Bi decays were simulated either on the inner surface of the can or uniformly distributed inside the cavity as the distribution was unknown - even though the ^{222}Rn would have been uniform there was concern that ^{214}Bi and ^{214}Pb may have plated out on the inside surface of the can.

Systematic uncertainties were assigned to the efficiencies to account for the following effects:

- *Accuracy of the Monte Carlo ^{214}Bi decay scheme.*

  This table shows a comparison of branching fractions in the Monte Carlo and published values [121] for the lines used in this study:

Gamma	Monte	Literature		Scale
keV	Carlo	Value	Unc.	factor
609	0.4673	0.461	0.005	0.9862
1120	0.1517	0.151	0.002	0.9951
1765	0.1622	0.154	0.002	0.9495
2204	0.0485	0.0508	0.0004	1.0468

  Scale factors were calculated to correct the Monte Carlo-derived efficiencies and a general uncertainty of 4.0%, equal to the standard deviation of the scale factors, was applied to all efficiencies. The experimental uncertainties on the branching fractions were also folded in.

- *Distribution of ^{214}Bi within the can.*

  As mentioned above, the distribution of ^{214}Bi within the can was unknown and separate simulations were run for the two extreme scenarios - with ^{214}Bi on the inner surface and distributed throughout the cavity. For each line the average value was taken as the central value and the difference between the two as a systematic uncertainty. The size of the uncertainty varied from 4.4% for the lowest energy peak to 0.2% for the highest energy peak.

- *Uncertainty in the dead layer thickness.*

  Monte Carlos were run with the best fit dead layer of 1.094 mm and the upper and lower bounds of 1.040 mm and 1.156 mm. The difference in efficiencies, ranging between 0.5% and 3.0%, was taken as a systematic uncertainty.

Other effects were more difficult to quantify, in particular the consequences of the change in detector geometry. It was not clear that it was justifiable to use the dead layer derived in the ^{24}Na analysis in simulations using the radon can. If, for example, the gamma ray attenuation in the plastic of the Marinelli beaker was modelled incorrectly then the dead layer thickness would have been tuned to compensate - while not a problem in the ^{24}Na analysis, this might give misleading results when the plastic was replaced by another material. It had to be assumed that the process of fitting the dead layer was tuning only that part of the geometry, internal to the Ge detector, that was common

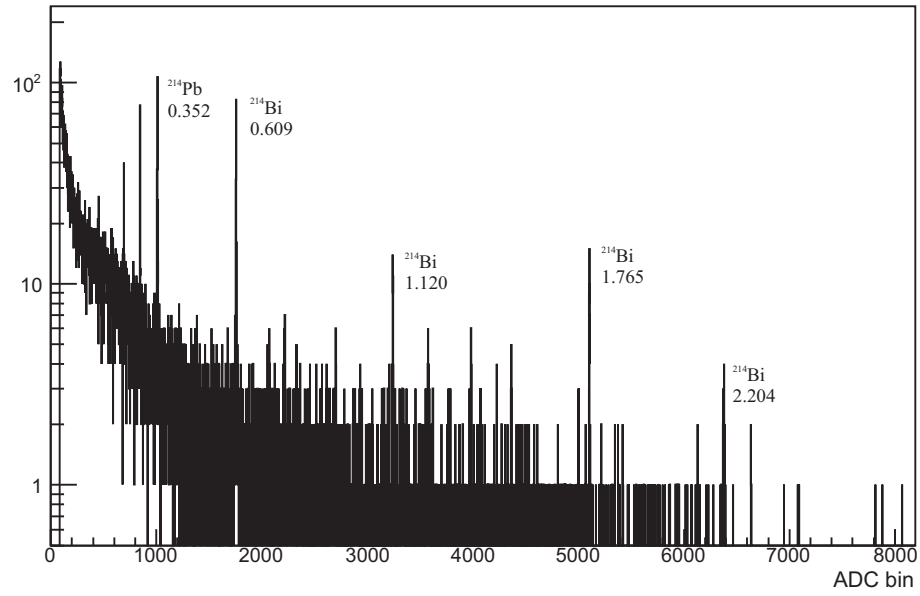

Figure 5.19: A measured radon spectrum with select gammas from ^{214}Pb and ^{214}Bi labelled.

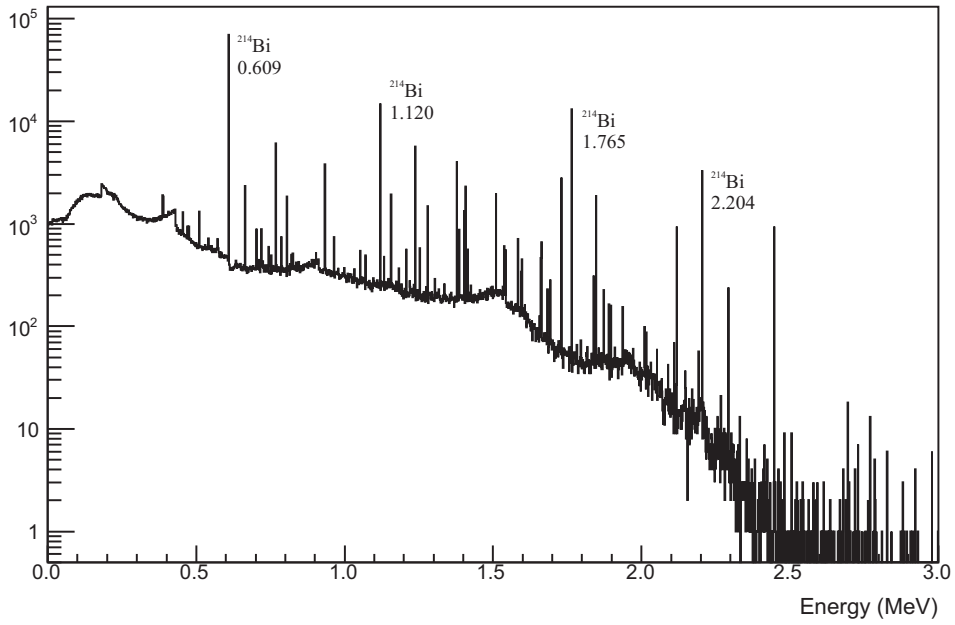

Figure 5.20: A Monte Carlo radon spectrum. Simulations runs with decays of the radon daughter ^{214}Bi only.

between the ^{24}Na and radon geometries. This hypothesis was supported by the good agreement as a function of energy seen in Figure 5.12.

Example experimental and Monte Carlo energy deposition spectra are shown in Figures 5.19 and 5.20. Notable differences between the two are the omission of low energy gammas and lines due to ^{214}Pb in the Monte Carlo. The efficiencies calculated using the Monte Carlo are given in Table 5.12.

Table 5.12: Monte Carlo efficiencies from ^{214}Bi simulations. The systematics are MC (accuracy of Monte Carlo decay scheme), BF (experimental uncertainties on branching fractions), ^{214}Bi (distribution of activity within the can) and D. layer (uncertainty on the dead layer thickness).

Gamma	Surface eff.		Cavity eff.		Systematics (fractional)				Corrected efficiency		
(keV)	Value	Unc.	Value	Unc.	MC	BF	^{214}Bi	D. layer	Value	Stat.	Syst.
609	0.008705	0.000033	0.008993	0.000033	0.0403	0.0108	0.0326	0.0052	0.008726	0.000016	0.000465
1120	0.001858	0.000015	0.001911	0.000015	0.0403	0.0132	0.0283	0.0181	0.001875	0.000008	0.000101
1765	0.001628	0.000014	0.001646	0.000014	0.0403	0.0130	0.0110	0.0106	0.001554	0.000007	0.000069
2204	0.000416	0.000007	0.000426	0.000007	0.0403	0.0079	0.0235	0.0298	0.000440	0.000004	0.000025

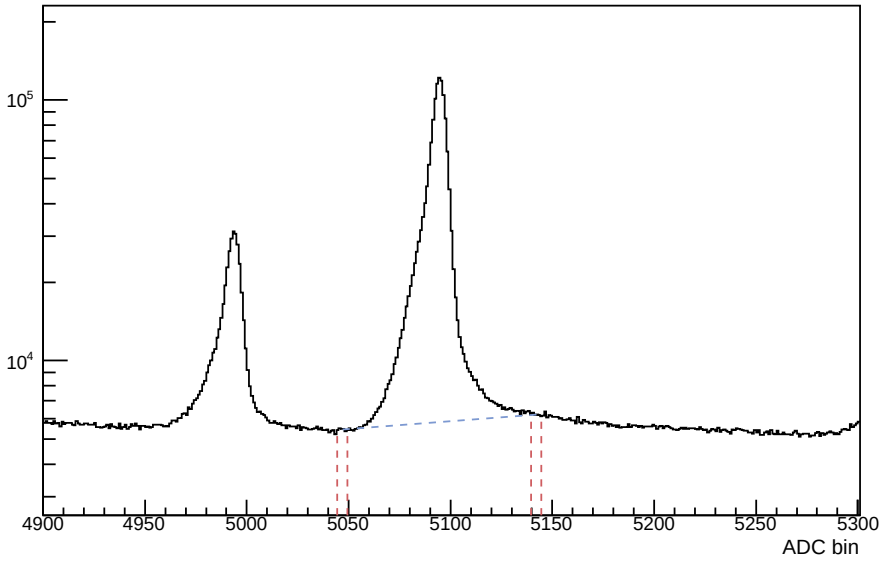

Figure 5.21: An example 1764 keV full-energy peak showing the background regions on both sides. Data is from the H_2O measurement.

5.7.3 Peak areas and dead time

The TPA peak area integration method had to be modified for use with ^{222}Rn spectra. By default it selected background regions a certain number of FWHM's either side of peaks but this caused problems with so many densely spaced lines and so the regions were instead chosen by hand. A systematic uncertainty was calculated by varying the positions of the regions by ± 5 ADC bins from their chosen positions and calculating the standard deviation of the results. An example peak is shown in Figure 5.21.

The high rate light water data fitted very well to an extendable dead time model and no trends are observed in the residuals. An example fit is shown in Figure 5.22.

In contrast, the very low rate heavy water data fitted poorly. This was attributed to a small amount of noise in the data and a very low absolute dead time. If the dead time constants τ were fixed to their light water values, then acceptable fits for n_0 could be obtained with no trends in the residuals. Varying τ by $\pm 1\sigma$ made a negligible difference to the results. An example fit is shown in Figure 5.21.

A summary of the fit results for all peaks is given in Table 5.13.

Table 5.13: Summary of dead time fit results.

Data set	Gamma	n_0 (s^{-1})		τ (μs)		χ^2 / d.o.f.	Count rate (Bq)	
	(keV)	Value	Unc.	Value	Unc.		Value	Unc.
D_2O	609	1.538	0.021	936.06	Fixed	2.08	175.82	10.16
	1120	0.343	0.011	4312.05	Fixed	0.56	180.96	10.47
	1765	0.313	0.007	4711.60	Fixed	1.05	198.95	11.57
	2204	0.082	0.004	18235.50	Fixed	0.88	193.60	15.33
	Ave.						184.90	9.10
H_2O	609	1089.35	0.94	936.06	0.41	0.90	124515	6983
	1120	245.20	0.59	4312.05	4.82	0.85	129512	6253
	1765	210.05	0.46	4711.60	5.95	1.01	133604	7083
	2204	57.49	0.26	18235.50	52.96	0.50	135152	8946
	Ave.						130135	6145

Table 5.14: Parameters used in the ^{222}Rn source strength analysis. All times Sudbury local times. The Ge detector computer runs on winter time all year round and D_2O start of counting time has been corrected by one hour.

Parameter	Value
Half-life of ^{222}Rn (days)	3.8235 ± 0.0004
D_2O start of Ge counting	11/08/2006 06:20:32
D_2O reference time	11/08/2006 10:40:00
H_2O start of Ge counting	03/11/2006 15:14:04
H_2O reference time	08/11/2006 20:21:00

5.7.4 Source strengths

This section describes how the four source strengths derived for each radon measurement - one for each gamma - were combined. Unlike ^{24}Na there was no good reason to prefer a source strength derived with any particular gamma. For each measurement the strengths were combined taking into account the correlations between them.

The uncertainties due to the modelling of the gamma cascade were taken to be random and the all others to be 100% correlated; numerically this corresponded to an almost equal division of the uncertainties into correlated and uncorrelated parts. The source strengths, with their uncorrelated errors, were combined in the standard way (see Appendix B). The reduced χ^2 for the heavy water measurement was 1.91 and so the final error was inflated accordingly; the reduced χ^2 for the light water spike was 0.79 so the error was not changed. The procedure was then repeated with the central values shifted up and down by the correlated parts of their uncertainties, with the largest change in central value for each measurement symmetrized to give the combined correlated uncertainty. Correlated and uncorrelated uncertainties were then added in quadrature.

The final activities, in ^{222}Rn decays per second, were:

Data set	Reference	Activity (Bq)		
	date / time	Value	Unc.	%
D_2O	11/08/2006 10:40:00	180.4	9.2	5.1
H_2O	08/11/2006 20:21:00	50700	2100	4.1

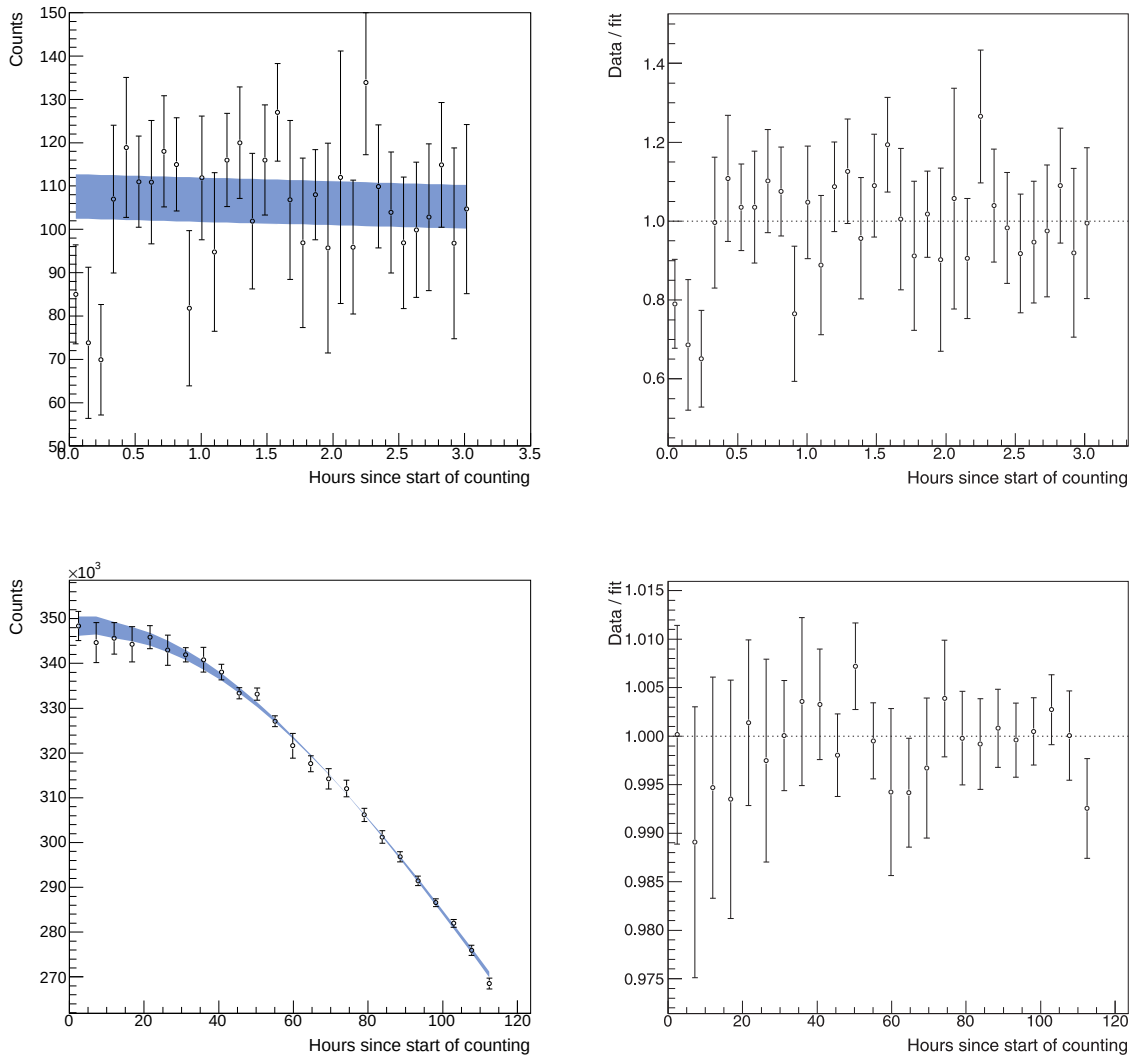

Figure 5.22: Dead time fit and residuals for the 1764 keV peak in the D_2O data (top) and for the 2204 keV peak in the H_2O data (bottom).

Chapter 6

Source strength measurements using the PMT array

Never express yourself more clearly that you are able to think.

NEILS BOHR

This chapter describes measurements of the strengths of the ^{252}Cf , ^{24}Na and AmBe neutron calibration sources. The ^{252}Cf source was calibrated absolutely and served as the standard reference source in the NCD phase. Its strength was measured using three separate methods, which are described in the first section. The ^{24}Na and AmBe sources were calibrated relative to the ^{252}Cf source using the SNO detector. In this *in situ* method they were positioned at the centre of the detector and the PMT neutron detection rates compared to those recorded with the ^{252}Cf source in the same position. The calibration of the ^{24}Na and AmBe sources is discussed in the second and third sections, respectively.

6.1 The ^{252}Cf source strength

6.1.1 Measurements

A physical description of the ^{252}Cf source can be found in Section 4.4.2. This section describes the measurement of its activity, defined as the number of neutrons produced per second at the site of the activity within the source housing (as distinct from the number of neutrons exiting the source housing). Three methods were used:

- *D_2O multiplicity.*

  In this technique [122, 123] the neutron multiplicity distribution measured during the D_2O phase was fit to an analytical model. The model gave the probability that in one unit of time - the data were divided into 2 second units - d neutrons would be detected from r produced in N ^{252}Cf fissions; it could be written

$$P(d) = \sum_{N=1}^{\infty} \sum_{r=d}^{\infty} \frac{r!\varepsilon^d \varepsilon^{r-d}}{d!(r-d)!} \cdot \frac{e^{-\frac{(r-N\mu)^2}{2N\sigma^2}}}{2N\pi\sigma^2} \cdot \frac{\lambda^N e^{-\lambda}}{N!} \tag{6.1}$$

  where λ is the ^{252}Cf fission rate, μ is the mean of the multiplicity distribution, σ is the width of the multiplicity distribution and ε is the neutron detection efficiency. The D_2O data were used because of the relative ease with which neutron events could be identified by cuts on event position and energy. In the salt phase the neutron diffusion length was much smaller so it became difficult to distinguish neutron events from high energy prompt gammas.

  The neutron detection efficiency ε was corrected for the sacrifice of the cuts used to identify neutrons to give a source strength of 16.33 ± 0.18 n s^{-1}.

- *Time series.*

  The time series analysis (see Appendix D), like the method described above, also harnessed the bursty nature of the ^{252}Cf source, but in a more complete and general way. It allowed five parameters to be fit independently: the source strength, neutron detection efficiency, neutron mean lifetime and the contamination of the neutron signal by prompt fission gammas and radioactive backgrounds. The inclusion of the prompt fission gammas meant that the method could be used in the salt phase. The source strength was found to be 16.46 ± 0.12 n s^{-1}.

- *Direct counting.*

  In the direct counting method [88] an array of ^{3}He proportional counters was used to directly measure the ^{252}Cf neutron production rate. The experimental arrangement (shown in Figure 6.1) consisted of three rings of ^{3}He proportional counters, supported by a polyethylene moderator, and surrounding a well where the sources were placed. There were 42 counters in all but only the inner 24 were used. The neutron detection efficiency of the array was evaluated using two methods:

  1. In the *fission-triggered evaluation* a sample of the same ^{252}Cf used to make the source was electroplated onto a Si(Li) surface barrier detector and covered by a further barrier detector. The detectors acted as fission triggers which opened

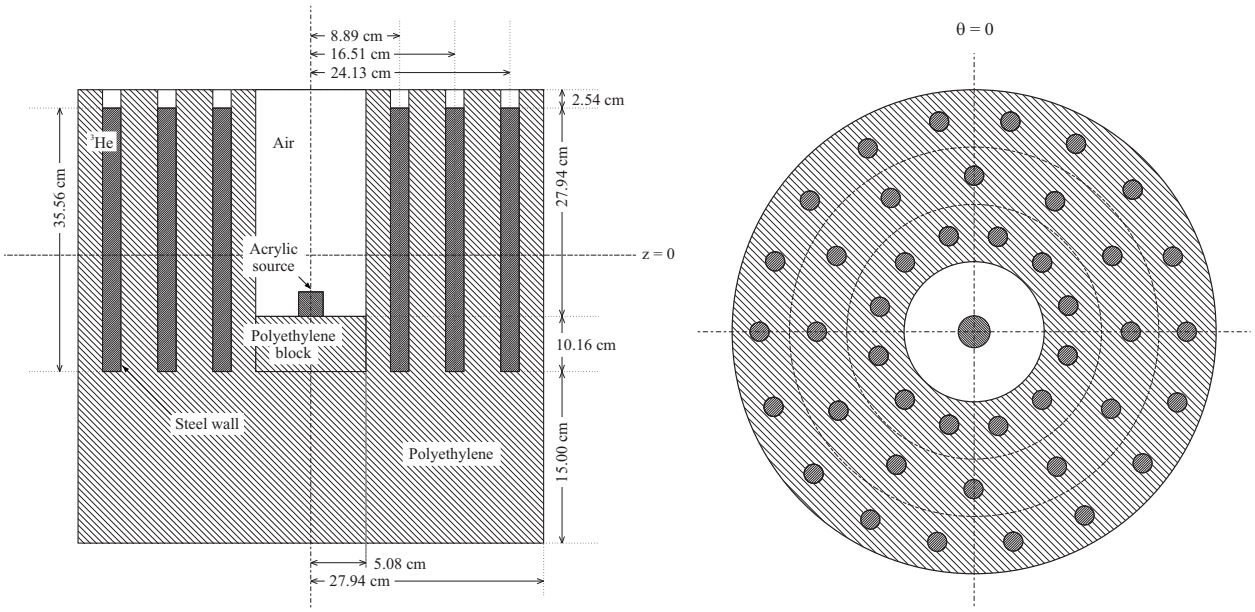

Figure 6.1: The ^{3}He proportional counter apparatus used in the direct counting measurement of the ^{252}Cf source strength. Section (left) and plan (right).

a 200 μs window for observing ^{252}Cf neutrons in the array. (This was assumed to contain the majority of the prompt neutrons but source strengths measured using this window were corrected to a long 1000 μs window to include the remaining prompt and delayed neutrons). The measured multiplicity distribution was fit to a model to determine the fission rate and therefore the array efficiency, which was found to be $\varepsilon_{ft} = 0.2668 \pm 0.0023$.

2. In the *Pt disk evaluation* ^{252}Cf was electroplated onto two platinum disks. The deposited activities were measured using a Frisch grid chamber before the disks were placed separately in the well and the event rates measured. The efficiency was found to be $\varepsilon_{Pt} = 0.2755 \pm 0.0020$, which is the weighted average of the values found using each disk: 0.2733 ± 0.0027 and 0.2792 ± 0.0029.

The ^{252}Cf source was placed in the array and the measured count rate converted into a source strength using each of the efficiencies. The source strength was initially found to be 17.78 ± 0.16 using the fission triggered efficiency and 17.22 ± 0.14 using the Pt disk efficiency. The weighted average of these was 17.45 ± 0.30 n s^{-1}

There were a few issues with this analysis that the author investigated. The first was the 2.2% (1.2σ) discrepancy between the two Pt disk measurements; the second was the 3.3% (2σ) discrepancy between the ε_{ft} and ε_{Pt} measurements; and the third was the discrepancy between the direct counting and the multiplicity and time series

measurements, which agreed well with each other.

One possible explanation for the first two was inconsistent positioning of sources inside the well. For the last, a possibility was moderation and absorption of neutrons by the acrylic in which the ^{252}Cf was encapsulated. A Monte Carlo simulation of the apparatus was built within the SNOMAN framework to help quantify the magnitude of these effects. The plots in Figure 6.2 show the results.

The top two figures show the dependence of the 200 and 1000 μs array efficiencies on the vertical position of the source in the well. The Monte Carlo efficiencies at $z = 0$ were within $\sim 3\%$ of the measured values, which was reassuring, particularly as no attempt was made to simulate the response of the counters - capture efficiencies were equated to detection efficiencies. This level of agreement was sufficient in a study of relative effects.

The 200 μs efficiency increased with increasing z because neutrons produced further up in the well were less likely to enter the mass of polyethylene below the well, where they were well moderated but less likely to reach a counter in 200 μs. The behaviour of the 1000 μs efficiency resulted from two competing effects: a tendency of the efficiency to fall with an increase in position because neutrons became less well moderated and therefore less likely to capture, and a tendency of it to rise because neutrons were produced closer to the centre of the array and were more likely to reach counters. The decrease won at smaller displacement and the increase at larger displacements.

If inconsistencies in the mounting of the Pt disks in the well caused differences in vertical position of 0.5 cm then the discrepancy between the values for the two discs would fall below 1σ. The difference between ε_{ft} and ε_{Pt} measurements could not be explained by any vertical displacement consistent with the experimental procedure.

The effect of the source housing was investigated by running simulations with and without the ^{252}Cf source encapsulated in acrylic. The hypothesis was that the acrylic surrounding the source might moderate the neutrons and thereby increase the efficiency of the array compared to what it would have been for the bare activity. The bottom right plot of Figure 6.2 shows the efficiency correction factor as a function of the position of the Pt disk/triggered source, when the acrylic source was placed at the bottom of the well (where its activity would be located at the centre of the acrylic housing, at $z = 1.28$ cm). Assuming the Pt disk/triggered source was at $z = 0$, the correction was found to be $2.25 \pm 0.08\%$. This result was confirmed by Hime [124] who found a correction of $2.15 \pm 0.20\%$ using an independent code. The correction was responsible for removing most of the discrepancy between the

Table 6.1: Results of the methods for determining the ^{252}Cf source strength. The reference date is June 12, 2001.

Method	Strength ($n\,s^{-1}$)	
	Value	Unc.
D_2O multiplicity	16.33	0.18
Salt time series	16.46	0.12
Frisch grid	16.75	0.14
Triggered Si(Li)	17.08	0.43
Weighted mean	16.55	0.11

direct counting and other methods.

Hime refined other aspects of the analysis [124] and the final source strengths were 17.08 ± 0.43 (fission triggered) and 16.75 ± 0.14 (Pt disks).

The source strengths from all methods are summarised in Table 6.1. They were combined using the standard method (see Appendix B); the error was scaled up by 1.37 to account for a slightly large χ^2 of 5.2.

6.2 The ^{24}Na source strengths

6.2.1 Overview

This section describes the calculation of the distributed ^{24}Na source strengths using a cross-calibration technique, which related the strength of the injected ^{24}Na to the strength of the ^{252}Cf source.

In each ^{24}Na measurement a sample of the activated brine was encapsulated in a small can (see Figure 4.6), which was attached to the source-manipulator system and positioned in the centre of the SNO detector. The neutron detection rate was measured in this configuration and then with the ^{252}Cf source in the same position. As the ^{252}Cf source strength was known the ^{24}Na source strength could be inferred. The analysis could be done using either the PMT or NCD array to detect the neutrons. The author was responsible for the PMT analysis.

If R_{Na} is the dead time-corrected neutron detection rate measured using the canned

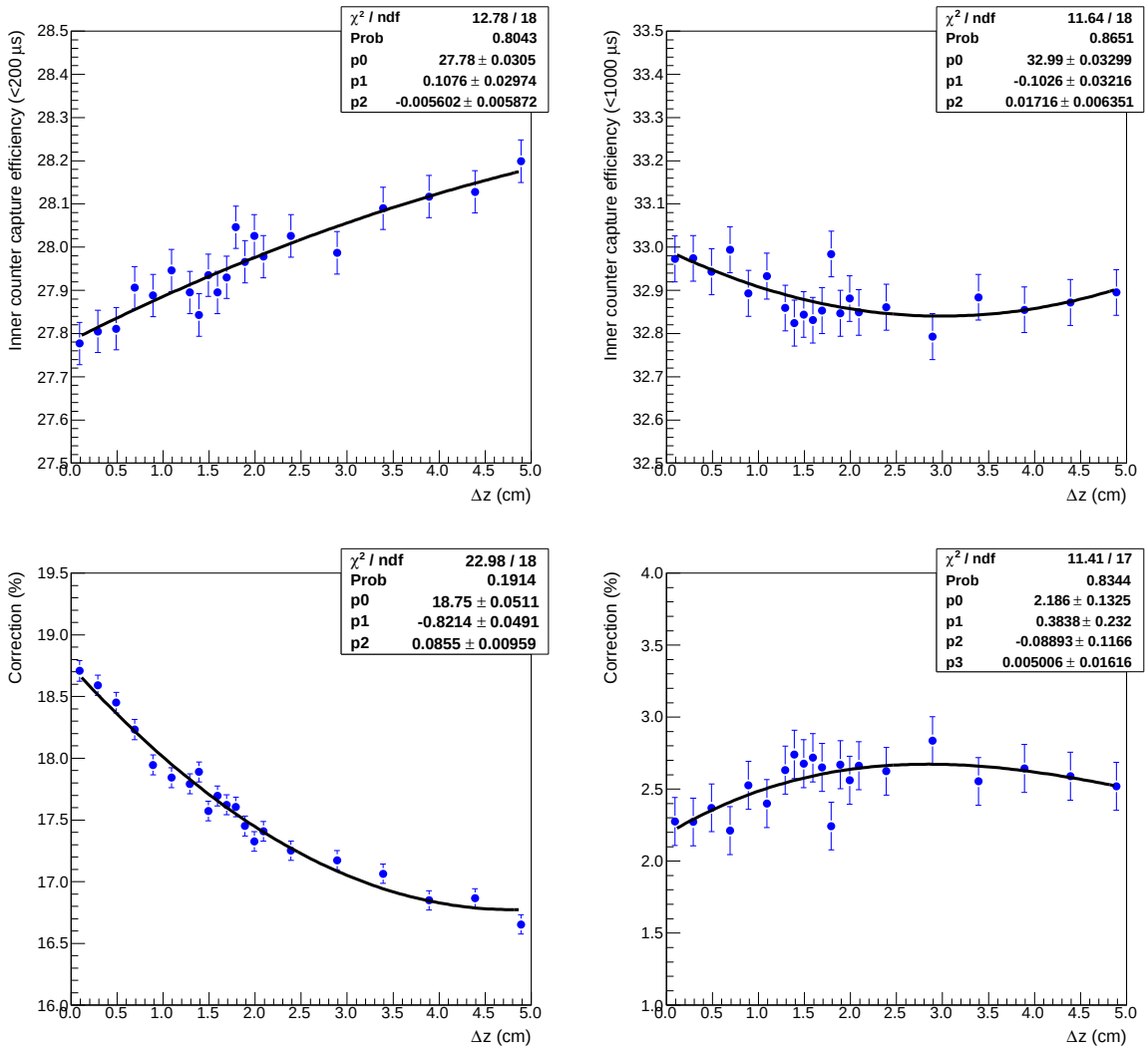

Figure 6.2: The 200 μs array capture efficiency (top left), 1000 μs capture efficiency (top right), 200-1000 μs correction factor (bottom left) and the correction to the efficiency measured with an unencapsulated source to make it applicable for the acrylic ^{252}Cf source (bottom right). All plots show the variation of the quantity as a function of the distance of the production point above the bottom of the well. Points are fit to polynomials to illustrate the general dependence - there is no physical motivation for the functional forms. The efficiencies in the top two plots are percentages.

^{24}Na source and R_{Cf} is the dead-time corrected corresponding to the production of 1 n s^{-1} by the ^{252}Cf source, both scaled to some reference time, then the strength of the ^{24}Na injected into SNO A_m is given by

$$A_m = \frac{1}{f_C} f_P \frac{R_{Na}}{R_{Cf}} \frac{m_m}{m_{Na}} \tag{6.2}$$

where m_m is the mass of the injected brine, m_{Na} is the mass of brine in the can and f_C and f_P are two correction factors, discussed below.

The correction factor f_C accounted for the different detection efficiencies of ^{252}Cf and ^{24}Na neutrons. The efficiencies differed because the former were produced within the source but the latter were generated by photodisintegration in a cloud extending some distance from the source (the radiation length of 2.754 MeV gammas was ~ 26 cm). The efficiencies were related by

$$\varepsilon^{Na} = f_C \, \varepsilon^{Cf}$$

where

$$f_C = \frac{\varepsilon^{Na}_{MC}}{\varepsilon^{Cf}_{MC}} \tag{6.3}$$

was calculated using Monte Carlo.

The correction factor f_P accounted for the different photodisintegration probabilities of gammas produced by the canned and distributed ^{24}Na sources. Gammas from the canned source could interact with the materials of the can, which reduced the photodisintegration probability compared to gammas from the distributed source. The photodisintegration probabilities were related by

$$A_m = f_P \frac{m_m}{m_{Na}} A_{Na}$$

where

$$f_P = \frac{P^m(PD)}{P^{Na}(PD)} \tag{6.4}$$

The quantities $P^m(PD)$ and $P^{Na}(PD)$ are photodisintegration probabilities for the distributed and canned sources, respectively, calculated using Monte Carlo.

The Monte Carlo simulations used to calculate these correction factors are described in the following section along with the measurement of the ratio R_{Na}/R_{Cf}. However, first is a discussion of the cuts used to identify neutrons events.

Table 6.2: Analysis cuts. Parameters are described in the text.

Cut
DAMN0 & `0xCCF56FE1^0x0400000`
$0.55 < ITR < 1.00$
$-1.0 < u \cdot r < 1.0$
$-0.12 < \beta_{14} < 0.95$
$5.5 < E_{RSP} < 10$ MeV
$200 < r < 450$ cm

6.2.2 Data selection

Cuts were developed to distinguish events in the PMT array due to neutrons from those due to backgrounds and instrumentals. They fell into two categories: 'standard' SNO analysis cuts to remove instrumental, muon and other events; and analysis-specific cuts to distinguish neutrons from gammas produced by the sources and by U and Th in the materials of the detector. The cuts are listed in Table 6.2. The analysis-specific cuts are shown below the line.

The analysis cuts are standard ones on $u.r$, which is the projection of the direction vector on the radius vector; β_{14}, which is a measure of the isotropy of PMT hits in the event; and ITR, which is the fraction of the detected photons falling in the prompt peak. These cuts were designed to remove non-physics events or events for which the position fitter returned non-sensical results. β_{14} and ITR are discussed further in Section 8.2.4. The DAMN mask is a specification of which low level instrumental cuts should be applied; the mask used in this analysis was identical to the one used in the analysis of neutrino data except that it excluded the burst cut. This cut could not be used with a bursty fission source.

The analysis-specific cuts were on event energy and position. Figure 6.3 shows measured energy-radius distributions for canned ^{24}Na and ^{252}Cf runs. These are the classes of event that compose the distributions:

- *Neutrons.*

  Neutrons mainly captured on deuterons producing 6.25 MeV gammas. The events were concentrated at low radii, close to the source, but the distribution had an exponential tail out to high radii.

- *Sources gammas.*

  In the ^{24}Na sources these were 1.37 and 2.54 MeV gammas from the decay of ^{24}Mg*, the beta decay final nucleus, and in the ^{252}Cf source they were gammas from the de-excitation of the fission fragments. These gammas could be reconstructed some distance from the source location because of two effects: first, a gamma could travel some distance before Compton scattering an electron (and thereby producing the Čerenkov signal that was detected) and second, the finite position resolution of the detector. Monte Carlo-generated distributions for ^{24}Na and ^{252}Cf source gammas are shown in the top plots of Figure 6.4.

- *Low energy U and Th backgrounds.*

  Gammas from the U and Th decay chains (see Appendix A) were a background at low energies and particularly at high radii, close to the relatively low-radiopurity AV and H_2O. The energy-radius distribution for a neutrino run, where the majority of the events are U and Th gammas, is shown in the lower plot of Figure 6.4.

- *Miscellaneous.*

  A number of minor processes could generate neutrons indistinguishable from those produced directly by the sources. Neutrons produced by (α, n) reactions in the acrylic of the AV, NC neutrino interactions and photodisintegration by U and Th gammas had low enough rates to be neglected. Those produced by photodisintegration by source gammas were included in the Monte Carlo.

The analysis region was selected to maximise the neutron rate and exclude background events; it lay within $200 < r < 450$ cm and $5.5 < T < 10$ MeV.

6.2.3 Radial neutron production profile (f_C)

The correction factor f_C accounted for the different neutron detection efficiencies of ^{252}Cf and ^{24}Na neutrons, resulting from the different radial neutron production profiles. It was defined in Eqn. 6.3

$$f_C = \frac{\varepsilon_{MC}^{Na}}{\varepsilon_{MC}^{Cf}}$$

To calculate ε_{MC}^{Na} it was important that the radial production profile (shown in Figure 6.5) be correct in the Monte Carlo. To test this the 2.754 MeV gamma radiation length was extracted from a simulation and compared to a calculation. The Monte Carlo distribution fitted to a decaying exponential with radiation length 25.80 ± 0.38 cm. A

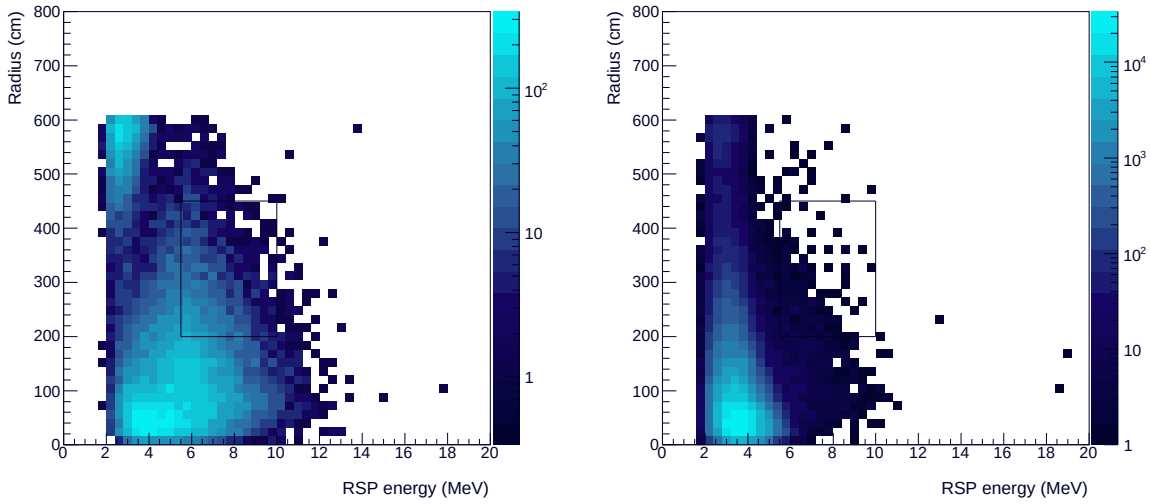

Figure 6.3: Measured energy-radius distributions for ^{252}Cf (left) and ^{24}Na (right). The box highlights the analysis region. These plots are intended to illustrate the relative distributions of events in energy-radius space; there happens to be more events in the ^{24}Na plot but this is of no consequence.

theoretical value was calculated using D_2O mass attenuation coefficients prepared by [125]. These were extrapolated to 2.754 MeV to give a coefficient of 0.0422 $cm^2\,g^{-1}$, which corresponded to a radiation length of 26.19 ± 0.52 using a D_2O density of 1.1056 $g\,cm^{-3}$. There was therefore good agreement between Monte Carlo and calculation.

The right hand plot of Figure 6.5 shows the simulated radial capture distributions for ^{252}Cf and ^{24}Na . The ^{252}Cf distribution is higher than Na at low radii, the distributions cross at about 100 cm, and ^{24}Na neutrons are preferentially detected at higher radii. The steep rise at low radii in both distributions is a volume effect.

Values of f_C were calculated using reconstructed Monte Carlo, that is, using Monte Carlo fit in the same way as the data to take into account any biases or artifacts in the position and energy reconstruction algorithms. For diagnostic purposes values were calculated as a function of radial bin and lower radial cut.

Figure 6.6 shows f_C by radial bin and as a function of lower radial cut. The Monte Carlo used was the sum of that produced for the dry run and the 2005 spike. The correction factors for the second spike were derived separately using dedicated Monte Carlo.

The task of predicting f_C was actually a demanding one for the Monte Carlo because it relied on proper modelling of the propagation of neutrons and gammas over distances

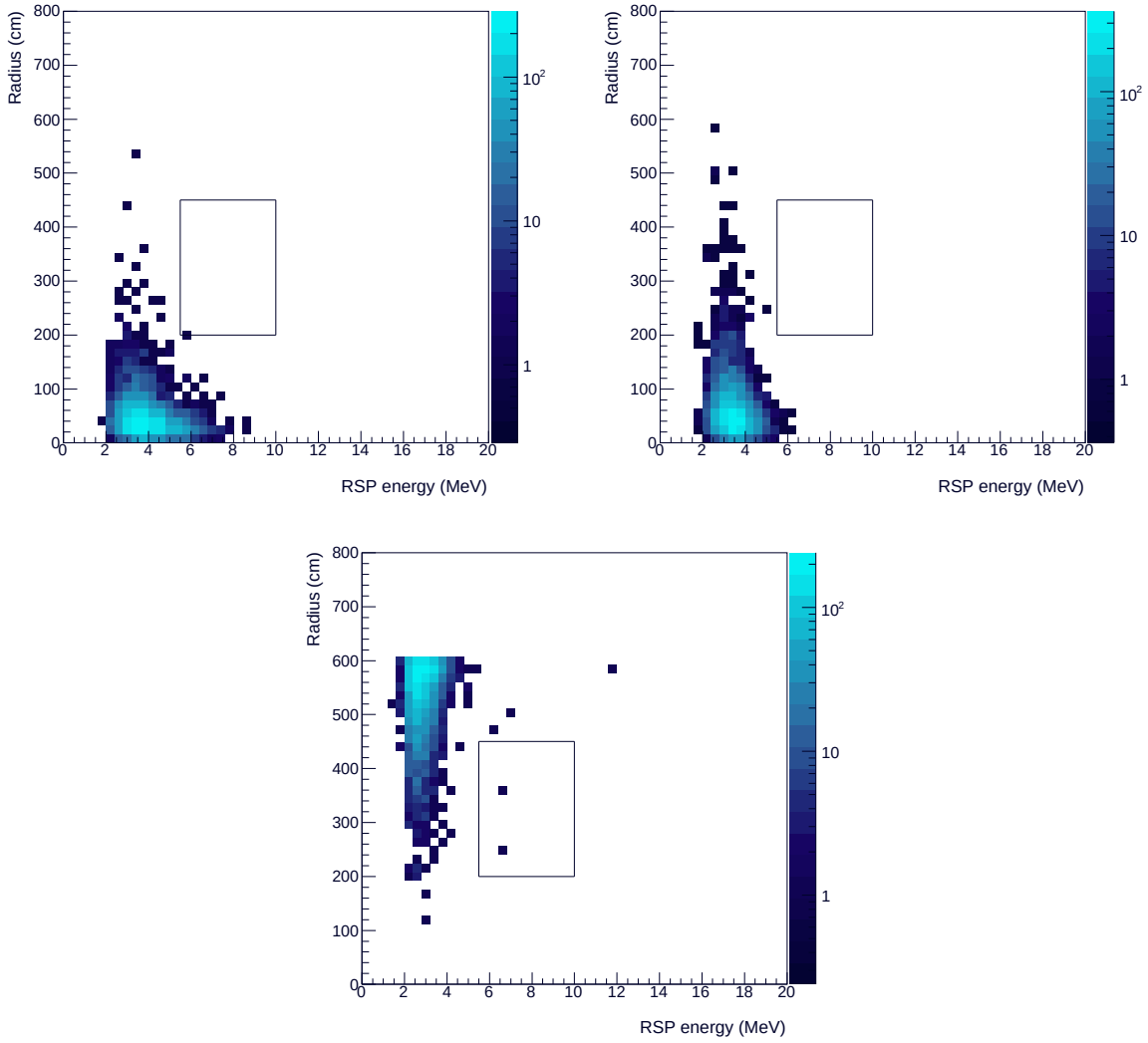

Figure 6.4: Energy-radius distributions for three PMT backgrounds: Monte Carlo simulation of ^{252}Cf gammas (top left), ^{24}Na gammas (top right) and (mainly) low energy background events from a neutrino run (bottom). The box highlights the analysis region.

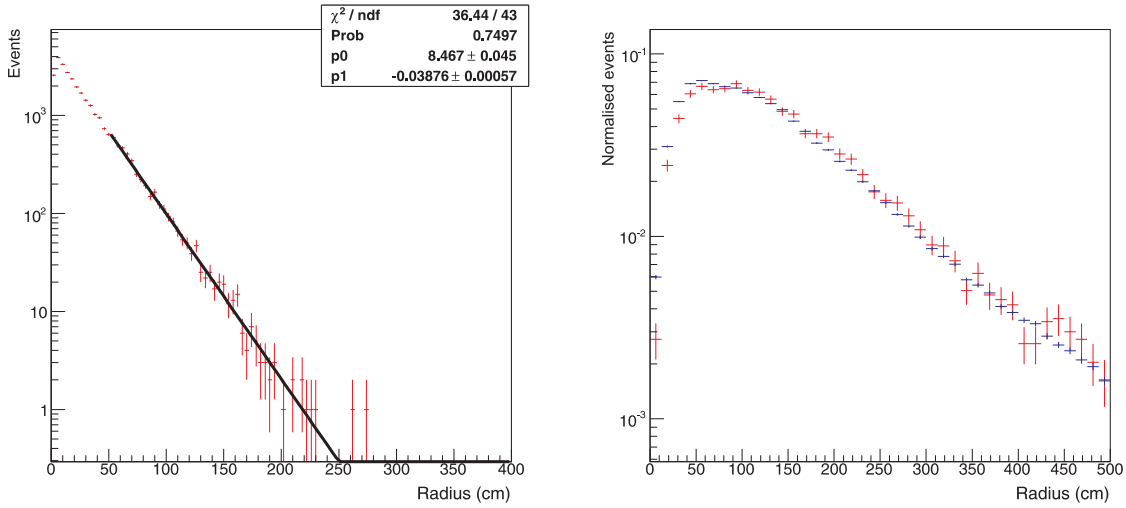

Figure 6.5: Radial neutron production profile of ^{24}Na photodisintegration neutrons (left) and radial capture profiles (right) of ^{24}Na neutrons (red) and ^{252}Cf neutrons (blue). The y-axis units are arbitrary. The plots show the actual positions of the verticies in the Monte Carlo rather than ones reconstructed using position fitters.

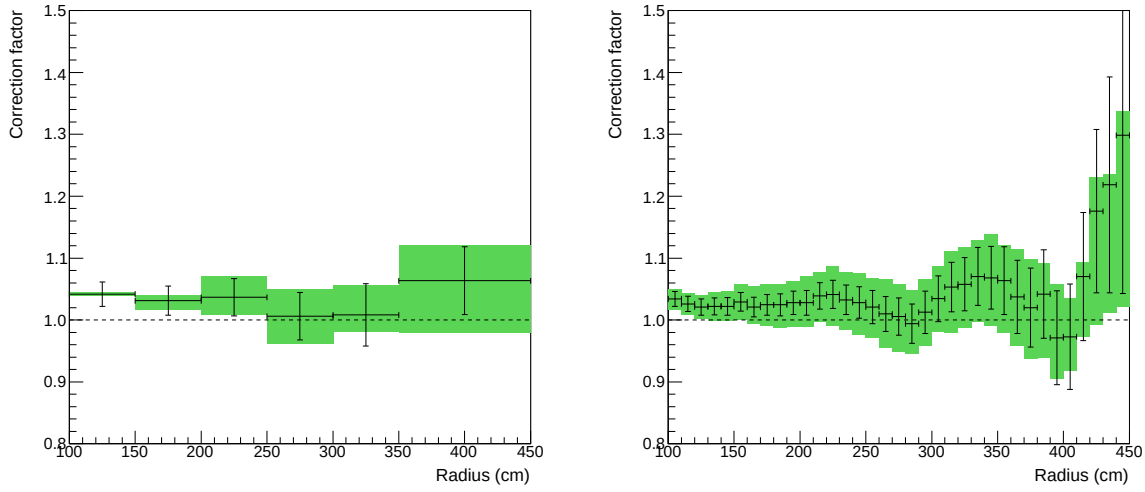

Figure 6.6: Correction factor f_C by radial bin (left) and as a function of lower radial cut (right). The error bars give the statistical uncertainties and the green bands give the systematic uncertainties.

Table 6.3: Values for the correction factor f_C.

Data set	Analysis window		f_C			
	r (cm)	E_{RSP} (MeV)	Value	Stat.	Sys. +	Sys. -
Dry / 2005	$200-450$	$6.0-10$	1.0362	0.0233	0.0439	0.0414
	$200-450$	$5.0-10$	1.0738	0.0184	0.0450	0.0415
	$250-450$	$5.5-10$	1.0210	0.0267	0.0478	0.0494
	$150-450$	$5.5-10$	1.0293	0.0152	0.0282	0.0291
	$200-450$	$5.5-10$	1.0279	0.0200	0.0423	0.0398
2006	$200-450$	$6.0-10$	1.0018	0.0391	0.0423	0.0328
	$200-450$	$5.0-10$	1.0503	0.0310	0.0480	0.0349
	$250-450$	$5.5-10$	1.0352	0.0465	0.0541	0.0419
	$150-450$	$5.5-10$	1.0101	0.0257	0.0304	0.0280
	$200-450$	$5.5-10$	1.0186	0.0341	0.0426	0.0346

of 200-450 cm, and the longer the distances the more the effects of model deficiencies are compounded. A systematic uncertainty was assigned to cover such effects. A radial shift was introduced between the ^{24}Na and ^{252}Cf Monte Carlo radial neutron capture distributions; they were scaled independently by $\pm 2\%$ and the mean of the two higher source strengths taken as the high systematic value and the mean of the two lower source strengths as the low systematic value. The scaling of $\pm 2\%$ was a conservative estimate of the relative uncertainty in the probabilities of ^{24}Na and ^{252}Cf neutrons reaching the analysis window. It encompassed the 1.5% difference between the Monte Carlo and calculated 2.754 MeV radiation lengths and equated to a 4 cm relative radial shift at 200 cm and a 9 cm relative radial shift at 450 cm.

The values used for f_C are summarised in Table 6.3 for the default analysis windows and for some variations. The ^{24}Na Monte Carlo used in deriving the correction factors was limited statistically because of the low probability that 2.754 MeV gammas photodisintegrate ($\sim 1/400$) and the low probability that neutrons so-produced make it into the analysis window ($\sim 3\%$).

6.2.4 Probability of photodisintegration (f_P)

The correction factor f_P accounted for the different deuteron photodisintegration probabilities for gammas from canned and distributed ^{24}Na . It was defined in Eqn. 6.4

$$f_P = \frac{P^m(PD)}{P^{Na}(PD)}$$

Gammas produced by the former could be absorbed or scattered by the material of the can before they had a chance to photodisintegrate and the probability of them doing so was therefore smaller. The can dimensions and materials are shown in Figure 4.6; in the first measurement the can was made entirely of Delrin but in the second it was fitted with a stainless steel lid.

Values for the probabilities of photodisintegration (PD) were taken from Monte Carlo simulations:

Type	P(PD)		1/P(PD)	
	Value	Unc.	Value	Unc.
Distributed	0.002596	0.000009	385.27	1.32
Can (2005)	0.002564	0.000007	389.97	1.03
Can (2006)	0.002523	0.000009	396.38	1.39

The probability was lower for the 2006 measurement because of the steel lid, which attenuated the gammas more strongly.

The main focus of this section is the uncertainty on f_P due to P(PD). Delrin was added to the SNOMAN Monte Carlo specifically to allow f_P to be calculated and it was important to check that interactions of gammas with Delrin were handled correctly. Information was available to do this - Evans [126, 127] performed an experiment to measure the mass attenuation coefficient of Delrin at 2.754 MeV. SNOMAN was used to simulate the experimental configuration and assign a systematic uncertainty on P(PD), and therefore on f_P, based on the ability of the Monte Carlo to reproduce the result of the experiment. The mass attenuation coefficient μ/ρ (see Appendix E) is a parameter well-characterising the interactions of gammas with a material.

In the experiment a small quantity of activated ^{24}Na brine was enclosed in a thin-walled vial and positioned a short distance from the face of a Ge detector. The 1.369 and 2.754 MeV full-energy peak counts R were measured with and without a Delrin disk placed between the source and the detector. The quantity A, given by

$$A = \frac{R_{with}}{R_{without}} = e^{-(\mu/\rho)x_\rho} \tag{6.5}$$

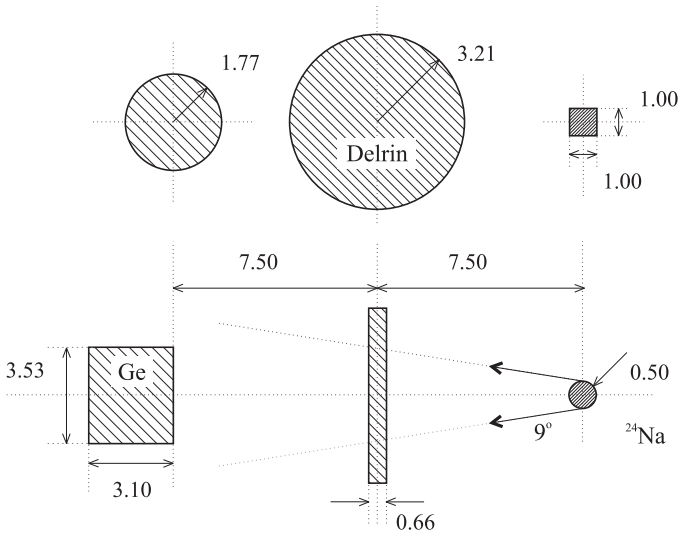

Figure 6.7: Delrin mass attenuation coefficient experimental configuration, as simulated in SNOMAN.

was calculated for each peak, corrected for the change in source strength between measurements and used to infer the mass attenuation coefficient. The measured values and mass attenuation coefficients were:

Gamma	A		μ/ρ ($\mathrm{cm^2 g^{-1}}$)	
(keV)	Value	Unc.	Value	Unc.
1369	0.9497	0.0014	0.0562	0.0016
2754	0.9631	0.0022	0.0410	0.0025

where the uncertainties are statistical only.

These coefficients can be compared to calculated values. Taking the chemical composition of Delrin to be $(CH_2O)_n$ [128] and using elemental mass attenuation coefficients from [129], the mass attenuation coefficients of Delrin were found to be 0.0572 at 1.369 MeV and 0.0398 $\mathrm{g\,cm^{-2}}$ at 2.754 MeV, which were in good agreement with the measured values.

The important features of the experimental setup were reproduced in the Monte Carlo. The geometry is shown in Figure 6.7. In constructing it several simplifications were made:

- *Materials.*

  The Ge detector had no outer casing and the crystal had no dead layer. No attempt was made to simulate the charge collection characteristics of the detector. The vial materials were neglected. No attempt was made to simulate materials surrounding the apparatus from which photons might scatter back into the detector. These simplifications were minor because the measurement was a relative one, concerned only with the change in count rate when the disk was placed in front of the detector.

- *Disk thickness.*

  The thickness of the Delrin disk differed slightly from the experiment to reflect the difference in densities - 1.4 $\mathrm{g\,cm^{-3}}$ in SNOMAN compared to 1.434(0.007) $\mathrm{g\,cm^{-3}}$ in the experiment. The thickness was adjusted to give the same mass per unit area of 0.9177 $\mathrm{g\,cm^{-2}}$.

The EGS4 photon and electron cut offs (see Section 5.2) were set to `PCUT = 0.025` and `ECUT = 0.526` to add detail to the energy deposition spectra. Following the experimental procedure, events were classed as falling in full-energy peaks if the deposited energy was within 0.5 keV either side of the nominal gamma energy.

This table shows the Monte Carlo-derived mass attenuation coefficients μ_{sim}/ρ along with the experimental and calculated values (uncertainties are statistical):

Gamma	A_{sim}		μ_{sim}/ρ ($\mathrm{g\,cm^{-2}}$)		μ_{exp}/ρ ($\mathrm{g\,cm^{-2}}$)		μ_{calc}/ρ ($\mathrm{g\,cm^{-2}}$)	
(keV)	Value	Unc.	Value	Unc.	Value	Unc.	Value	Unc.
1367	0.9518	0.0030	0.0538	0.0034	0.0562	0.0016	0.0572	n/a
2754	0.9662	0.0045	0.0375	0.0051	0.0410	0.0025	0.0398	n/a

All results were consistent, but it was decided to take convert the difference between the simulated and experimental central values into a systematic uncertainty. A difference in mass attenuation coefficients would imply an uncertainty in the probability of gammas scattering from the source material and, because scattered and unscattered gammas have different energy distributions and the photodisintegration cross section is energy-dependent, this would imply an uncertainty in the photodisintegration probability.

The probability of a 2.754 MeV gamma causing a photodisintegration $P(PD)$ could be written

$$\begin{aligned} P(PD) &= P(PD\,|\,s)\cdot P(s) + P(PD\,|\,ns)\cdot P(ns) \\ &= P(PD\,|\,s)\cdot P(s) + P(PD\,|\,ns)\cdot (1-P(s)) \\ &= P(s)\cdot [P(PD\,|\,s) - P(PD\,|\,ns)] + P(PD\,|\,ns) \end{aligned} \tag{6.6}$$

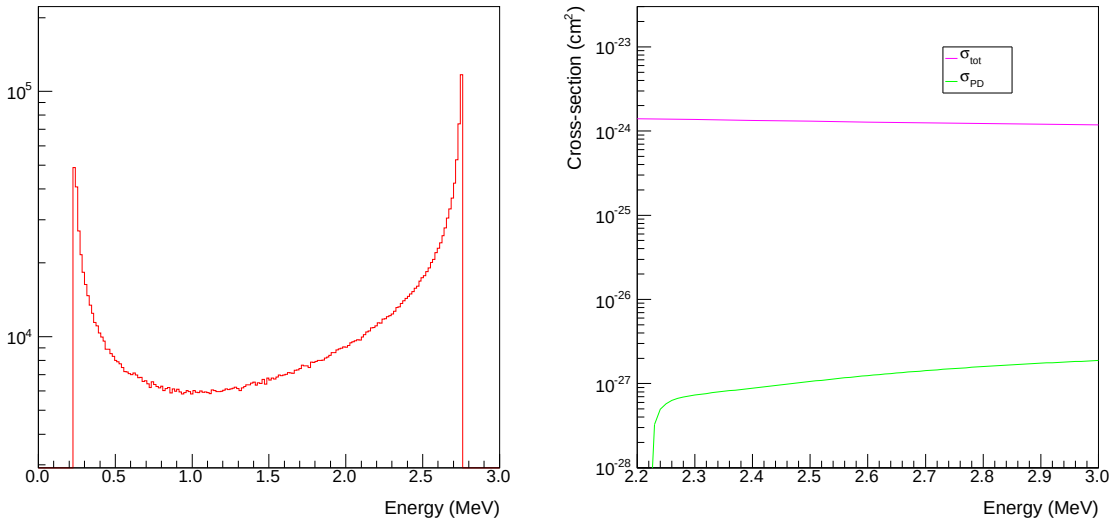

Figure 6.8: Energy distribution of 2.754 MeV gammas after a single Compton Scattering (left); D_2O total and photodisintegration cross sections (right).

where $P(s)$ is the probability of scattering and $P(ns) = 1 - P(s)$ is the probability of not scattering. An uncertainty due to the difference in mass attenuation coefficients would create an uncertainty $\delta P(s)$ on $P(s)$. The resultant uncertainty on $P(PD)$ was

$$\frac{\delta P(PD)}{P(PD)} = \frac{P(PD\,|\,s) - P(PD\,|\,ns)}{[P(PD\,|\,s) - P(PD\,|\,ns)] \cdot P(s) + P(PD\,|\,ns)} \cdot \delta P(s) \tag{6.7}$$

To evaluate this, the quantities $P(s)$, $\delta P(s)$, $P(PD\,|\,s)$ and $P(PD\,|\,ns)$ had to be calculated.

$P(s)$ was calculated using μ_{exp}/ρ and an estimate of 0.6 cm for the characteristic thickness of material gammas passed though before entering the D_2O. The uncertainty $\delta P(s)$ was the change in $P(s)$ when μ_{exp}/ρ was replaced by μ_{sim}/ρ. The calculated value was $P(s) = 0.033 \pm 0.003$.

$P(PD\,|\,ns)$ could be found simply, but $P(PD\,|\,s)$ required a knowledge of the energy distribution after scattering as well as the photodisintegration cross section.

To calculate the energy distribution after scattering, the intensity as a function of angle was first found using the Klein-Nishina formula [130]

$$\frac{I(\theta)}{I(\theta = 0)} = \frac{1}{[1 + \gamma(1 - \cos\theta)]^2} \cdot \left(1 + \cos^2\theta + \frac{\gamma^2(1 - \cos\theta)^2}{1 + \gamma(1 - \cos\theta)}\right) \tag{6.8}$$

where $\gamma = E_\gamma / m_e c^2$ and θ is the angle through which the gamma was scattered. An-

Table 6.4: Values for the correction factor f_P taken from Monte Carlo.

Data set	f_P		
	Value	Stat.	Sys.
Dry run / 2005	1.0122	0.0044	0.0019
2006	1.0288	0.0050	0.0019

gles were sampled randomly from this distribution and converted to energies using the standard Compton formula

$$E'(\theta) = \frac{E_\gamma}{1 + \gamma(1 - \cos\theta)} \tag{6.9}$$

The resulting energy distribution is shown in Figure 6.8. The probability of twice-scattered gammas photodisintegrating was neglected; any such events would have reduced the systematic uncertainty and neglecting them made the value of the systematic conservative.

$P(PD \,|\, s)$ was given by

$$P(PD \,|\, s) = \int \frac{\sigma_{PD}(E)}{\sigma_{tot}(E)} \,\mathrm{d}E \tag{6.10}$$

where the integral is over the energy distributions. σ_{PD} was taken from [70] and σ_{tot} calculated using D_2O mass attenuation coefficients from [125][1]. It was found that $P(PD \,|\, s) = 0.00041$. Using Eqn. 6.10 with $E = 2.754$ MeV gave $P(PD \,|\, ns) = 0.00122$. And substituting both of these into Eqn. 6.7 gave $\frac{\delta P(PD)}{P(PD)} = 0.0019$, which was the final systematic uncertainty. The values of f_P are summarised in Table 6.4.

6.2.5 Source strengths

The ^{252}Cf data were used to determine R_{Cf}, which was the count rate within analysis cuts that corresponded to the production of 1 n s^{-1}. For each ^{24}Na run the count rate at the start of the run R_{Na} was calculated from the number of counts within the analysis cuts N using

$$R_{Na} = \frac{N\lambda}{1 - e^{-\lambda L}} \tag{6.11}$$

[1] $\mu/\rho = \sigma_{tot}/m$ where μ/ρ is the mass attenuation coefficient and m is the atomic/molecular mass.

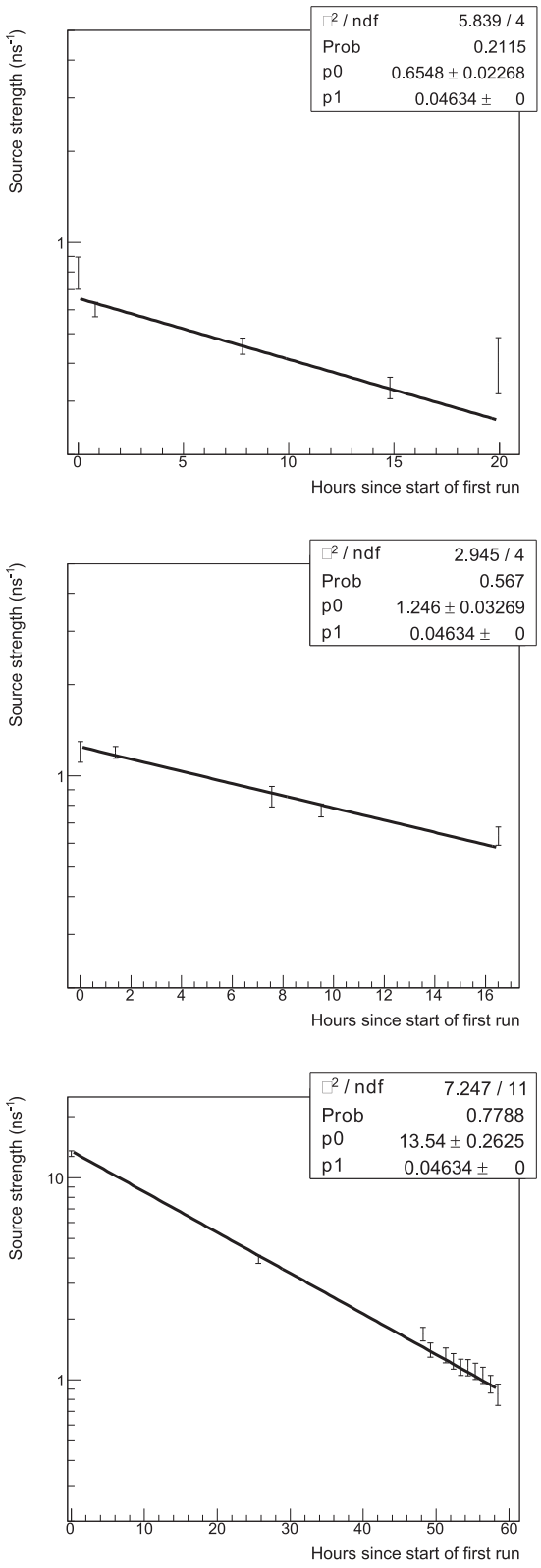

Figure 6.9: Fits to the radioactive decay law, with the ^{24}Na half life fixed, yielding activities at the start of the first run in each data set. Dry run (top), 2005 (middle) and 2006 (bottom).

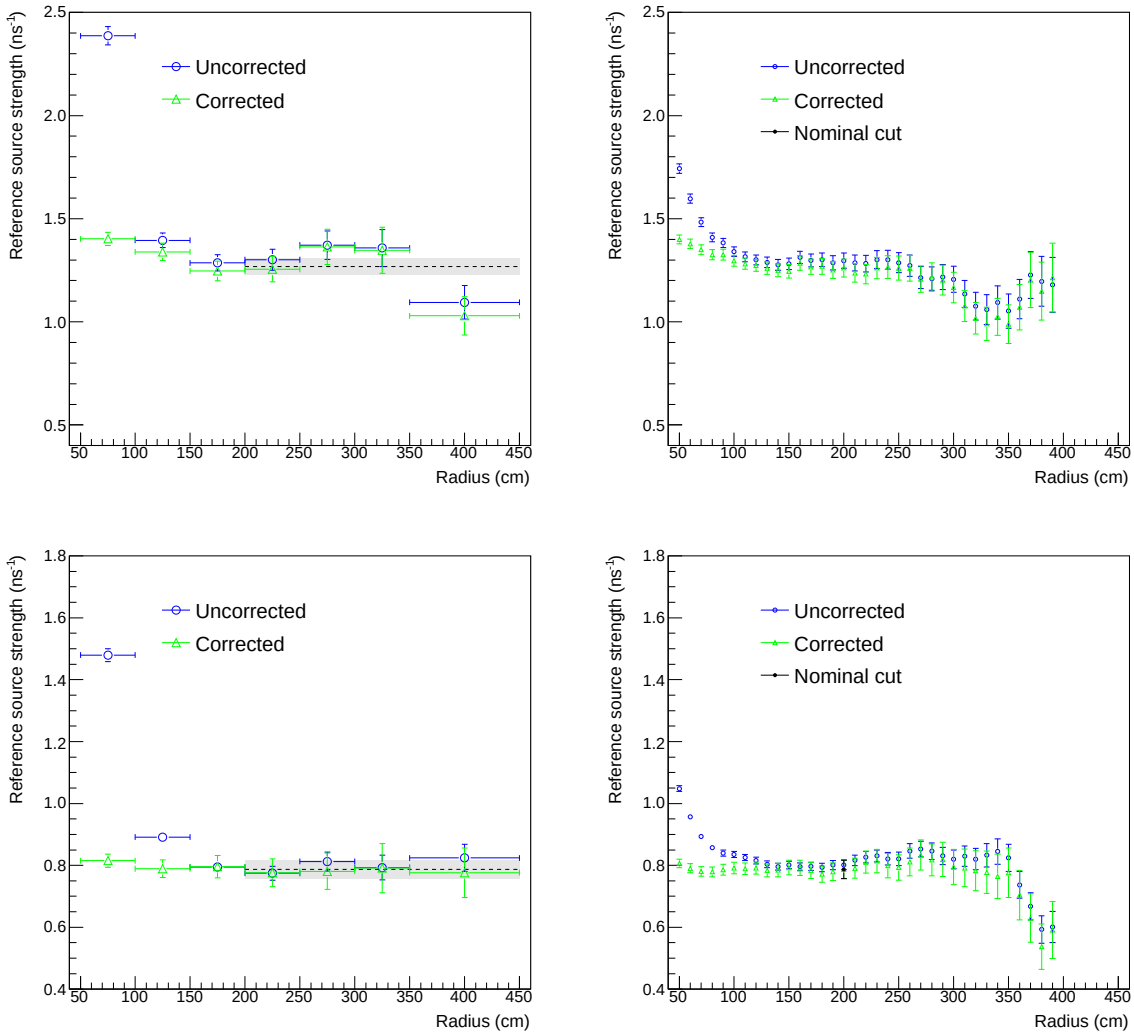

Figure 6.10: Raw and corrected source strengths by bin (left) and as a function of lower radial cut (right) for the 2005 measurement (top) and 2006 measurement (bottom). Error bars are statistical.

Table 6.5: Reference masses and times. The reference (injected) mass for the dry run is arbitrary as no injection took place.

Data set	Sample mass (g)		Ref. mass (g)		Reference date / time
	Value	Unc.	Value	Unc.	
Dry run	10.92	0.02	1406.2	0.0	Sep 12th 2005 16:16:00 EDT
2005	10.36	0.02	968.7	0.1	Oct 7th 2005 12:37:00 EDT
2006	10.80	0.02	549.8	0.4	Nov 2nd 2006 21:20:00 EST

Table 6.6: Mixed source strengths (A_m) in $\mathrm{n\,s^{-1}}$. The last value in the section for each data set corresponds to the default analysis cuts.

Data set	Analysis window		Raw		Corrected source strength (A_m)			
	r (cm)	E_{RSP} (MeV)	Value	Unc.	Value	Sys. +	Sys. -	Stat.
Dry run	$200-450$	$6.0-10$	83.46	3.39	81.53	3.50	3.30	3.78
	$200-450$	$5.0-10$	87.94	2.69	82.90	3.52	3.25	2.91
	$250-450$	$5.5-10$	83.81	3.89	83.08	3.93	4.06	4.42
	$150-450$	$5.5-10$	86.30	2.26	84.86	2.40	2.47	2.55
	$200-450$	$5.5-10$	84.37	2.93	83.08	3.47	3.27	3.30
2005	$200-450$	$6.0-10$	1.301	0.040	1.271	0.055	0.051	0.048
	$200-450$	$5.0-10$	1.364	0.032	1.286	0.055	0.050	0.037
	$250-450$	$5.5-10$	1.304	0.046	1.293	0.061	0.063	0.057
	$150-450$	$5.5-10$	1.296	0.026	1.275	0.036	0.037	0.032
	$200-450$	$5.5-10$	1.304	0.034	1.284	0.054	0.050	0.042
2006	$200-450$	$6.0-10$	0.804	0.018	0.824	0.038	0.028	0.028
	$200-450$	$5.0-10$	0.841	0.015	0.810	0.034	0.028	0.031
	$250-450$	$5.5-10$	0.821	0.022	0.816	0.043	0.034	0.042
	$150-450$	$5.5-10$	0.801	0.012	0.816	0.025	0.023	0.024
	$200-450$	$5.5-10$	0.802	0.016	0.810	0.034	0.028	0.031

Table 6.7: Contributions to the uncertainties on the ^{24}Na source strengths measured using the PMT array.

Item	Unc. (%)	
	2005	2006
Correction factor f_P	0.47	0.52
Correction factor f_C (statistical)	1.95	3.35
Correction factor f_C (radial scaling))	3.99	3.79
Ratio of sample and injected masses	0.19	0.20

where λ is the ^{24}Na decay constant and L is the run length. These were converted into source strengths by dividing by R_{Cf}.

The sets of source strengths for each measurement (dry run, 2005 or 2006) were fitted to the radioactive decay law with the ^{24}Na half-life fixed to find the strength at the start of the first run (see Figure 6.9). These were scaled to the reference times and masses, and the Monte Carlo corrections applied, using Eq. (6.2).

Corrected and uncorrected source strengths are shown in Figure 6.10 for each of the data sets, by radial bin and as a function of lower radial cut. The analysis was done in a single large radial bin so plots with many radial bins are for illustration only. The correction factors were successful in accounting for most of the strong radial dependence of the uncorrected source strengths. Final source strengths for different radial and energy cuts are shown in Table 6.6. Contributions to the final uncertainties are shown in Table 6.7.

6.3 The AmBe source strengths

6.3.1 Overview

This section describes the calculation of the strengths of the AmBe sources using a cross-calibration method similar to that outlined above. A physical description of the two AmBe sources used in the NCD phase can be found in Section 4.4.3.

Pairs of AmBe and ^{252}Cf runs were identified that were taken close to the centre of the detector at similar times. They were distributed relatively uniformly over the periods of time when each source was in use - the *medium rate* source was used mainly towards the beginning of the NCD phase and the *high rate* source towards the end. For each pair, the PMT neutron detection rates R_{AmBe} and R_{Cf} were measured and the AmBe source strength A_{AmBe} was calculated using

$$A_{AmBe} = \frac{R_{AmBe}}{R_{Cf}} A_{Cf} \tag{6.12}$$

where A_{Cf} is the activity of the ^{252}Cf source. Detection rates were corrected for dead time, which was non-negligible, particularly for the high rate AmBe runs. The same analysis window was used as before; AmBe gammas are somewhat higher in energy than those from ^{252}Cf and ^{24}Na but not enough to affect the choice of cuts.

For each of the sources a straight line was fit to the time series of source strengths, with only the statistical (uncorrelated) errors included on each point. If the reduced χ^2

was greater than 1 then the fit uncertainty was scaled up by $\sqrt{\chi^2/d.o.f.}$ to compensate (see Appendix B). Figure 6.11 shows the results run-by-run, which were consistent over time.

Each of the fit source strengths was then scaled by a correction factor f_C, which accounted for the different detection efficiencies of AmBe and ^{252}Cf neutrons. These differed because the sources produced different numbers of photodisintegration neutrons and because different amounts of neutrons captured back on the source materials. f_C was defined by

$$\varepsilon^{AmBe} = f_C\, \varepsilon^{Cf}$$

where

$$f_C = \frac{\varepsilon^{AmBe}_{MC}}{\varepsilon^{Cf}_{MC}} \tag{6.13}$$

such that

$$< A_{AmBe} >_{corrected} = \frac{< A_{AmBe} >}{f_C} \tag{6.14}$$

where $< A_{AmBe} >$ is the fitted source strength. f_C was assumed to be the same for all source pairs, with the same rate AmBe source, and was calculated by summing together Monte Carlo for the relevant AmBe runs and using a single very high statistics ^{252}Cf simulation. f_C was 1.015 ± 0.007 for the medium rate source and 1.012 ± 0.007 for the high rate source.

The uncertainties on the ^{252}Cf source strength and the correction factor f_C were combined in quadrature with the scaled fit uncertainty.

6.3.2 Source strengths

The final source strengths were 23.63±0.27 Hz for the medium rate source and 68.70±0.74 Hz for the high rate source. The uncertainties were split almost equally between statistics and the ^{252}Cf source strength uncertainty.

Figure 6.12 shows the dependence of the source strengths on radius. The lack of a strong dependence on radius across the analysis region gives confidence in the modelling of neutron propagation in the Monte Carlo and indicated an absence of contamination, which would be unlikely to be uniform in radius. No explanation has been found for the slight turn down in the highest radius bin, which was also seen in the ^{24}Na analysis; the bin carried little weight because the number of events was small.

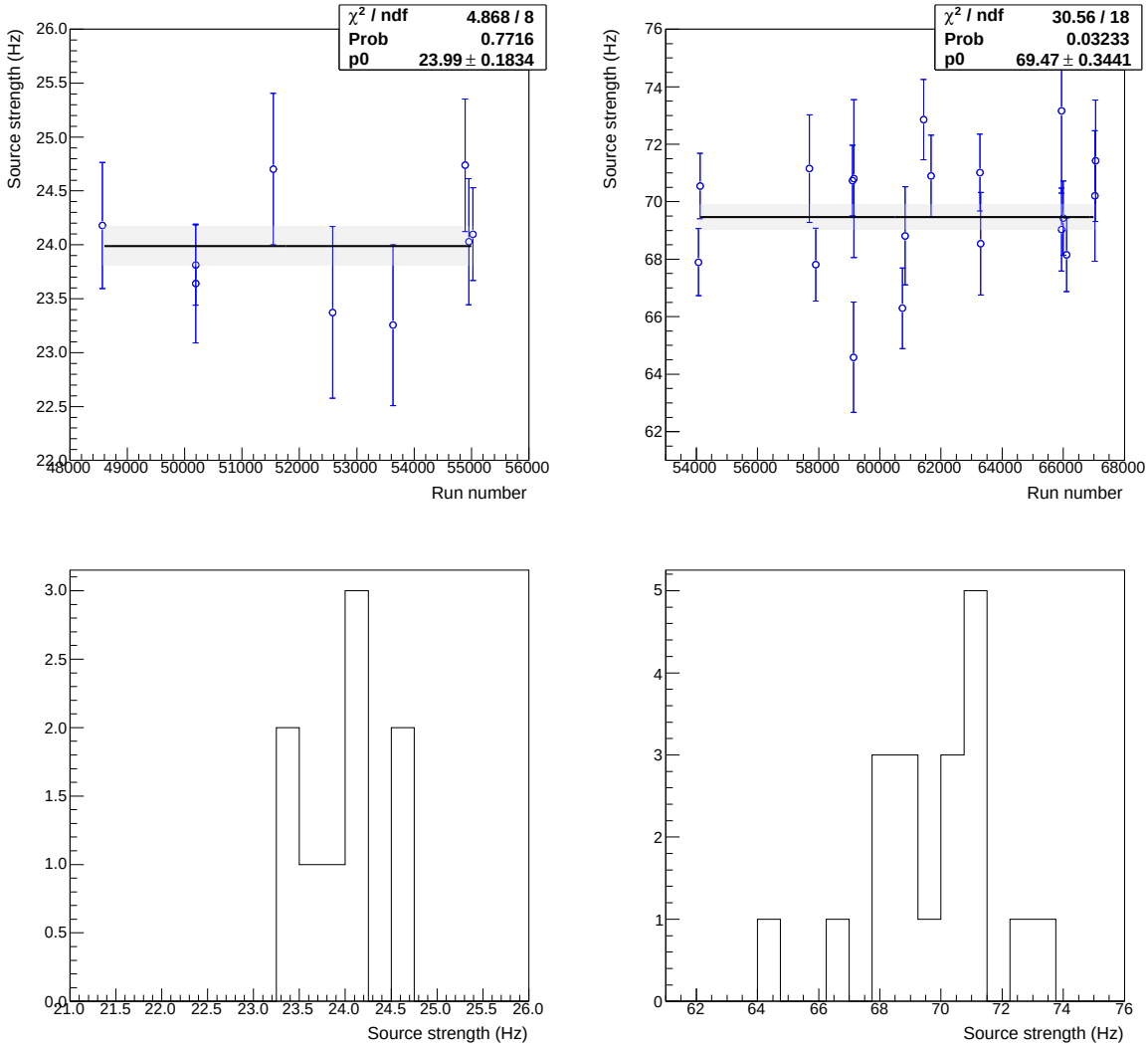

Figure 6.11: Source strengths as a function of run number (top) projected onto the y-axes (bottom). Medium rate source (left) and high rate source (right). Uncertainties are statistical only.

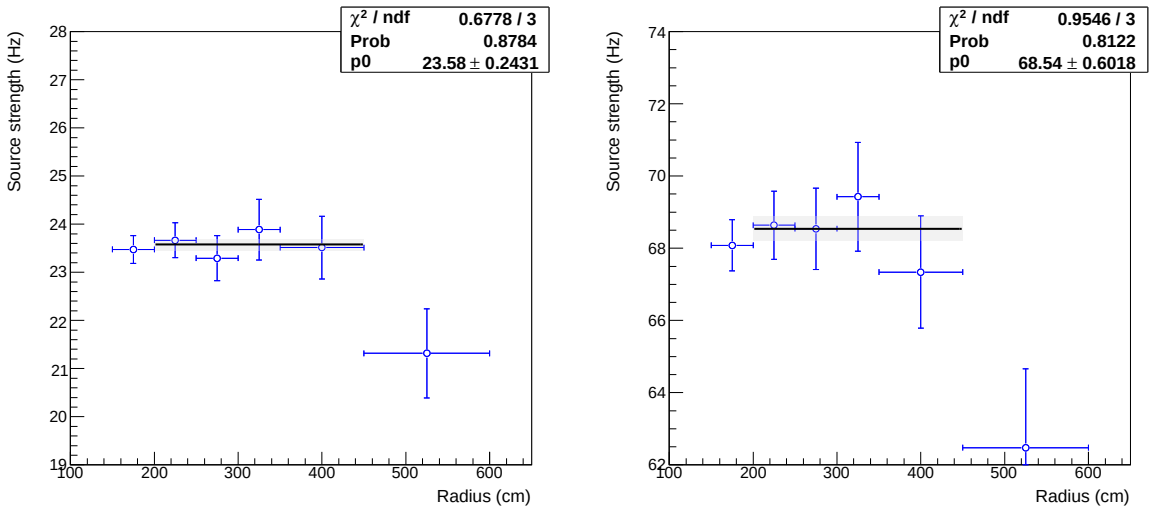

Figure 6.12: Source strengths as a function of radial bin. Medium rate source (left) and high rate source (right). Uncertainties are statistical only and the central values have been corrected with f_C.

6.4 Summary

In the chapter measurements of the strengths (neutron production rates) of the two ^{24}Na sources and the two AmBe sources used in the NCD phase have been reported. They are summarised in the table below, with errors symmetrised. Reference dates are given for the ^{24}Na sources as ^{24}Na has a half-life which is not long on the timescale of the experiment.

Source	Data set	Reference	Source strength (n s^{-1})		
		date / time	Value	Unc.	%
^{24}Na	2005	7/10/2005 12:37:00	1.284	0.067	5.2
^{24}Na	2006	2/11/2006 21:20:00	0.810	0.044	5.4
AmBe med			23.63	0.27	1.1
AmBe high			68.70	0.74	1.1

Chapter 7

The Neutron Detection Efficiency Using Point Sources

But there are also unknown unknowns - the ones we don't know we don't know.

A member of the US administration.
(2002)

The goal of this analysis was to make a theoretical prediction of the NCD NC neutron detection efficiency - the probability that an NC neutron produced in the heavy water was detected by the NCD array.

The prediction was made using a Monte Carlo simulation of the detector, tuned using AmBe point source neutron calibration data. The tunable parameter was the hydrogen concentration in the heavy water, referred to as the *hydrogen fraction*, on which there was a significant experimental uncertainty. The performance of the tuned Monte Carlo was evaluated by making comparisons between data and simulations with a larger set of point source data than were used for the tuning. The systematic uncertainty on the prediction of the detection efficiency was evaluated by propagating uncertainties on the Monte Carlo input parameters, including those relating to the isotopic composition of the heavy water and the detector geometry. This approach complemented the ^{24}Na measurement in a number of ways:

- *It was independent.*

  The point source method used a different set of calibration data and was therefore largely independent. The two methods acted as powerful checks of each other.

- *It did not depend on the strength of a calibration source.*

  It was not limited by the precision with which the strength of any particular calibration source was known; it relied instead on the high precision of MCNP and a detailed model of the detector geometry. As a theoretical number, it was limited only by the completeness of the model and the uncertainties on its input parameters. Point source data was used to tune the Monte Carlo in a relative way, such that source strengths cancelled.

  The absolute point source strengths were used only when testing the ability of the tuned Monte Carlo to reproduce the measured efficiencies. These tests were of the *consistency* of the data with the tuned Monte Carlo and *no uncertainty was applied based on the ability to make the comparison* (the degree of knowledge of the source strengths is one part of this uncertainty).

- *It had different systematics.*

  It did not suffer from the dominant systematic in the ^{24}Na measurement associated with the ability to demonstrate the uniformity of the source. There was an analogue, associated with the knowledge of the positions of the point sources used to tune the Monte Carlo, but it was more easily dealt with.

The first section of this chapter describes the point source data taken during the NCD phase and how it was analysed; the second section covers the tuning of the hydrogen fraction; the third evaluates the performance of the tuned Monte Carlo by making comparisons with calibration data; and the fourth describes the evaluation of NC efficiency and its systematic uncertainties. A final section describes the measurement of efficiencies for NC neutrons in the PMT array and for photodisintegration neutrons in the PMT and NCD arrays.

7.1 Point source data

7.1.1 Overview

This section describes the point source data taken during the NCD phase and how it was analysed for this study. The aim was to form a data set that was suitable for use in fitting the hydrogen fraction and for making comparisons between data and Monte Carlo. A set of source positions were identified and, for each of these, a representative average efficiency was evaluated, which could be compared with average simulated efficiencies generated for the same points.

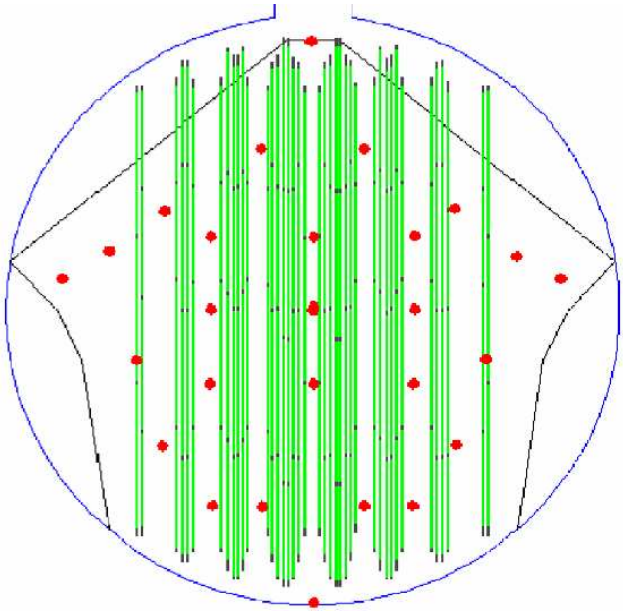

Figure 7.1: Source positions in one of the vertical planes (red dots) in a full AmBe scan [16].

7.1.2 The point source data

Point source calibration data was taken with AmBe and ^{252}Cf neutron sources. Most runs were taken with the AmBe sources because they were of much higher rate. This maximised statistics and reduced the amount of lost neutrino live time associated with neutron calibrations.

The sources could be positioned at various points on two perpendicular planes intersecting on the z-axis of the detector (see Figure 2.10). The manipulator system could not reach positions on the diagonals because the ropes would have become entangled with the array. Some runs at large absolute x and y had to be very long to ensure that a significant number of neutrons reached the counters of the inaccessible strings on the diagonals.

Sets of measurements taken with the AmBe sources, referred to as *scans*, were acquired on approximately a monthly basis; they were either *mini* scans, for which the source positions were selected to ensure that each *string* received a large number of counts, or full scans, which had larger numbers of source positions such that all *counters* received a large number of counts. The source positions in one plane for a full scan are shown in Figure 7.1.

Around 5% of the NCD phase detector live time was devoted to collecting AmBe neutron calibration data. Such a large amount of data was necessary so that significant

numbers of neutron events could be collected on each of the 156 counters on a regular basis. The data was used in a variety of studies on the neutron detection efficiency and response of the counters to neutron events.

^{252}Cf data were taken less frequently and in a smaller subset of positions, typically at, or towards, the centre of the array, though there was one comprehensive scan along the central z-axis of the detector. The ^{252}Cf runs were mainly used by the time series analysis (see Appendix D).

7.1.3 Run selection

A subset of 103 AmBe runs were selected for this analysis out of the several hundred taken during 13 scans in the NCD phase. The run selection criteria were:

- *AmBe runs only.*

  Only runs taken with the medium and high rate AmBe sources were selected. The ^{252}Cf data were lower rate, deployed less frequently and its burstiness generated dead time behaviour in the NCDs that was difficult to model.

  The strengths of the two AmBe sources were determined in Section 6.3. The dominant contribution to the strength of each source was that of the ^{252}Cf source, which they were calibrated with reference to. The uncertainties on the strengths of the two AmBe sources are therefore largely correlated and so, in this analysis, nothing was to be gained by treating them as distinct sources.

- *Good spatial and temporal coverage.*

  A set of source positions was identified that provided good spatial coverage of the array and a large number of runs at each position spread over time, providing a good temporal coverage. There were 7 source positions within the array at $(0, 0, 0)$, $(\pm 200, 0, 0)$, $(0, \pm 200, 0)$, $(0, 0, \pm 150)$ and 6 outside the array at $(0, 0, \pm 550)$, $(\pm 480, 0, 65)$, $(0, \pm 480, 65)$, making 13 positions in total. Selected runs typically lay within 5 cm of these positions. The source positions are shown in Figure 7.2 with the ID numbers that are referred to in this chapter.

- *One run in each position per scan.*

  A maximum of one run from each scan was included at each position to ensure relatively uniform statistics over time. If there was more than one run close to a given position in a given scan then the longer run was selected. Within the array

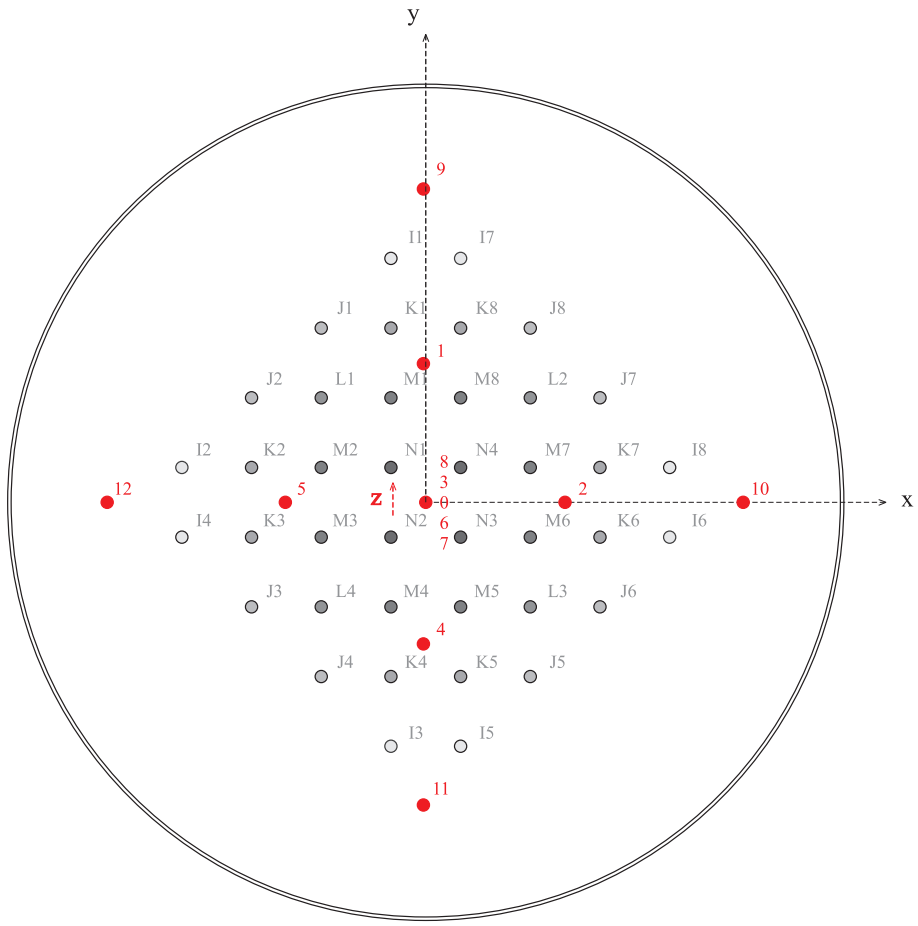

Figure 7.2: Source positions selected for use in this analysis (red dots).

there were at least 11 runs at all positions except $z = \pm 150$, which had only 2 each. There were fewer than 11 runs at positions outside the array

7.1.4 Source positions

The run selection process described above was carried out using source positions recorded by the manipulator system but source positions could also be fit using light generated by the sources. It was important to carefully gauge the uncertainties on the source positions because the neutron detection efficiencies of individual NCDs were very sensitive to the source-string separation. Within the array the sensitivity could be significantly reduced by considering groups of strings surrounding positions but this could not be done outside the array, where the knowledge of source positions was therefore particularly important.

- *Manipulator system positions.*

  Manipulator positions were taken from the central database of source runs maintained by the author. A model of the source position uncertainties was built with advice from Kraus [131]; it assigned no uncertainties to positions within the array, where the actual uncertainty was less than 1 cm, and outside the array applied an uncertainty of $\delta z = \pm 2.0$ to positions at $z = \pm 550$ cm and δx or $\delta y = \pm 2.5$ cm to positions at x or $y = \pm 480$ cm.

- *Fit positions.*

  The distribution of event positions about a source, reconstructed using light detected by the PMT array, had two components: one due to the gammas produced following neutron captures and one due to the prompt gammas produced by the source. In the x- and y-coordinates the sum of the distributions was symmetric but in the z-coordinate it was not, because the materials of the source were positioned only above the activity. The resultant bias meant that fit positions were only derived in the xy-plane - manipulator positions were always used for z-coordinates. Fits could not be used for positions at large absolute z because of the close proximity of the acrylic vessel and string ends, which interfered with the light.

  The positions, in each coordinate separately, were derived using unbinned likelihood fits of Gaussians to distributions of reconstructed event positions. Fits were performed over a range of ± 25 cm about the estimated source positions to focus the fits on the narrow peak of prompt gammas rather than the broad distribution of gammas from neutron captures.

  Uncertainties on fit positions were derived from the systematic uncertainties associated with the position reconstruction algorithm, which were a coordinate scale uncertainty of 0.6% and a coordinate offset uncertainty of ± 4 cm (see Section 8.4). For positions at large absolute x and y the radial scale systematic gave an uncertainty of δx or $\delta y = \pm 2.5$ cm and the position shift systematic gave an uncertainty of δx or $\delta y = \pm 4.0$ cm.

The effect of the source position uncertainties was evaluated by running simulations with the source systematically shifted to produce models of the variation of the efficiency with position. Two such models are shown in Figure 7.3. Source position systematic uncertainties are summarised in Table 7.1.

It was felt that the most robust source positions and uncertainties were obtained by using manipulator source positions within the array and at large absolute z; and fit source positions outside the array at large absolute x and y.

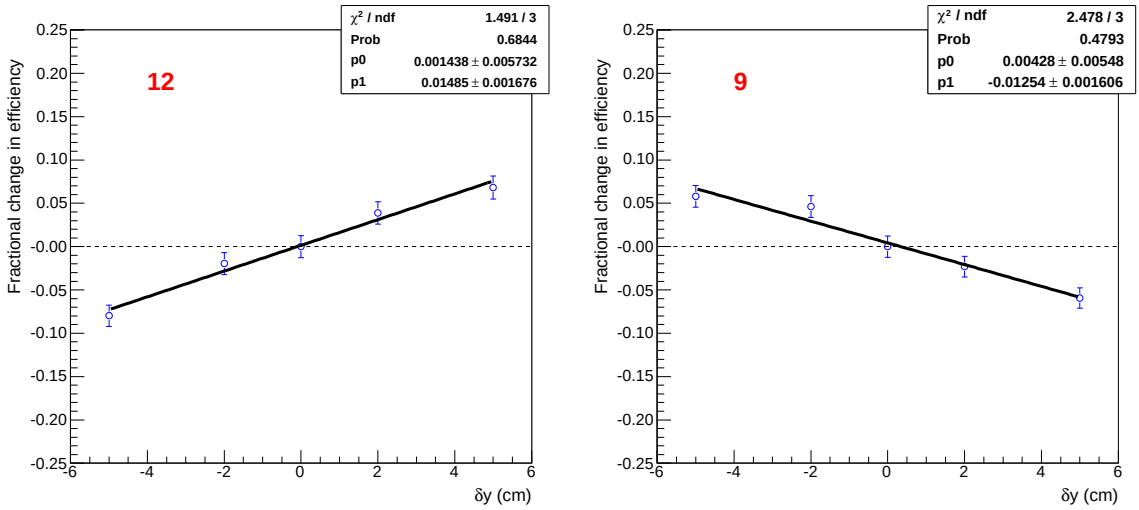

Figure 7.3: The dependence of neutron capture efficiency on source position for positions 12 and 9, which were the extreme positions in y. Simulations were generated using the OCA (see text) NCD array geometry.

Table 7.1: Source position systematic uncertainties for the source positions and coordinates to which they were applied. The uncertainties are those on the neutron detection efficiencies measured at each point resulting from the uncertainties on the source positions.

Posn.	Av. manip. posn. (cm)			Manip. sys.		Av. fit posn. (cm)			Fit sys.	
ID	x	y	z	Coord.	Unc. (%)	x	y	z	Coord.	Unc. (%)
7	-0.43	-1.04	-549.74	z	2.78					
8	0.81	-10.08	549.72	z	3.44					
9	-0.75	482.61	59.43	y	3.11	-1.21	485.83	60.13	y	6.10
10	478.76	-1.60	63.11	x	3.14	481.79	-0.61	65.58	x	6.15
11	-2.05	-481.77	63.25	y	2.47	-2.08	-482.17	62.11	y	4.84
12	-481.79	-0.31	64.95	x	3.71	-483.55	1.30	66.69	x	7.27

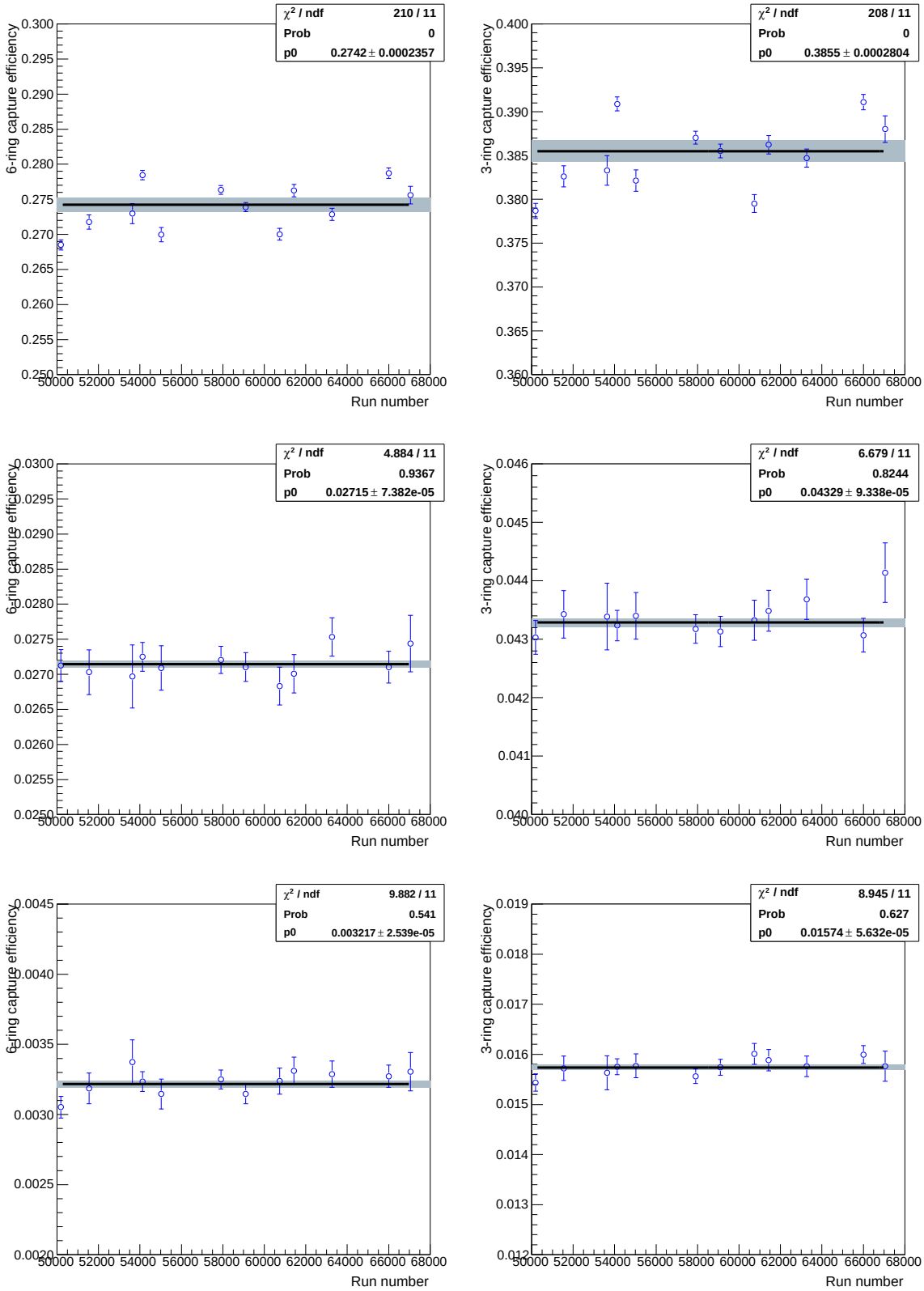

Figure 7.4: Representative examples of the measured efficiencies of different rings as a function of time. The data points are for central runs. The grey boxes indicate the fit uncertainties. 6-ring efficiencies are shown on the left (N, L and I rings) and 3-ring efficiencies on the right (N+M, L+K and J+I rings).

7.1.5 Detection efficiencies

String-by-string capture rates were calculated by [132] using the method described in Section 3.3.3. They were converted into efficiencies using the AmBe source strengths derived in Section 6.3. The following analyses were performed using the statistical components of the rate uncertainties; the correlated components were reintroduced, where appropriate, at the end of the analyses. The ^{4}He strings and the ^{3}He strings that were excluded from the neutrino analysis (see Section 8.2.4) were omitted.

The efficiencies measured at each source position were combined into a single data point for each position by averaging over time. For each position, the efficiency time series was fit to a straight line and the fit uncertainty was increased, where necessary, to give a reduced χ^2 of 1 (see Appendix B). This procedure generated a data point for each position that was averaged over the temporal variations and had an uncertainty that included them. Examples are shown in Figure 7.4.

7.1.6 Simulations

Monte Carlo simulations were generated for all positions at the weighted average manipulator source location and, for locations at large absolute x and y, also at the weighted average fit locations. The weights were equal to the estimated number of neutrons generated in each run ($live\ time \times source\ strength$). Simulations thus generated were suitable for comparison with the average data points for each position discussed above.

Simulations were generated separately using the NCD array geometry (string positions and orientations) extracted from the optical calibration data, referred to as the *OCA geometry* and that extracted using a laser range finder, referred to as the *LRF geometry* (see Section 4.3.2). Recall that the uncertainties on the OCA positions were estimated to be 50% of those on the LRF positions. Simulations were run separately, rather than for the average geometry, so that the effects of the uncertainty on the geometry could be propagated through the analyses - OCA and LRF were two independent measurements of the true geometry and the difference between the results obtained using them was a good estimate for the systematic uncertainty associated with the geometry.

7.2 The hydrogen fraction

7.2.1 Method

Point source neutron calibration data was used to tune the isotopic composition of the heavy water in the Monte Carlo in a way that was independent of the source strength. The particular method used was based on an idea by Robertson [133].

For each source position the relative neutron detection rates in rings of NCDs about the position were compared between data and Monte Carlo. The concentration of hydrogen in the heavy water - a parameter on which there was significant experimental uncertainty - was tuned in the Monte Carlo to get the best agreement between data and simulation. If the hydrogen fraction was low in the Monte Carlo then the neutron absorbing power of the heavy water would have been reduced and there would have been preferentially more captures on the outer rings, compared to the data. If it was high then there would have been preferentially less captures on the outer rings.

The ring efficiencies were derived by combining the string efficiencies into efficiencies for either 3 or 6 rings about each position; the hydrogen fraction fits were performed in both *3-ring* and *6-ring* versions. For source positions on the central axis the 6-rings matched the lettered rings I, ..., N in Figure 7.2 and the 3-rings were combinations of pairs of adjacent 6-rings. For source positions away from the central axis the rings groupings were determined by hand to give a reasonable distribution of statistics; the rings furthest away from these positions typically contained more strings than the ones closer. Only runs taken within the array were used in the tuning process because there the ring efficiencies were relatively insensitive to source positions.

The prediction for the neutron capture efficiency ε_r^{model} in ring r was given by

$$\varepsilon_r^{model}(\eta, f_H) = \eta \cdot g_r(f_H) \tag{7.1}$$

where r is the ring number, f_H is the hydrogen fraction, and η is the efficiency scale. The function $g_r(f_H)$ was constructed using Monte Carlo; f_H and η are defined as follows:

- *Hydrogen fraction (f_H).*

  This was the relative number density of H atoms, compared to D atoms, in the heavy water. It had a nominal value of 0.000982 ± 0.000050 [134]. f_H affected predictions for both the overall array efficiency and the relative efficiencies of different rings. Fits were performed with and without the nominal value applied as a constraint.

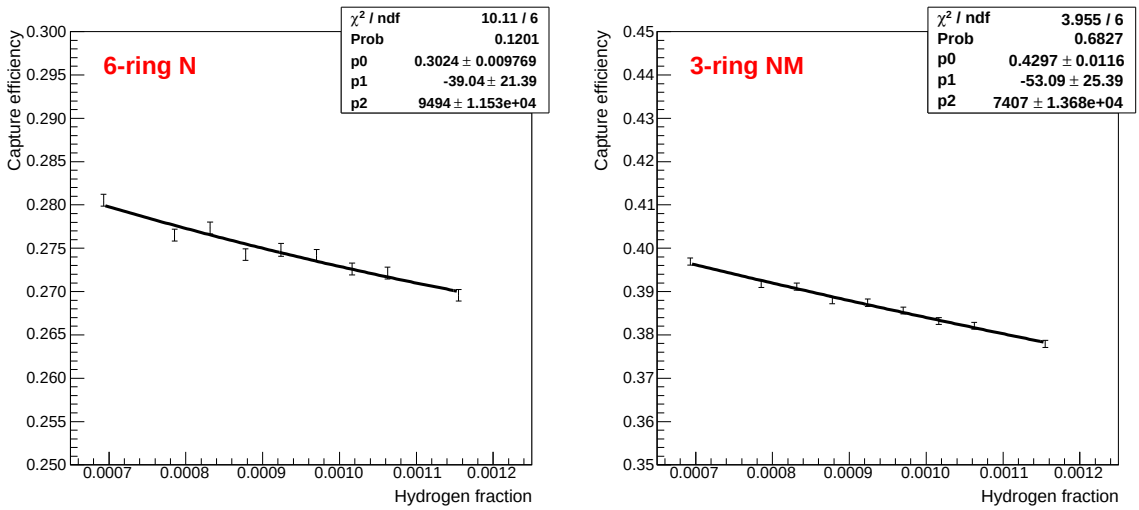

Figure 7.5: Example Monte Carlo models $g_r(f_H)$ showing ring efficiencies as a function of the hydrogen fraction. Simulations are for the central position and used the OCA geometry. The 6-ring efficiency for the N strings is shown on the left and the 3-ring efficiency for the N+M rings combined on the right.

- *Efficiency scale (η).*

  This was a scale or normalisation factor between data and Monte Carlo with a nominal value of 1.0. Effects causing it to deviate from 1.0 would be an error on the source strength, an error on the threshold, cut and data cleaning efficiencies, or a mis-modelling of the ^{3}He end regions. η affected predictions of the overall array efficiency but did not change the relative efficiencies of different rings.

The functions $g_r(f_H)$ were generated by running Monte Carlo at various values of f_H and fitting second order polynomials to the resultant efficiencies to allow interpolation.

Maximum likelihood fits were performed to extract the most likely values for f_H and η at each source position. The negative log-likelihood function was

$$L = -\ln \mathcal{L} = \frac{1}{2}\sum_r \left(\frac{\varepsilon_r - \varepsilon_r^{model}(\eta, f_H)}{\sigma_r} \right)^2 + \frac{1}{2}\left(\frac{f_H - \bar{f_H}}{\sigma_{\bar{f_H}}} \right)^2 \tag{7.2}$$

where ε_r are the data points, η and f_H are the fit parameters, and $\bar{f_H}$ and $\sigma_{\bar{f_H}}$ are the central values and uncertainty on the optional f_H external constraint. Example fits and residuals are shown in Figure 7.6.

The values of f_H and η for source positions within the array were averaged to give

Table 7.2: Results of hydrogen fraction tuning. The NC efficiencies are from Monte Carlo simulations run with the relevant fit hydrogen fractions. The uncertainty on the parameter η was not included in the uncertainty on the NC efficiency.

Geometry	Rings	f_H const.	Efficiency scale (η)		Hydrogen fraction (f_H)		NC efficiency	
			Val.	Unc.	Val.	Unc.	Val.	Unc.
LRF	3	no	0.9924	0.0218	0.0009205	0.0001456	0.2106	0.0037
		yes	0.9974	0.0153	0.0009337	0.0000940	0.2102	0.0012
	6	no	0.9863	0.0217	0.0008579	0.0001324	0.2106	0.0037
		yes	0.9845	0.0238	0.0008854	0.0001089	0.2115	0.0028
OCA	3	no	0.9904	0.0196	0.0008838	0.0001497	0.2116	0.0038
		yes	1.0019	0.0100	0.0009484	0.0000470	0.2100	0.0012
	6	no	0.9879	0.0153	0.0008875	0.0000973	0.2122	0.0035
		yes	0.9935	0.0111	0.0009204	0.0000616	0.2116	0.0024
LRF+OCA	3	no	0.9936	0.0202	0.0009068	0.0001381		
		yes	1.0018	0.0121	0.0009464	0.0000642		
	6	no	0.9863	0.0217	0.0008820	0.0001049		
		yes	0.9915	0.0183	0.0009115	0.0000804		

the final values and uncertainties. The uncertainties were scaled, where necessary, to give a reduced χ^2 of 1.

7.2.2 Results

Across all source positions the 3-ring fits were generally of higher quality than the 6-ring fits. In the 6-ring fits the larger residuals were for rings closer to the source. This was perhaps to be expected as the closest 6-ring to each position contained only 4 strings, which reduced the benefit of the averaging effect of combining strings. It was also the ring where the uncertainties on the source-string separations mattered most - a difference between the source positions in data and Monte Carlo of say 2 cm is considerably more important when the average source-string separation is 70 cm, as it is for the closest ring, rather than 2 or 3 m. In a 3-ring fit the nearest and next-nearest rings were combined into a single ring that increased the amount of averaging and improved the fit quality. Results from 3-ring fits were therefore preferred over those from 6-ring fits.

Fit values for f_H and η across all runs are shown in Figure 7.7 and the results, averaged over the source positions, are given in Table 7.2; in the OCA+LRF fit the OCA

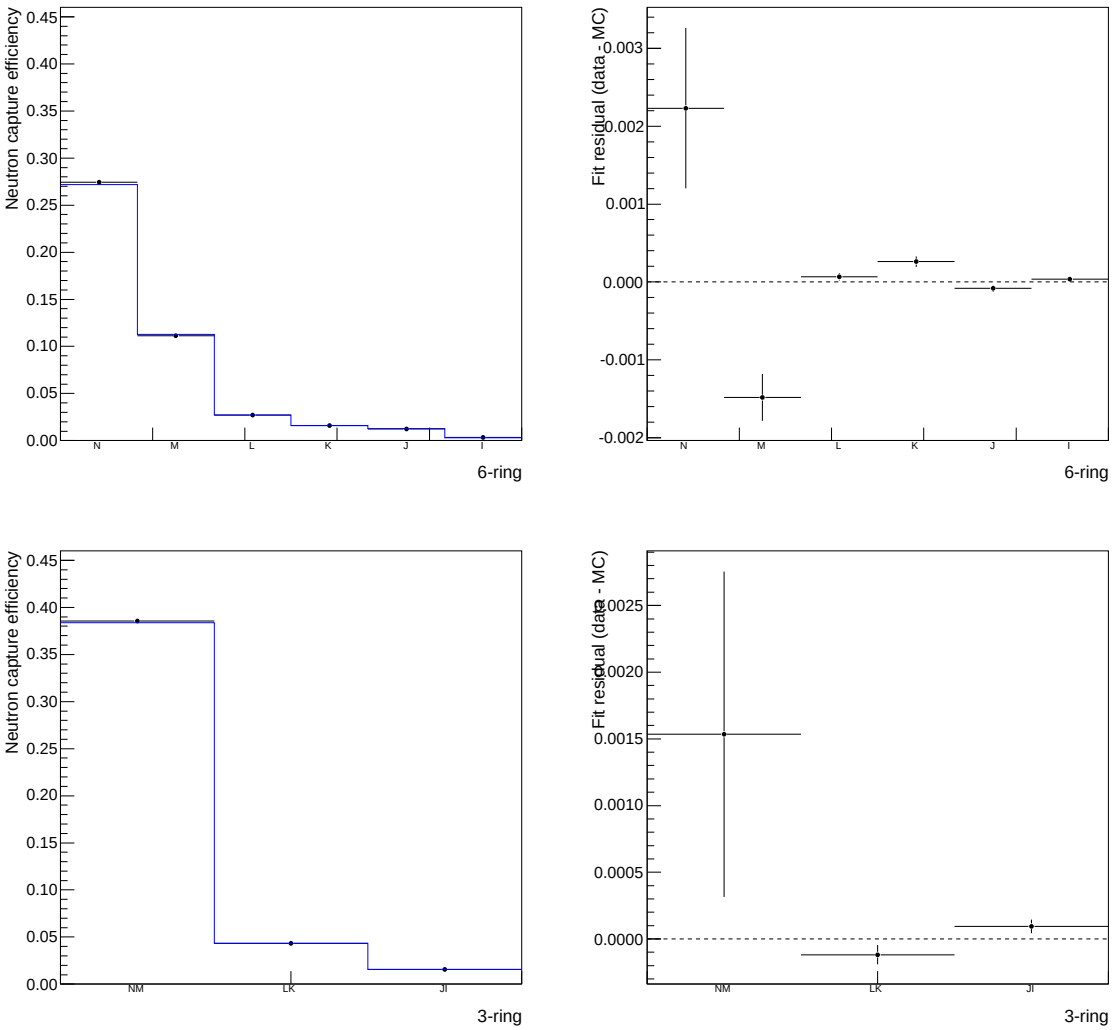

Figure 7.6: Example hydrogen fraction fits for the central source position using the OCA geometry. Shown are fit results (left) and residuals (right) for 6-rings (top) and 3-rings (bottom).

points were given twice the weight of the LRF points to reflect the better knowledge of the string positions and orientations. It was pleasing that in all fits the efficiency scale was consistent with 1 and that similar hydrogen fractions were fit with and without the external constraint applied as a penalty term in the likelihood.

The preferred values of the hydrogen fraction were those obtained using 3 rings, with the external constraint on the hydrogen fraction applied. They were 0.000934 ± 0.000094 for the LRF geometry and 0.000948 ± 0.000047 for the OCA geometry. The uncertainties are mainly due to the variations in fit hydrogen fraction from point to point around the array.

7.3 The quality of the Monte Carlo

The ability of the Monte Carlo to reproduce the results of point source calibration measurements was assessed by making comparisons for all 13 source positions (the 7 positions used to tune the hydrogen fraction and the 6 positions outside the array at large absolute x, y and z).

Figure 7.8 shows the ratio of the average measured array-wide efficiency to the average simulated array-wide efficiency as a function of source position. The plot shows the values obtained for the OCA and LRF geometries separately and splits the uncertainty on each point into its systematic and statistical components. The statistical uncertainties were primarily those on the data points rather than the simulations. The systematic uncertainties were due to the hydrogen fraction and, for points outside the array and at high and low z, due to the source position. The yellow band shows the correlated uncertainty on the data points due to the AmBe source strength uncertainties.

The ability to test the quality of the Monte Carlo using point source data outside the array was limited by the significant uncertainties on the source positions and consequent large systematic uncertainties on the Monte Carlo predictions. However, there was pleasing agreement within the array and consistency outside the array.

Figure 7.9 shows an additional test of the performance of the Monte Carlo using the TSA analysis (see Appendix D) applied to ^{252}Cf point source data taken on the central, vertical axis of the detector. There is again pleasing agreement between data and Monte Carlo.

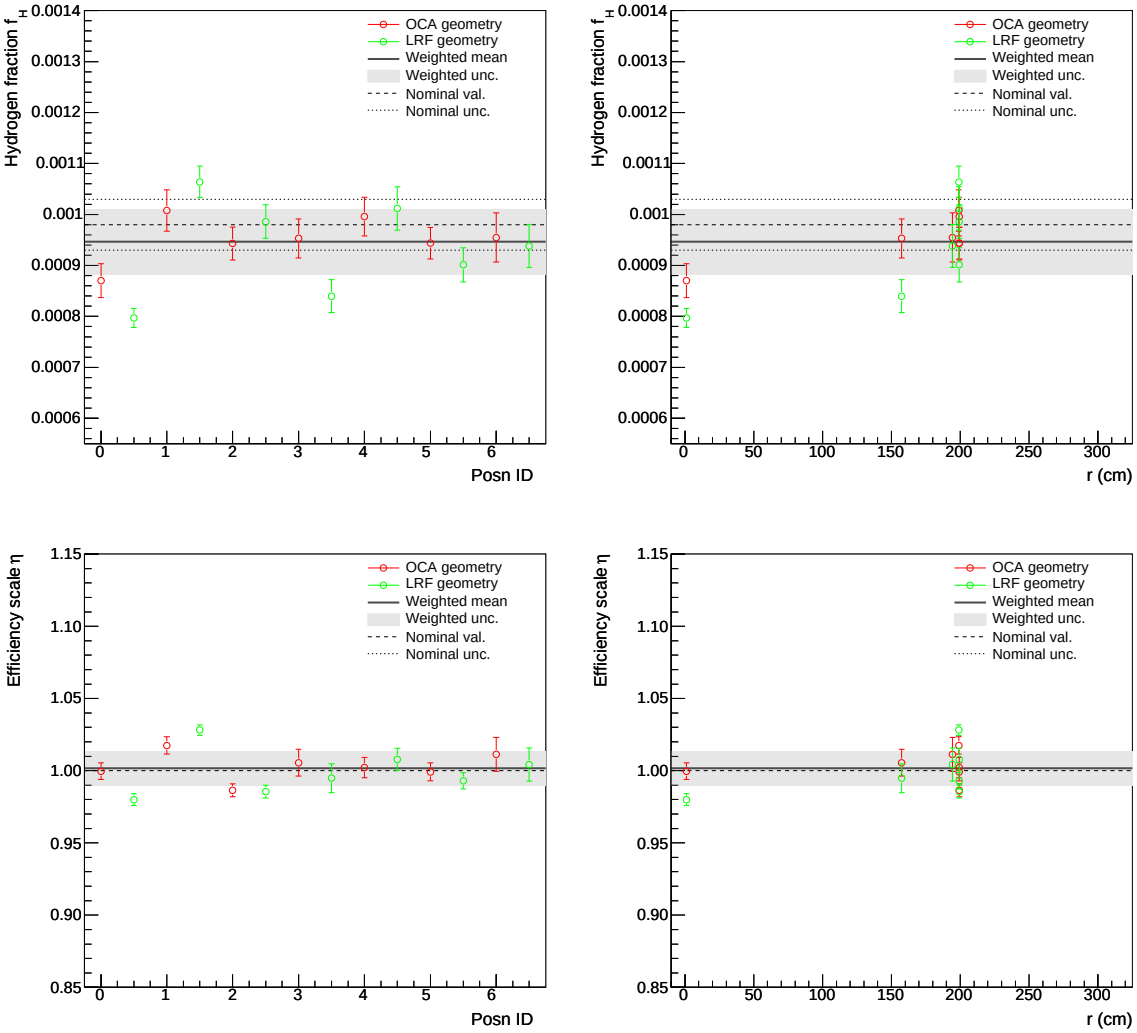

Figure 7.7: 3-ring fit hydrogen fractions (top) and efficiency scale (bottom) by fit number (left) and manipulator source radius (right).

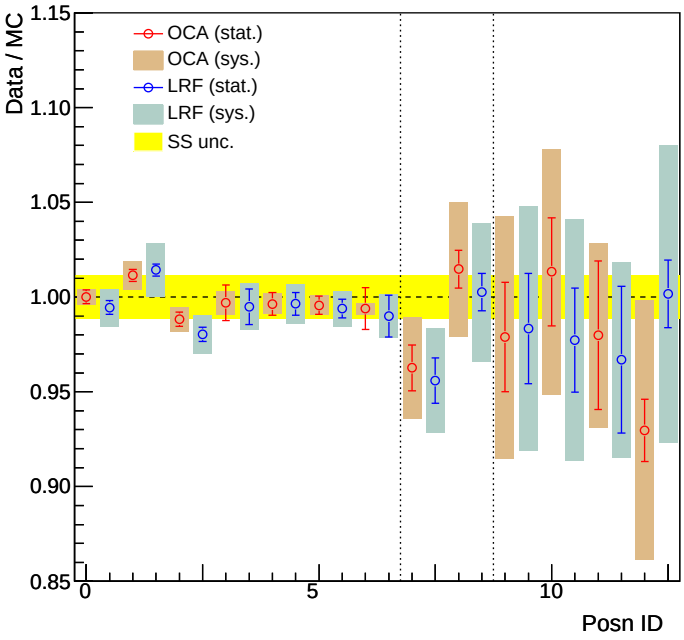

Figure 7.8: The ratio of measured to predicted efficiencies at 13 source positions. The left section contains the data points within the array, used to tune the hydrogen fraction. The middle section contains the points at the top and bottom of the array. And the right section contains points outside the array. The source positions for the left two sections are from the manipulator. Those in the right section are fit. The yellow bar gives the correlated uncertainty on the data due to the AmBe source strengths.

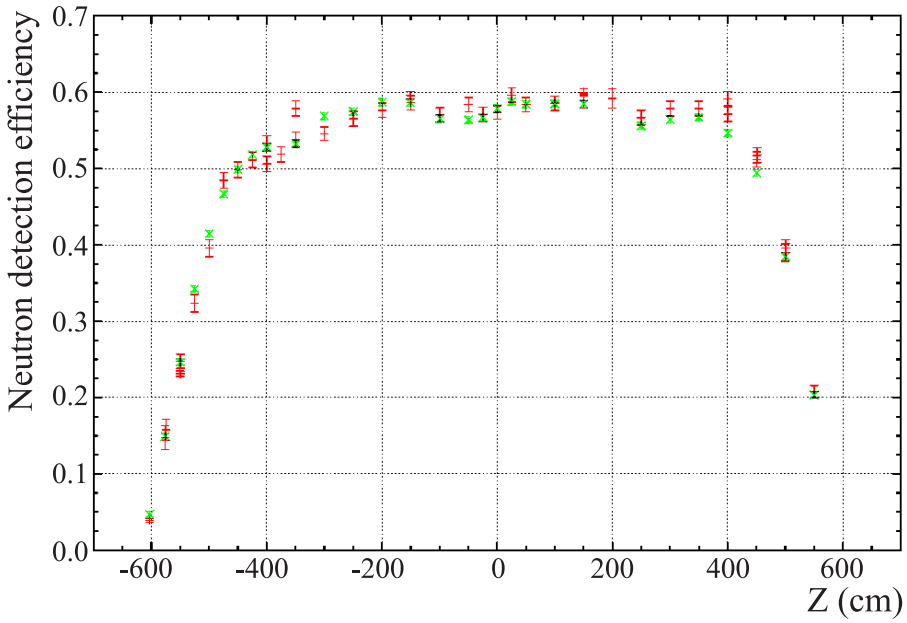

Figure 7.9: Comparison of ^{252}Cf source data (red points) and Monte Carlo (green points) along the central, vertical axis of the detector [17]. Efficiencies were determined using the TSA analysis (see Appendix D). The error bars are statistical only.

7.4 The NC neutron detection efficiency

7.4.1 Result

Models of the dependence of the NC neutron detection efficiency on hydrogen fraction, for the OCA and LRF geometries, were produced using Monte Carlo simulations. They are shown in Figure 7.10. They were used to calculate the NC efficiencies corresponding to the hydrogen fractions in Table 7.2.

The recommended value for the NC efficiency was taken to be the average of the efficiencies found using 3 rings with the OCA and LRF geometries. The result was 0.2101 ± 0.0012.

The uncertainty include statistics, the uncertainty on the NCD geometry and the uncertainty on the hydrogen fraction. It small magnitude reflects the small sensitivity of the efficiency to latter two effects. The following section considers additional systematic uncertainties that amount to 1.54% or 0.0032. The final NC neutron detection efficiency was found to be 0.2101 ± 0.0035.

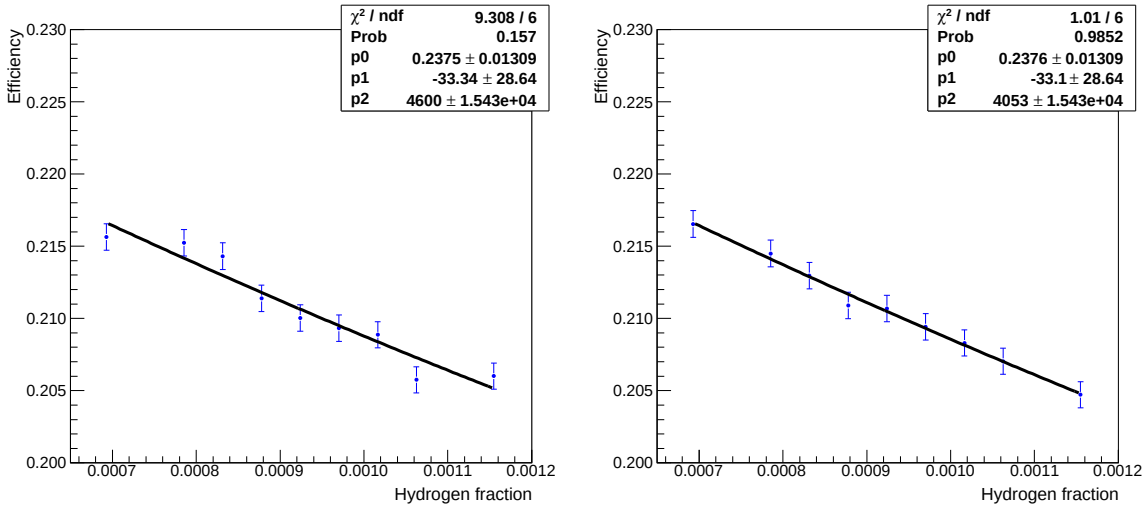

Figure 7.10: NC capture efficiencies as a function of hydrogen fraction for OCA geometry (left) and LRF geometry (right).

7.4.2 Systematic uncertainties

This section contains a list of systematic effects whose impact on the NC neutron detection efficiency was investigated. They are summarised in Table 7.3.

- *Hydrogen fraction and array geometry.*

  These were naturally taken into account in the procedure for fitting the hydrogen fraction, described above.

- *Acrylic vessel and light water.*

  Approximately 29% of NC neutrons were captured in the acrylic vessel and 6% in the light water and so it was important to investigate the quality of the modelling of these regions.

  The geometry of the acrylic vessel was modelled in the Monte Carlo in some detail. The most significant geometry parameter was the inner radius of the vessel, which was 600.50 cm in the Monte Carlo, close to the true value of 600.54 cm. The only significant omission was the simulation of the acrylic NCD anchor blocks but their collective volume was small and their effect on the neutron detection efficiency was expected to be negligible.

  The modelling of the material of the acrylic vessel as a potential source of uncertainty was studied by varying the density of hydrogen in the acrylic vessel in the Monte

Table 7.3: Systematic uncertainties on the Monte Carlo NC neutron detection efficiency.

Item	Unc. (%)
Hydrogen fraction (f_H) and string positions / tilts	0.57
AV modelling	~ 0.0
Number of deuterons	0.2
Counter dead regions	1.0
Counter Ni wall thickness	~ 0.0
Counter gas pressure	~ 0.0
^{3}He cross section	~ 0.0
Residual NaCl concentration	~ 0.0
NCD thresholds, data cleaning etc.	1.0
Total	1.54

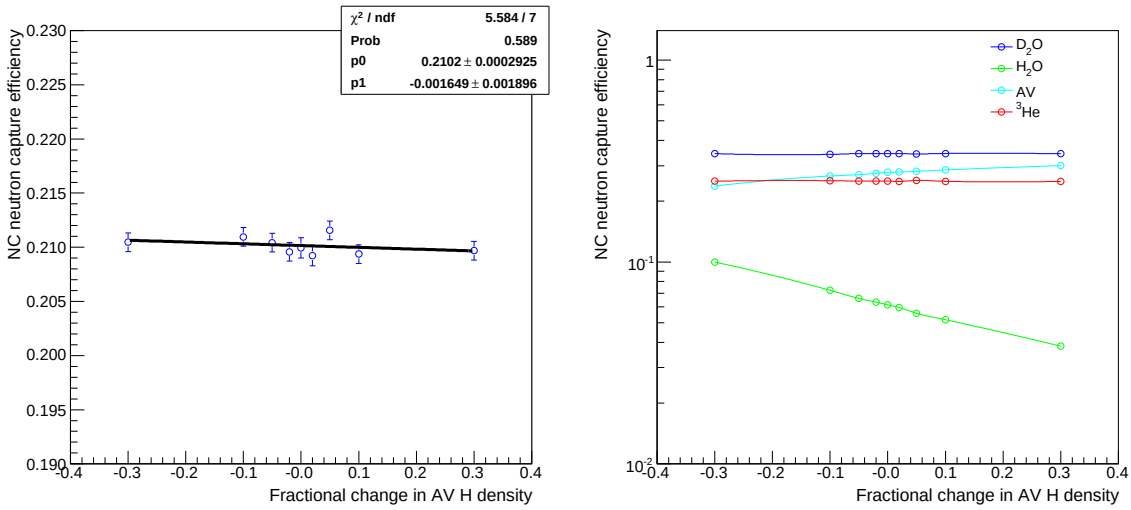

Figure 7.11: The effect of absorption in the acrylic vessel on the NC neutron capture efficiency. The parameter varied is the density of hydrogen in the acrylic vessel. The left hand plot shows the NC efficiency as a function of the change in density; the right hand plot shows the variation of captures in various geometry regions.

Carlo to simulate a change in the ability of the acrylic vessel to absorb neutrons. The results of these simulations are shown in Figure 7.11. The left hand plot shows the variation in the NC neutron capture efficiency as a function of fractional change in hydrogen density. A change in density of 30% resulted in a 0.02% change in efficiency, indicating that there was an extreme insensitivity to neutron-absorbing properties of the acrylic vessel. This was because the acrylic vessel and light water contained large amounts of hydrogen and so were very strongly absorbing; the main effect of varying the density was altering the depth the neutrons penetrated into the acrylic vessel, rather than the probability that they were captured, having entered the acrylic. This behaviour can be seen in the right hand plot of Figure 7.11, which shows that when the density increased the ^{3}He capture efficiency remained constant but the fraction of neutrons capturing in the light water (i.e. those passing all the way through the acrylic vessel) decreased. The modelling of the acrylic vessel was neglected as a source of uncertainty in the Monte Carlo.

Neutron propagation in the light water region was described by a dedicated ENDF table in MCNP [68] and it captured a relatively small fraction of neutrons. There was no reason to suspect any mis-modelling would have had any significant effect, so it too could be neglected as a source of uncertainty.

- *Counter end regions.*

  If the uncertainty on the size of the end regions was conservatively estimated at 50%, there would be an uncertainty on the active volume of ^{3}He gas, and therefore on the neutron detection efficiency, of 1%. This was taken as a systematic uncertainty.

- *Counter nickel wall thickness.*

  There was no significant uncertainty on the nickel wall thicknesses or on the overall mass of nickel in the detector. The thicknesses of the counter walls varied in the Monte Carlo based on measurements the masses and lengths of the nickel tubes from which the counters were constructed (see Section 4.3.2). The counter walls captured 2.2% of NC neutrons or around $1/10^{\text{th}}$ of the number capturing on ^{3}He; a 0.5% change in the ^{3}He capture efficiency would require an implausible error of $\sim 5\%$ in the mass of Nickel. No systematic uncertainty was assigned.

- *Counter gas pressure.*

  There was some variation in the pressure of the ^{3}He gas from counter to counter. The limit on this variation was derived from the tolerance on the counter gain of 3%. The gain of each counter was measured before deployment and if it fell outside this tolerance it had to be refilled. The gain was very sensitive to gas pressure and

Robertson [135] estimated that the gain tolerance of 3% was equivalent to a gas pressure tolerance of 0.5%.

The effect of such a change on the NC efficiency was expected to be negligible as the large ^{3}He cross section meant that the counters were effectively black to neutrons. A small change in the gas pressure would have changed the mean capture depth but would have had little effect on the efficiency.

A leak of ^{3}He gas from a counter would have been manifest as a change in gain of the counter or by the appearance of ^{3}He in the heavy water. No systematic gain changes were found and a ^{3}He detection system found no evidence of ^{3}He in the heavy water. The ^{3}He detection system, which was integrated into the existing water systems, searched for a mass-3 signal in exhaust gas from the D_2O degasser. It is described in more detail in [136].

No systematic uncertainty was assigned.

- *^3He cross section.*

  This was checked in Section 4.2.1 and found to be set correctly in the Monte Carlo. No systematic uncertainty was assigned.

- *Residual NaCl concentration.*

  This was considered in Section 4.2.2. The small effect of the residual salt concentration is likely to have been calibrated out by the hydrogen fraction tuning (the effect on neutron propagation would be indistinguishable from a slightly increased hydrogen fraction) and so no correction factor was applied. Likewise no systematic uncertainty was assigned.

- *Number of deuterons.*

  The density of the D_2O in the Monte Carlo was found to be too small by 1.3%. The effect of this on the detection efficiency is likely to have been tuned away by the hydrogen fraction fitting. Taking this into account Robertson [135] estimated a conservative uncertainty of 0.2%.

- *Threshold efficiencies, data cleaning etc.*

  The effect of the NCD threshold efficiencies and other inefficiencies on the NC efficiency was conservatively estimated by Guillian [132] to be 1%.

7.5 Other neutron detection efficiencies

Most of this thesis has been concerned with calculating the neutron detection efficiency for NC neutrons in the NCD array. The PMT efficiency for NC neutrons was also required as well as the PMT and NCD efficiencies for all classes of background neutron. These efficiencies were less important, and therefore given less attention, because of the small number of neutrons detected in each case and, for the backgrounds, the large uncertainties on the numbers of neutrons produced in the detector.

Efficiencies were taken directly from Monte Carlo and systematics assigned based on the result for NC neutrons in the NCD array. The systematic on the NCD efficiencies was taken to be the same as the uncertainty on the NC NCD efficiency (1.54%). The systematic on the PMT efficiencies was 1.17%, which was the part of the NCD systematic that did not relate directly to detection (as opposed to capture) of neutrons by the NCD array; the main contribution removed was the one due to the size of the NCD end regions. Systematic uncertainties associated with energy reconstruction, position reconstruction, cut acceptance etc. were naturally handled in the fits to extract the neutrino fluxes described in the next chapter. The results were:

Background	PMT eff.		NCD eff.	
	Value	Unc.	Value	Unc.
K2 PD	0.0641	0.0008	0.2603	0.0047
K5 PD	0.0700	0.0009	0.3039	0.0054
Bulk PD	0.0595	0.0010	0.4095	0.0071
NC	0.0485	0.0006		

The efficiencies for the acrylic vessel (α,n) neutrons and others originating at or near the acrylic vessel were evaluated in a separate study by [61].

7.6 Summary

This chapter has described theoretical determinations of the neutron detection efficiencies for neutrons from various sources in the PMT and NCD arrays. The NCD NC neutron detection efficiency was found to be

$$0.2101 \pm 0.0035$$

where the systematic contributions to the uncertainty are given in Table 7.3. The non-NCD-non-NC efficiencies are given in the table above.

Chapter 8

Measuring the NC flux

If your experiment needs statistics, you ought to have done a better experiment.

ERNEST RUTHERFORD

This chapter describes the statistical extraction of the ^{8}B solar neutrino fluxes from the NCD phase data. A maximum likelihood technique was used to estimate the numbers of neutrino candidate events that were due to neutrino interactions (CC, ES or NC) and backgrounds. Events were described by a set of observable parameters, such as event energy or radius, and the data were fit to a combination of probability distribution functions (PDFs) for each of the signals in each of the observables. PDFs were constructed using Monte Carlo or calibration data.

The numbers of events belonging to each class of background were constrained in the fit by external measurements. Systematic uncertainties, such as neutron detection efficiencies, which were also constrained by external measurements, were either allowed to float in the fit, as nuisance parameters, or the fit was repeated with the parameters set to the positive and negative $1\,\sigma$ limits allowed by the external measurements. Where possible, systematic uncertainties were floated, as this allowed the data to constrain their values and allowed central values to move within their constraints.

This chapter begins with the maximum likelihood method and the particular formalism used in this analysis. Following this is a description of the way that the systematic uncertainties were handled and of the analysis code. Finally the results are presented - the neutrino fluxes and the inferred solar neutrino mixing parameters.

8.1 Fitting using maximum likelihood

8.1.1 Overview

The maximum likelihood technique is a procedure for estimating model parameters. It is widely used because of its simplicity and ideal asymptotic behaviour - in the limit of a large number of data points uncertainties on fit parameters take their smallest possible values and fits are unbiased [137].

The data is described by a set of *observables* and the model parameter values are those which maximise the probability of the observed data. Parameter uncertainties are assigned using the variation of the probability with parameter value about the best fit point, with all other parameters unconstrained.

In this analysis the neutrino data were described as a sum of CC, ES, NC and background events. Each of these classes of event is referred to as a *signal*; the fit parameters were the numbers of events (or equivalently fluxes) corresponding to each signal. The observables were quantities measured by SNO, such as event energy.

8.1.2 The NCD phase formalism

The likelihood function $\mathcal{L}$ is given by

$$\mathcal{L} = \prod_{d=1}^{N_d} f(\bar{x_d}; \bar{\theta}) \tag{8.1}$$

where N_d is the number of data events and $f(\bar{x_d}; \bar{\theta})$ is the PDF giving the probability of measuring observable values $\bar{x_d}$, given a set of parameters $\bar{\theta}$. The best fit parameters are those which maximise $\mathcal{L}$.

In this analysis the PDF was given by

$$f(\bar{x_d}; \bar{\theta}) = \sum_{s=1}^{N_s} \frac{n_s}{N_d} f_s(\bar{x_d}) \tag{8.2}$$

where N_s is the number of signals, n_s is the number of data events belonging to signal s, N_d is the number of events in the data set, and $f_s(\bar{x_d})$ is a PDF obtained from Monte Carlo or calibration data, which gave the probability of measuring $\bar{x_d}$ for signal s. Substituting

Eq. (8.2) into Eq. (8.1) gives

$$\mathcal{L} = \prod_{d=1}^{N_d} \sum_{s=1}^{N_s} \frac{n_s}{N_d} f_s(\bar{x_d}) \tag{8.3}$$

The total number of events N_d is distributed about the expected number of events μ_0 according to Poisson statistics. The probability of observing N_d given μ_0 can be included in the likelihood function in what is known as the extended maximum likelihood method. Eq. (8.3) becomes

$$\mathcal{L} = \frac{\mu_0^{N_d} e^{-\mu_0}}{N_d!} \prod_{d=1}^{N_d} \sum_{s=1}^{N_s} \frac{n_s}{N_d} f_s(\bar{x_d}) = \frac{e^{-\mu_0}}{N_d!} \prod_{d=1}^{N_d} \mu_0 \sum_{s=1}^{N_s} \frac{n_s}{N_d} f_s(\bar{x_d}) \tag{8.4}$$

Rather than maximise $\mathcal{L}$ it is conventional to minimise the negative log-likelihood $L = -\log \mathcal{L}$. The logarithm is introduced because likelihoods can take large absolute values and the minus sign because widely used codes minimise rather than maximise functions. Taking the negative logarithm of Eq. (8.4) gives

$$L = -\sum_{d=1}^{N_d} \log \left(\sum_{s=1}^{N_s} \mu_0 \frac{n_s}{N_d} f_s(\bar{x_d}) \right) + \mu_0 + \log(N_d!) \tag{8.5}$$

The expected number of events μ_s of signal s can be written

$$\mu_s = \mu_0 \frac{n_s}{N_d} \tag{8.6}$$

such that

$$\mu_0 = \sum_{s=1}^{N_s} \mu_s \tag{8.7}$$

Substituting these into Eq. (8.5) gives

$$L = -\sum_{d=1}^{N_d} \log \left(\sum_{s=1}^{N_s} n_s f_s(\bar{x_d}) \right) + \sum_{s=1}^{N_s} n_s \tag{8.8}$$

where the constant term in N_d has been omitted.

If external measurements provide constraints on any of the fit parameters then constraint terms may be added to the likelihood. Eq. (8.8) becomes

$$L = -\sum_{d=1}^{N_d} \log \left(\sum_{s=1}^{N_s} n_s f_s(\bar{x_d}) \right) + \sum_{s=1}^{N_s} n_s - \frac{1}{2} \sum_{p=1}^{N_p} \left(\frac{\lambda_p - \bar{\lambda_p}}{\bar{\sigma_p}} \right)^2 \tag{8.9}$$

where $\bar{\lambda_p}$ is the central value of the Gaussian constraint on parameter λ_p and $\bar{\sigma_p}$ is its width. Constraints may also be applied to parameters used when forming the PDFs $f_s(\bar{x_d})$, such as the energy scale, or in the conversion of fluxes into numbers of events, such as neutron detection efficiencies.

It was physically interesting to make no assumption on the energy spectra of CC and ES events, which was equivalent to making no assumption on the ^{8}B neutrino energy spectrum. The number of events in each energy bin was treated as an independent fit parameter and the probability inside each energy bin taken to be constant. This type of fit is referred to as an *unconstrained* fit. The PDF $f(\bar{x_d};\bar{\theta})$ becomes

$$f(\bar{x_d};\bar{\theta}) = \sum_{s=CC,ES}\left(\sum_{i=1}^{N_{spec}} n_{si} f_{si}(\bar{x_d})\right) + \sum_{s\neq CC,ES} n_s f_s(\bar{x_d}) \tag{8.10}$$

where N_{spec} is the number of CC and ES spectral bins. The negative log-likelihood L is modified accordingly.

In this analysis there were two data streams from largely independent detectors - the PMT and NCD arrays. Some signals were unique to each detector, such as CC neutrino events in the PMTs and alpha backgrounds in the NCD, while others could be recorded by both detectors, such as NC and photodisintegration background neutrons. With two data streams the negative log-likelihood becomes

$$L = L_{PMT} + L_{NCD} \tag{8.11}$$

$$L_{PMT} = -\sum_{d=1}^{N_d}\log\left(\sum_{s=1}^{N_s} n_s f_s(\bar{x_d})\right) + \sum_{s=1}^{N_s} n_s - \frac{1}{2}\sum_{p=1}^{N_p}\left(\frac{\lambda_p - \bar{\lambda_p}}{\bar{\sigma_p}}\right)^2 \tag{8.12}$$

$$L_{NCD} = -\sum_{d=1}^{N'_d}\log\left(\sum_{s=1}^{N'_s} n'_s f'_s(\bar{x_d})\right) + \sum_{s=1}^{N'_s} n'_s - \frac{1}{2}\sum_{p=1}^{N'_p}\left(\frac{\lambda'_p - \bar{\lambda'_p}}{\bar{\sigma'_p}}\right)^2 \tag{8.13}$$

where the unprimed quantities refer to to the PMT stream and primed quantities to the NCD stream. When a pair of event classes have a common source, the event numbers n_i and n'_i are not independent and are related by

$$n_i = F_i \times S_i \times E_i \tag{8.14}$$

$$n'_i = F_i \times S'_i \times E'_i \tag{8.15}$$

where E_i and E'_i are the numbers of events expected to be observed in each stream, given predictions for the source production rate and detector response; S_i and S'_i are corrections

Table 8.1: Summary of signals included in the fit. The last two columns indicate whether the signal is present in the PMT and NCD streams. PD stands for photodisintegration.

Type	Name	Events	Data	
			PMT	NCD
Physics	CC	CC neutrino	yes	
	ES	ES neutrino	yes	
	NC	NC neutrino	yes	yes
Neutron backgrounds	AV	AV (α,n) + H_2O PD n	yes	yes
	K2 PD	K2 hotspot PD n	yes	yes
	K5 PD	K5 hotspot PD n	yes	yes
	NCD PD	NCD Ni PD n + (α,n)$^{17/18}$O	yes	yes
	Uniform	D_2O PD n	yes	yes
	n-like	Atmos. ν + NCD cable PD n + ^{16}N	yes	yes
NCD-only backgrounds	Alphas	Alphas from NCD components		yes
	J3	J3 instrumentals		yes
	N4	N4 instrumentals		yes

to E_i and E_i' to account for the change in the expected number of events after application of a shift in a systematic parameter; and F_i is the fraction of the expected number of events observed. In general, it is the quantities F_i, referring to fluxes or source terms, which are fit for, rather than numbers of events.

Uncertainties on fit parameters are defined as the variations in parameter values that cause increases in the negative log-likelihood of 0.5. For example, the uncertainty δn_s on n_s is defined by

$$L(n_s \pm \delta n_s) = L(n_s) + 0.5 \tag{8.16}$$

8.2 Probability distribution functions

8.2.1 Signals and backgrounds

A list of the signals included in the likelihood function is given in Table 8.1. They were grouped into three categories:

- *Physics signals.*

Table 8.2: Neutron detection efficiencies.

Signal	PMT		NCD	
	Val.	Unc.	Val.	Unc.
NC	0.0485	0.0006	0.211	0.007
AV	0.0068		0.0113	
K2	0.0641	0.0008	0.2603	0.0027
K5	0.0700	0.0009	0.3034	0.0027
Bulk	0.0595	0.0010	0.4095	0.0032
Uniform	See NC		See NC	

The physics signals were events due to CC, ES and NC neutrino interactions. CC and ES events were detected by the PMT array and NC events by both the PMT and NCD arrays. All signals were fit as solar neutrino fluxes, which were converted into numbers of events using Eq. (8.14) and Eq. (8.15), to allow the likelihood function to be evaluated.

- *Neutron and neutron-like backgrounds.*

  There were three main sources of neutrons in the detector, other than NC interactions: deuteron photodisintegration by gammas from U and Th in the H_2O, D_2O, bulk materials of the NCD array, the acrylic vessel, the two NCD hotspots and the NCD cables; (α,n) reactions in the acrylic vessel; and interactions of atmospheric neutrinos in the D_2O. These produced events in both the PMT and NCD arrays.

  In addition, there were two non-negligible sources of neutron-like events in the PMT array only: the decay of ^{16}N produced in the reactions $^{16}O(\mu^-,\nu_\mu)^{16}N$ and $^{16}O(n,p)^{16}N$; and atmospheric neutrino interactions other than those producing neutrons.

  In previous SNO analyses most neutron and neutron-like backgrounds were deducted from the fit number of NC events, but because there were two detectors in the NCD phase they now had to be included in the fit. This was because, for some of the backgrounds, the relative event rates between the detectors and radial distributions differed from NC neutrons. The differences in radial profiles were not large enough to allow the data to help significantly in distinguishing the backgrounds from each other, or from NC neutrons, but they had the potential to bias the fit results.

  The backgrounds were divided into 6 groups, each containing backgrounds with similar detection efficiencies and with similar distributions in the observables. In

the first 5 in Table 8.1 (AV to Uniform) the fit parameter was the number of neutrons produced during the NCD phase, which was related to the number of events detected by the detection efficiencies in Table 8.2. A final group contained minor neutron backgrounds and neutron-like events; because these had varying detection efficiencies (or none at all in the case of the neutron-like events) the numbers of events detected by the PMT and NCD arrays were treated as two independent fit parameters. A constraint was placed in the likelihood function on the number of events produced in the detector by each group.

- *NCD-only backgrounds.*

  This category consisted of backgrounds internal to NCD counters, which were alphas and the instrumental events identified on strings J3 and N4. Each had its own PDF and fit parameter - the number of events detected. No constraints were placed on the numbers of events detected, even though such constraints were available (see, for example [138] and [139]). The constraints on the numbers of J3 and N4 instrumentals were not applied because they came largely from the neutrino data set and were thus not independent. The constraints on the number of alphas came mainly from fits at high energies around the Po peak but the model of the alpha energy spectrum was not felt to be robust enough to extrapolate the constraints down to the neutron region.

8.2.2 Observables in the PMT array

There were three observables in the PMT stream:

- *Energy (T_{eff}).*

  The first PMT observable was effective kinetic energy T_{eff}. This was the total energy returned by the RSP energy estimator minus the electron mass. It was binned in 13 bins between 6 and 20 MeV, and is shown, along with the other PMT observables, in Figure 8.1. Energy was little use in distinguishing between different classes of event because no assumption was made on the CC and ES energy spectra; the 13 bin values for CC and ES were separate parameters in the fit.

- *Direction ($\cos\theta_{\odot}$).*

  The second observable was the cosine of the reconstructed event direction with respect to the Sun, $\cos\theta_{\odot}$, calculated using the FTN event reconstruction algorithm.

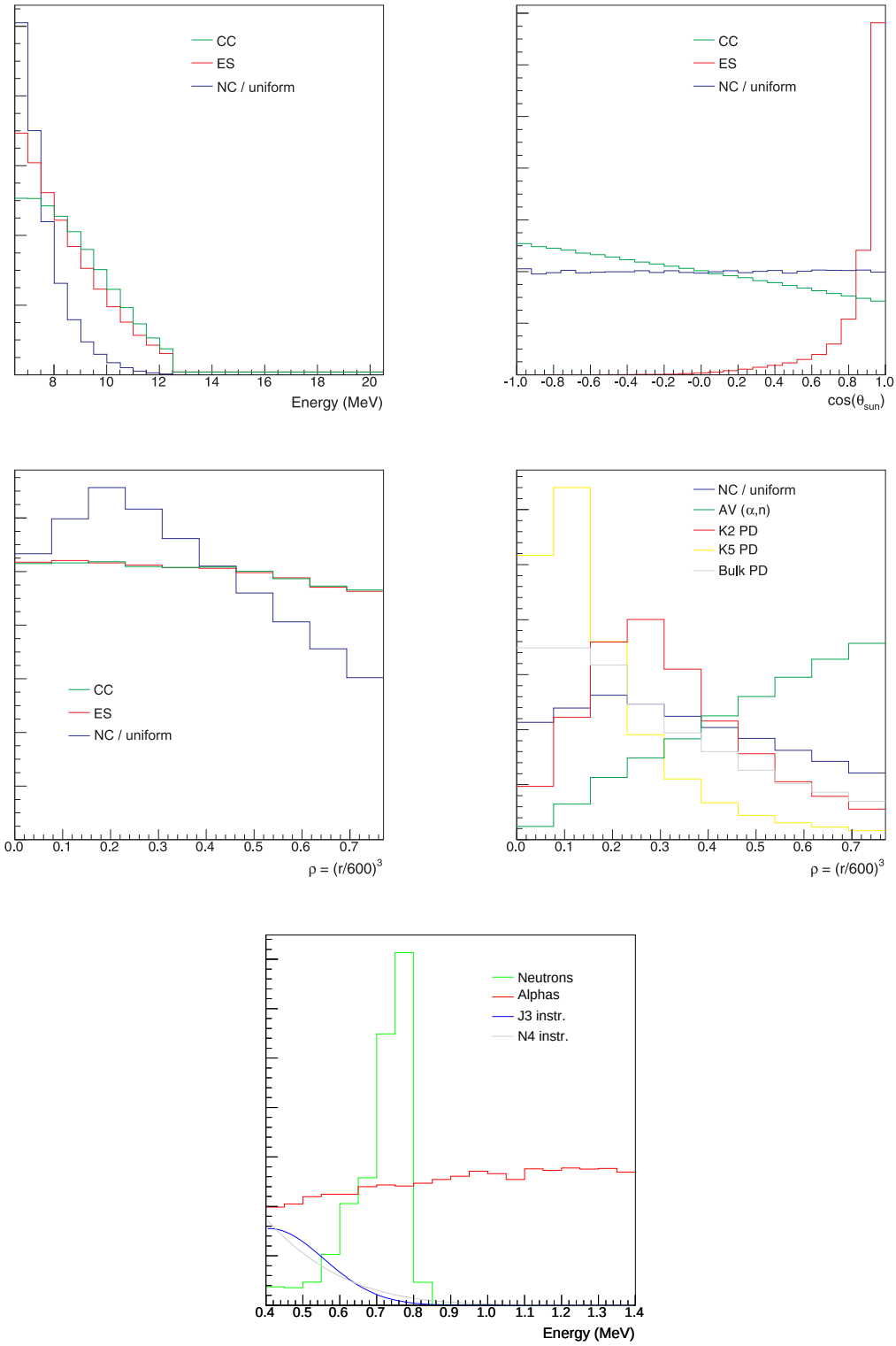

Figure 8.1: Signal PDFs. The distributions in the PMT observables for CC, ES and NC are shown in energy (top left), cosine of reconstructed direction with respect to that of the Sun (top right) and radius (centre left). Note that the shapes of the energy PDFs for CC and ES events were allowed to float in the fits. The background radial distributions are shown centre right. The bottom plot shows the distributions in the NCD observable shaper-ADC energy. Normalisations should be considered arbitrary.

Table 8.3: High level cuts.

Stream	Parameter	Cut
PMT	T_{eff}	$6 < T_{eff} < 20$
	ρ	$0 < \rho < (\frac{550}{600})^3$
	$\cos\theta_\odot$	$-1.0 < \cos\theta_\odot < 1.0$
	β_{14}	-0.12 $< \beta_{14} <$ 0.95
	ITR	$ITR > 0.55$
NCD	E_{ADC}	$0.4 < E_{ADC} < 1.4$
	String	Cut ^{4}He strings 3, 10, 20, 30
		Cut bad strings 0, 1, 8, 18, 26, 31 [140]

It was binned in 25 bins between -1 and 1. $\cos\theta_\odot$ placed a strong constraint on the number of ES events.

- *Radius (ρ).*

  The third observable was event radius in the form of the radial parameter $\rho = (r/r_{AV})^3$, where $r_{AV} = 600$ cm was the nominal radius of the acrylic vessel. ρ was binned in 10 bins from 0 to $(550/r_{AV})^3$. The volume within 550 cm is known as the fiducial volume. ρ provided some ability to distinguish NC from CC and ES events - the former had a non-uniform distribution because the NCD array mainly absorbed neutrons at small radii and the acrylic vessel at larger radii.

PMT PDFs were generated using binned Monte Carlo events. The overall PMT PDF was factorised into two parts

$$f(T_{eff}, \cos\theta_\odot, \rho) = f(T_{eff}, \rho) \times f(\cos\theta_\odot)$$

The reason that a full 3 dimensional PDF was not used was to increase the number of PDF events in each bin. This was desirable because it reduced the potential for fit biases by reducing the effect of statistical fluctuations on the PDF shapes. For example, moving from 3D to 2D×1D increased the average number of events per bin in the NC PDF (the physics signal with the least statistics) from 60 to 1500. However, any factorisation of this sort did have the potential to *introduce* a bias because the PDF then explicitly neglected the correlations between some of the observables. Tests (see Section 8.5.2) were performed to establish that correlations between $\cos\theta_\odot$ and either T_{eff} or ρ did not cause biases in the fit fluxes.

8.2.3 Observables in the NCD array

There was a single observable in the NCD stream:

- *Energy (E_{ADC}).*

  The NCD observable was shaper-ADC energy E_{ADC} in which neutrons, alphas, J3 and N4 instrumentals had different distributions. The energy range was from 0.4 to 1.4 MeV in 20 bins. This range included the neutron peak and a region above ~ 0.8 MeV where there were no neutron events.

  The lower energy cut resulted in sacrifice of the 6% of neutron events occurring below 0.4 MeV but the loss of statistics was more than compensated for by removing the need to model the alpha spectrum down to these energies. An added advantage was that it excluded the region where most J3 and N4 instrumental events occurred; the energy spectrum of these events was difficult to model.

  The region above 0.8 MeV was included to provide information on the alpha background, which helped constrain its magnitude underneath the neutron peak. The reason alpha events above 1.4 MeV were not included, even though they would have provided more statistics for the constraint, was because of the demands it would have placed on the ability to model the alpha spectrum over a large energy range.

Neutrons for all sources had identical energy spectra and so the NCD array could not distinguish between NC and background neutrons. This ability would have been provided by a spatial variable as not all classes of background neutron produced captures uniformly distributed over the array. Various possibilities were considered including a 40 string PDF and 6 ring PDFs where the rings of strings were centred on the detector z-axis or on the strings containing the hotspots. However, given the strength of the external constraints on the background neutron production rates there was little to gain from the added complexity of including a spatial PDF. This is discussed further in Section 8.5.2.

The neutron energy PDF was generated using data from the 2005 ^{24}Na measurement. The nominal alpha PDF was generated using Monte Carlo. The following analytical PDFs from [139, 141] were used for the J3 and N4 instrumentals

$$f'_{J3}(E_{ADC}) = Ce^{-\left(\frac{E_{ADC}-\beta_{J3}}{0.34\,E_{ADC}}\right)^2}\,(1+\mathrm{erf}(-2.0(E_{ADC}-\beta_{J3})) \tag{8.17}$$

$$f'_{N4}(E_{ADC}) = Ce^{-\left(\frac{E_{ADC}-\beta_{N4}}{-19.6\,E_{ADC}}\right)^2}\,(1+\mathrm{erf}(-1.59(E_{ADC}-\beta_{N4})) \tag{8.18}$$

where $\beta_{J3} = 0.4584 \pm 0.0262$ and $\beta_{N4} = 0.0257 \pm 0.0138$. These functional forms had no physical basis other than that they provided good fits to samples of the events. The production mechanism for J3 and N4 instrumental events has not been identified. The particular characteristics of these events are described in the next section.

There was a period during the development of this analysis when the pulse shapes of alpha events could not be simulated satisfactorily and it was unclear how to treat events such as the J3 and N4 instrumentals. The particular concern with the alpha simulation was that, with no Monte Carlo, there was no reliable way of determining the shape of the background underneath the neutron peak, particularly as the radioactivity on the ^{4}He strings turned out to be rather unrepresentative, in its composition, of that of the ^{3}He strings. The collaboration actively considered running with a neutron-absorbing isotope, such as Gadolinium, dissolved in the heavy water to remove the neutron signal from the NCDs and allow a direct measurement of the background. A study of the statistical power of such a measurement is described in Appendix H.

These concerns were allayed by improvements in the understanding of alpha pulse formation - particularly by Wan [142] who discovered that alpha events with anomalously long pulses originated from radioactivity on the NCD wires - and by exhaustive, negative searches for non-physics events on other strings (see, for example, [143]). The Monte Carlo used for the alpha background in this analysis could reproduce all classes of alpha pulse shape and the energy spectrum of the ^{4}He strings.

8.2.4 Instrumental and high level cuts

Neutrino candidate events in the PMT stream were events that passed a set of low level instrumental cuts and a set of more sophisticated high level cuts on the following parameters:

- $ITR > 0.55$

  The *in-time ratio* (ITR) was a measure of the proportion of the PMT hits in an event arriving in the prompt peak; larger values corresponded to a larger proportion. This cut was effective at removing low energy background events that occurred in the light water but mis-reconstructed inside the fiducial volume.

- $-0.12 < \beta_{14} < 0.95$

  The parameter β_{14} was a measure of event isotropy. It was constructed from the β_l parameters, which were the average values of the Legendre polynomials P_l of the

cosine of the angles, with respect to the reconstructed position, between each pair of PMT hits in an event [144]. $\beta_{14} = \beta_1 + 4\beta_4$ increased with increasing event isotropy. The range was chosen to include all physics events originating within the acrylic vessel.

There were 146 431 247 raw PMT triggers during the NCD phase, composed mainly of instrumental and low energy background events. 2 381 of these were selected as neutrino candidates.

In the NCD stream there was again a set of low level instrumental cuts. There were no high level cuts but events on all ^{4}He strings and on 6 ^{3}He strings [140] were removed. The ^{3}He strings that were cut were:

- *K5 (hotspot and leak).*

  This string suffered from a slow leak of ^{3}He from one of the counters into an interspace region which caused distortions to the energy spectrum that varied slowly over the NCD phase; this made energy calibration difficult. In addition, K5 was the site of one of the radioactive hotspots and registered 47% of the detected neutron events arising from it.

- *K2 (hotspot and electrical disconnect).*

  This string suffered from intermittent electrical disconnects and consequently had a live time that was difficult to quantify. It was also the site of one of the radioactive hotspots and registered 47% of the detected neutron events arising from it.

- *M8 (electrical disconnect).*

  This string suffered a permanent electrical disconnect.

- *J3 (neutron-like instrumentals).*

  This string contained an excess of the low energy events referred to as J3 instrumentals that had pulse shapes that were difficult to distinguish from neutrons. They had a different energy spectrum to neutrons, peaking much lower in energy. Both the pulse shapes and energy distributions were consistent with the events being betas but no source has been identified. The string itself was removed and a J3 PDF included in the fit to pick up these events if they occurred on other strings.

- *N4 (neutron-like instrumentals).*

  Like string J3, string N4 contained low energy instrumental events and they were dealt with in the same way.

- *K7 (gain changes).*

  This string suffered from sporadic gain changes that made its energy calibration unreliable.

The were 1 417 811 raw NCD triggers during the NCD phase. After instrumental cuts this was reduced to 91 636 and, after removal of strings and imposing the energy cut, to 7 302 events, of which $\sim 80\%$ were alphas.

8.3 Fluxes and events

For classes of event detected in both the PMT and NCD data streams the fit parameter was the flux of neutrinos or the number of background neutrons produced rather than the number of events in each stream. However, numbers of events were required to evaluate the likelihood function in Eq. (8.11) so conversion factors were required. This section describes how the quantities E and E', which governed the conversion of fluxes or production rates into events via Eq. (8.14) and Eq. (8.15), were calculated.

The signals that were fit as fluxes or neutrons produced were the CC, ES and NC neutrino events and the 5 groups of neutron backgrounds. The expected numbers of events for each, in each stream, were given by

$$E_{CC,ES} = N_{mc} \cdot (\eta_{target} \cdot \eta_{nuclei} \cdot r_{geom} \cdot \varepsilon_{cut} \cdot t_{cut}) \quad (8.19)$$

$$E_{NC}^{PMT} = R_{mc} \cdot \varepsilon_{nc}^{PMT} \cdot T_{live} \cdot (\omega \cdot r_{\odot} \cdot \varepsilon_{cut}) \quad (8.20)$$

$$E_{NC}^{\prime NCD} = R_{mc} \cdot \varepsilon_{nc}^{NCD} \cdot T_{live} \cdot (\omega \cdot r_{\odot} \cdot \varepsilon_{cut}) \quad (8.21)$$

$$E_{bkgrd}^{PMT} = R_{gen} \cdot \varepsilon_{bkgrd}^{PMT} \cdot T_{live} \cdot (\varepsilon_{cut}) \quad (8.22)$$

$$E_{bkgrd}^{\prime NCD} = R_{gen} \cdot \varepsilon_{bkgrd}^{NCD} \cdot T_{live} \cdot (\varepsilon_{cut}) \quad (8.23)$$

The expression for CC and ES has a slightly different form than the one for NC. This is because for CC and ES the Monte Carlo is used to predict the number of events for each unit of neutrino flux, whereas for NC that relationship is measured via the neutron detection efficiencies.

The values of the quantities in these expressions are given in Table 8.4 or elsewhere, as indicated below. They are defined as follows:

- N_{mc}

  The number of Monte Carlo events within cuts per standard solar model assuming an undistorted ^{8}B neutrino energy spectrum. The model used was BP2000 [145], which predicted a ^{8}B flux of $5.145 \times 10^6\,\nu\,\mathrm{cm}^2\,\mathrm{s}^{-1}$.

- R_{mc}

  NC neutron production rate of $13.2745\ \mathrm{day}^{-1}$ predicted, by SNOMAN, to correspond to a flux of $5.145 \times 10^6\,\nu\,\mathrm{cm}^2\,\mathrm{s}^{-1}$.

- η_{target}

  A correction for the number of deuteron or electron targets, which differed slightly between data and Monte Carlo.

- η_{nuclei}

  A correction for neutrino interactions on oxygen and nickel that were not included in the Monte Carlo.

- ϵ_{geom}

  A correction for the number of CC and ES Monte Carlo events aborted during simulation because of errors in the SNOMAN geometry code [146].

- ε_{cut}

  In the PMT stream this was a correction for the difference in cut efficiencies between data and Monte Carlo. In the NCD stream this included contributions due to the sacrifice of neutrons below 0.4 MeV and instrumental cuts.

- $\varepsilon_{nc/bkgrd}^{PMT/NCD}$

  Neutron detection efficiencies (see Table 8.2).

- t_{cut}

  A correction for the difference in livetimes between data and Monte Carlo.

- T_{live}

  The NCD phase livetime of 385.17 ± 0.14 days [147].

- $r_{\odot}$

  A correction to the number of predicted NC events to account for the mean orbital radius during data taking.

Table 8.4: Correction factors used when converting fluxes into numbers of events.

Correction		CC	ES	NC	NC	PD	PD
Symbol	Description			PMT	NCD	PMT	NCD
$r_\odot$	Mean orbital radius	1	1	1.00101	1.00101	1	1
η_{target}	Number of D / e^-	1.01218	1.0131	1	1	1	1
η_{nuclei}	CC interactions on O, Ni	1.0078	1	1	1	1	1
ε_{cut}	Cut acceptance	0.9917	0.9917	0.9917	0.862	0.9917	0.862
t_{cut}	Livetime correction	0.9804	0.9804	1	1	1	1
ε_{geom}	Geometry errors	1.0123	1.0073	1	1	1	1
ω	Radiative correction	1	1	1/1.024	1/1.024	1	1
	Net correction	1.00398	0.99219	0.96944	0.84265	0.9917	0.862

- ω

  A correction to account for radiative corrections to the neutrino interaction cross sections as implemented in the Monte Carlo. These were small and so applied 'on average' rather than event-by-event.

- R_{gen}

  The measured background neutron production rates (see Table 8.5).

After application of all these correction factors and using the central values of all systematic parameters, the numbers of events expected for 1 standard solar model (a flux of $5.145 \times 10^6\,\nu\,\mathrm{cm}^{-2}\,\mathrm{s}^{-1}$) were 5583.670 CC events, 480.471 ES events, 240.398 NC events in the PMT array and 909.071 NC events in the NCD array.

8.4 Systematic uncertainties

8.4.1 Using the data

There were two classes of systematic uncertainty in this analysis: the first was uncertainties on PDF shapes and the second was uncertainties on the conversions between fluxes and number of events. The detector energy scale is an example of the former and the neutron detection efficiencies are examples of the latter. The values and uncertainties on systematic parameters were assessed using calibration data.

Table 8.5: Numbers of background events produced and detected. For the neutron backgrounds the fit constraints were the numbers produced and for the neutron-like backgrounds the fit constraints were the numbers detected.

Background	Produced		PMT detected		NCD detected	
	Value	Unc.	Value	Unc.	Value	Unc.
AV	2719.30	1359.65	18.34	9.17	26.49	13.24
K2	146.37	23.50	9.30	1.50	32.84	5.27
K5	120.56	13.87	8.37	0.96	31.53	3.63
Bulk	78.27	36.51	4.62	2.16	27.63	12.89
Uniform	170.59	25.88	8.21	1.25	31.03	4.71
n-like			27.99	5.20	36.12	15.60
Total			76.82	10.98	185.63	25.46

In previous SNO ^{8}B flux analyses systematic uncertainties were handled using the *shift and re-fit method*. In this technique the full fit, with all parameters free, was run using the central values of all systematic parameters and then again when each systematic was shifted to its $\pm 1\sigma$ limits. The changes in the flux values due to each systematic were assumed to be independent and were added in quadrature.

This method is not ideal for a number of reasons, all stemming from the fact that it does not use the information provided by the neutrino data. For example, if that data strongly favoured one value of a systematic, the $\pm 1\sigma$ shifts, derived from the calibration data, might change the fit likelihood by much more than 0.5, leading to an overestimate of the error. The shift-and-refit procedure also does not allow the central value systematics to move, given the information provided by the data. The ideal method is one in which all systematics are included as parameters in the fit, subject to constraints from external measurements. This is referred to as the *floating systematics method*.

The technical challenges involved in floating systematics in fits to SNO data can be substantial because most PDFs are binned and constructed from large numbers of Monte Carlo events. During the fit every time the value of a systematic parameter associated with a PDF shape is changed then the PDFs need to be rebuilt. As well as being CPU-intensive this procedure can cause convergence problems because discontinuities are introduced into the likelihood space when events move between bins.

Three different approaches were taken to the problem of handling systematic uncertainties in the NCD flux analysis, in three independent codes (described in Section 8.5.1).

Table 8.6: PDF shape systematic uncertainties with their one sigma constraints. The units are cm for distances and MeV for energies.

Stream	Param.	Description	Value	Unc.	Type
PMT	a_o^x	x-coordinate shift	0.0	4.0	Shift
	a_0^y	y-coordinate shift	0.0	4.0	Shift
	a_0^z	z-coordinate shift	5.0	4.0	Shift
	b_0^{xyz}	xyz-coordinate scale	0.000	0.009	Shift
	c_0^{xy}	xy-resolution constant	0.06546	0.02860	Shift
	c_1^{xy}	xy-resolution linear	-0.00005501	0.00006051	Shift
	c_2^{xy}	xy-resolution quadratic	3.9×10^{-7}	2.0×10^{-7}	Shift
	c_0^z	z-resolution constant	0.07096	0.02805	Shift
	c_1^z	z-resolution linear	0.0001155	0.00008251	Shift
	$a_0^\odot$	Angular resolution	0.00	0.06	Shift
	b_0^T	Energy scale	0.0000	0.0109	Shift
	c_0^T	Energy resolution (n)	0.0119	0.0104	Shift
	c_0^T	Energy resolution (e^-)	0.0162	0.0142	Shift
NCD	b_0^A	Neutron energy scale	0.0	0.01	Shift
	c_0^A	Neutron energy resolution	0.0	+0.01	Shift
	b_0^α	Alpha Po depth variation	0	1	Float
	b_1^α	Alpha Bu depth variation	0	1	Float
	b_2^α	Alpha drift time variation	0	1	Float
	b_3^α	Alpha avalanche width offset variation	0	1	Float
	b_4^α	Alpha avalanche grad. offset variation	0	1	Float
	b_5^α	Alpha Po/Bu fraction variation	0	1	Float
	b_6^α	Alpha ion mobility	0	1	Float
	α_{J3}	J3 3NA shape parameter	0.458419	0.026243	Float
	α_{N4}	N4 3NA shape parameter	0.025720	0.013758	Float

In the analysis reported here systematics associated with the shapes of binned PDFs were handled using the shift and re-fit method but all others - those associated with the shapes of analytical PDFs and with the conversion of fluxes into numbers of events were floated in the fit, subject to their external constraints.

The systematic parameters in this analysis are shown in Table 8.6. For systematics handled using the shift and re-fit method the values of the systematics in the table were used for the central fits. Note that a large number of the values differed from zero. The PDF shape systematics are described in turn in the following sections.

8.4.2 PMT stream

- *Energy.*

  Scale and resolution uncertainties associated with the estimated event energy were calculated by [148]. The energy used in the fit T'_{eff} was related to the raw estimated energy T_{eff} by

  $$T'_{eff} = (1 + b_0^T)\, T_{eff} + c_0^T\, (T_{eff} - T_{eff,gen}) \tag{8.24}$$

  where b_0^T is the energy scale, c_0^T is the energy resolution and $T_{eff,gen}$ is the energy of the generated Monte Carlo event. The energy scales for neutrons and electrons were different but completely correlated; they differed because of the different characteristics of the neutron and electron (^{16}N) calibration sources and were correlated because the detector was the same for both. In the shift-and-refit-procedure b_0^T and c_0^T were moved independently to their $1\,\sigma$ limits. In the shifts of b_0^T the electron and neutron energy scales were shifted together.

- *Vertex.*

  Vertex offset, scale and resolution uncertainties arose from the knowledge of the optical response of the detector and the performance of the FTN fitter [59]. Coordinates used in the fit were related to the reconstructed positions by

  $$x' = a_0^x + (1 + b_0^{xyz})\, x + (c_0^{xy} + c_1^{xy} z + c_2^{xy} z^2)\, (x - x_{gen}) \tag{8.25}$$

  $$y' = a_0^y + (1 + b_0^{xyz})\, y + (c_0^{xy} + c_1^{xy} z + c_2^{xy} z^2)\, (y - y_{gen}) \tag{8.26}$$

  $$z' = a_0^z + (1 + b_0^{xyz})\, z + (c_0^z + c_1^z z)\, (z - z_{gen}) \tag{8.27}$$

  where a_0^x, a_0^y, a_0^z are coordinate shifts, b_0^{xyz} is vertex scaling common to each coordinate, $c_0^{xy}, \ldots, c_1^z$ are resolution parameters and x_{gen}, y_{gen} and z_{gen} are event generation points in the Monte Carlo. The resolution parameters were correlated but in this analysis, where they were handled by the shift and re-fit procedure, they were treated as being independent. Vertex resolution uncertainties were so small (see results) that neglecting the correlation between the parameters cannot have affected the final uncertainties.

- *Angular resolution.*

  The PMT angular resolution systematic uncertainty was applied only to the ES signal, because only that signal had a distribution in $\cos\theta_\odot$ that was not slowly varying; CC and NC PDFs in this parameter were close to uniform. A convenient

parametrisation of the uncertainty was derived by [149], in which the value $\cos\theta_\odot$ used in the fit was related to that reported by the position fitter by

$$\cos\theta'_\odot = 1 + (1 + c_0^\odot)\,(\cos\theta_\odot - 1) \tag{8.28}$$

During the shift and re-fit procedure if $\cos\theta_\odot$ for a particular event was pushed outside the physical region $-1 < \cos\theta_\odot < 1$ then the event was assigned a random value of $c_0^\odot$ between -1 and 1. This was to avoid artificial peaks being created in the first and last bins because of pile up events. The number of events affected was negligible, less than $1/100^{\text{th}}$ of a percent.

8.4.3 NCD stream

- *Neutron energy.*

  Scale and resolution systematic uncertainties were assigned to the neutron shaper-ADC energy PDF in an analysis by [150]. The energy used in the fit was related to calibrated neutron energy from the ^{24}Na measurement by

  $$E'_{ADC} = (1 + b_0^A)\,E_{ADC} + \mathrm{g}(0, c_0^A)\,E_{ADC} \tag{8.29}$$

  where b_0^A is the scale and c_0^A is the resolution. The neutron energy PDF was unique in being formed from calibration data and thus had a resolution that could only be broadened. The broadening was done by sampling from a Gaussian $g(0, c_0^A)$ with mean 0 and width c_0^A.

- *Alpha energy.*

  The NCD alpha energy PDF was generated using Monte Carlo [151, 152]. Seven systematic uncertainties, each accounting for the uncertainty on a different Monte Carlo input parameter, were each assigned a second-order polynomial re-weighting factor $f_s(E_{ADC})$ that parametrised the effect of the uncertainty on the PDF. Each polynomial was multiplied by a systematic parameter b_s that was included in the fit and constrained by a Gaussian of mean 0 and width 1.

  The probability p_i in energy bin i was modified using

  $$p'_i = \left(1 + \sum_{s=0}^{6} b_s^\alpha\, f_s(E_{ADC})\right) p_i \tag{8.30}$$

  where

  $$f_0 = -2.06 + 6.58\,E_{ADC} - 6.56\,E_{ADC}^2 + 2.11\,E_{ADC}^3 \tag{8.31}$$

$$f_1 = -0.0684 + 0.0892\,E_{ADC} \tag{8.32}$$

$$f_2 = -0.131 + 0.252\,E_{ADC} - 0.117\,E_{ADC}^2 \tag{8.33}$$

$$f_3 = -0.0541 + 0.0536\,E_{ADC} \tag{8.34}$$

$$f_4 = -0.0166 \tag{8.35}$$

$$f_5 = -0.00405\,E_{ADC} + 0.0386\,E_{ADC}^2 \tag{8.36}$$

$$f_6 = 0.861 - 2.77\,E_{ADC} + 2.72\,E_{ADC}^2 - 0.87\,E_{ADC}^3 \tag{8.37}$$

are the seven re-weighting polynomials and b_s are the contributions of each. The polynomials were evaluated at the bin centres. They correspond to uncertainties in the following :

f_0 Depth of Po alphas in the Ni counter walls

f_1 Depth of bulk U and Th alphas in the Ni counter walls

f_2 Drift time

f_3 Avalanche width offset

f_4 Avalanche width gradient and ion mobility

f_5 The relative amounts of Po and bulk alphas

f_6 Data cleaning

- *J3 and N4 instrumental energies.*

  The functional forms for these analytical PDFs are given in Eq. (8.17) and Eq. (8.18). Each depended on a single shape parameter, which was floated in the fit within a constraint that came from fits to samples of the events.

8.5 The MXF code

8.5.1 Three codes

There were three independent flux analyses of the NCD phase data, each handling systematics in a different way.

This analysis, as indicated above, included some systematic parameters in the fit and used the shift and re-fit procedure for the rest. The code was based on the MXF signal extraction code developed by McGregor [153], Wilson [7], Dunford [154], Orebi Gann [155] and others. The author adapted this code for the NCD phase analysis by

Table 8.7: Summary of fit parameters.

Stream	Parameter
PMT & NCD	NC flux
	AV neutrons produced
	K2 neutrons produced
	K5 neutrons produced
	Bulk neutrons produced
	Uniform neutrons produced
PMT	CC flux in 13 energy bins
	ES flux in 13 energy bins
	Misc. events detected
	NC neutron detection efficiency
NCD	Alpha background events
	J3 3NA events
	N4 3NA events
	Misc. events detected
	NC neutron detection efficiency
	Slope of linear alpha background
	MC alpha Po alpha depth variation
	MC alpha bulk alpha depth variation
	MC alpha drift time variation
	MC alpha avalanche width offset variation
	MC alpha avalanche gradient offset and ion mobility variation
	MC alpha Po/Bu fraction variation
	MC alpha data cleaning
	J3 3NA shape parameter
	N4 3NA shape parameter

adding the ability to float systematic parameters associated with analytical PDF shapes and with conversion of fluxes to numbers of events, amongst other improvements. MXF was implemented within the SNOMAN framework and used the MINUIT minimisation package [156].

A second analysis [157] also used a variant of the MXF code but employed a statistical sampling method invented by Oser [158, 159] to float systematic uncertainties associated with the shapes of binned and analytical PDFs. Many fits were performed in parallel, each taking a different set of values for the systematic parameters, randomly sampled from the external constraints. The results for each output parameter were then weighted by the likelihood, so that fits with greater likelihood were given more weight, and histogrammed. The fit values were the means of these distributions and the uncertainties were the widths. The author developed a code to study this method but did not carry it forward because of concerns over the number of fits required to reach convergence on the correct central values and uncertainties; this would be a particular concern if systematic parameters were strongly correlated or if there was a large difference in the central values favoured by systematic parameters and by the data [160].

A third analysis [161] used a Markov Chain Monte Carlo, and the Metropolis-Hastings algorithm [162, 163] in particular, to integrate over systematic parameters. In this algorithm the Markov Chain Monte Carlo maps out a function - the chain moves from point to point around the function and, after a period of 'burn-in' or convergence, samples points with a frequency proportional to the magnitude of the function at each point. After convergence the values of each parameter at every step of the chain were histogrammed, which built up distributions that could be fitted with Gaussians to extract the best fit values and uncertainties. Because this method integrated over systematic parameters it was not sensitive to discontinuities introduced into the likelihood when events changed bins, but it did require extensive CPU resources, particularly as it did not lend itself to parallelisation. It was the primary NCD phase flux analysis technique because of its complete handling of systematic uncertainties.

8.5.2 Bias testing

The fitting code was tested on ensembles of fake data sets to check for biases. Two sets of data were prepared for this purpose: one for use with a cut down version of the code to study PDF factorisations and variables, and another for use with the full, final version of the code. They were constructed using Monte Carlo simulations generated using SNOMAN, estimates of event numbers from published SNO results and preliminary

estimates for the NCD phase backgrounds.

The bias B_i and pull P_i of a fit to a fake data set i are defined by

$$P_i = \frac{N_i - \bar{E}}{\sigma_i}, \tag{8.38}$$

and

$$B_i = \frac{N_i - \bar{E}}{\bar{E}}, \tag{8.39}$$

where N_i is the fit number of events, with uncertainty σ_i, and $\bar{E}$ is the expected number of events. Values of P_i and B_i were histogrammed; the means of the bias and pull distributions were checked for consistency with 0 and the width of the pull distribution for consistency with 1.

The first ensemble of 100 fake data sets contained only the physics signals and the NCD alpha background. It was used for the preliminary choice of observables and PDF factorisations. The fake data sets and PDFs were independent, no systematic shifts were applied to any of the observable values and the alphas were split into their bulk and Po components. Bias test results for various PDF factorisations are shown in Table 8.8. The lowest dimension PDF factorisation exhibiting zero bias was $f(T_{eff}, \rho) \times f(\cos\theta_\odot) \times f'(E_{ADC)}$; the bias in the PMT-only fit with this factorisation was suppressed by the constraint on the NC flux provided by the NCD array. The PMT part of this PDF was selected instead over a 3D PDF to increase the number of events per bin. The other result to note in Table 8.8 is the small decrease in the uncertainty on the NCD flux with the addition of a string-by-string PDF. At face value the 9% reduction *is* significant but it does not include the uncertainty on the string PDF which would have reduced the benefit substantially.

The second ensemble of 100 fake data sets contained all signals and was used to verify the mechanics of the code to guard against unexpected biases or coding errors. The data set, which was common to all three codes, was prepared by Jamieson [164]. The values of the observables for each event were smeared by values randomly sampled from the constraints on the systematic parameters. The fake data sets and PDFs were not independent but this was not expected to have any impact on the quality of the tests because the number of events in each PDF bin was very large and the neutrino PDFs contained $\sim$ 500 or 1000 times as many events as each fake data set. Bias test results are shown in Figure 8.2. There was no evidence for bias in the means or widths of the distributions.

Table 8.8: Results of bias tests run on the ensemble of minimal fake data sets.

Factorisation	Signal	Bias		Frac. Unc.	
		Value	Unc.	Value	Unc.
$f(T_{eff}, \rho, \cos\theta_\odot)$	CC	-0.0006	0.0023	0.0350	0.0001
	ES	-0.0005	0.0071	0.1022	0.0010
	NC	0.0054	0.0183	0.2234	0.0049
$f(T_{eff}, \rho) \times f(\cos\theta_\odot)$	CC	-0.0033	0.0023	0.0353	0.0001
	ES	-0.0026	0.0071	0.1023	0.0010
	NC	0.0276	0.0184	0.2190	0.0048
$f(T_{eff}, \rho) \times f(\cos\theta_\odot \vert E)$	CC	-0.0013	0.0022	0.0335	0.0001
	ES	-0.0010	0.0071	0.1019	0.0009
	NC	0.0110	0.0172	0.2025	0.0038
$f(T_{eff}, \rho) \times f(\cos\theta_\odot) \times f'(E_{ADC})$	CC	0.0007	0.0014	0.0269	0.0001
	ES	-0.0007	0.0069	0.1015	0.0009
	NC	0.0008	0.0107	0.0634	0.0005
	Bu	-0.0052	0.0149	0.1404	0.0023
	Po	0.0081	0.0206	0.1971	0.0047
$f(T_{eff}, \rho) \times f(\cos\theta_\odot) \times f'(E_{ADC}) \times f'(str)$	CC	0.0003	0.0014	0.0268	0.0001
	ES	-0.0009	0.0070	0.1015	0.0010
	NC	0.0049	0.0108	0.0578	0.0004
	Bu	-0.0039	0.0052	0.0561	0.0003
	Po	0.0043	0.0072	0.0762	0.0006

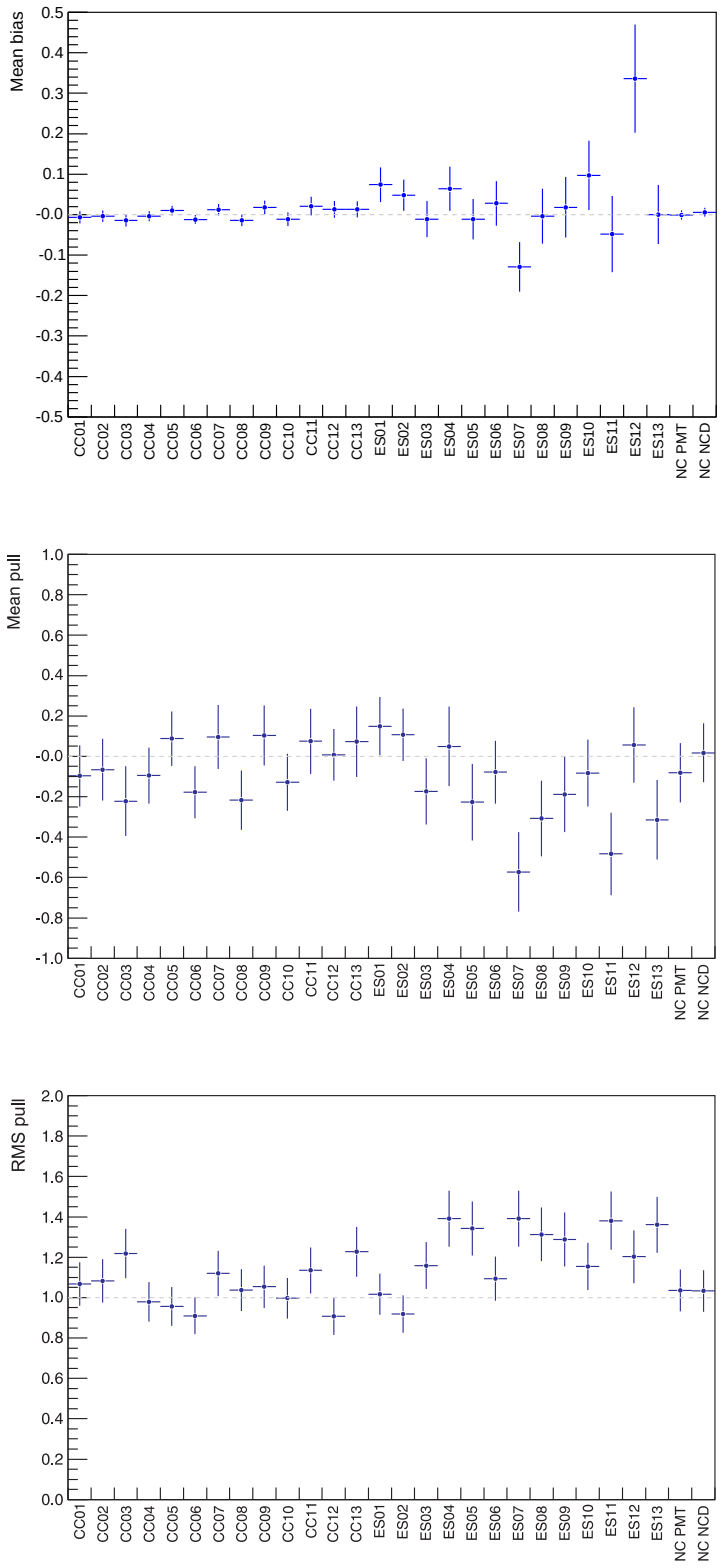

Figure 8.2: Results of bias tests run on the ensemble of fake data sets with properties equivalent to the neutrino data set.

8.5.3 Blindness

A blind analysis procedure was used to prevent bias when developing the analysis techniques described in the preceding sections.

The particular scheme that was adopted allocated 20% of the data for developing instrumental cuts, randomly tagged and removed between 10% and 30% of the events in the data set and introduced extra neutron events into the data set. The extra neutron events were neutrons produced following muon interactions in the detector, which were usually removed by a cut that identified muons and removed events recorded immediately following them. The scheme changed the number of events fitted as NC and also the ratio of the numbers of CC and NC events.

When the blindness was lifted a number of small but statistically significant differences were found between the results of the three codes. The only one relating to this analysis was an error in the coding of the shaper-ADC energy resolution, which was corrected.

8.6 Results

The fit results obtained with the Monte Carlo alpha PDF are shown in Figure 8.3. Appendix I gives the values and uncertainties for all fit parameters.

There was one post-processing modification made to the fit results and that was a correction for what are known as *Čerenkov tail* events. These were events in the D_2O that occurred outside the fiducial volume or in the H_2O, but reconstructed inside the fiducial volume. The former are known as *internal tails* and the latter as *external tails*. The expected number of internal tail events was $0.70^{+0.37}_{-0.38}$ [165] and the expected number of external tail events was $5.1^{+9.7}_{-2.9}$ [166]. These events were CC- or ES-like and were deducted from the fit numbers of CC and ES events; 10% were deducted from ES and 90% from CC on the basis that the ES peak, which is the only means of distinguishing them, covers $\sim$10% of the range of $\cos\theta_\odot$.

The final fit neutrino fluxes were (in units of $10^6\,\nu\,\mathrm{cm}^{-2}\,\mathrm{s}^{-1}$)

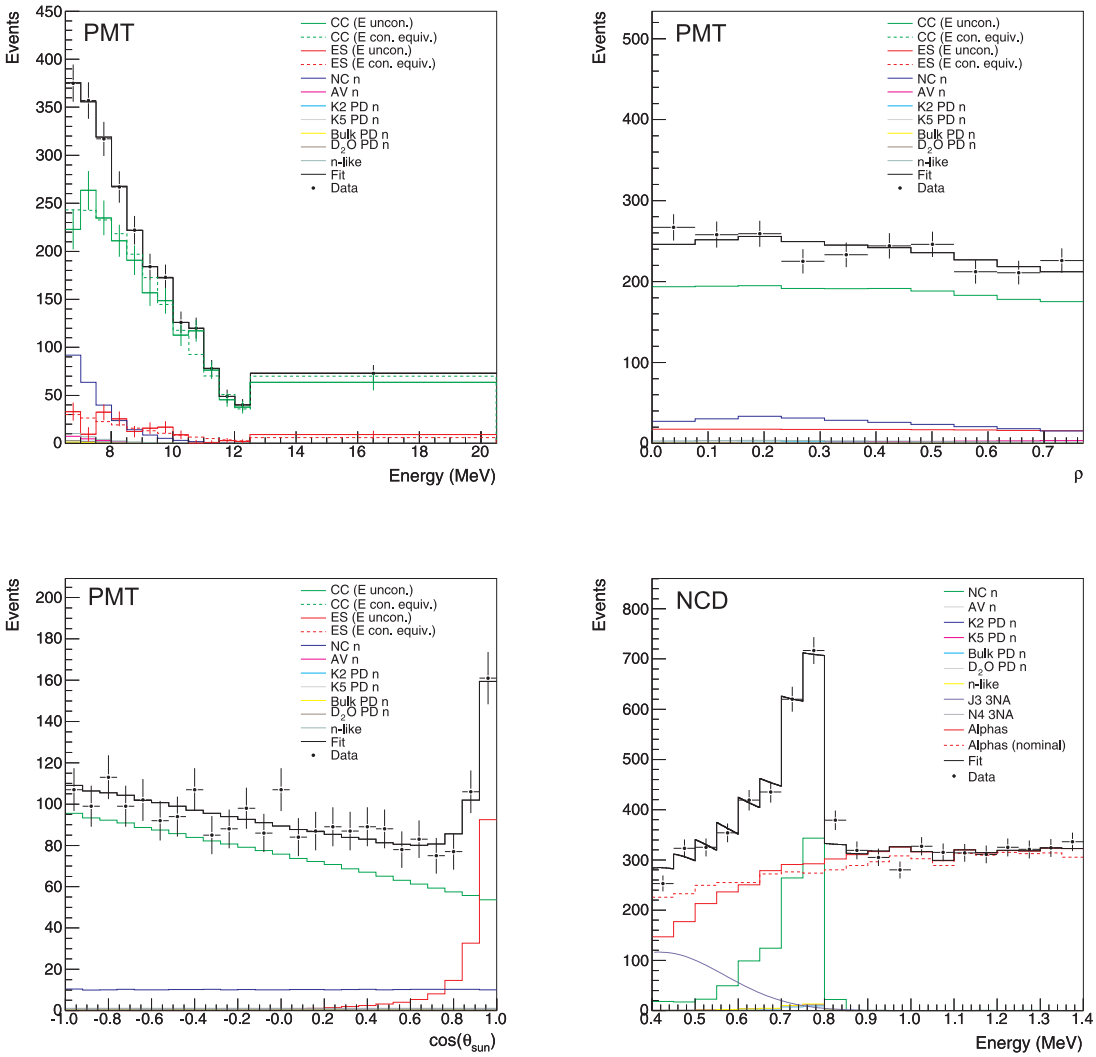

Figure 8.3: Fit results obtained using the Monte Carlo alpha PDF. In the PMT energy plot two spectra are shown for both ES and CC: the ones labelled 'E con. equiv.' are the Monte Carlo energy spectra normalised to the total number of ES or CC events; the ones labelled 'E uncon.' are the fit, energy-unconstrained, spectra.

Signal	Flux			
	Value	Stat.	Syst.	Total
CC	1.728	$^{+0.049}_{-0.047}$	$^{+0.068}_{-0.068}$	$^{+0.084}_{-0.083}$
ES	1.811	$^{+0.238}_{-0.214}$	$^{+0.080}_{-0.073}$	$^{+0.251}_{-0.226}$
NC	5.443	$^{+0.329}_{-0.327}$	$^{+0.318}_{-0.301}$	$^{+0.458}_{-0.444}$

These fluxes were in reasonable agreement with those obtained using the Markov Chain Monte Carlo [161]:

Signal	Monte Carlo	
	Value	Unc.
CC	1.669	$^{+0.082}_{-0.092}$
ES	1.768	$^{+0.255}_{-0.234}$
NC	5.543	$^{+0.483}_{-0.456}$

The flux results are compared with previous SNO measurements in Figure 8.4. The p-value for agreement between the NCD phase CC, ES and NC fluxes with results from the D_2O and salt phases, calculated using the numbers from the Markov Chain analysis, was 32.8%.

The uncertainty on the CC flux was improved compared to previous SNO phases. This had two causes: first, the sensitivity to CC events was maintained, despite the scattering and absorption of Čerenkov light by the NCDs, by improvements to the optical calibration and the removal of most neutron events from the PMT stream by the NCD array; and second, the relatively high energy threshold, which reduced the contamination of the CC signal by background events.

The ES flux was 2.2σ low compared to that found by Super-Kamiokande-I [167], with which previous SNO measurements were in good agreement. There was no reason to suspect that this was anything other than a statistical fluctuation. Figure 8.5 shows the $\cos\theta_\odot$ distribution in the three lowest energy bins and the virtual absence of the ES peak in the second bin can be clearly seen - this was the main statistical fluctuation.

The NC flux was in good agreement with previous phases and in excellent agreement with the BS2005 standard solar model which predicted a ^{8}B flux of $5.69 \times 10^6\,\nu\,\mathrm{cm}^{-2}\,\mathrm{s}^{-1}$. The ratio of the ^{8}B flux measured with the CC and NC interactions was

$$\frac{\Phi_{\mathrm{CC}}}{\Phi_{\mathrm{NC}}} = 0.318^{+0.030}_{-0.031} \tag{8.40}$$

where the uncertainty is the combined statistical and systematic uncertainty.

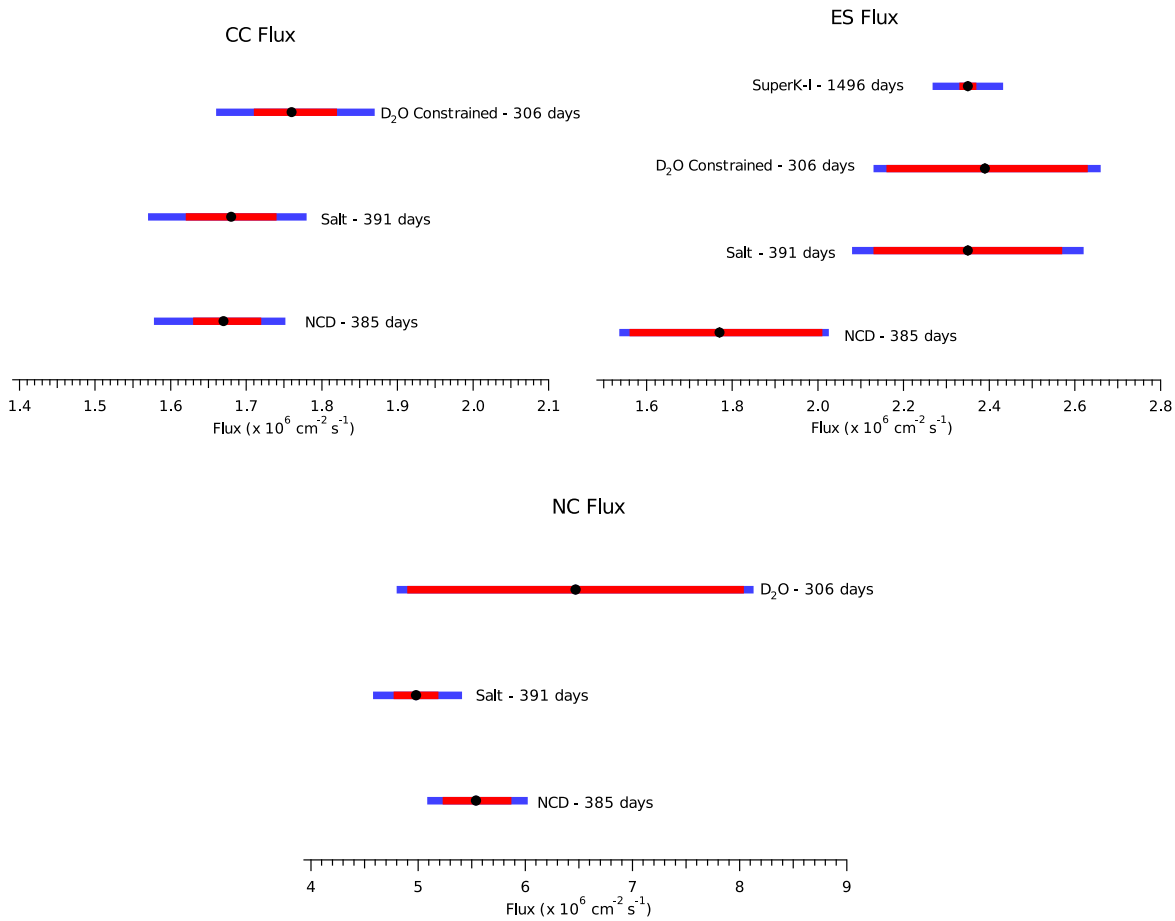

Figure 8.4: Comparison of the flux results in different phases and, for ES, also with the results of Super Kamiokande-I [18]. The red bars are the statistical uncertainties and the blue bars are the total uncertainties.

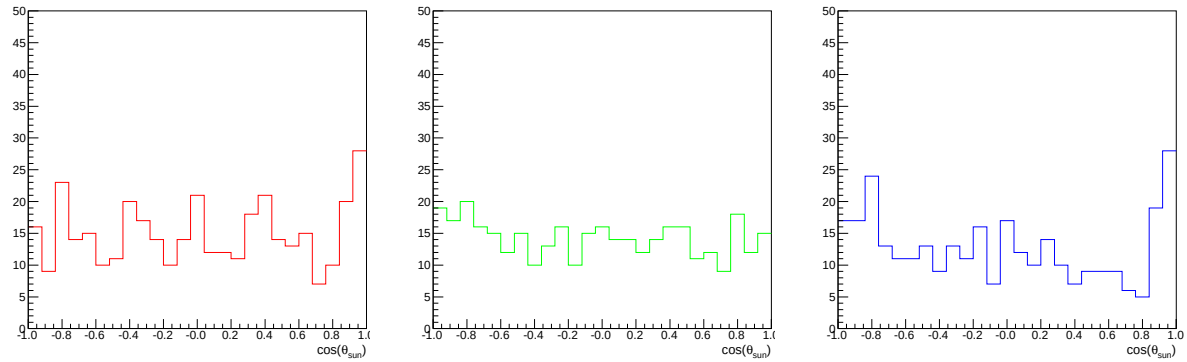

Figure 8.5: The $\cos\theta_{\odot}$ distribution in the three lowest energy bins. 6.0-6.5 MeV (left) to 7.0-7.5 MeV (right).

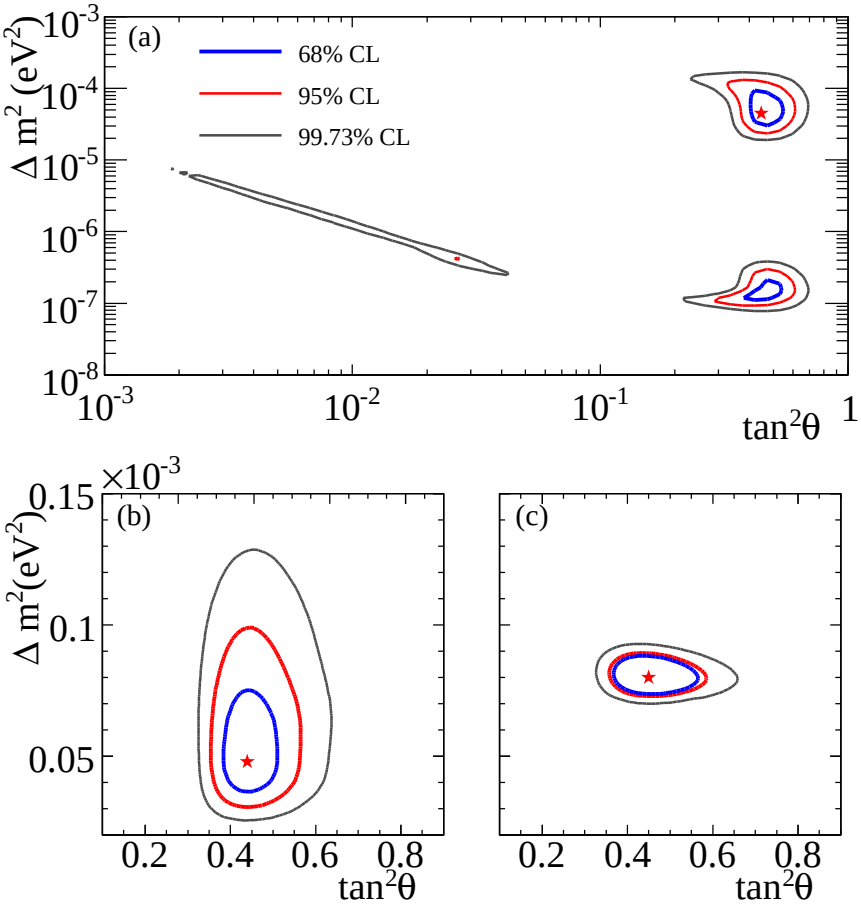

Figure 8.6: Neutrino oscillation contours from a combined fit to the three phases of SNO data (top), global fit to all solar data (bottom right) and global fit to all solar data and KamLAND.

Figure 8.6 shows the regions of Δm^2-$\tan^2\theta$ parameter space from a combined χ^2 fit [136] to the SNO D_2O, salt and NCD phase data (the numbers from the Markov Chain analysis), as well as those of a global analysis including all solar experiments, and all solar experiments plus the 766 ton-year KamLAND reactor anti-neutrino results [48]. The best fit point to the global solar plus KamLAND fit was at

$$\Delta m^2 = 7.94^{+0.42}_{-0.26} \times 10^{-5}\ \text{eV}^2 \qquad \theta = 33.8^{+1.4}_{-1.3}\ \text{degrees}$$

Chapter 9

Conclusions

It's the sides of the mountain which sustain life, not the top. Here's where things grow.

ROBERT PIRSIG
Zen and the Art of Motorcycle Maintenance (1974)

The Sudbury Neutrino Observatory (SNO) was a heavy water Čerenkov detector that had the unique ability to measure both the total active flux of ^{8}B solar neutrino, using a neutral current (NC) interaction, and the flux of electron neutrinos, using a charged current (CC) interaction. The signature of the NC interaction was the production of a neutron, which was detected differently in each phase of the experimental program.

In the D_2O phase neutrons were detected via the gamma produced following their capture on deuterons. The results of this phase demonstrated, if the ^{8}B neutrino energy spectrum was assumed, that neutrinos change flavour and that the total active neutrino flux was consistent with the predictions of standard solar models.

In the Salt phase NaCl was added to the heavy water to increase the sensitivity to neutrons. They were detected via the cascade of gammas produced following neutron capture on ^{35}Cl. The neutron capture efficiency was increased, as was the ability to distinguish CC and NC events, by using the difference in isotropy of the light produced by CC interactions and the cascade of gammas following neutron capture. Precision measurements of the CC and NC fluxes could be made with no assumption on the shape of the ^{8}B neutrino energy spectrum.

This thesis has presented results from the final phase of the experiment, in which

neutrons were detected using an array of ^{3}He proportional counters, known as NCDs (Neutral Current Detectors), deployed in the heavy water. The NCD and PMT arrays were effectively independent detectors so using the PMT array to detect CC events and NCD array to detect most NC events largely broke the correlation between the measurements of the CC and NC fluxes, which had been significant in previous phases. The systematic uncertainties on the NC measurement in this phase were also very different to previous phases; SNO was a systematics-limited experiment and the exchange of one set of systematics on the NC flux for another was an extremely powerful check that the estimates for both sets of systematic uncertainties were robust.

This thesis has described two analyses contributing to the neutrino flux measurements in the NCD phase: the statistical extraction of the ^{8}B neutrino solar neutrino fluxes from the NCD phase data, and the measurement of one of the most important parameters in that analysis - the probability that a neutron produced in an NC interaction was detected.

There were two approaches to the problem of determining the neutron detection efficiency. The first was to mimic the NC signal using a distributed neutron source - the radioisotope ^{24}Na was injected into the heavy water to produce a uniform source of neutrons by photodisintegrating deuterons. The second was to calculate the efficiency theoretically, using a Monte Carlo simulation, which was tuned and tested using point neutron source data. Chapter 3 gave overviews of both techniques and the following chapters described analyses carried out by the author.

Chapter 4 presented a series of improvements to the modelling of neutron propagation in the detector. These changes were important for many aspects of the neutron detection efficiency analyses but particularly for the theoretical determination of the efficiency. A detailed model of the NCD array was constructed and various refinements made to other parts of the detector geometry. Improvements were also made to the modelling of the distributions of the neutrons and gammas produced by the calibration sources.

Chapters 5 and 6 described two methods for determining the strengths of the ^{24}Na sources. The first used a Ge detector to count gammas produced by samples of ^{24}Na brine. The efficiency of the Ge detector was determined using a Monte Carlo that was tuned using a well-calibrated mixed radioisotope source. The second method used the SNO detector itself. A sample of ^{24}Na brine was put in a small capsule and positioned at the centre of the detector and the neutron detection rate, as measured by the PMT array, was compared to that of a well-calibrated ^{252}Cf source placed in the same position, allowing the strength of the source to be inferred. This latter method was also used to

determine the strengths of the AmBe sources.

Chapter 7 described the theoretical determination of the neutron detection efficiency using a Monte Carlo simulation. The simulation was tuned using AmBe point source neutron calibration data to fix the hydrogen concentration in the heavy water, a parameter on which there was a significant experimental uncertainty. The tuning was done in a relative way that was independent of the strengths of the sources. The performance of the tuned Monte Carlo was evaluated by making comparisons between data and simulations with a larger set of point source data than was used for the tuning. Systematic uncertainties on the final result were evaluated by propagating uncertainties on the Monte Carlo input parameters, including those relating to the isotopic composition of the heavy water and to the detector geometry.

Both methods for determining the neutron detection efficiency were found to be excellent agreement.

Chapter 8 described the statistical extraction of the ^{8}B solar neutrino fluxes from the NCD phase data. A maximum likelihood technique was used to estimate the numbers of neutrino candidate events that were due to neutrino interactions (CC, ES or NC) and backgrounds. Events were described by a set of observable parameters, such as event energy or radius, and the data were fit to a combination of probability distribution functions for each of the signals in each of the observables. The numbers of events belonging to each class of background were constrained in the fit by external measurements.

Systematic uncertainties, such as neutron detection efficiencies, which were also constrained by external measurements, were either allowed to float in the fit, as nuisance parameters, or the fit was repeated with the parameters set to the positive and negative $1\,\sigma$ limits allowed by the external measurements. Where possible, systematic uncertainties were floated, as this allowed the data to constrain their values and allowed central values to move within their constraints.

The measured fluxes were

$$\Phi_{\mathrm{CC}} = 1.728^{+0.049}_{-0.047}\,(\mathrm{stat.})\,^{+0.068}_{-0.068}\,(\mathrm{syst.})\ \times 10^6\,\nu\,\mathrm{cm}^{-2}\,\mathrm{s}^{-1}$$

$$\Phi_{\mathrm{ES}} = 1.811^{+0.238}_{-0.214}\,(\mathrm{stat.})\,^{+0.080}_{-0.073}\,(\mathrm{syst.})\ \times 10^6\,\nu\,\mathrm{cm}^{-2}\,\mathrm{s}^{-1}$$

$$\Phi_{\mathrm{NC}} = 5.443^{+0.329}_{-0.327}\,(\mathrm{stat.})\,^{+0.318}_{-0.301}\,(\mathrm{syst.})\ \times 10^6\,\nu\,\mathrm{cm}^{-2}\,\mathrm{s}^{-1}$$

The ratio of CC to NC fluxes, which is the fraction of electron neutrinos in the active neutrino flux, was found to be

$$\frac{\Phi_{\mathrm{CC}}}{\Phi_{\mathrm{NC}}} = 0.318^{+0.030}_{-0.031}\,(\mathrm{total})$$

The uncertainty on the CC flux was improved compared to previous SNO measurements. This was because improvements in the optical calibration of the detector were able to compensate for the scattering and absorption of Čerenkov light by the NCDs; NC events were removed from the PMT stream by the NCD array; and because of the relatively high energy threshold, which reduced the contamination of the CC signal by background events. The NC flux was found to be in good agreement with previous phases and with the BS2005 standard solar model, which predicted a flux of $5.69 \times 10^6\, \nu\, \mathrm{cm}^{-2}\, \mathrm{s}^{-1}$. The probability of agreement between the CC, ES and NC fluxes measured during the NCD phase and those in the D_2O and Salt phases was estimated to be 32.8%.

On the assumption that the reduced flux of electron neutrinos was due to neutrino oscillations and that CPT invariance holds, a global fit to the results of earlier SNO phases, other solar experiments and the reactor anti-neutrino experiment KamLAND yielded the neutrino mixing parameters

$$\Delta m^2 = 7.94^{+0.42}_{-0.26} \times 10^{-5}\ \mathrm{eV}^2 \qquad \theta = 33.8^{+1.4}_{-1.3}\ \mathrm{degrees}$$

The NCD phase thus met its stated goals of making an independent measurement, of comparable precision, of the total active flux of ^{8}B neutrinos, with systematic uncertainties different to those in previous phases of the experiment. The results were in agreement with previous phases and with the predictions of standard solar models.

This thesis has presented an analysis of the final set of ^{8}B neutrino data taken by the SNO experiment. Even so, the most precise results of the experiment are yet to come, and will be achieved though joint fits to data taken in different phases. The first step in this program will be combining the results of the D_2O and Salt phase; it will be concluded by a joint analysis of all three phases. The results of these fits, in combination with the results of the KamLAND experiment, will likely provide the most accurate measurements of the solar sector neutrino mixing parameters for many years to come.

Appendix A

The decay schemes of ^{232}Th and ^{238}U

Figures A.2 and A.1 show the decay chains of ^{232}Th and ^{238}U respectively.

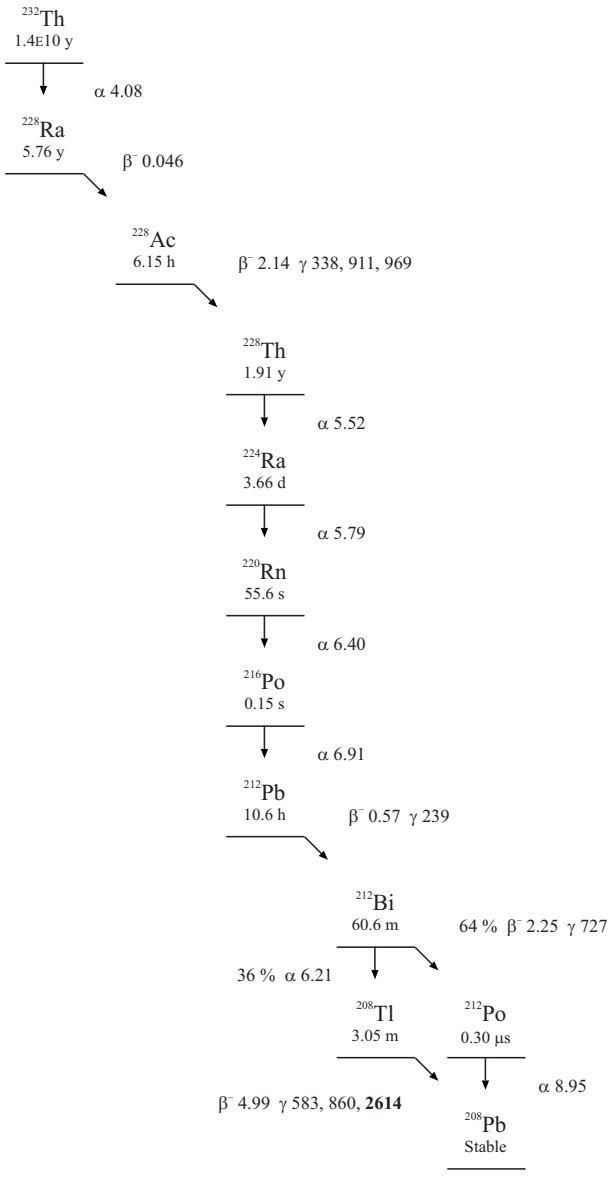

Figure A.1: The ^{232}Th decay chain. The Q-values are quoted in MeV and the gamma energies in keV. Adapted from [19].

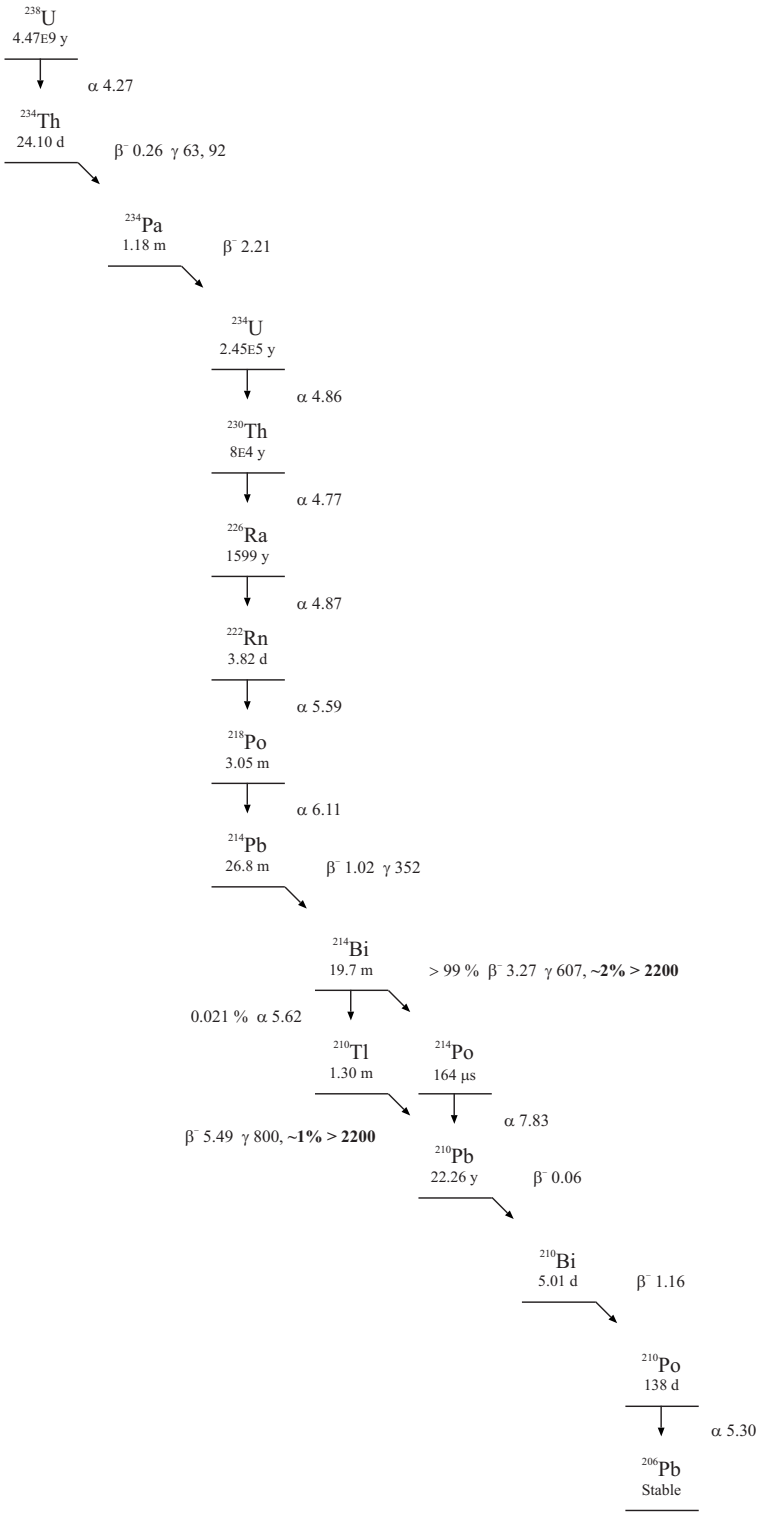

Figure A.2: The ^{238}U decay chain. The Q-values are quoted in MeV and the gamma energies in keV. Adapted from [19].

Appendix B

Combining measurements

This appendix describes the method used in this thesis to combine statistically independent measurements of the same quantity. It is taken from [168].

The weighted average of a set of N uncorrelated measurements $x_i \pm \delta x_i$ of the same quantity is given by

$$\bar{x} \pm \delta\bar{x} = \frac{\sum_i w_i x_i}{\sum_i w_i} \pm \frac{1}{\left(\sum_i w_i\right)^2} \tag{B.1}$$

where the weights w_i are $w_i = 1/\delta x_i^2$.

The quantity $\chi^2 = \sum_i w_i(\bar{x} - x_i)^2$ can be compared to $N-1$, which is the expected value if the measurements are Gaussian distributed. Three situations can be distinguished:

1. If $\chi^2/(N-1)$ is less than or equal to one then the measurements are compatible and $\bar{x} \pm \delta\bar{x}$ can be accepted.

2. If $\chi^2/(N-1)$ is very large there may be a problem with some of the data and the cause should be investigated.

3. If $\chi^2/(N-1)$ is a little greater than 1 there is evidence that one or more of the error bars may be under-estimated. This can be compensated for by scaling up $\delta\bar{x}$ by S, which is defined as

   $$S = \frac{\chi^2}{\sqrt{N-1}} \tag{B.2}$$

   It should be noted that finding $\chi^2/(N-1) > 1$ does not mean that any any error has definitely been underestimated as $\chi^2/(N-1)$ itself has a distribution that extends above 1 even for compatible measurements. Scaling by S will therefore tend to give a conservative uncertainty.

Appendix C

The SNOMAN geometry

This appendix gives a brief overview of the SNOMAN geometry code (a more detailed account can be found in [169]). The author was responsible for increasing the scope and complexity of the geometry model, but made few modifications to the organisation of the of the code.

C.1 Requirements and structure of the code

The SNOMAN geometry code supplied information on the detector geometry to other areas of the code, most notably those concerned with particle propagation. It was designed to deal with 4 types of request, through a standard interface:

NEXT Return the distance to the next boundary in a given direction.

NEAR Return the distance to the closest boundary in any direction.

PICK Randomly pick a point in a region.

REGION Find the region corresponding to a given point.

The principle requirements of the code were speed and flexibility. SNOMAN balanced these often conflicting demands by using the following structure:

- Geometry *regions* representing distinct parts of the detector, such as a calibration source can or the AV, were constructed from combinations of geometry *primitives* such as cylinders and spheres. Each region was composed of a single material and is assigned a *region code*.

- The logical relationships between the primitives constituting a region, or between different regions, were hardwired. The exact dimensions and positions were specified in data files.
- Each data file was divided into *design* and *deployment* sections. The design section listed the dimensions and relative positions of the primitives; the deployment section gave the absolute position of the region in the detector.
- Each region knew only about other regions with which it shares internal or external boundaries.
- Boundaries between regions were decided based on relative priorities, which were specified for each region in its data file.

Each primitive was described by a routine that could handle NEXT, NEAR and PICK requests. Each region had a routine defining the relationship between its primitives, which called their routines as appropriate, and handed the net result to the geometry interface.

To maximise speed and efficiency, similar objects (defined as objects differing in dimension and position, but not in structure) were grouped together into *arrays*, under a single region code. Each member of the array had a different *serial number*. The array routines knew about their members and efficiently answered requests relating to them; for example, in a NEAR request for the NCD array the routine identified the closest string to the reference point by simple geometry and make a NEAR call to that string only; this saved 39 unnecessary NEAR calls to the other strings.

There were additional routines for handling special cases, such as the ^{4}He NCD strings. From the point of view of the geometry code these had an identical structure to ^{3}He strings, but from the point of view of particle propagation they were of course different. The ^{4}He string *boundary manager* removed the need for large amounts of code repetition by concealing the difference between ^{3}He and ^{4}He strings from the geometry code, while keeping the differences visible to the rest of SNOMAN.

C.2 Testing the geometry

The hybrid structure of the geometry code, partly hardwired and partly specified in data files, meant objects can only be visualised by building up images using a Monte Carlo method: simulated neutrinos were propagated through the geometry and the positions

of their boundary interactions recorded. These positions were used to form images that allowed the relative positions and orientations of primitives and regions to be checked. A typical example is shown in Figure C.1.

Geometry errors were failures of the code due to inconsistencies in the geometry specification. The structure of the code made these easy to introduce and challenging to debug. They were located as part of the viewing process - when a trajectory failed one of the in-built consistency checks the cause was found by examining the coordinates and nature of the failure. Geometry errors always occurred in SNOMAN at some level and keeping that level low was important as they could bias the results of simulations.

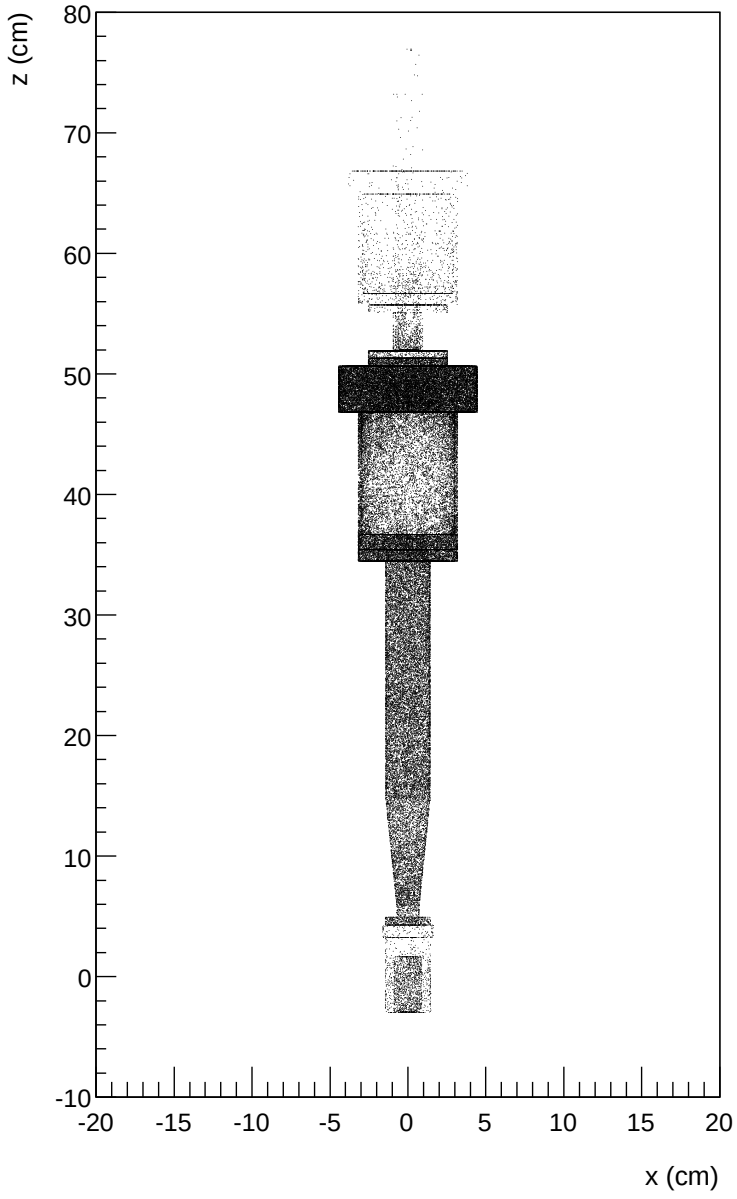

Figure C.1: The canned ^{24}Na source and manipulator, as modelled in SNOMAN. The dots are the intersections of simulated neutrino events with the boundaries of geometry regions.

Appendix D

Time series analysis

The time series analysis (TSA) [170, 92, 171] was used to analyse data taken using the ^{252}Cf fission source, which produced bursts of neutrons and prompt fission gammas.

TSA fitted the joint distribution of time intervals before and after events to an analytical model whose parameters were

- Neutron detection efficiency.
- Prompt fission gamma ray detection efficiency.
- Source strength.
- Background event rate.
- Neutron mean life.

Neutron events tended to occur in bursts; the first event in a burst could be a prompt gamma; and a lone event was likely to be a gamma or a background. The main assumptions were the shape of the neutron multiplicity distribution and that the media was homogeneous and large on the scale of the neutron mean free path. The latter assumption was a good one in the salt phase and, despite the introduction of the NCD counters, was adequate in the NCD phase, where the TSA could be used with pleasing results.

Appendix E

The mass attenuation coefficient

A beam of gammas is attenuated via absorption and scattering as it passes through material. For 1 MeV gammas, the chief mechanisms are pair production and Compton scattering, with the latter being dominant. Pair production becomes dominant at higher energies and photoelectric absorption at lower energies.

The *linear attenuation coefficient* is defined [172] as the fraction of gammas removed from a monoenergetic beam per unit thickness of material. The *mass attenuation coefficient* μ/ρ is the linear attenuation coefficient normalised for unit density of material. It has units of $\mathrm{cm}^2\,\mathrm{g}^{-1}$.

For a monoenergetic beam of gammas incident on a slab of material with mass attenuation coefficient μ/ρ the fraction transmitted through a *mass thickness* x without interacting is

$$\frac{N}{N_0} = e^{-(\mu/\rho)x_\rho} \tag{E.1}$$

where x_ρ is measured in $\mathrm{g\,cm}^{-2}$.

Tables listing mass attenuation coefficients as a function of energy are available for different elements [129]. The mass attenuation coefficients of compounds and mixtures can be calculated from these using the formula

$$\mu/\rho = w_i \sum_i (\mu/\rho)_i, \tag{E.2}$$

where w_i is the fraction by weight of the i^{th} atomic constituent.

Appendix F

The total peak area method

The total peak area method for peak integration described here is a variant of the method detailed in [173] and the book by Gilmore [174].

Regions of spectrum either side of a peak are used to estimate the background beneath it, on the assumption that the background is linear. Linearity is often a reasonable assumption but can fail if the peak lies on the Compton edge of another. The regions are located at set multiples of the peak full width at half maximum (FWHM) above and below the peak centroid. The inferred background count rate is deducted from the integral of the spectrum between the regions. This subtraction is shown schematically in Figure F.1 and the algorithm is described below.

- *Choosing the region of interest.*

  A *region of interest* (ROI) about each peak is identified by eye. It encompasses the peak and excludes significant distortions to the background shape caused by neighbouring peaks.

- *Identifying background regions.*

  The background regions have width m bins and are located at set multiples of the peak FWHM above and below the peak.

  1. The maximum bin in the ROI is used as the first estimate for the peak centroid. This first estimate is refined by fitting a Gaussian over a small range (in this study, ± 4 bins) about the peak.
  2. The average count rate at the extremes of the ROI C_0 is used as a first estimate of the background rate. The expected count at half-height $C_{1/2}$ is given in terms

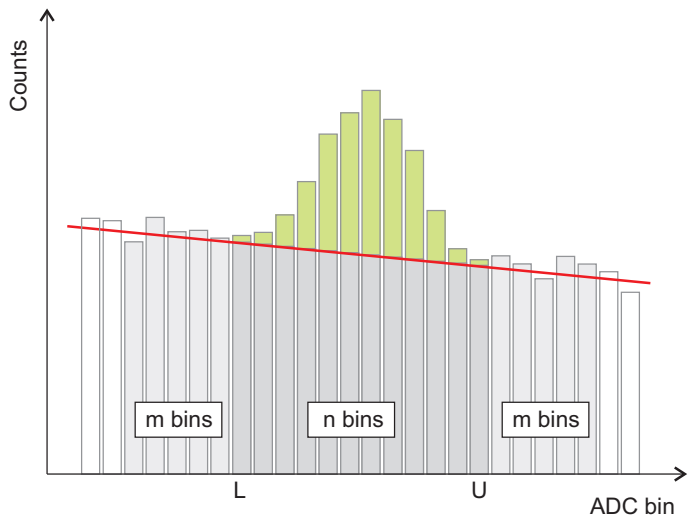

Figure F.1: Schematic diagram illustrating the TPA method.

of C_0 and the peak height C_T by

$$C_{1/2} = \frac{C_T - C_0}{2}$$

3. An interpolation is performed between the channels with counts just above and below $C_{1/2}$ either side of the peak (channels A and B below, and channels C and D above) identifying the bin values at the lower and upper ends of the FWHM, denoted by H_L and H_U. The FWHM is then given by

$$\Gamma = H_U - H_L$$

where,

$$H_L = A + \left(\frac{C_{1/2} - C_A}{C_B - C_A} \right)$$

and,

$$H_U = C + \left(\frac{C_C - C_{1/2}}{C_C - C_D} \right)$$

C_A, C_B, C_C, C_D are the counts in channels A, B, C and D respectively.

- *Subtracting the background.*

  The edges of the high and low background regions nearest to the peak begin at set numbers of FWHMs above and below the peak centroid. The lower region runs

from bins $(L-m)$ to $(L-1)$ and the upper region from bins $(U+1)$ to $(U+m)$. The peak area A is then given by

$$A = \sum_{i=L}^{U} C_i - n\left[\sum_{i=L-m}^{L-1} C_i + \sum_{U+1}^{U+m} C_i\right] / 2m \tag{F.1}$$

where C_i is the number of counts in each bin, n is number of bins between L and U inclusive and m is the number of bins in each background region.

- *Calculating uncertainties.*

  The statistical uncertainty on A due to the number of counts in the background integration regions is given by

$$\sigma_A^2 = \sum_{i=L}^{U} C_i + n^2\left[\sum_{i=L-m}^{L-1} C_i + \sum_{U+1}^{U+m} C_i\right] / 4m^2 \tag{F.2}$$

  To estimate a systematic uncertainty, the location of the background regions can be varied, and the standard deviation taken of the resulting peak counts. In this study the default position of the background region below the peak was 5.5×FWHM and above was 4.0×FWHM. To calculate the systematic uncertainty the positions above and below were varied by ±0.5×FWHM.

The method was found to be robust when tested on idealised fake data composed of Gaussians on a linear background, with bin contents fluctuated according to Poisson statistics.

Appendix G

The composition of the mixed source

Table G.1 shows the composition of the mixed source epoxy matrix, derived from information supplied by [20].

Table G.1: The atomic composition of the epoxy media [20].

Element	Isotope	Number (%)	Mass (%)
Hydrogen	^{1}H	43.9246	4.2395
	^{2}H	0.0026	0.0005
Carbon	^{12}C	18.2585	20.9831
	^{13}C	0.1822	0.2269
Oxygen	^{16}O	20.9047	32.0220
	^{17}O	0.0075	0.0122
	^{18}O	0.0382	0.0658
Sodium	^{23}Na	8.0847	17.8000
Silicon	^{28}Si	4.2168	11.2982
	^{29}Si	0.2067	0.5737
	^{30}Si	0.1317	0.3782
Sulphur	^{32}S	3.8475	11.7808
	^{33}S	0.0299	0.0943
	^{34}S	0.1637	0.5324
	^{36}S	0.0007	0.0025

Appendix H

Neutron poison in the NCD phase

H.1 Introduction

This appendix presents an investigation into the use of a neutron poison as a technique for measuring the non-neutron background in the NCD array.

Neutron poisons are isotopes with large neutron capture cross sections that can be dissolved in the heavy water to absorb neutrons to prevent them reaching the NCD array. Running with poison can effectively switch off the NC signal and allow a data set of background events to be collected. These can be used to form background PDFs or to directly measure the event rate.

The use of a poison would only have been attractive if there were large systematics associated with a poor understanding of the background. It was actively considered at a time when there were difficulties in reproducing measured alpha pulse shapes and after the discovery of instrumental events on strings J3 and N4 that that had similar pulse shapes to neutrons. A poison run turned out not to be necessary and so this study, of the statistical power of a poison run, is presented only as an appendix.

The first section investigates the effectiveness of different compounds as neutron poisons. The next two sections examine the sensitivity of different ways to use the poison data: in a statistical subtraction of poison from neutrino (non-poison) data, and using it to create background PDFs for fits to the neutrino data.

H.2 Neutron poisons

A good candidate for a neutron poison is an isotope that will absorb a large fraction of the NC neutrons per unit mass added to detector. It should dissolve in D_2O, be easily introduced and removed using existing water systems, and be available in high purity. Importantly, it should introduce only small amounts of radioactivity into the detector; radioactive contaminants could lessen the effect of the poison, by generating photodisintegration neutrons, or contaminate the NCDs and AV, limiting their use in further experiments.

The SNO water group suggested compounds which met these criteria [175] and their effectiveness was compared. NaCl, at its salt phase concentration of 1.96 t per 1000 t of D_2O, was used as a reference. For this concentration, NCD phase NaCl Monte Carlo simulations gave an array capture efficiency of 5.8%. The masses of the various compounds required to reach this efficiency and also 2.5%, 1.0% and 0.5% were calculated by scaling this result by the ratio of atomic masses and cross sections (see Table H.1). The results are given in Table H.2. Gadolinium compounds were promising candidates; they have extraordinarily high neutron capture cross sections (120 kg of $Gd_2(CO_3)_3$ would absorb 98% of the neutrons) and a history of use in low background neutrino experiments (see, for example, [176]).

Table H.1: Isotopic and elemental neutron capture cross sections [24].

Element / isotope	Mass (u)	σ (b)	Abundance
^{10}B	3835.00	10.01	0.199
^{35}Cl	44.10	34.97	0.758
^{155}Gd	61100.00	154.92	0.148
^{157}Gd	259000.00	156.92	0.157
^{113}Cd	20600.00	112.90	0.122
Gd	157.250	49705.80	
Cd	112.411	2513.20	
B	10.811	763.17	
Cl	35.453	33.43	
N	14.007	1.90	
O	15.999	0.00019	
H	1.008	0.33	
Na	22.990	0.53	
C	12.011	0.0035	

Table H.2: Candidate neutron poisons. The figures in the 'injected mass' column indicate the mass of the compound required to reduce the NCD array capture efficiency to each of the specified levels. The 'H_2O contamination' column indicates the masses of H_2O added to detector in the form of H_2O molecules.

Name	Formula		Mass	σ	Injected mass (t)				H_2O contamination			
	Full	Calculation	(u)	(b)	5.8%	2.5%	1.0%	0.5%	5.8%	2.5%	1.0%	0.5%
Gadolinium nitrate	$Gd(NO_3)_3.xH_2O$	$Gd(NO_3)_3$	295.27	49706	0.0070	0.0217	0.0636	0.1596				
Gadolinium chloride	$GdCl_3.6H_2O$	$GdCl_3$	263.61	49706	0.0062	0.0193	0.0567	0.1425				
	$GdCl_3.6H_2O$	$GdCl_3.6H_2O$	291.70	49706	0.0069	0.0214	0.0628	0.1576	0.0026	0.0079	0.0233	0.0584
Gadolinium carbide	$Gd_2(CO_3)_3.xH_2O$	$Gd_2(CO_3)_3$	446.53	99412	0.0053	0.0164	0.0481	0.1207				
Gadolinium acetate	$Gd(O_2C_2H_3)_3.4H_2O$	$Gd(O_2C_2H_3)_3$	334.38	49706	0.0079	0.0245	0.0720	0.1807				
	$Gd(O_2C_2H_3)_3.4H_2O$	$Gd(O_2C_2H_3)_3.4H_2O$	406.44	49706	0.0096	0.0298	0.0875	0.2196	0.0017	0.0053	0.0155	0.0389
Cadmium chloride	$CdCl_2$	$CdCl_2$	183.32	2513	0.0855	0.2661	0.7805	1.9593				
Boric acid	H_3BO_3	H_3BO_3	61.83	763	0.0950	0.2955	0.8670	2.1763				
Sodium chloride	NaCl		58.44	35	1.9600	6.0960	17.8833	44.8917				

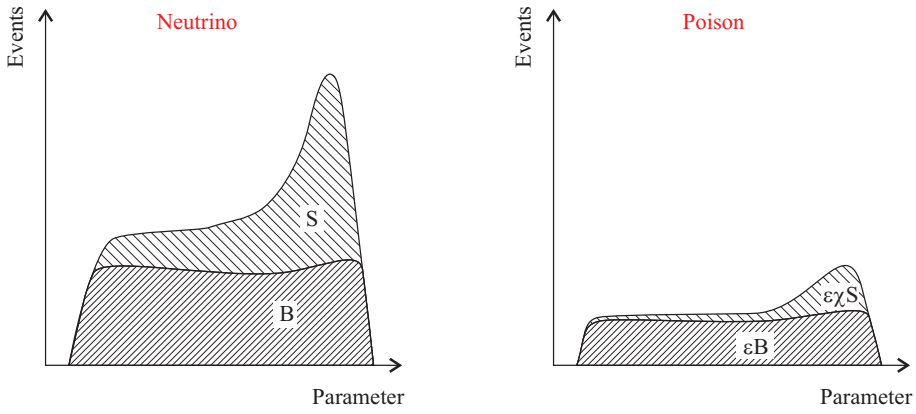

Figure H.1: Schematic diagram showing the effect of adding poison on the signal counts S and background counts B in a region of pulse parameter space. ε is the ratio of neutrino and poison livetimes and χ is the ratio of signal detection rates in the neutrino and poison phases (the effectiveness of the poison).

H.3 Statistical subtraction

H.3.1 Overview

This calculation applies to a worst case scenario in which neutron-background separation is reduced to the weighted subtraction of the number of counts in the neutrino and poison phases. It is the safest but least powerful way of using poison data. The subtraction is performed over a region of pulse parameter space (in this study, shaper-ADC energy). An analytical calculation shows how the uncertainty on the extracted number of neutrons depends on the length of the poison phase and on the effectiveness of the poison.

H.3.2 Method

N_ν and N_p are the numbers of detected events, in the region of pulse parameter space, in the neutrino and poison phases. They can be written in terms of the number of signal pulses S and background pulses B (see Figure H.1)

$$N_\nu = S + B \tag{H.1}$$

$$N_p = \varepsilon\chi S + \varepsilon B, \tag{H.2}$$

where ε is the ratio of the poison and neutrino livetimes and χ is the *effectiveness* of the poison, the ratio of signal detection rates in the neutrino and poison phases. No account

is taken of external neutrons, photodisintegration neutrons, or any other background whose rate would be altered by the use of poison; the background consists of alphas and instrumentals. Due to the geometry of the NCD array, external neutrons would be preferentially removed compared with NC neutrons; most photodisintegration neutrons would be removed with similar probability.

Eliminating B between Equations H.1 and H.2 gives an expression for S in terms of the measured numbers of events N_ν and N_p

$$S = \frac{1}{1-\chi}\Big(N_\nu - \frac{1}{\varepsilon}N_p\Big) \tag{H.3}$$

Assuming Gaussian errors, the variance of S is

$$\sigma_S^2 = \frac{1}{(1-\chi)^2}\Big(S + B + \frac{\chi}{\varepsilon}S + \frac{1}{\varepsilon}B\Big) \tag{H.4}$$

If there are α background events observed per signal event in the neutrino phase then

$$B = \alpha S \tag{H.5}$$

which, substituted into H.4, gives the uncertainty on S

$$\sigma_S = \sqrt{S}\cdot\frac{1}{1-\chi}\sqrt{1+\alpha+\frac{\chi}{\varepsilon}+\frac{\alpha}{\varepsilon}} \tag{H.6}$$

For a perfect poison $\chi = 0$ and

$$\sigma_S = \sqrt{S}\cdot\sqrt{1+\alpha\Big(1+\frac{1}{\varepsilon}\Big)} \tag{H.7}$$

Equation H.6 shows that the uncertainty on S can be reduced by increasing the ratio of the poison and neutrino livetimes ε, by decreasing the background to signal ratio α and by increasing the effectiveness of the poison χ. Only the last of these does not involve a sacrifice of signal statistics. Altering the signal-background ratio means placing a cut in the pulse parameter space and increasing the length of the poison phase means a reduction in signal livetime.

H.3.3 Results

Estimates for parameters needed to evaluate σ_S are given in Table H.3. The background to signal ratio in the neutron region has the largest uncertainty: Stonehill [138] analysed

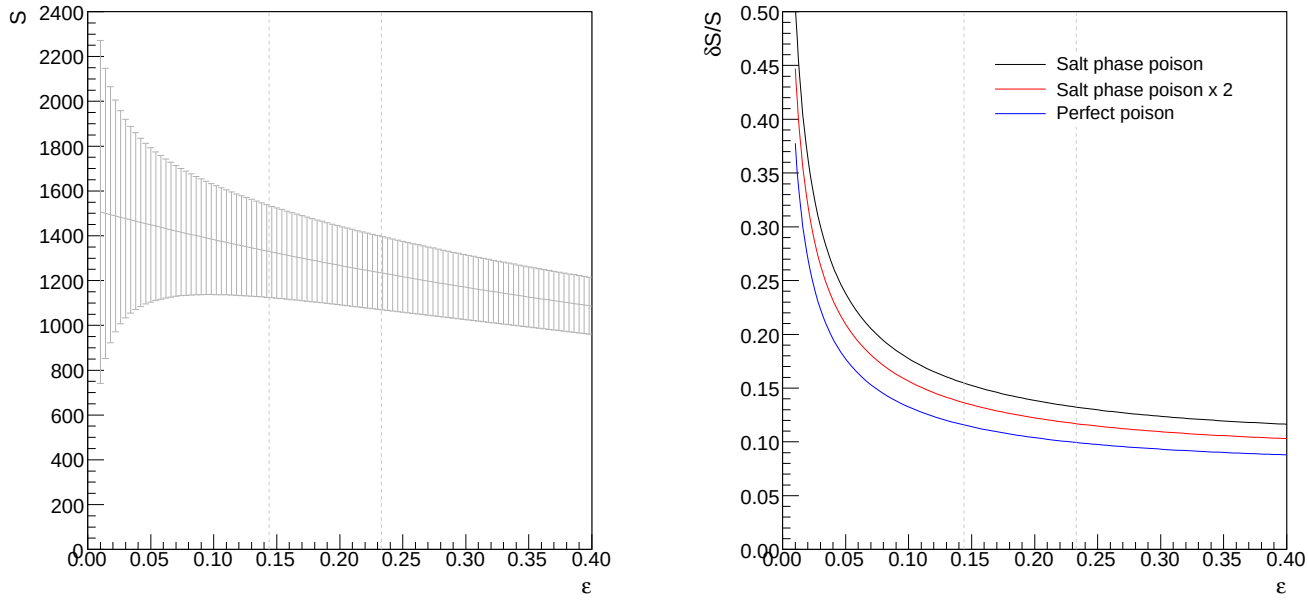

Figure H.2: Extracted number of neutrons and fractional error as a function of the ratio of neutrino and poison livetimes. Salt phase poisoning is assumed in the left hand plot. The vertical lines correspond to poison livetimes of 60 and 90 days.

Table H.3: Assumptions made on parameters relevant to signal-background discrimination.

Parameter	Value
NCD phase live days	477
NC neutron production rate	12.5 day^{-1}
NCD array neutron capture efficiency	26.5%
Extrapolation background to signal ratio	6.636
Fit background to signal ratio	2.115

Table H.4: Uncertainties on the extracted number of neutrons for various model parameters. χ is the ratio of signal rates in the neutrino and poison phases (the effectiveness of the poison) and E is the shaper-ADC energy.

Poison level	Cut	Bkgrd. to signal ratio (α)	Poison phase (d)	Subtraction neutrons		
				Mean	Unc.	Frac. (%)
Perfect ($\chi = 0.0$)	None	2.115	60	1381	156.9	11.36
			120	1183	105.5	8.92
		6.636	60	1381	272.5	19.73
			120	1183	179.9	15.22
Perfect ($\chi = 0.0$)	$650 < E < 820$ MeV	0.891 (from 2.115)	60	997	89.8	9.00
			120	854	62.3	7.29
		2.795 (from 6.636)	60	997	152.2	15.26
			120	854	101.7	11.91
Salt ($\chi = 0.22$)	None	2.115	60	1381	209.6	15.17
			120	1183	139.8	11.83
		6.636	60	1381	354.3	25.65
			120	1183	233.4	19.74

the open (non-blind) neutrino data set, by extrapolating the background into the neutron region from higher energy, and found a ratio of 6.636 with an estimated uncertainty of $\sim$15%. A subset of the blind neutrino data gave a ratio of 2.115 in an analysis where the energy spectrum in the neutron region was fit to a combination of ^{24}Na neutron and ^{4}He background energy spectra. The difference was due to the blindness scheme and the simplicity of the open data analysis. Both ratios are used in this analysis and can be considered upper and lower limits.

Figure H.2 shows fractional and absolute uncertainties on S as a function of ε for different poison strengths. Similar results were obtained if a cut was placed on pulse energy.

Table H.4 shows the uncertainties on S for various model parameters and cuts. The improvement in fractional uncertainty with an energy cut was substantial.

H.4 Poison phase background PDFs

H.4.1 Overview

This study considers a scenario in which the poison is effectively perfect and the poison data provides a background PDF for use in neutrino flux fits. Neutrino data were fit to a combination of the ^{24}Na neutron and poison background PDFs.

The low statistics on the poison background introduced a significant uncertainty into the fit result. It was accounted for by using the elegant method of Barlow and Beeston [177], which fits data to a combination of PDFs taking into account statistical uncertainties of both the data and PDFs. It is an extension of the standard maximum likelihood technique that allows the Monte Carlo predictions to float in the fit using an analytical approximation. The technique also allows for empty PDF bins.

An ensemble of neutrino flux fits on fake data were used to assess the statistical power of fits based on background PDFs extracted from poison phase data.

H.4.2 Method

For convenience energy was chosen as the observable. Pulse width or a combination of pulse shape parameters could equally well have been used.

A neutron energy PDF was formed using 2005 ^{24}Na data. The true background energy spectrum was assumed to be flat and 1000 fake poison data sets were randomly sampled, allowing the total number of events in each data set to vary according to Poisson statistics.

1000 fake neutrino data sets were sampled from the neutron and true background PDFs, again allowing the total numbers of events to vary. Each fake data set was fit using the neutron PDF and one of the poison background PDF. The fit numbers of neutrons from each fit were binned and fit to a Gaussian whose width was taken as the uncertainty.

H.4.3 Results

An example fit is shown in Figure H.3 and the results of the ensemble tests are shown in Table H.5. As might be expected, using the poison data to form a background PDF improves on the results of the statistical subtraction, though the improvement is small if an energy cut applied to the latter.

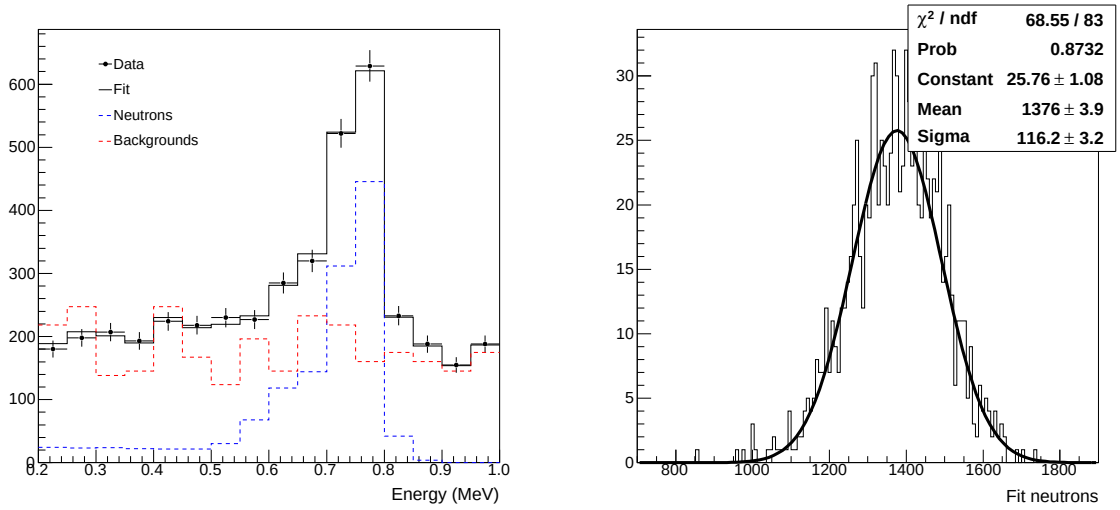

Figure H.3: Example fit using a 60 day poison phase PDF and a background to signal ratio of 2.115.

Table H.5: Fit results.

Bkgrd. to signal ratio (α)	Poison phase (days)	Mean neutrino events		Poison events	Fit neutrons		
		Neutron	Bkgrd.		Mean	Unc.	Frac. (%)
2.115	60	1381	2921	420	1376.0	116.2	8.45
2.115	120	1183	2501	841	1184.6	75.6	6.38
6.636	60	1381	9166	420	1367.9	183.1	13.38
6.636	120	1183	7847	841	1181.2	122.8	10.40

Appendix I

Neutrino flux fit results

This appendix presents a more detailed breakdown of neutrino flux fit results

Table I.1: Physics signal fluxes (Monte Carlo alpha PDF).

Signal	Value	Fit.	Sys.	Total
Fit neutrino fluxes ($10^6\,\nu\,\mathrm{cm}^{-2}\,\mathrm{s}^{-1}$)				
CC	1.733	0.049	0.068	0.084
ES	1.817	0.226	0.078	0.239
NC	5.443	0.430	0.136	0.451
CC01	1.588	0.149	0.056	0.159
CC02	1.882	0.145	0.059	0.156
CC03	1.748	0.134	0.054	0.145
CC04	1.674	0.132	0.052	0.141
CC05	1.676	0.134	0.053	0.144
CC06	1.575	0.138	0.060	0.150
CC07	1.779	0.159	0.076	0.176
CC08	1.660	0.167	0.084	0.187
CC09	2.197	0.219	0.127	0.253
CC10	1.885	0.226	0.133	0.262
CC11	1.544	0.239	0.127	0.271
CC12	1.819	0.308	0.167	0.350
CC13	1.774	0.235	0.236	0.333
ES01	2.005	0.570	0.070	0.574
ES02	0.657	0.508	0.036	0.509
ES03	2.600	0.663	0.092	0.670
ES04	2.417	0.726	0.101	0.733
ES05	1.403	0.675	0.059	0.678
ES06	2.171	0.826	0.090	0.831
ES07	2.884	1.065	0.151	1.076
ES08	1.902	0.967	0.080	0.970
ES09	0.088	0.899	0.040	0.899
ES10	0.248	0.920	0.027	0.921
ES11	1.475	1.252	0.102	1.256
ES12	1.434	1.531	0.148	1.538
ES13	3.095	1.368	0.353	1.413

Table I.2: Physics signal events (Monte Carlo alpha PDF).

Signal	Value	Fit.	Sys.	Total
Derived neutrino events				
CC	1881.1	53.6	19.5	57.0
ES	169.7	21.1	3.5	21.4
NC PMT	254.3	20.1	16.5	26.0
NC NCD	962.8	76.0	24.1	79.8
CC01	222.8	20.9	4.6	21.4
CC02	263.5	20.2	4.6	20.8
CC03	234.8	18.0	3.5	18.4
CC04	210.9	16.6	2.5	16.8
CC05	190.6	15.2	1.4	15.3
CC06	156.9	13.7	1.1	13.7
CC07	148.6	13.3	0.8	13.3
CC08	112.8	11.3	0.5	11.3
CC09	117.2	11.7	0.4	11.7
CC10	76.2	9.1	0.2	9.1
CC11	45.3	7.0	0.1	7.0
CC12	37.6	6.4	0.1	6.4
CC13	63.6	8.4	0.2	8.4
ES01	33.1	9.4	0.7	9.4
ES02	9.5	7.4	0.4	7.4
ES03	32.4	8.3	0.5	8.3
ES04	25.6	7.7	0.6	7.7
ES05	12.3	5.9	0.3	5.9
ES06	15.8	6.0	0.3	6.0
ES07	16.9	6.2	0.5	6.3
ES08	8.9	4.5	0.1	4.5
ES09	0.3	3.2	0.2	3.2
ES10	0.7	2.5	0.0	2.5
ES11	3.0	2.5	0.1	2.5
ES12	2.1	2.2	0.1	2.2
ES13	9.2	4.1	0.2	4.1

Table I.3: Background events and fit systematics (Monte Carlo alpha PDF).

Signal	Value	Fit.	Sys.	Total
Fit background detected events				
α	5672.1	214.1	20.8	215.2
J3 3NA	479.2	203.2	100.7	226.8
N4 3NA	0.0	0.9	97.2	97.2
n-like (PMT)	27.9	5.2	0.0	5.2
n-like (NCD)	36.4	15.6	0.1	15.6
Fit background PD / AV(α,n) produced neutrons				
AV(α,n)	2764.0	1343.5	32.7	1343.9
K2	146.0	23.5	0.1	23.5
K5	120.9	13.9	0.0	13.9
Bulk	79.0	36.5	0.1	36.5
Uni.	170.6	25.9	0.0	25.9
Derived background PD / AV(α,n) detected neutrons				
AV(α,n) (PMT)	18.6	9.1	1.7	9.2
K2 (PMT)	9.3	1.5	0.5	1.6
K5 (PMT)	8.4	1.0	0.5	1.1
Bulk (PMT)	4.7	2.2	0.2	2.2
Uni. (PMT)	8.2	1.2	0.5	1.3
AV(α,n) (NCD)	26.9	13.1	0.3	13.1
K2 (NCD)	32.8	5.3	0.0	5.3
K5 (NCD)	31.6	3.6	0.0	3.6
Bulk (NCD)	27.9	12.9	0.1	12.9
Uni. (NCD)	31.0	4.7	0.0	4.7
Total n bkgrd. (PMT)	77.1	10.9	3.2	11.4
Total n bkgrd. (NCD)	186.6	25.4	0.4	25.4
Fit systematics				
b_0	1.200	0.703	0.078	0.707
b_1	-0.017	0.838	0.078	0.842
b_2	-0.262	0.992	0.027	0.992
b_3	0.011	0.946	0.045	0.947
b_4	0.028	1.001	0.004	1.001
b_5	-0.051	0.968	0.039	0.969
b_6	-0.415	0.952	0.025	0.952
α_{J3}	0.469	0.022	0.010	0.024
α_{N4}	0.026	0.014	0.002	0.014
$\varepsilon_{NC}(PMT)$	0.049	0.001	0.000	0.001
$\varepsilon_{NC}(NCD)$	0.211	0.007	0.000	0.007

Table I.4: PMT correlation matrix (Monte Carlo alpha PDF).

	C01	C02	C03	C04	C05	C06	C07	C08	C09	C10	C11	C12	C13	E01	E02	E03	E04	E05	E06	E07	E08	E09	E10	E11	E12	E13	NC	AV	K2	K5	Bulk	Uni.
CC01	1.00	0.09	0.06	0.04	0.03	0.02	0.01	0.01	0.00	0.00	0.00	0.00	0.00	-0.24	0.01	0.01	0.00	0.00	0.00	0.00	0.00	0.00	0.00	0.00	0.00	0.00	-0.28	-0.12	0.00	0.00	0.02	-0.00
CC02	0.09	1.00	0.04	0.03	0.02	0.01	0.01	0.01	0.00	0.00	0.00	0.00	0.00	0.01	-0.27	0.00	0.00	0.00	0.00	0.00	0.00	0.00	0.00	0.00	0.00	0.00	-0.21	-0.07	0.00	0.00	0.02	-0.00
CC03	0.06	0.04	1.00	0.02	0.01	0.01	0.01	0.00	0.00	0.00	0.00	0.00	0.00	0.01	0.01	-0.22	0.00	0.00	0.00	0.00	0.00	0.00	0.00	0.00	0.00	0.00	-0.14	-0.05	0.00	0.00	0.01	0.00
CC04	0.04	0.03	0.02	1.00	0.01	0.01	0.00	0.00	0.00	0.00	0.00	0.00	0.00	0.00	0.00	0.00	-0.25	0.00	0.00	0.00	0.00	0.00	0.00	0.00	0.00	0.00	-0.09	-0.03	-0.00	-0.00	0.01	0.00
CC05	0.03	0.02	0.01	0.01	1.00	0.00	0.00	0.00	0.00	0.00	0.00	0.00	0.00	0.00	0.00	0.00	0.00	-0.24	0.00	0.00	0.00	0.00	0.00	0.00	0.00	0.00	-0.06	-0.02	-0.00	-0.00	0.00	0.00
CC06	0.02	0.01	0.01	0.01	0.00	1.00	0.00	0.00	0.00	0.00	0.00	0.00	0.00	0.00	0.00	0.00	0.00	0.00	-0.24	0.00	0.00	0.00	0.00	0.00	0.00	0.00	-0.04	-0.01	-0.00	-0.00	0.00	0.00
CC07	0.01	0.01	0.01	0.00	0.00	0.00	1.00	0.00	0.00	0.00	0.00	0.00	0.00	0.00	0.00	0.00	0.00	0.00	0.00	-0.26	0.00	0.00	0.00	0.00	0.00	0.00	-0.03	-0.00	-0.00	-0.00	0.00	0.00
CC08	0.01	0.01	0.00	0.00	0.00	0.00	0.00	1.00	0.00	0.00	0.00	0.00	0.00	0.00	0.00	0.00	0.00	0.00	0.00	0.00	-0.22	0.00	0.00	0.00	0.00	0.00	-0.02	-0.00	-0.00	-0.00	0.00	0.00
CC09	0.00	0.00	0.00	0.00	0.00	0.00	0.00	0.00	1.00	0.00	0.00	0.00	0.00	0.00	0.00	0.00	0.00	0.00	0.00	0.00	0.00	-0.35	0.00	0.00	0.00	0.00	-0.01	-0.00	-0.00	-0.00	0.00	0.00
CC10	0.00	0.00	0.00	0.00	0.00	0.00	0.00	0.00	0.00	1.00	0.00	0.00	0.00	0.00	0.00	0.00	0.00	0.00	0.00	0.00	0.00	0.00	-0.25	0.00	0.00	0.00	-0.01	-0.00	-0.00	-0.00	0.00	0.00
CC11	0.00	0.00	0.00	0.00	0.00	0.00	0.00	0.00	0.00	0.00	1.00	0.00	0.00	0.00	0.00	0.00	0.00	0.00	0.00	0.00	0.00	0.00	0.00	-0.19	0.00	0.00	-0.01	-0.00	-0.00	-0.00	0.00	0.00
CC12	0.00	0.00	0.00	0.00	0.00	0.00	0.00	0.00	0.00	0.00	0.00	1.00	0.00	0.00	0.00	0.00	0.00	0.00	0.00	0.00	0.00	0.00	0.00	0.00	-0.20	0.00	-0.00	-0.00	-0.00	0.00	0.00	0.00
CC13	0.00	0.00	0.00	0.00	0.00	0.00	0.00	0.00	0.00	0.00	0.00	0.00	1.00	0.00	0.00	0.00	0.00	0.00	0.00	0.00	0.00	0.00	0.00	0.00	0.00	-0.21	-0.00	-0.00	0.00	0.00	-0.00	0.00
ES01	-0.24	0.01	0.01	0.00	0.00	0.00	0.00	0.00	0.00	0.00	0.00	0.00	0.00	1.00	0.00	0.00	0.00	0.00	0.00	0.00	0.00	0.00	0.00	0.00	0.00	0.00	-0.03	-0.02	-0.00	0.00	0.00	-0.00
ES02	0.01	-0.27	0.01	0.00	0.00	0.00	0.00	0.00	0.00	0.00	0.00	0.00	0.00	0.00	1.00	0.00	0.00	0.00	0.00	0.00	0.00	0.00	0.00	0.00	0.00	0.00	-0.03	-0.00	-0.00	-0.00	0.00	-0.00
ES03	0.01	0.00	-0.22	0.00	0.00	0.00	0.00	0.00	0.00	0.00	0.00	0.00	0.00	0.00	0.00	1.00	0.00	0.00	0.00	0.00	0.00	0.00	0.00	0.00	0.00	0.00	-0.01	-0.00	0.00	-0.00	0.00	0.00
ES04	0.00	0.00	0.00	-0.25	0.00	0.00	0.00	0.00	0.00	0.00	0.00	0.00	0.00	0.00	0.00	0.00	1.00	0.00	0.00	0.00	0.00	0.00	0.00	0.00	0.00	0.00	-0.01	-0.00	-0.00	0.00	0.00	0.00
ES05	0.00	0.00	0.00	0.00	-0.24	0.00	0.00	0.00	0.00	0.00	0.00	0.00	0.00	0.00	0.00	0.00	0.00	1.00	0.00	0.00	0.00	0.00	0.00	0.00	0.00	0.00	-0.01	-0.00	-0.00	-0.00	0.00	0.00
ES06	0.00	0.00	0.00	0.00	0.00	-0.24	0.00	0.00	0.00	0.00	0.00	0.00	0.00	0.00	0.00	0.00	0.00	0.00	1.00	0.00	0.00	0.00	0.00	0.00	0.00	0.00	-0.00	-0.00	-0.00	0.00	0.00	0.00
ES07	0.00	0.00	0.00	0.00	0.00	0.00	-0.26	0.00	0.00	0.00	0.00	0.00	0.00	0.00	0.00	0.00	0.00	0.00	0.00	1.00	0.00	0.00	0.00	0.00	0.00	0.00	-0.00	0.00	-0.00	-0.00	0.00	0.00
ES08	0.00	0.00	0.00	0.00	0.00	0.00	0.00	-0.22	0.00	0.00	0.00	0.00	0.00	0.00	0.00	0.00	0.00	0.00	0.00	0.00	1.00	0.00	0.00	0.00	0.00	0.00	-0.00	-0.00	-0.00	0.00	0.00	0.00
ES09	0.00	0.00	0.00	0.00	0.00	0.00	0.00	0.00	-0.35	0.00	0.00	0.00	0.00	0.00	0.00	0.00	0.00	0.00	0.00	0.00	0.00	1.00	0.00	0.00	0.00	0.00	-0.00	0.00	0.00	-0.00	0.00	0.00
ES10	0.00	0.00	0.00	0.00	0.00	0.00	0.00	0.00	0.00	-0.25	0.00	0.00	0.00	0.00	0.00	0.00	0.00	0.00	0.00	0.00	0.00	0.00	1.00	0.00	0.00	0.00	-0.00	0.00	0.00	-0.00	0.00	0.00
ES11	0.00	0.00	0.00	0.00	0.00	0.00	0.00	0.00	0.00	0.00	-0.19	0.00	0.00	0.00	0.00	0.00	0.00	0.00	0.00	0.00	0.00	0.00	0.00	1.00	0.00	0.00	-0.00	0.00	0.00	-0.00	0.00	0.00
ES12	0.00	0.00	0.00	0.00	0.00	0.00	0.00	0.00	0.00	0.00	0.00	-0.20	0.00	0.00	0.00	0.00	0.00	0.00	0.00	0.00	0.00	0.00	0.00	0.00	1.00	0.00	-0.00	-0.00	-0.00	-0.00	-0.00	-0.00
ES13	0.00	0.00	0.00	0.00	0.00	0.00	0.00	0.00	0.00	0.00	0.00	0.00	-0.21	0.00	0.00	0.00	0.00	0.00	0.00	0.00	0.00	0.00	0.00	0.00	0.00	1.00	-0.00	-0.00	-0.00	0.00	0.00	0.00
NC	-0.28	-0.21	-0.14	-0.09	-0.06	-0.04	-0.03	-0.02	-0.01	-0.01	-0.01	-0.00	-0.00	-0.03	-0.03	-0.01	-0.01	-0.01	-0.00	-0.00	-0.00	-0.00	-0.00	-0.00	-0.00	-0.00	1.00	-0.17	-0.07	-0.05	-0.17	-0.06
EN	-0.12	-0.07	-0.05	-0.03	-0.02	-0.01	-0.00	-0.00	-0.00	-0.00	-0.00	-0.00	-0.00	-0.02	-0.00	-0.00	-0.00	-0.00	-0.00	0.00	-0.00	0.00	0.00	0.00	-0.00	-0.00	-0.17	1.00	0.00	0.00	0.00	-0.00
K2	0.00	0.00	0.00	-0.00	-0.00	-0.00	-0.00	-0.00	-0.00	-0.00	-0.00	-0.00	0.00	-0.00	-0.00	0.00	-0.00	-0.00	-0.00	-0.00	-0.00	0.00	0.00	0.00	-0.00	-0.00	-0.07	0.00	1.00	-0.00	-0.00	-0.00
K5	0.00	0.00	0.00	-0.00	-0.00	-0.00	-0.00	-0.00	-0.00	-0.00	-0.00	0.00	0.00	0.00	-0.00	-0.00	0.00	-0.00	0.00	-0.00	0.00	-0.00	-0.00	-0.00	-0.00	0.00	-0.05	0.00	-0.00	1.00	-0.00	-0.00
Bulk	0.02	0.02	0.01	0.01	0.00	0.00	0.00	0.00	0.00	0.00	0.00	0.00	-0.00	0.00	0.00	0.00	0.00	0.00	0.00	0.00	0.00	0.00	0.00	0.00	-0.00	0.00	-0.17	0.00	-0.00	-0.00	1.00	-0.00
Uniform	-0.00	-0.00	0.00	0.00	0.00	0.00	0.00	0.00	0.00	0.00	0.00	0.00	0.00	-0.00	-0.00	0.00	0.00	0.00	0.00	0.00	0.00	0.00	0.00	0.00	0.00	0.00	-0.06	-0.00	-0.00	-0.00	-0.00	1.00

Table I.5: NCD correlation matrix (Monte Carlo alpha PDF).

	NC	EN	K2	K5	Bulk	Uni.	J3 3NA	N4 3NA	Alphas	b_0	b_1	b_2	b_3	b_4	b_5	b_6	α_{J3}	α_{N4}	ε_{NC}
NC	1.00	-0.17	-0.07	-0.05	-0.17	-0.06	0.04	-0.05	-0.13	-0.09	0.16	0.08	0.08	-0.00	0.06	-0.02	-0.16	-0.01	-0.42
EN	-0.17	1.00	0.00	0.00	0.00	-0.00	0.00	-0.00	-0.00	-0.00	0.00	0.00	0.00	-0.00	0.00	-0.00	-0.00	-0.00	-0.00
K2	-0.07	0.00	1.00	-0.00	-0.00	-0.00	-0.00	0.00	0.00	0.00	-0.00	-0.00	-0.00	0.00	-0.00	0.00	0.00	0.00	0.00
K5	-0.05	0.00	-0.00	1.00	-0.00	-0.00	-0.00	0.00	0.00	0.00	-0.00	-0.00	-0.00	0.00	-0.00	0.00	0.00	0.00	0.00
Bulk	-0.17	0.00	-0.00	-0.00	1.00	-0.00	0.00	-0.00	-0.00	-0.00	0.00	0.00	0.00	-0.00	0.00	-0.00	-0.00	-0.00	0.00
Uniform	-0.06	-0.00	-0.00	-0.00	-0.00	1.00	-0.00	-0.00	-0.00	-0.00	0.00	0.00	0.00	-0.00	0.00	-0.00	-0.00	-0.00	0.00
J3 3NA	0.04	0.00	-0.00	-0.00	0.00	-0.00	1.00	0.23	0.85	-0.72	-0.38	-0.28	-0.21	-0.01	-0.13	0.24	0.10	0.03	-0.00
N4 3NA	-0.05	-0.00	0.00	0.00	-0.00	-0.00	0.23	1.00	-0.08	0.05	0.03	0.01	0.02	0.00	0.01	-0.01	0.05	0.15	0.00
Alphas	-0.13	-0.00	0.00	0.00	-0.00	-0.00	0.85	-0.08	1.00	-0.66	-0.42	-0.29	-0.23	-0.01	-0.15	0.24	0.14	-0.01	0.00
b_0	-0.09	-0.00	0.00	0.00	-0.00	-0.00	-0.72	0.05	-0.66	1.00	0.29	0.06	0.13	-0.02	0.14	0.31	-0.29	0.01	0.00
b_1	0.16	0.00	-0.00	-0.00	0.00	0.00	-0.38	0.03	-0.42	0.29	1.00	0.05	-0.22	-0.00	-0.15	0.05	0.03	0.00	-0.00
b_2	0.08	0.00	-0.00	-0.00	0.00	0.00	-0.28	0.01	-0.29	0.06	0.05	1.00	0.02	-0.01	0.03	-0.02	0.02	0.00	-0.00
b_3	0.08	0.00	-0.00	-0.00	0.00	0.00	-0.21	0.02	-0.23	0.13	-0.22	0.02	1.00	-0.00	-0.08	0.02	0.01	0.00	-0.00
b_4	-0.00	-0.00	0.00	0.00	-0.00	-0.00	-0.01	0.00	-0.01	-0.02	-0.00	-0.01	-0.00	1.00	-0.00	-0.01	-0.00	0.00	0.00
b_5	0.06	0.00	-0.00	-0.00	0.00	0.00	-0.13	0.01	-0.15	0.14	-0.15	0.03	-0.08	-0.00	1.00	0.03	0.02	0.00	-0.00
b_6	-0.02	-0.00	0.00	0.00	-0.00	-0.00	0.24	-0.01	0.24	0.31	0.05	-0.02	0.02	-0.01	0.03	1.00	0.04	-0.00	0.00
α_{J3}	-0.16	-0.00	0.00	0.00	-0.00	-0.00	0.10	0.05	0.14	-0.29	0.03	0.02	0.01	-0.00	0.02	0.04	1.00	0.01	0.00
α_{N4}	-0.01	-0.00	0.00	0.00	-0.00	-0.00	0.03	0.15	-0.01	0.01	0.00	0.00	0.00	0.00	0.00	-0.00	0.01	1.00	0.00
ε_{NC}	-0.42	-0.00	0.00	0.00	0.00	0.00	-0.00	0.00	0.00	0.00	-0.00	-0.00	-0.00	0.00	-0.00	0.00	0.00	0.00	1.00

Bibliography

[1] J. N. Bahcall. "Neutrino Astrophysics". Cambridge University Press (1989).

[2] J. N. Bahcall, A. M. Serenelli & S. Basu. *Astrophys J.*, **621** (2005) 85–88.

[3] J. N. Bahcall, M. H. Pinsonneault & S. Basu. *Astrophys J.*, **555** (2001) 990–1012.

[4] H. A. Bethe. *Phys. Rev. Lett.*, **56** (1986) 1305.

[5] S. Abe et al. *Phys. Rev. Lett.*, **100** (2008) 221803.

[6] P. Adamson et al. *hep-ex*, **arXiv:0807.2424v1**.

[7] J. Wilson. "A Measurement of the ^{8}B Solar Neutrino Energy Spectrum at the Sudbury Neutrino Observatory". Ph.D. thesis, University of Oxford (2004).

[8] The SNO Collaboration. *Nucl. Instrum. Meth. A*, **449**, 1–2 (2000) 172–207.

[9] B. Aharmin et al. *Phys. Rev. C*, **72** (2005) 055502.

[10] G. Guillian. "The Determination of the NCD Capture Rate of Neutrons Produced by ^{24}Na Brine Injected and Mixed in the SNO D_2O Volume". Technical report, The Sudbury Neutrino Observatory (2008).

[11] A. W. P. Poon. Private Communication (2004).

[12] M. Burke J. W. Marsh, D. J. Thomas. *Nucl. Instrum. Meth. A*, **255** (1975) 267–274.

[13] K. S. Krane. "Introductory Nuclear Physics". Wiley (1987).

[14] R. B. Firestone, C. M. Baglin & S. Y. F. Chu. "Table of Isotopes, 8th Edition". Wiley-Interscience (1999).

[15] Y. Nir-El. Private Communication (2008).

[16] S. J. Peeters. Private Communication (2006).

[17] J. Law. Private Communication (2008).

[18] S. Fukuda et al. *Phys. Lett. B*, **539** (2002) 179–187.

[19] C. Sims. "Background Determination in the Salt Phase of the Sudbury Observatory Experiment". Ph.D. thesis, University of Oxford (2005).

[20] "Zusammensetzung von Geometriestrahlern mit Zusatzstoffen für Dichten bis 1,55 g/cm^3". Technical report, AEA Technology QSA GmbH (2005).

[21] B. T. Cleveland, I. T. Lawson & J. C. Loach. "KCl in D_2O source". Technical report, SNO (2006).

[22] B. T. Cleveland. Private Communication (2006).

[23] Y. Nir-El. Private Communication (2006).

[24] NIST. `http://www.ncnr.nist.gov/resources/n-lengths/list.html`.

[25] B. T. Cleveland et al. *Astrophys J.*, **496** (1998) 505–526.

[26] C. S. N. Pouillet. *Compt. rend.*, **7** (1838) 24–28.

[27] C. A. Young. "The Sun". Appleton and Co. (1897).

[28] J. R. Mayer. "Beiträge zur Dynamik des Himmels in populärer Darstellung". Heilbronn: Johann Ulrich Landherr (1848).

[29] J. J. Waterston. *The Atenaeum*, **1351** (1853) 1099–1100.

[30] J. J. Waterston. *Phil. Trans. R. Soc.*, **183** (1892) 1–79.

[31] C. R. Darwin. "On the Origin of Species". Murray (1859).

[32] B. B. Boltwood. *Amer. J. Sci.*, **23** (1907) 77–88.

[33] J. L. Tassoul & M. Tassoul. "A Concise History of Solar and Stellar Physics". Princeton University Press (2004).

[34] T. C. Chamberlin. *Science*, **9** (1899) 12.

[35] W. D. Harkins & E. D. Wilson. *Phil. Mag.*, **30** (1915) 723.

[36] J. Perrin. *Annales de physique*, **xi** (1919) 90–91.

[37] J. Perrin. *La revue du mois*, **xxi** (1920) 158–164.

[38] A. S. Eddington. *Nature*, **106** (1920) 13.

[39] H. A. Bethe. *Phys. Rev.*, **55** (1939) 434–456.

[40] N. Grevesse, A. Noels & A. J. Sauval. *Astronomical Society of the Pacific Conference Series*, **99** (1996) 117–126.

[41] C. Arpesella et al. *Phys. Rev. C*, **57** (1998) 2700–2710.

[42] C. Broggini. *astro-ph/0308537*.

[43] L. Wolfenstein. *Phys. Rev. D*, **17** (1978) 2369.

[44] S. P. Mikhaev & A. Y. Smirnov. *Nuov. Cim.*, **9C** (1986) 17.

[45] S. J. Parke. *Phys. Rev. Lett.*, **57** (1986) 1275.

[46] M. Apollonio et al. *Phys. Lett. B*, **466** (1999) 415–430.

[47] K. Eguchi et al. *Phys. Rev. Lett.*, **90** (2003) 021802.

[48] T. Araki et al. *Phys. Rev. Lett.*, **94** (2005) 081801.

[49] Y. Fukuda et al. *Phys. Rev. Lett.*, **81** (1998) 1562–1567.

[50] S. Yamamoto et al. *Phys. Rev. Lett.*, **96** (2006) 181801.

[51] U. Seljak, A. Slosar & P. McDonald. *J. Cosmol. Astropart. Phys.*, **0610** (2006) 014.

[52] H. H. Chen. *Phys. Rev. Lett.*, **55** (1985) 1534–1536.

[53] J. A. Formaggio. "The True Depth of SNO". Technical report, The Sudbury Neutrino Observatory (2007).

[54] Q. R. Ahmad et al. *Phys. Rev. Lett.*, **87** (2001) 071301.

[55] Q. R. Ahmad et al. *Phys. Rev. Lett.*, **89** (2002) 011301.

[56] H. M. O'Keeffe. "Low Energy Background in the NCD Phase of the Sudbury Neutrino Observatory". Ph.D. thesis, University of Oxford (2008).

[57] O. Simard et. al. "Optical Calibrations in the NCD Phase". Technical report, The Sudbury Neutrino Observatory (2007).

[58] P.-L. Drouin. "FTN: A Time Fitter for the NCD Phase (UNIDOC)". Technical report, The Sudbury Neutrino Observatory (2008).

[59] P-L. Drouin. "FTN: A Time Fitter for the NCD Phase (Version 5.0)". Technical report, The Sudbury Neutrino Observatory (2008).

[60] R. MacLellan. "RSP for the NCD Phase". Technical report, The Sudbury Neutrino Observatory (2007).

[61] M. Huang. "Detection efficiency of external neutrons for NCD phase". Technical report, The Sudbury Neutrino Observatory (2007).

[62] G. Guillian. "A Summary of Measurements of the ^{24}Na Source Strength". Technical report, The Sudbury Neutrino Observatory (2008).

[63] G. Guillian et .al. "A Description of the Direct Counting Technique Used to Determine the NCD Neutron Capture Rate from Data". Technical report, The Sudbury Neutrino Observatory (2008).

[64] K. Boudjemline & S. Peeters. "Non-Uniformity Correction for Mixed ^{24}Na in the NCD Phase". Technical report, The Sudbury Neutrino Observatory (2008).

[65] N. A. Jelley et al. "Neutron topic committee final report". Technical report, The Sudbury Neutrino Observatory (2008).

[66] The SNO Collaboration. "SNOMAN User Manual". Technical report, The Sudbury Neutrino Observatory (2008).

[67] M. D. Lay. "Creation and Detection of Čerenkov Light in the Sudbury Neutrino Observatory". Ph.D. thesis, University of Oxford (1994).

[68] J. F. Breismeister. "MCNP-4C - A general Monte Carlo N-particle transport code". Technical report, Los Alamos National Laboratory (2000).

[69] W. R. Nelson. "The EGS4 Code System". Technical report, SLAC (1985).

[70] M. J. Lyon. "Neutron Transport in the Sudbury Neutrino Detector". Ph.D. thesis, University of Oxford (1996).

[71] P. F. Rose. "ENDF-201: ENDF/B-VI summary documentation". Technical report, BNL (1991).

[72] A. Hime and J. Heise. "(n,2n) corrections to the neutron capture efficiency". Technical report, The Sudbury Neutrino Observatory.

[73] G. Pauletta and F. D. Brooks. *Nucl. Phys. A*, **255** (1975) 267–274.

[74] A. B. McDonald et al. *Nucl. Phys. A*, **281** (1977) 325–344.

[75] D. R. Tilley et al. *Nucl. Phys. A*, **595** (1995) 409–480.

[76] R. Ford and H. Robertson. "Hydrogen Isotope Abundance in Heavy Water during NCD Phase of SNO (SNO-STR-2008-01)". Technical report, The Sudbury Neutrino Observatory (2008).

[77] R. Ford. Private Communication (2007).

[78] J. C. Loach. "The Neutral Current Detector Geometry in SNOMAN". Technical report, The Sudbury Neutrino Observatory (2004).

[79] J. C. Loach. "NCD Geometry Titles Banks". Technical report, The Sudbury Neutrino Observatory (2005).

[80] J. C. Loach. "The Thickness of the NCD Counter Walls". Technical report, The Sudbury Neutrino Observatory (2006).

[81] H. Robertson and J. Amsbaugh. Private Communication (2008).

[82] Jaret Heise. Private Communication (2006).

[83] Keith Rielage. Private Communication (2006).

[84] K. M. Heeger. "Model-Independent Measurement of the Neutral Current Interaction Rate of Solar ^{8}B Neutrinos with Deuterium in the Sudbury Neutrino Observatory". Ph.D. thesis, University of Washington (2002).

[85] C. Kraus. Private Communication (2008).

[86] S. Seibert. "Optical Effects of the NCD Anchors". Technical report, The Sudbury Neutrino Observatory (2006).

[87] B. G. Nickel. Private Communication (2004).

[88] M. R. Dragowsky et al. "Measurement of the ^{252}Cf Acrylic Source Standard". Technical report, The Sudbury Neutrino Observatory (2001).

[89] E. J. Axton. *Nucl. Stand. Ref. Data*, **214**.

[90] H. Märten et al. *J. NSE*, **106** (1990) 353.

[91] A. C. Wahl. *Atomic Data and Nuclear Data Tables 39*, **1** (1988) 1–156.

[92] H. Labranche, J. Law & B. G. Nickel. "Efficiency of neutron detection from ^{252}Cf source time series". Technical report, The Sudbury Neutrino Observatory (2003).

[93] H. Nifenecker et al. *Nucl. Phys. A*, **189** (1972) 285–304.

[94] International Commission on Radiation Units & Measurements (1977). Report No. 26 - Neutron Dosimetry for Biology and Medicine.

[95] G. Brunson. "Multiplicity and Correlated Energy Gamma Rays Emitted in the Spontaneous Fission of Californium-252 (LA-9408-T)". Technical report, LANL (1982).

[96] T. E. Valentine. "Evaluation of Prompt Fission Gamma Rays for Use in Simulating Nuclear Safeguard Measurements (ORNL/TM-1999/300)". Technical report, ORNL (1999).

[97] S. Croft. *Nucl. Instrum. Meth. A*, **281** (1989) 103–116.

[98] L. Van der Zwan. *Can. J. Phys.*, **46** (1968) 1527.

[99] J. S. Jayakar G. Venkataraman, Dayashankar. *Nucl. Instrum. Meth.*, **82** (1970) 49–50.

[100] B. K. Kamboj & M. G. Shahani. *Nucl. Instrum. Meth. A*, **244** (1986) 513–515.

[101] U. Fano. *Phys. Rev.*, **72**, 1 (1947) 26–29.

[102] H. R. Bilger. *Phys. Rev.*, **163** (1967) 238–253.

[103] Y. Nir-El. "Recent Measurements with the Ge Detector". Technical report, SNO (2004).

[104] AEA Technology QSA GmbH. Private Communication (2006).

[105] R. G. Helmer et al. *Nucl. Instrum. Meth. A*, **511** (2003) 360–381.

[106] E. L. Brady & M. Deutsch. *Phys. Rev.*, **78**, 5 (1950) 558–566.

[107] G. B. Lee, S. Ko & S. K. Nha. *New. Phys. (Korean Phys. Soc.)*, **32**, 4 (1992) 457–465.

[108] M. F. Annunziata. "Handbook of Radioactivity Analysis, Second Edition". Academic Press (2003).

[109] G. Norman et al. *Phys. Lett. B*, **519** (2001) 15–22.

[110] G. Norman. Private Communication (2006).

[111] W. R. Leo. "Techniques for Nuclear and Particle Physics Experiments: A How-To Approach". Springer (1994).

[112] B. T. Cleveland. "Ge detector deadtime". Technical report, SNO (2006).

[113] P. Rossi et al. *Phys. Rev. C*, **40** (1989) 2412–2415.

[114] H. Pierre Noyes. *Nucl. Phys.*, **74** (1965) 508–532.

[115] J.-W. Chen & M. J. Savage. *Phys. Rev. C*, **60** (1999) 065205.

[116] R. Moreh, T. J. Kennett & W. V. Prestwich. *Phys. Rev. C*, **39**, 4 (1989) 1247–1250.

[117] W. R. McMurray & C. H. Collie. *Proc. Phys. Soc. A*, **68**, 3 (1954) 181–188.

[118] G. R. Bishop et al. *Phys. Rev.*, **80**, 2 (1950) 211–222.

[119] H. M. O'Keeffe. "*In-situ analysis of the* H_2O ^{222}*Rn spike.*" Technical report, SNO (2006).

[120] H. M. O'Keeffe. "*In-situ analysis of the* D_2O ^{222}*Rn spike.*" Technical report, SNO (2006).

[121] National Nuclear Data Center. `http://www.nndc.bnl.gov/nndc/`.

[122] J. J. Simpson. "The Strength of the Strong Cf-Source and the Efficiency for Detecting Neutrons". Technical report, The Sudbury Neutrino Observatory (2002).

[123] M. R. Dragowsky and A. Hime. "Neutron Response and Efficiency for the Pure-D_2O Phase in SNO Draft v1.1". Technical report, The Sudbury Neutrino Observatory (2002).

[124] A. Hime. Private Communication (2004).

[125] C. Kanchanawarin. "Photon Mass Attenuation Coefficient of Heavy Water from 1 MeV to 20 MeV". Technical report, SNO (c1998).

[126] H. C. Evans. "Measurement of Gamma-ray Attenuation in Delrin". Technical report, The Sudbury Neutrino Observatory (2005).

[127] H. C. Evans. Private Communication (2005).

[128] P. Andre. *J. Phys. D: Appl. Phys.*, **29** (1996) 1963–1972.

[129] National Institute of Standards & Technology. `http://physlab2.nist.gov/PhysRefData/XrayMassCoef/cover.html`.

[130] O. Klein and T. Nishina. *Z. Physik*, **52** (1929) 853–868.

[131] C. Kraus. Private Communication (2008).

[132] E. Guillian. Private Communication (2008).

[133] H. Robertson. "Calibrating the Neutron Monte Carlo for the NCD Phase". Technical report, The Sudbury Neutrino Observatory (2008).

[134] R. Ford and H. Robertson. "Hydrogen Isotope Abundance in Heavy Water during NCD Phase of SNO". Technical report, The Sudbury Neutrino Observatory (2008).

[135] H. Robertson. "Uncertainties in the Neutron Monte Carlo in the NCD Phase". Technical report, The Sudbury Neutrino Observatory (2008).

[136] B. Aharmim et al. *hep-ex*, **arXiv:0806.0989v1**.

[137] G. Cowan. "Statistical Data Analysis". Oxford University Press (1998).

[138] L. C. Stonehill. "Deployment and Background Characterization of the Sudbury Neutrino Observatory Neutral Current Detectors". Ph.D. thesis, University of Washington (2005).

[139] B. Monreal. "NNNA spectra on N4 and J3". Technical report, The Sudbury Neutrino Observatory (2008).

[140] K. Rielage. "Proposal to Remove NCD Strings From Final NC Analysis". Technical report, The Sudbury Neutrino Observatory (2007).

[141] N. Tolich. Private Communication (2008).

[142] H. S. Wan Chan Tseung. "In preparation". Ph.D. thesis, University of Oxford (2008).

[143] B. Monreal. "PSA bump hunt: updates and new discoveries". Technical report, The Sudbury Neutrino Observatory (2008).

[144] J. A. Dunmore. "Separation of CC and NC Events in the Sudbury Neutrino Observatory". Ph.D. thesis, University of Oxford (2004).

[145] J. N. Bahcall, M. H. Pinsonneault & S. Basu. *Astrophys J.*, **555** (2001) 990.

[146] B. Jamieson. "NCD Phase Geometry and Roundoff Correction (MANN-7CDRV6)". Technical report, The Sudbury Neutrino Observatory (2008).

[147] J. Detwiler et al. "Livetime for the Full NCD Data Set". Technical report, The Sudbury Neutrino Observatory (2008).

[148] J. Secrest. "Energy Systematics for Phase III". Technical report, The Sudbury Neutrino Observatory (2007).

[149] S. Oser. "A Comment on Implementing the Angular Resolution Uncertainty in Sigex". Technical report, The Sudbury Neutrino Observatory (2008).

[150] A. Wright. "Systematic Uncertainties Associated with the Use of the ^{24}Na Neutron PDF". Technical report, The Sudbury Neutrino Observatory (2008).

[151] J. Monroe. Private Communication (2008).

[152] J. Monroe. "Monte Carlo Systematics (v2.0)". Technical report, The Sudbury Neutrino Observatory (2008).

[153] G. A. McGregor. "The Measurement of the Neutral Current Interaction at the Sudbury Neutrino Observatory". Ph.D. thesis, University of Oxford (2002).

[154] M. Dunford. "Measurement of the ^{8}B Solar Neutrino Energy Spectrum at the Sudbury Neutrino Observatory". Ph.D. thesis, University of Pennsylvania (2006).

[155] G. D. Orebi Gann. "An Improved Measurement of the ^{8}B Solar Neutrino Energy Spectrum at the Sudbury Neutrino Observatory". Ph.D. thesis, University of Oxford (2008).

[156] CERN Program Library Long Writeups. "D506 HEPDB" (1998).

[157] J. Goon. "MXF with Scott's SS method for the NCD Phase V 4.1". Technical report, The Sudbury Neutrino Observatory (2008).

[158] S. Oser. "An Example Where Conventional Systematic Error Propagation Fails". Technical report, The Sudbury Neutrino Observatory (2006).

[159] S. Oser. "Scott's Statistical Sampling (SSS) Method of Floating SNO Systematics". Technical report, The Sudbury Neutrino Observatory (2007).

[160] J. C. Loach. "A Comment on Scott's Statistical Sampling Method". Technical report, The Sudbury Neutrino Observatory (2007).

[161] B. Jamieson. "SNO NCD Phase Signal Extraction with Integration over Systematic Nuisance Parameters by Markov-Chain Monte-Carlo". Technical report, The Sudbury Neutrino Observatory (2008).

[162] N. Metropolis et al. *Journ. Chem. Phys.*, **21** (1953) 1087.

[163] W. K. Hastings. *Biometrika*, **57** (1970) 97.

[164] B. Jamieson. Private Communication (2008).

[165] H. M. O'Keeffe. "Čerenkov Tails in the D_2O region". Technical report, The Sudbury Neutrino Observatory (2008).

[166] J. Goon. "External Čerenkov Tails Analysis in the NCD Phase". Technical report, The Sudbury Neutrino Observatory (2008).

[167] J. Hosaka et al. *Phys. Rev. D*, **73** (2006) 112001.

[168] W. M. Yao et al. *Particle Data Group*, **33** (2006) 1–1232.

[169] S. J. Brice. "Monte Carlo and Analysis Techniques for the Sudbury Neutrino Observatory". Ph.D. thesis, University of Oxford (1996).

[170] H. Labranche. "Time Series Analysis for the Cf Source in the Sudbury Neutrino Observatory". Master's thesis, The University of Guelph (2003).

[171] H. Labranche, J. Law & B. G. Nickel. "Time series analysis of SNO ^{252}Cf source". Technical report, The Sudbury Neutrino Observatory (2003).

[172] J. T. Bushberg, J. A. Seibert, E. M. Leidholdt & J. M. Boone. "The Essential Physics of Medical Imaging". Lippincott Williams & Wilkins (2002).

[173] G. Kennedy. *Nucl. Instrum. Meth. A*, **299** (1990) 349–353.

[174] G. Gilmore & J. D. Hemmingway. "Practical Gamma-Ray Spectrometry". John Wiley & Sons (1995).

[175] N. A. Jelley. Private Communication (2006).

[176] M. Apollonio et al. *Phys. Lett. B*, **420** (1998) 397–404.

[177] R. Barlow & C. Beeston. *Comput. Phys. Commun.*, **77** (1993) 219–228.